

INFORMATION TO USERS

This manuscript has been reproduced from the microfilm master. UMI films the text directly from the original or copy submitted. Thus, some thesis and dissertation copies are in typewriter face, while others may be from any type of computer printer.

The quality of this reproduction is dependent upon the quality of the copy submitted. Broken or indistinct print, colored or poor quality illustrations and photographs, print bleedthrough, substandard margins, and improper alignment can adversely affect reproduction.

In the unlikely event that the author did not send UMI a complete manuscript and there are missing pages, these will be noted. Also, if unauthorized copyright material had to be removed, a note will indicate the deletion.

Oversize materials (e.g., maps, drawings, charts) are reproduced by sectioning the original, beginning at the upper left-hand corner and continuing from left to right in equal sections with small overlaps.

Photographs included in the original manuscript have been reproduced xerographically in this copy. Higher quality 6" x 9" black and white photographic prints are available for any photographs or illustrations appearing in this copy for an additional charge. Contact UMI directly to order.

**ProQuest Information and Learning
300 North Zeeb Road, Ann Arbor, MI 48106-1346 USA
800-521-0600**

UMI[®]

**Design, Simulation and Testing of
Micromachined Flexible Joints**

by

Heiko M. Fettig

Submitted
in Partial Fulfilment of the Requirements
for the Degree of

DOCTOR OF PHILOSOPHY

Major Subject: Mechanical Engineering

at

DALHOUSIE UNIVERSITY

Halifax, Nova Scotia

May, 2001

© Copyright by Heiko M. Fettig, 2001



**National Library
of Canada**

**Acquisitions and
Bibliographic Services**

**395 Wellington Street
Ottawa ON K1A 0N4
Canada**

**Bibliothèque nationale
du Canada**

**Acquisitions et
services bibliographiques**

**395, rue Wellington
Ottawa ON K1A 0N4
Canada**

Your file Votre référence

Our file Notre référence

The author has granted a non-exclusive licence allowing the National Library of Canada to reproduce, loan, distribute or sell copies of this thesis in microform, paper or electronic formats.

The author retains ownership of the copyright in this thesis. Neither the thesis nor substantial extracts from it may be printed or otherwise reproduced without the author's permission.

L'auteur a accordé une licence non exclusive permettant à la Bibliothèque nationale du Canada de reproduire, prêter, distribuer ou vendre des copies de cette thèse sous la forme de microfiche/film, de reproduction sur papier ou sur format électronique.

L'auteur conserve la propriété du droit d'auteur qui protège cette thèse. Ni la thèse ni des extraits substantiels de celle-ci ne doivent être imprimés ou autrement reproduits sans son autorisation.

0-612-63476-0

Canada

Dalhousie University
Faculty of Engineering

The undersigned hereby certify that they have examined, and recommend to the Faculty of Graduate Studies for acceptance, the thesis entitled "Design, Simulation and Testing of Micromachined Flexible Joints" by Heiko M. Fettig in partial fulfilment of the requirements for the degree of Doctor of Philosophy.

Dated: June 22 / 01

Supervisor:



Ted Hubbard

External Examiner:

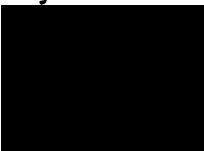



Niall Tait, Carleton University

Examiners:



Guy Kember



Marek Kujath


Dalhousie University
Faculty of Engineering

DATE: June 25, 2001

AUTHOR: Heiko M. Fettig

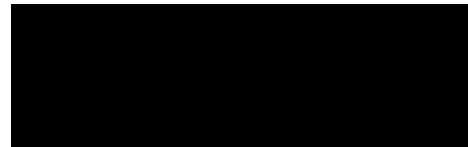
TITLE: Design, Simulation and Testing of Micromachined Flexible Joints

MAJOR SUBJECT: Mechanical Engineering

DEGREE: Doctor of Philosophy

CONVOCATION: October, 2001

Permission is herewith granted to Dalhousie University to circulate and to have copied for non-commercial purposes, at its discretion, the above thesis upon the request of individuals or institutions.

A large black rectangular box redacting the author's signature.

Signature of Author

The author reserves other publication rights, and neither the thesis nor extensive extracts from it may be printed or otherwise reproduced without the author's written permission.

The author attests that permission has been obtained for the use of any copyrighted material appearing in this thesis (other than brief excerpts requiring only proper acknowledgement in scholarly writing), and that all such use is clearly acknowledged.

In Memory of Dr. Adolf Fettig (1909 - 1998)
Citizen of the World

Table of Contents

List of Figures	ix
List of Tables	xii
Symbols and Abbreviations	xiv
Acknowledgements	xviii
Abstract	xx
1 Introduction	1
2 Micro-Machining and Micro-Joints	4
2.1 Surface Micromachining	4
2.1.1 Layer Deposition	4
2.1.2 Layer Patterning	5
2.1.3 Layout	7
2.1.4 Design Rules	9
2.1.5 Device Fabrication	10
2.2 Micro-Joints	12
2.2.1 Scaling Laws	12
2.2.2 Flexible Joints	14
3 Joint Types	16
3.1 Introduction	16
3.2 Design and Nomenclature	16
3.3 Kinematic Equivalents	20
3.4 Fabricated Joints	22
4 Standard Joint FE Analysis	24
4.1 Introduction	24
4.2 The Finite Element Method	24
4.2.1 Areas of Application	25
4.2.2 General Description of FEA	27
4.2.3 The Displacement Method	28
4.2.4 Coupled Energy Domains	30
4.3 FEA Models	30
4.3.1 FEA Software	30
4.3.2 Units	31
4.3.3 Material Properties	31
4.3.4 Solid vs Beam Model	32
4.4 FEA Methods	36
4.4.1 Modal Analysis	36
4.4.2 Non-Linear Static Analysis	37

5	Primary FEA Results	40
5.1	Introduction	40
5.2	Centre of Rotation	40
5.3	Resonant Modes	44
5.4	In-Plane Rotational Stiffness	46
5.5	In-Plane Axial Stiffness	50
6	Secondary FEA Results	55
6.1	Introduction	55
6.2	Out-of-Plane Rotational Stiffness	55
6.3	In-Plane Lateral Stiffness	62
6.4	Non-Linear Joint Stiffness	66
6.5	Centroides	69
7	Standard Joint Experiments	75
7.1	Introduction	75
7.2	Experimental Methods	75
7.2.1	Non-Contacting Laser Reflectance System	75
7.2.2	Aerodynamic Excitation	78
7.2.3	The 'Flick'-Test	80
7.2.4	Calculation of Corresponding Stiffnesses	83
7.3	Experimental Results	84
7.3.1	Aerodynamic Excitation	84
7.3.2	The 'Flick'-Test	86
7.3.3	Damping	87
7.4	Discussion	89
7.5	External Measurements	92
7.5.1	Compact Micro-Positioner	92
7.5.2	Atomic Force Microscopy	93
8	Joint Layout Variations	94
8.1	Introduction	94
8.2	Double Layer Joints	94
8.2.1	FEA Results	96
8.2.2	Experimental Results	101
8.2.3	Discussion	105
8.3	Joint Width Variations	106
8.4	Joint Spacing Variation: The Paper-Clip Joint	109
9	Joint Design Guidelines	112
9.1	Joint Observations	112
9.1.1	In-Plane Rotational Stiffness (K_{θ})	112
9.1.2	Out-of-Plane Rotational Stiffness (K_{ϕ})	112
9.1.3	Angular Range of Motion	113
9.1.4	Degrees of Freedom	113

9.1.5	I-Joint	114
9.1.6	Asymmetric Joints	114
9.2	Joint Selection Guide	116
9.2.1	Designing a Pseudo Slide (Slider) Joint	118
9.2.2	Designing a Pseudo Rotary (Pin) Joint	119
9.3	Examples for Joints as Part of Mechanisms	121
9.3.1	Flexural Motion Amplifiers	121
9.3.2	Three Degrees of Freedom Micro-Stage	124
10	Conclusion	128
11	References	131
A	Summary of Joint Properties	134
A.1	Joint Variation Identifiers	134
A.2	The ANSYS Co-Ordinate System	137
A.3	Total Unfolded Joint Length	138
A.4	H-Joints	139
A.4.1	Layout Schematics	139
A.4.2	FEA Results	141
A.4.3	Derived Equations	143
A.5	I-Joints	144
A.5.1	Layout Schematics	144
A.5.2	FEA Results	144
A.6	S-Joints	146
A.6.1	Layout Schematics	146
A.6.2	FEA Results	148
A.6.3	Derived Equations	149
A.7	U-Joints	150
A.7.1	Layout Schematics	150
A.7.2	FEA Results	152
A.7.3	Derived Equations	153
A.8	V-Joints	154
A.8.1	Layout Schematics	154
A.8.2	FEA Results	156
A.8.3	Derived Equations	157
A.9	X-Joints	158
A.9.1	Layout Schematics	158
A.9.2	FEA Results	161
A.9.3	Derived Equations	163
A.10	PC-Joints	164
A.10.1	Layout Schematics	164
A.10.2	FEA Results	165
A.10.3	Derived Equations	166

B	ANSYS Macros	167
	B.1 Interactive Session.....	167
	B.2 Creating an ANSYS Macro.....	170
	B.3 Using an ANSYS Macro.....	170
C	L-Edit Macros for Joint Creation	171
D	Experimental Procedures	172
	D.1 Aerodynamic Excitation	172
	D.2 The ‘Flick’-Test.....	174
E	MUMPs Chips Fabricated	175
F	Finite Element Analysis of MEMS Devices.	177
	F.1 Introduction.....	177
	F.2 Modelling MEMS	178
	F.2.1 Coupled Energy Domains	178
	F.2.2 Approaches.....	179
	F.2.3 Do It Yourself.....	179
	F.2.4 Specific Programs	180
	F.2.5 Commercial Simulation Packages	181
	F.3 Analysis Packages.....	182
	F.3.1 MEMS Packages	182
	F.3.1.1 MEMCAD.....	182
	F.3.1.2 IntelliSuite.....	185
	F.3.1.3 MEMS Pro.....	187
	F.3.2 General Packages	189
	F.3.2.1 ANSYS	189
	F.3.2.2 ABAQUS.....	193
	F.3.3 Comparison	194
	F.4 Conclusion.....	195
	F.4.1 Status Quo	195
	F.4.2 Recommendations	195
	F.5 References.....	197

List of Figures

2-1	Patterning of a Layer Using Photolithography	6
2-2	The Physical Layers of the MUMPs Process.	8
2-3	Fused Poly 1 Structure due to Violation of the Minimum Spacing Design Rule	10
2-4	Typical Deposition Process of a Cantilever Structure	11
3-1	The Six Basic Joint Shapes: H, I, S, U, V, X	17
3-2	Layout Schematic of the Joint-Mass Setup (Top and Side View)	18
3-3	The First Seven Prototypes (Small End-Mass).	19
3-4	Folded Joint Length L_f for Various Joints	20
3-5	Example Diagrams of Rigid Kinematic Pairs and Their Flexure Counterparts .	21
3-6	SEM Micrographs of the Six Basic Joints (CJ2 chip)	22
4-1	The Roof of the Olympic Stadium in Munich	25
4-2	Two-Dimensional Continuum Divided Into Triangular Elements	27
4-3	Solid Model of an H-Joint (close-up)	33
4-4	Beam Model of an H-Joint (close-up)	34
4-5	A Fishing Rod Demonstrates Geometric Non-Linearities	38
4-6	Loadsteps for In-Plane and Out-of-Plane Rotational Stiffness Calculations . .	39
5-1	Centre of Rotation for a Cantilever Beam	41
5-2	Calculation of the Centre of Rotation.	42
5-3	Centre of Rotation for U- and V-Joints for Different Joint Length (FEA). . . .	43
5-4	Mode Shapes of the First Four Modes of an H 50 Joint.	45
5-5	In-Plane Rotational Motion	46
5-6	In-Plane Rotational Stiffness K_θ for Various Joint Types and Lengths (FEA) .	47
5-7	Normalised In-Plane Rotational Stiffness $K_\theta \cdot (L/250\mu\text{m})$ for Various Joint Types and Lengths (FEA).	49
5-8	In-Plane Axial Motion	50
5-9	Axial Stiffness K_x for Various Joint Types and Lengths (FEA)	51
5-10	Normalised Axial Stiffness $K_x \cdot (L/250\mu\text{m})$ for Various Joint Types and Lengths (FEA)	54
6-1	In-Plane Versus Out-of-Plane Motion (Top View)	56
6-2	Out-of-Plane Rotational Stiffness K_ϕ for Various Joint Types and Lengths (FEA)	58
6-3	Normalised Out-of-Plane Rotational Stiffness $K_\phi \cdot (L/250\mu\text{m})$ for Various Joint Types and Lengths (FEA)	60
6-4	In-Plane Rotational Motion Due to Pure Moment (a) and Pure Force (b)	62
6-5	Two Degree of Freedom Motion	62
6-6	In-Plane Lateral Stiffness K_y for Various Joint Types and Lengths (FEA) . . .	64
6-7	Stiffness Non-Linearity in Applied Force for an H 100 joint.	66
6-8	Shape Change of an H-Joint During Axial Loading (FEA, exaggerated)	67

6-9	Shape Change of an H-Joint During Axial Loading by a Probe Needle (Large Force Used for Demonstration)	68
6-10	Fixed and Moving Centroides of a Joint Link System	70
6-11	Centroide of I 30, H 50, X 45, S 100 (Shaded Area Represents Joint Beam)	72
6-12	Radius of Curvature of a Centroide at Location of 0° COR	73
6-13	Radii of Curvature for Various Joint Types	74
7-1	Schematic of the Non-Contacting Laser Probe Microscope System	76
7-2	Photograph of the Non-Contacting Laser Probe Microscope System	77
7-3	The Hypodermic Needle Air Excitation Setup	78
7-4	Photograph of Resonating X-Joint with Laser Reflection (Aerodynamic Excitation)	79
7-5	Oscilloscope Trace of a Resonating X-Joint (Aerodynamic Excitation)	80
7-6	Manually Displaced Joint-Mass System	81
7-7	Recorded Oscilloscope Trace of a Decaying Oscillation of a U-Joint (‘Flick’-Test)	82
7-8	Recorded Spectrum Analyser Trace of the Transient Response of a U-Joint (‘Flick’-Test)	82
7-9	Two Joints Vibrating Side-by-Side	85
7-10	Destructive Power of Aerodynamic Excitation	86
7-11	Exponential decay of transient response: $\zeta = 0.06$ and $Q = 8$	88
7-12	In-Plane Rotational Stiffness K_{θ} for Various Joints (‘Flick’-Test and FEA)	89
7-13	Normalised In-Plane Rotational Stiffness $K_{\theta} \cdot (L/250 \mu\text{m})$ for Various Joints (‘Flick’-Test and FEA)	90
8-1	Layout of a Double Layer H 100 Joint (Top View and Cross-Section)	95
8-2	In-Plane Rotational Stiffness K_{θ} for Various Double Layer (DL) and Single Layer (SL) Joint Types and Lengths (FEA)	97
8-3	Axial Stiffness K_x for Various Double Layer (2) and Single Layer (1) Joint Types and Lengths (FEA)	98
8-4	Out-of-Plane Rotational Stiffness K_{ϕ} for Various Double Layer (2) and Single Layer (1) Joint Types and Lengths (FEA)	99
8-5	Normalised Out-of-Plane Rotational Stiffness $K_{\phi} \cdot (L/250 \mu\text{m})$ for Various Double Layer Joint Types and Lengths (FEA)	100
8-6	Destroyed Double Layer Joints as Delivered from Foundry	102
8-7	In-Plane Rotational Stiffness K_{θ} for Various Double Layer Joints (‘Flick’-Test and FEA)	103
8-8	Normalised In-Plane Rotational Stiffness $K_{\theta} \cdot (L/250 \mu\text{m})$ for Various Double Layer Joints (‘Flick’-Test and FEA)	104
8-9	H 100 and X 80 Along with Four Layout Variations	106
8-10	Transformation from H 25 to PC 25 Joint	109
8-11	Various H-Joints and the Corresponding PC-Joints	110
9-1	Schematic of a Flexural Motion Amplifier	121
9-2	Flexural Motion Clamping Mechanism (PS1 chip)	122

9-3	Motion of a Flexural Motion Amplifier (top: 0V, bottom: 6V, CJ2 chip)	123
9-4	3 DOF Parallel Manipulator Mechanism (Kinematic Representation)	124
9-5	Uni-Directional 3 DOF Micro-Stage with Long S-Joints (Layout, CM2 chip)	125
9-6	Uni-Directional 3 DOF Micro-Stage with Long S-Joints (SEM Micrograph, CM2 chip)	126
9-7	SEM Micrograph of Polysilicon Micro-Stage (Close-Up, CM2 chip)	127
A-1	The “World” and the ANSYS Co-Ordinate System	137
A-2	Geometric Layout of an H-Joint	139
A-3	Geometric Layout of an I-Joint	144
A-4	Geometric Layout of an S-Joint	146
A-5	Geometric Layout of an U-Joint	150
A-6	Geometric Layout of an V-Joint	154
A-7	Geometric Layout of an X-Joint	158
A-8	Geometric Layout of a PC-Joint	164

List of Tables

2-1	The MUMPs Physical Layers	7
2-2	The MUMPs Lithography Levels	9
2-3	Scaling of Stiffness, Mass, Deflection, Angular Deflection, Frequency and Reynolds Number	14
3-1	Fabricated Standard Joints	19
4-1	Mechanical Conversion Factors for MKS to μ MKS	31
4-2	Comparison Solid/Beam Model	35
5-1	FEA Predicted First- and Higher-Order Modes for Various Joints	44
5-2	In-Plane Rotational Stiffness K_{θ} of Various Joints (FEA)	46
5-3	In-Plane Axial Stiffness K_x of Various Joints (FEA)	50
5-4	Long Joints: Axial Stiffness K_x Governed by Joint Arm Angle	52
5-5	Short Joints: Axial Stiffness K_x Governed by Curved Joint Length	53
6-1	Out-of-Plane Rotational Stiffnesses K_{ϕ} of Various Joints (FEA)	55
6-2	“Safe” Distance d_0 for Various Joints (FEA)	63
6-3	Stiffness Variation for Various Joints Between a 10μ N Compression and a 10μ N Tension Load (FEA)	67
6-4	Angle of Centroides for Various Joints	71
6-5	Radii of Curvature of Centroides for Various Joints	73
7-1	Measured and FEA In-Plane Rotational Resonance Frequencies and Stiffnesses for Various Joints (Large End-Mass, Aerodynamic Excitation)	84
7-2	Measured and FEA In-Plane Rotational Resonance Frequencies and Stiffnesses for Various Joints (Small End-Mass, ‘Flick’-Test)	87
7-3	Measured and FEA Axial Stiffness of Various H- and X-joints (CMP)	92
7-4	Measured and FEA Axial Stiffness of Various H-joints (AFM)	93
8-1	Stiffnesses K_{θ} , K_x , K_{ϕ} of Various Double Layer Joints (FEA)	96
8-2	Measured and FEA In-Plane Rotational Resonance Frequencies and Stiffnesses for Various Double Layer Joints (‘Flick’-Test)	102
8-3	In-Plane Rotational and Axial Stiffnesses of Various H- and X-Joint Variations (FEA)	107
8-4	In-Plane Stiffnesses of Various PC-Joints and (H-joints) of Same Length (FEA)	110
9-1	In-Plane Stiffnesses for Standard Joints (FEA, Regression)	116
9-2	In-Plane Stiffness Trends for Standard Joints (FEA, Regression)	117
A-1	Identifiers of Examined Joint Variations (H, X, S)	135
A-2	Identifiers of Examined Joint Variations (I, U, V, PC)	136
A-3	Relation Between ANSYS and “World” Co-Ordinate System	137

A-4	Total Unfolded Joint Length.	138
A-5	H-Joint Variations.	139
A-6	Joint Segments of an H-Joint	140
A-7	H-Joint-Mass Resonance Frequencies (FEA).	141
A-8	H-Joint Stiffnesses (FEA).	142
A-9	I-Joint Variations	144
A-10	Joint Segments of an I-Joint	144
A-11	I-Joint-Mass Resonance Frequencies	144
A-12	I-Joint Stiffnesses (FEA)	145
A-13	S-Joint Variations	147
A-14	Joint Segments of an S-Joint.	147
A-15	S-Joint-Mass Resonance Frequencies (FEA).	148
A-16	S-Joint Stiffnesses (FEA)	149
A-17	U-Joint Variations.	150
A-18	Joint Segments of an U-Joint	151
A-19	U-Joint-Mass Resonance Frequencies (FEA).	152
A-20	U-Joint Stiffnesses (FEA).	153
A-21	V-Joint Variations.	155
A-22	Joint Segments of an V-Joint	155
A-23	V-Joint-Mass Resonance Frequencies (FEA).	156
A-24	V-Joint Stiffnesses (FEA).	157
A-25	X-Joint Variations.	159
A-26	Joint Segments of an X-Joint	160
A-27	X-Joint-Mass Resonance Frequencies (FEA).	161
A-28	X-Joint Stiffnesses (FEA).	162
A-29	PC-Joint Variations.	164
A-31	PC-Joint Stiffnesses (FEA).	165
A-30	Joint Segments of an PC-Joint	165
E-1	MUMPs Chips Designed by the Dalhousie MEMS Lab	175
E-2	Complete Chip Design Names	175
E-3	Chip Designers	176
F-1	ANSYS Licensing Options.	192
F-2	Comparison of Some Important Features of the Different Programs.	194

Symbols and Abbreviations

Abbreviations and Acronyms

AFM	Atomic Force Microscopy
CJ2	Compliant Joints 2 (MUMPs chip)
CMC	Canadian Microelectronics Corporation
CMP	Compact Micro-Positioner
COR	Centre of Rotation
CRC	Centre of Radius of Curvature
CVD	Chemical Vapour Deposition
DOF	Degrees of Freedom
DL	Double Layer
FE	Finite Element
FEA	Finite Element Analysis
FEM	Finite Element Method
FFT	Fast Fourier Transform
IPR	In-Plane Rotation
IP Rot	In-Plane Rotation
LPCVD	Low Pressure Chemical Vapour Deposition
MEM	Micro-Electro-Mechanical
MEMS	Micro-Electro-Mechanical Systems
MKS	Standard SI Unit System
μMKS	SI Unit System for Micro-Systems
MUMPs	Multi-User-MEMS-Processes
OPR	Out-of-Plane Rotation
OP Rot	Out-of-Plane Rotation
PECVD	Plasma Enhanced Chemical Vapour Deposition
Poly	Polysilicon
PSG	Phosphosilicate Glass
R	Rotary Joint
RT2	Ratcheting Torsional Motors 2 (MUMPs chip)
S	Slide Joint
SL	Single Layer
Tors	Torsion

Variables

A	Cross-Section
a	Square Cross-Section Width/Height
α	Angle Between Joint Arm and Joint Axis
b	Rectangular Cross-Section Width
d	Distance from Centre of Rotation
d_o	“Safe” Distance for the Application of Lateral Force Loads
δ	Deflection
E	Young’s Modulus
F	Force
\vec{F}	Nodal Force Vector
F_o	Pure Force
f	Resonance Frequency
f_{exp}	Experimentally Measured Resonance Frequency
f_i	i^{th} Natural Resonance Frequency
f_n	n^{th} Natural Resonance Frequency
f_ϕ	Out-of-Plane Rotational Resonance Frequency
f_θ	In-Plane Rotational Resonance Frequency
f_x	In-Plane Axial Resonance Frequency
G	Shear Modulus
Γ	Continuum Boundary
h	Rectangular Cross-Section Height
I	Cross-Sectional Moment of Inertia
I_{yy}	Mass Moment of Inertia about the Out-of-Plane Axis
\mathbf{K}	Stiffness Matrix
K	Stiffness
K_{bend}	Bending Stiffness of a Cantilever Beam
$K_{\text{bend, IP}}$	Bending Stiffness of a Cantilever Beam (In-Plane)
$K_{\text{bend, OP}}$	Bending Stiffness of a Cantilever Beam (Out-of-Plane)
K_{comp}	Axial Stiffness at a $10\mu\text{N}$ Compressive Load
K_ϕ	Out-of-Plane Rotational Stiffness
K	Torsional Section Property
K_θ	In-Plane Rotational Stiffness
$K_{\theta, \text{exp}}$	Experimentally Measured In-Plane Rotational Stiffness
$K_{\theta, \text{std}}$	In-Plane Rotational Stiffness (Standard Joint)

$K_{\theta, \text{var}}$	In-Plane Rotational Stiffness (Joint Variation)
K_{tens}	Axial Stiffness at a 10 μN Tensile Load
K_{tors}	Torsional Stiffness of a Cantilever Beam
K_x	In-Plane Axial Stiffness
$K_{x, \text{H}}$	In-Plane Axial Stiffness (H-Joint)
$K_{x, \text{PC}}$	In-Plane Axial Stiffness (PC-Joint)
$K_{x, \text{std}}$	In-Plane Axial Stiffness (Standard Joint)
$K_{x, \text{var}}$	In-Plane Axial Stiffness (Joint Variation)
K_y	In-Plane Lateral Stiffness
L	Total Unfolded Joint Length
L_a	Folded Length Anchor Side Joint Arm
L_b	Folded Length End-Mass Side Joint Arm
L_c	Curved Joint Length
L_f	Folded Joint Length
L_g	Gap Size
L_s	Static Joint Length
M	Moment
\mathbf{M}	Mass Matrix
M_o	Pure Moment
M_{rot}	In-Plane Rotational Moment
M_{up}	Out-of-Plane Rotational Moment
μ	Viscosity
μ_k	Kinematic Viscosity
ν	Poisson's Ratio
Ω	Continuum
ω_{damped}	Damped Circular Resonance Frequency
ω_i	Eigenvalue/ i^{th} Circular Resonance Frequency
ω_n	Undamped n^{th} Circular Resonance Frequency
$\vec{\phi}_i$	Eigenvector
ϕ	Out-of-Plane Angular Position/Deflection
Q	Quality Factor
R^2	Coefficient of Determination
Re	Reynolds Number
ρ	Density
s	Scale Factor

t	Time
θ	In-Plane Angular Position/Deflection
\vec{u}	Nodal Displacement Vector
v	Linear Velocity
x	In-Plane Axial Position (parallel to the joint-mass arms)
X	In-Plane Axial Position (ANSYS)
y	In-Plane Lateral Position
Δy	In-plane Lateral Displacement
Δy_{rot}	In-plane Lateral Displacement Due to Rotation
Δy_{trans}	In-plane Lateral Displacement Due to Translation
Y	Out-of-Plane Lateral Position (ANSYS)
z	Out-of-Plane Lateral Position
Z	In-Plane Lateral Position (ANSYS)
ζ	Damping Factor

Glossary

Centre of Joint	Centre of the line connecting the end-points of the joints
Centrode	Path on which the centre of rotation travels during loading
Pseudo Rotary Joint	Two or three DOF joint whose translational compliances are negligible relative to its rotational compliance
Pseudo Slide Joint	Two or three DOF joint whose second translational and rotational compliances are negligible relative to its first translational compliance
Pure Rotary Joint	One DOF joint with rotational freedom
Pure Slide Joint	One DOF joint with translational freedom
Rotary-Slide Joint	Two DOF joint with rotational and translational freedom

Trademarks

ABAQUS is a trademark of Hibbitt, Karlsson & Sorensen, Inc.

ANSYS is a trademark of Ansys Inc.

GDSII is a trademark of Calma, Valid, Cadence.

IntelliSuite is a trademark of IntelliSense Corporation.

L-Edit is a trademark of Tanner Research Inc.

MEMCAD is a trademark of Coventor Inc.

MEMS Pro is a trademark of MEMSCAP Inc.

MUMPs is a trademark of Cronos Integrated Microsystems, A JDS Uniphase Company.

Acknowledgements

This thesis would not have been possible without the continued help and support of a lot of people. Studying and conducting research in a foreign country can be difficult and the author would like to thank everybody who helped making it as easy as it was.

First I would like to thank my supervisor Dr. Ted Hubbard for fighting the administration in order to make my stay at Dalhousie University possible in the first place and for the continued support and supervision of my work during the last three years. I doubt that I could have had a more dedicated supervisor anywhere else.

Special thanks also go to Dr. Marek Kujath for planting the idea in my head of folding long slender beams into various shapes to form joints. I would also like to thank him for continuously trying to teach a physicist to think like an engineer. I do not know if he succeeded but he did try.

I would like to thank Dr. Guy Kember for his support on the mathematical side of my research and for suggesting the investigation of asymmetric joints.

Special thanks go to all the members of the Dalhousie MEMS Lab who, in one way or another, supported my research: James Wylde and Ryan Hickey for their continued support and input; Yongjun Lai, Ralph Wilke and Dan Sameoto for helping me out with pictures and measurements; the micro-positioner design team Laura, Paul, Robert, and Gavin for providing me with axial stiffness measurements; Dr. Manfred Jericho from the Department of Physics for letting me use his AFM stiffness measurements.

For their input on the simulation part of this thesis I would like to thank the members of the CAE group of the Institute for Machine and Automotive Design of the University of Karlsruhe, namely Pascal Häußler, Ottmar Müller, and Bernd Ilzhöfer.

I would like to thank the faculty and staff of the Department of Mechanical Engineering, especially Peter Jones, and Greg Jollimore for their continued support.

The author would like to acknowledge financial support by the Dalhousie Faculty of Graduate Studies, the Estate of Bruce and Dorothy Rosetti, and the Estate of George and Lucille Reid.

A very special thanks goes to Suzanne Kolmer and her staff at International Student Services and the DalTech Student Service Centre for their continued help with administrative and other problems during the last years.

During the last three years a lot of people here in Canada and back home in Germany have helped me stay sane and made me feel at home in a foreign country. I would like to thank all of them and especially the Chaddock family, the Schöpfes, Ryan and Stacey, Pauline and Lucas, Pascal, Leslie, Suzanne, James and Nicole, Jens and Annie, and the Crombies.

Last but not least I would like to thank my parents and my sister for their love and support. I could not have done it without you. I am sorry that I am so far away but I inherited my grandfather's travel bug. I love you.

Abstract

This thesis examines the design, simulation and testing of micromachined flexible joints. Micromachined devices or MEMS (Micro-Electro-Mechanical Systems) combine mechanical parts as well as electronic parts on a micro-scale. The objective of this research is to mimic the kinematics of classical macro rotating and sliding joints with flexural micro-joints.

The joints consist of long slender beams that are folded in a variety of shapes: 'I', 'H', 'X', 'S', 'U' and 'V' shaped joints are considered. Finite element simulations are used to calculate in-plane rotational, axial and lateral stiffness, out-of-plane rotational stiffness and examine the effect of variations in joint length and beam angles.

The simulation results are compared to a series of dynamic tests of polysilicon micro-machined joints. The resonant frequencies of joint-mass systems are measured using a non-contacting laser reflectance system and the derived experimental in-plane rotational stiffnesses are found to agree with simulations.

Design guidelines for the selection of the best suited joint shape and length for given functional requirements such as directional stiffness, selective compliance, and range of motion are presented. Two examples of joint use in planar micro-mechanisms are given.

1 Introduction

In 1959 the renowned physicist Richard Feynman [7, 8] first predicted the development of MEMS - Micro-Electrical-Mechanical Systems [26]. In the early 1970s the first micro-machined product was produced: ink jet nozzles. Today, about 25 years after the introduction of the first micro-machined product to the market, MEMS research is increasing rapidly.

The name MEMS - Micro-Electro-Mechanical Systems - refers to the fact that MEMS devices combine mechanical parts as well as electronic parts on a micro-scale.

Probably the most prominent examples of MEMS devices are ink jet nozzles and the accelerometers which release the airbags in a modern car. Researchers all over the world are currently working on MEMS devices in areas as different as the aerospace industry and DNA analysis.

New fabrication technologies have further decreased the minimum size of manufacturable devices, giving rise to problems associated with area forces, which predominate on the micro-scale. Increased sliding friction and stiction severely limit the use of sliding or rotating structures, such as pin- or slider-joints.

This thesis examines the possibility of taking long slender beams and folding them into a variety of shapes to connect two links at a fixed distance. Using finite element analysis models of 93 variations of joints were analysed. The models were used to calculate joint stiffnesses in various directions as well as resonant modes and frequencies.

Chapter 2 gives background information about the surface micromachining process, and introduces the motivation behind designing flexible joints.

Chapter 3 introduces the basic designs of the flexible joints examined in this thesis. It explains the nomenclature ('H', 'I', 'S', 'U', 'V', 'X') and how experimental considerations influenced the design of the joints. SEM micrographs of some of the fabricated joints are shown.

Chapter 4 introduces Finite Element Analysis and the choice of software. It explains the reasoning behind using beam models and describes the calculation methods used in this thesis.

Chapter 5 presents the primary results of the FE analysis. Results for centres of rotation and stiffnesses for the in-plane rotational and in-plane axial directions are presented.

Chapter 6 presents FEA results for joint properties that exist along with the desired stiffnesses presented in the previous chapter. It discusses out-of-plane motion, non-linear joint behaviour, and joint response to force loading. It introduces centrodes and procedures to calculate the radii of curvature of the centrodes. The results of these calculations are presented and discussed.

Chapter 7 introduces the experimental methods used to measure the resonance frequencies of fabricated joints. The joints were included in joint-mass systems which allowed the measurement of the resonant frequency through aerodynamic excitation and transient response analysis. The experimental results are compared to the simulation results and found to be in good agreement.

Chapter 8 presents variations of the standard joint layout and examines their influence on joint behaviour. Double layer joints and joints with non-constant width are introduced. A variation of the H-joint, the Paper-Clip joint, is examined.

Chapter 9 derives rules from the previously presented results and presents guidelines for designing joints for use in planar mechanisms. Using trends found in the simulation results rules are derived, and joint design and joint selection guidelines are formulated. These will allow designers of planar micro-mechanisms to choose the right joint for their requirements without the need of an extensive trial and error approach. The chapter also introduces some example mechanisms that use the joints discussed in this thesis.

Contributions of the Thesis

This research presents the first attempt to systematically investigate flexible micro-joints using finite element analysis and dynamic testing. The FEA results are verified by comparison to experimental measurements. Conclusions are drawn from the simulation results and generalisable guidelines are presented.

Limitations of the Thesis

The joints examined in this thesis were designed for fabrication using the Cronos MUMPs process. The numerical results presented and some of the encountered effects related to the minimum width and the thickness of the joint beams are specific to the MUMPs process. The derived guidelines, however, are generalisable and similar results should be obtainable using different foundry processes.

Since the examined joints were designed for the use in planar micro-mechanisms this thesis concentrates on the examination of planar motion and related effects. Only specific properties, primarily in-plane rotational, axial, and lateral stiffnesses, out-of-plane rotational stiffnesses, as well as centredes were examined.

2 Micro-Machining and Micro-Joints

This chapter gives background information about the surface micromachining process, and introduces the motivation behind designing flexible joints.

2.1 Surface Micromachining

The most wide spread fabrication methods for MEMS devices are bulk and surface micromachining. The research described in this thesis only involves surface micromachined structures. There are a large number of different processes for surface micromachining. However, all of them have the same basic concepts in common.

A number of different layers are stacked vertically on top of a silicon wafer. They usually start with a structural layer directly on top of the wafer followed by alternating sacrificial and structural layers. Depending on the process additional layers may be included.

Structural layers make up the final structures. Two structural layers are usually separated by a sacrificial layer. After all layers have been deposited and patterned the sacrificial layers are removed using a release etchant. Holes in the sacrificial layers provide contacts between the structural layers. Chapter 2.1.5 on page 10 outlines the typical fabrication process of a cantilever structure.

2.1.1 Layer Deposition

Although a wide variety of materials can be used in surface micromachining the most common materials are polysilicon (Poly), phosphosilicate glass (PSG), and metals.

The layers are deposited using a variety of different processes. The choice of process depends on the type of layer deposited. Processes include thermal oxidation, low pressure chemical vapour deposition (LPCVD), chemical vapour deposition (CVD), plasma enhanced vapour deposition (PECVD) and others. The choice of process along with the material and the thickness determines the residual stress in the layer. Furthermore, certain materials can only be deposited using certain processes.

Metal layers (e.g. aluminium, gold, etc.) are usually deposited by evaporation or sputtering. These layers are commonly used for electrical connections, or as surfaces for mirrors or bonding pads.

The fact that different processes require different temperatures limits the order of layers deposited. For example, once an aluminium layer has been deposited, processes that require temperatures of more than 660°C, the melting point of aluminium, cannot be used any more. Furthermore, around 900°C recombination begins in doped silicon, causing transistors to fail.

2.1.2 Layer Patterning

Once a layer is deposited (Figure 2-1b on page 6) onto the substrate (Figure 2-1a) it is patterned using photolithography. A liquid film of photoresist is deposited on top of the layer to be patterned by placing a drop in the centre of the wafer and spreading it by spinning the wafer (Figure 2-1c). In a photographic process, the UV sensitive photoresist is patterned using an optical stepper or an electron beam (Figure 2-1d).

An optical stepper uses basic geometrical shapes like rectangles or triangles to approximate the desired pattern. Using optical lens systems the shapes can be reduced in size to reach minimum feature sizes as low as 0.35 μm . Due to restrictions in the wavelength of light used in this process it is not expected to ever reach minimum feature sizes under 0.1 μm . Utilising an electron or ion beam and a process similar to the scanning of a television picture feature sizes of less than 0.1 μm can be achieved. Unfortunately the cost of the equipment seems to be inversely proportional to the minimum feature size.

Using an etchant, which only etches photoresist but not any of the other layers, all exposed photoresist is removed creating an image of the mask made out of photoresist on top of the layer to be patterned (Figure 2-1e). With a second etchant, which only etches the layer to be patterned but not the photoresist, the pattern is transferred to the layer (Figure 2-1f). Finally, using a third etch, the remaining photoresist is stripped (Figure 2-1g). What remains is the patterned layer.

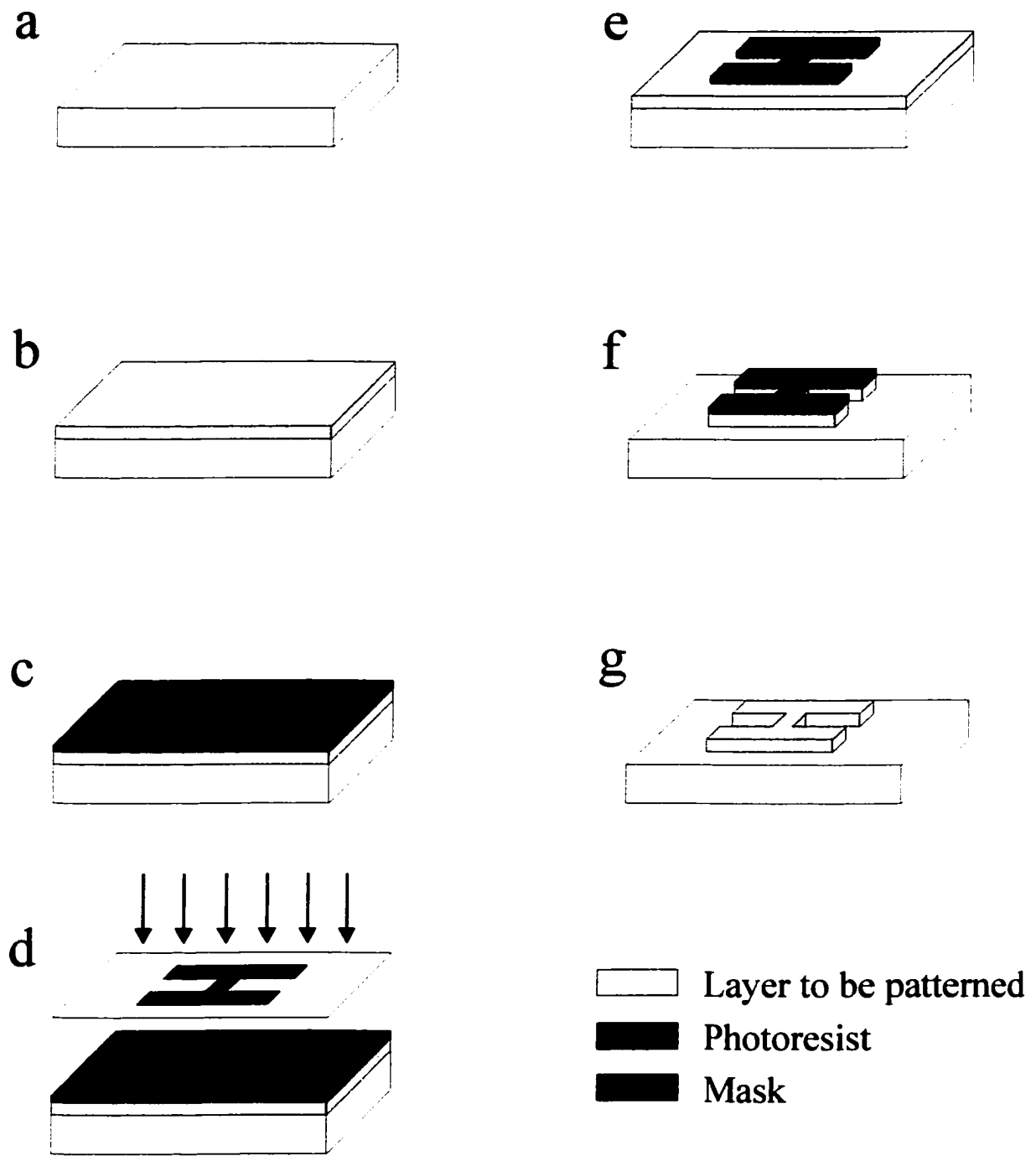


Figure 2-1: Patterning of a Layer Using Photolithography

2.1.3 Layout

All devices created for this thesis were fabricated using the Cronos MUMPs (Multi-User-MEMS-Processes) process. Figure 2-2 on page 8 shows the physical layers of the MUMPs process while Table 2-1 shows a list of the physical layers and the corresponding lithography levels used in the computer layout process.

Table 2-1: The MUMPs Physical Layers^a

Physical Layer	Material	Thickness [μm]	Lithography Level Names
Nitride	Silicon Nitride	0.6	
Poly 0	Polysilicon	0.5	POLY0 HOLE0
First Oxide	Phosphosilicate Glass (PSG)	2.0	DIMPLE ANCHOR1
Poly 1	Polysilicon	2.0	POLY1 HOLE1
Second Oxide	Phosphosilicate Glass (PSG)	0.75	POLY1_POLY2_VIA ANCHOR2
Poly 2	Polysilicon	1.5	POLY2 HOLE2
Metal	Gold	0.5	METAL HOLEM

a. see [17] p. 11

Design layouts are created using a 2.5D CAD process. Using computer software (in this thesis MEMS Pro/L-Edit) the design is created by drawing structures onto different levels, so-called lithography levels. To simplify the layout process different lithography levels can be used to shape the same physical level.

There are two types of lithography levels: negative and positive levels, sometimes known as dark and light levels. Positive levels are patterned by drawing the structures that will be present in the actual design, while on negative levels the structures drawn will be removed from the corresponding physical layer, i.e. the holes are drawn. All structural layers POLY n as well as METAL are positive levels. ANCHOR n and all other levels are negative. Table 2-2 on page 9 lists all the lithography levels and their purposes.

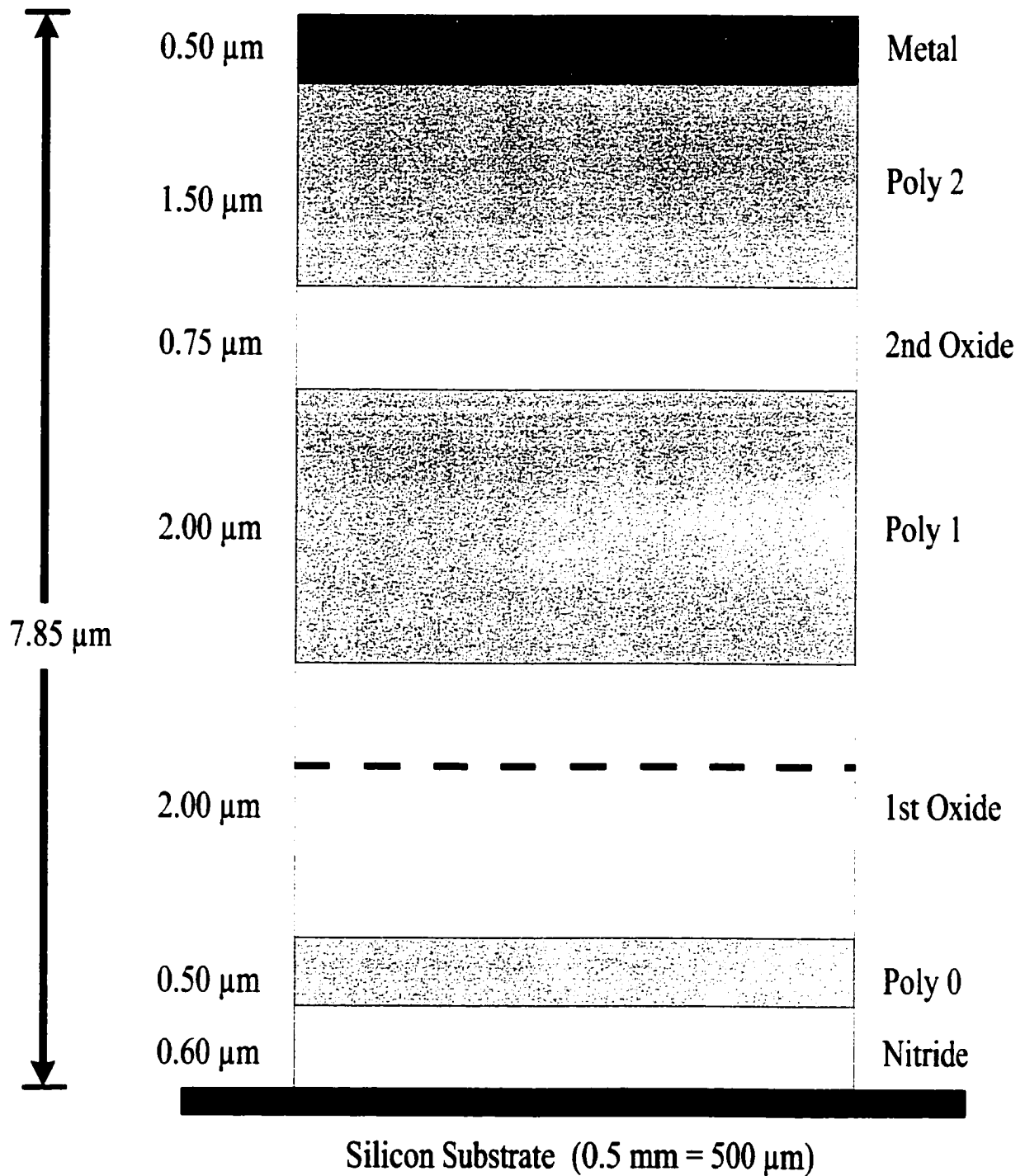


Figure 2-2: The Physical Layers of the MUMPs Process.

Table 2-2: The MUMPs Lithography Levels^a

Lithography Level Name	Level Type	Purpose
POLY0	positive	pattern ground plane
ANCHOR1	negative	open holes for Poly 1 to Nitride or Poly 0 connection
DIMPLE	negative	create dimples/bushings for Poly 1
POLY1	positive	pattern Poly 1
POLY1_POLY2_VIA	negative	open holes for Poly 1 to Poly 2 connection
ANCHOR2	negative	open holes for Poly 2 to Nitride or Poly 0 connection
POLY2	positive	pattern Poly 2
METAL	positive	pattern Metal
HOLE0	negative	provide holes for POLY0
HOLE1	negative	provide release holes for POLY1
HOLE2	negative	provide release holes for POLY2
HOLEM	negative	provide release holes in METAL

a. see [17] p. 12

There are almost twice as many lithography levels used in the computer layout process than actual physical layers present. Extra levels like HOLE1 or ANCHOR2 are provided to simplify the design of etch holes, connections between Poly 2 and Poly 0, etc. To avoid confusion lithography levels are spelled in capital letters without blank spaces while the actual physical layers are described using regular spelling.

2.1.4 Design Rules

MUMPs is a multi-user process. This means that chip designs from numerous clients are collected and fabricated next to each other on the same wafer. Design errors on a chip that result in free floating structures after the release etch can therefore seriously contaminate the neighbouring chips. In order to avoid this, Cronos has set 26 mandatory and 19 advisory design rules.

The mandatory design rules dictate the minimum feature size and spacing of objects on different levels, as well as the separation of release etch holes on Poly 1 and Poly 2 structures. The minimum feature size and spacing is governed by the physical patterning proc-

ess. Large Poly 1 or Poly 2 structures need etch holes at a specific separation in order for them to be completely released. Violating these mandatory design rules will result in unconnected, fused, or unreleased structures.

For MUMPs the minimum feature size and spacing is $2\ \mu\text{m}$.

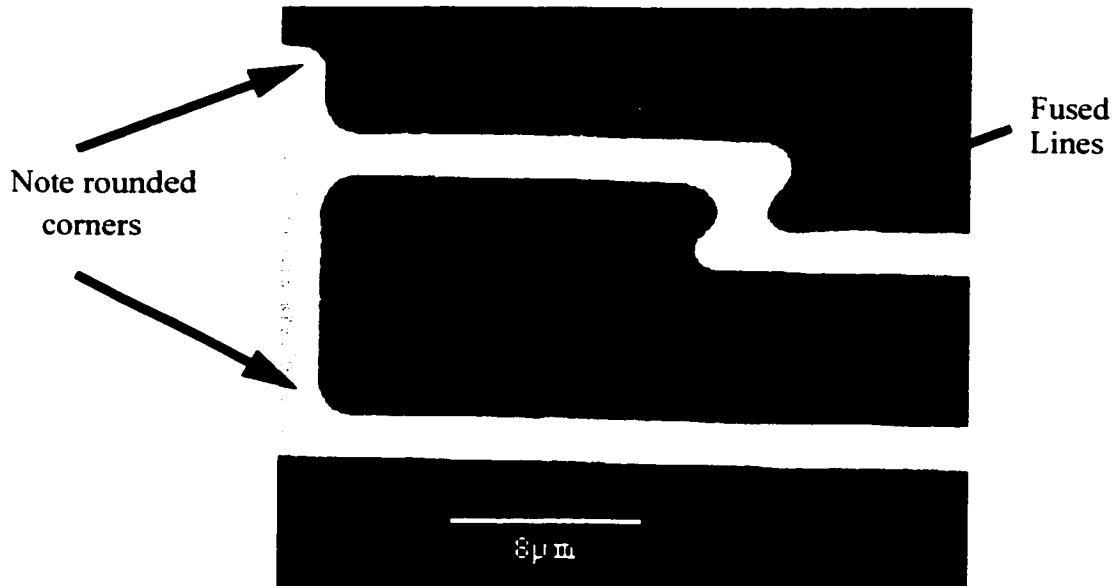


Figure 2-3: Fused Poly 1 Structure due to Violation of the Minimum Spacing Design Rule

The advisory design rules regulate interaction between structures on different levels. For example, layers can only be stacked in certain ways. The rules are based on experience from previous runs. If these rules are followed Cronos guarantees that the design will be fabricated.

2.1.5 Device Fabrication

Figure 2-4 on page 11 shows the typical deposition process for a cantilever structure. First a sacrificial layer (Figure 2-4b) is deposited onto the substrate (Figure 2-4a) and patterned as described in Chapter 2.1.2 on page 5 (Figure 2-4c). Next a structural layer is deposited (Figure 2-4d) and patterned (Figure 2-4e). Finally the sacrificial layer is etched away, releasing the cantilever structure (Figure 2-4f).

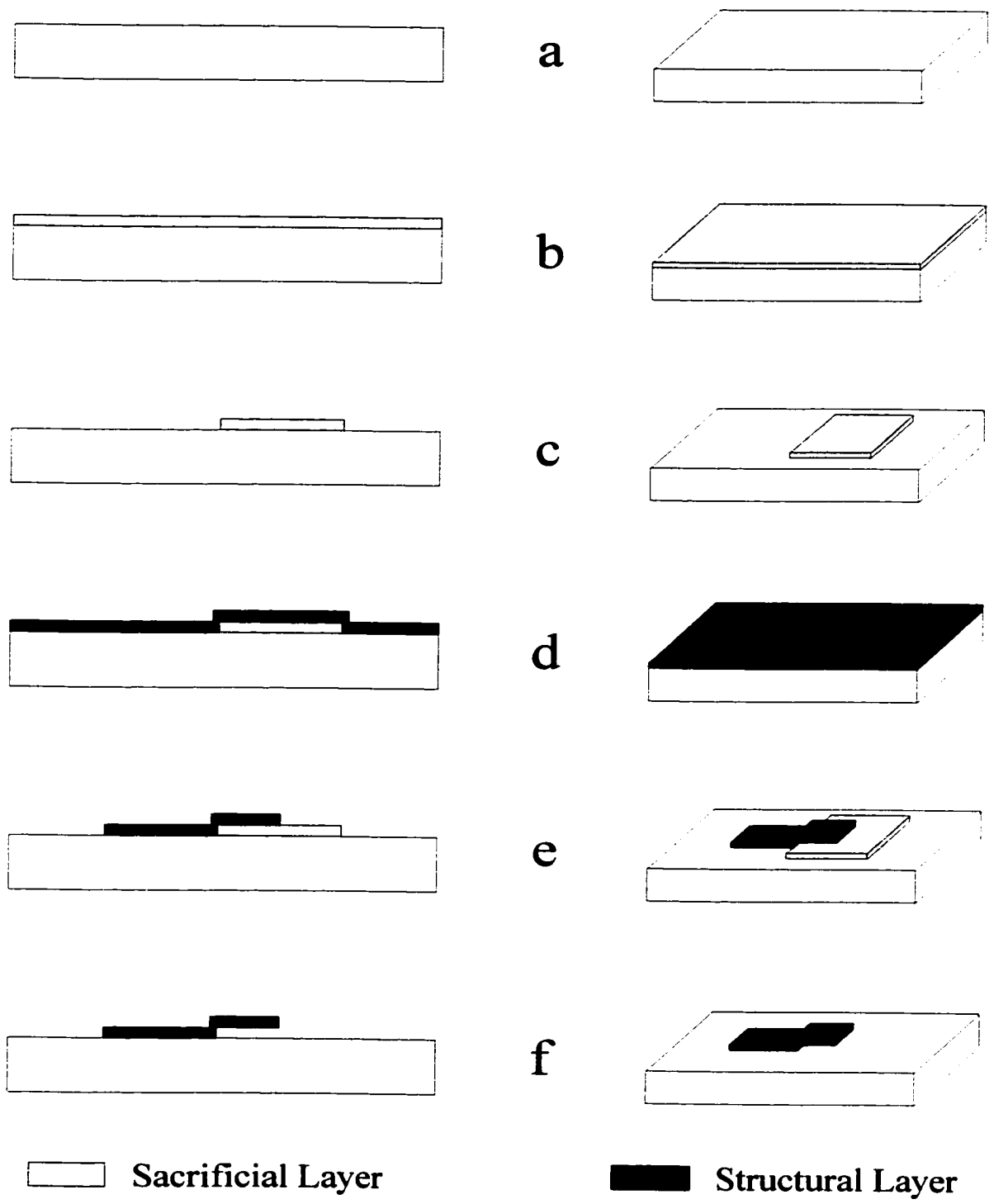


Figure 2-4: Typical Deposition Process of a Cantilever Structure

2.2 Micro-Joints

As laid out in the previous section, surface micromachining uses sacrificial layers to form thin, high resolution structures on the surface of a silicon wafer with overall dimensions in the $100\mu\text{m}$ to $1000\mu\text{m}$ range and feature sizes of approximately $1\mu\text{m}$ to $10\mu\text{m}$. Complex micro-structures that mimic macro-scale mechanical devices have been constructed. As on the macro-scale, the output motion can be reduced or amplified by the use of mechanisms such as bar linkages with sliding or rotating joints. On the micro-scale, high sliding friction and high wear rates dramatically limit the use of members involving surface contact and sliding.

Another limiting factor on the micro-scale is an effect known as stiction. It refers to the effect that cantilevered structures that come into physical contact with the surface usually stick to it. The effect is not well understood but is generally assumed to be related to residual moisture from release etches and humidity. This moisture is believed to cause the structures to stick to the surface through surface tension.

2.2.1 Scaling Laws

When a macro-scale mechanism design is transferred to the micro-scale, adjustments have to be made to take into account the fact that physical properties and effects scale differently during size reduction. This effect is commonly referred to as the scaling laws.

For example, a cube with an edge length of 1 m has a surface area of 6 m^2 and a volume of 1 m^3 . Its surface to volume ratio is $6/\text{m}$. A cube with an edge length of $1\mu\text{m}$ on the other hand has a surface area of $6\mu\text{m}^2$ and a volume of $1\mu\text{m}^3$. Its surface to volume ratio is $6/\mu\text{m}$ or $6,000,000/\text{m}$. It is obvious that this dramatic increase in the surface to volume ratio will result in a change of the dominant forces during the transition from macro- to micro-scale. While in the macro-scale body (i.e. volume related) forces like weight dominate, area related forces such as friction or stiction tend to reduce the importance of body forces to negligibility on the micro-scale.

Therefore design parts that involve surface contact and sliding have to be replaced by more suitable designs on the micro-scale.

Consider a simple cantilevered beam. The stiffness K is given by:

$$K \propto \frac{EI}{L^3} \propto E \frac{bh^3}{L^3} \quad (2-1)$$

where E is the Young's modulus, I is the cross-sectional Moment of inertia of the beam ($= bh^3/12$ for a rectangular cross-section with width b and height h) and L is the beam length. If all dimensions b , h , and L are scaled by a factor s , the stiffness is proportional to $\frac{s s^3}{s^3} = s$.

The deflection due to gravity δ is given by:

$$\delta = \frac{mg}{K} \propto \frac{\rho bhL}{K} \propto \frac{\rho L^4}{E h^2} \quad (2-2)$$

The deflection is proportional to $\frac{s^4}{s^2} = s^2$.

The angular deflection due to gravity θ is given by:

$$\theta = \frac{\delta}{L} \propto \frac{\rho L^3}{E h^2} \quad (2-3)$$

The angular deflection is proportional to $\frac{s^3}{s^2} = s$.

The scaling of the resonance frequency f can be found from the deflection:

$$f = \frac{1}{2\pi} \sqrt{\frac{g}{\delta}} \propto \sqrt{\frac{E h^2}{\rho L^4}} \quad (2-4)$$

The frequency is proportional to $\sqrt{\frac{s^2}{s^4}} = \frac{1}{s}$. Measurements of resonance and free decay frequencies of oscillations are important because stiffness is difficult to measure on the micro-scale. Knowing the natural frequency f_n allows the computation of the stiffness from the relation $f_n = \sqrt{K/m}$. The mass m can be reasonably accurately computed.

The Reynolds number Re is given by:

$$Re = \frac{\rho v L}{\mu} = \frac{v L}{\mu_k} \propto \frac{f L^2}{\mu_k} \quad (2-5)$$

where v is the linear velocity, L is the length of the object, ρ is the density of the fluid, μ is the viscosity of the fluid, and μ_k is the kinematic viscosity of the fluid. The Reynolds number is proportional to $\frac{1}{s^2} = s$.

Thus, if a 1 cm pin-joint (in air) is shrunk by a factor of 1,000 to $10\mu\text{m}$, the Reynolds number decreases by a factor of 1,000 as well. Therefore the micro-joint is effectively surrounded by a 1,000 fold more viscous fluid, say glycerin or heavy machine oil.

Table 2-3 summarises the previous scaling equations.

Table 2-3: Scaling of Stiffness, Mass, Deflection, Angular Deflection, Frequency and Reynolds Number

Property	Scaling
Surface Area / Volume	$1/s$
Stiffness K	s
Mass m	s^3
Deflection δ	s^2
Angular Deflection θ	s
Frequency f	$1/s$
Reynolds Number Re	s

2.2.2 Flexible Joints

The pin-joints used in macro-scale mechanisms are often unsuitable for micro-devices. The nature of surface micro-machining and the design rules of the MUMPs process make it almost impossible to connect two free arms using a pin-joint. The MUMPs process features three structural layers but only two of those can be released. To form a pin-joint, however, a third layer would be needed in order to prevent the members from constantly disconnecting. Design rules that require a $4\mu\text{m}$ gap between the pin and the connecting member also drastically limit the design of pin-joints.

In addition, as seen above, micro-machines operate at very low Reynolds number. Therefore viscous forces dominate along with friction and high wear rates, further limiting the use of pin-joints.

In their place, compliant mechanisms with flexure joints can be used. The flexure joints can have the form of long slender beams possibly folded so as to be more compact. Compliant members that bend rather than slide have been used both at the macro-scale [19, 20] and at the micro-scale [6, 21, 22, 29]. The function of kinematic joints is to constrain and control motion of connected links. Typically, the motion is constrained in most directions (axes) and controlled in one or two directions.

There are two main disadvantages to flexure joints:

1. They are not totally compliant in the direction of motion, they have a finite stiffness.
2. They are not totally stiff in the directions of the constraints.

The design of surface micromachined joints is limited by the fabrication technology which imposes restrictions on joint dimensions, minimum widths and maximum thicknesses. For example, surface micromachined structures are relatively thin compared to their planar dimensions, with typical maximum height to width aspect ratios of 1 to 2. Thus, such joints are relatively stiff in-plane and relatively compliant out-of-plane, complicating the design of flexible micromachined joints.

Chapter 3 introduces the proposed designs of flexural joints examined in this thesis.

3 Joint Types

This chapter introduces the basic designs of the flexible joints examined in this thesis. It explains the nomenclature and how experimental considerations influenced the design of the joints. SEM micrographs of some of the fabricated joints are shown.

3.1 Introduction

As mentioned in Chapter 2.2 the use of pin-joints on the micro-scale is severely limited. In order to build micro-mechanisms a replacement for pin-joints has to be found. This thesis examines a variety of flexural joints.

Pseudo classical kinematics can be achieved from flexure of a specially designed beam. Although the motion from these joints is realised by flexure or bending, a properly designed compliant mechanism can allow motion that is primarily rotational or primarily translational.

In order to increase the joint's rotational compliance, the beam length can be increased. To reduce the joint linear size or footprint, the beam can be 'folded' into a variety of shapes. Joints shaped in forms resembling letters, 'H', 'I', 'S', 'U', 'V', 'X', are considered in this research. Figure 3-1 on page 17 shows the computer layouts of these six basic joints.

3.2 Design and Nomenclature

The most interesting properties of the different joint designs are their stiffnesses in different directions, namely in-plane rotation and axial translation. Stiffnesses can be challenging to measure on the micro-scale due to the difficulty in applying a known force or measuring the reaction force caused by a specific displacement. However, the natural frequency of a body is directly related to its stiffness in the respective direction of motion and can easily be measured.

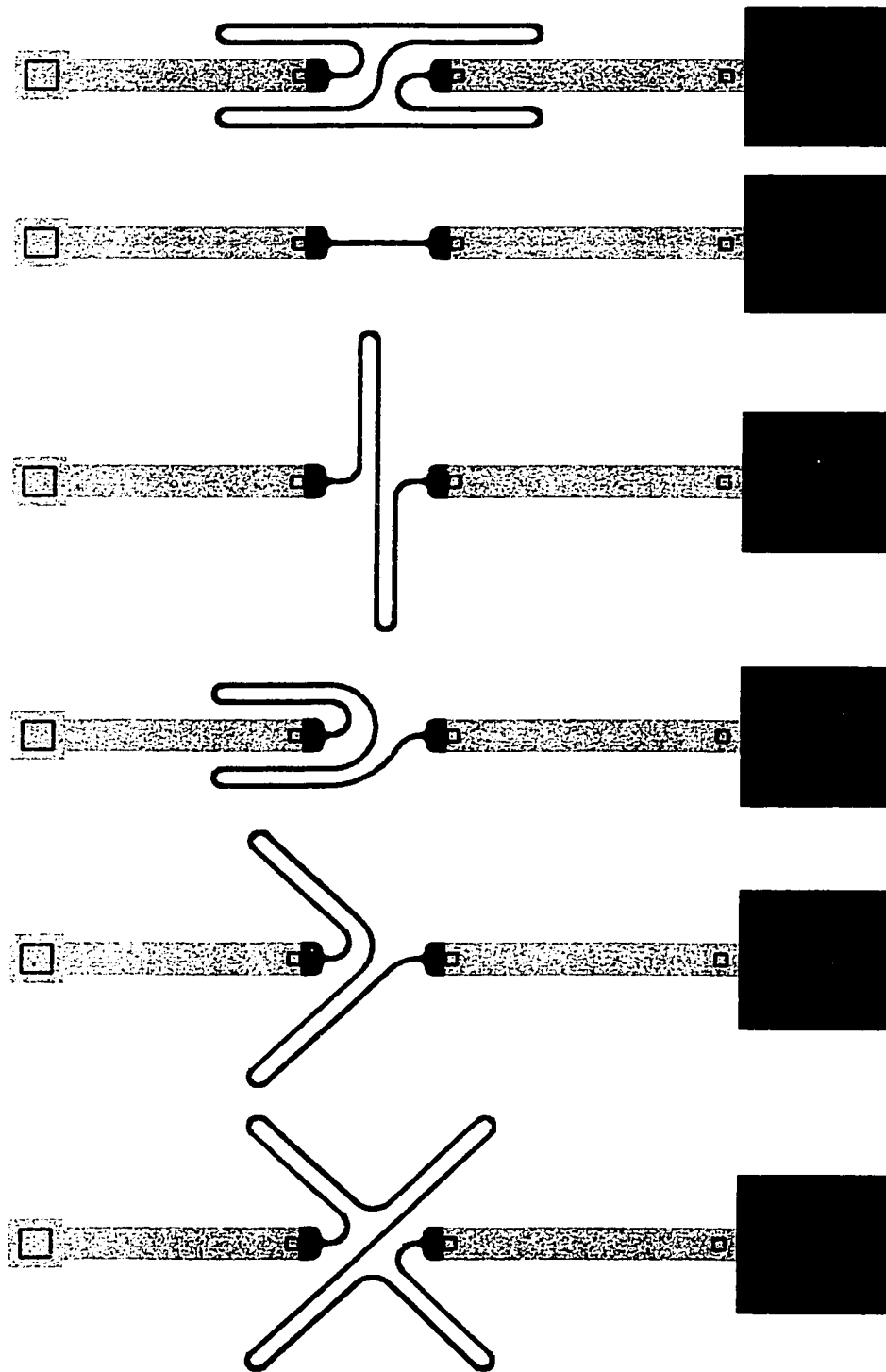


Figure 3-1: The Six Basic Joint Shapes: H, I, S, U, V, X

Figure 3-2 shows the schematic layout of the joint-mass setup used to measure the natural frequency for the horizontal rotational mode of the different joints. The setup consists of two $105\ \mu\text{m}$ polysilicon (Poly 1) beams, one anchored to the substrate, the other connected to a $50\ \mu\text{m} \times 50\ \mu\text{m}$ endmass. The arms are separated by a $30\ \mu\text{m}$ gap which will be bridged by the different joints. In order to increase the stiffness of the arms a second layer of polysilicon (Poly 2) was attached on top of them. The end-mass was designed in two different versions, a single layer version (Poly 1) and a double layer version (Poly 1 and 2). Dimples were added to minimise possible contacts with the surface thereby limiting stiction.

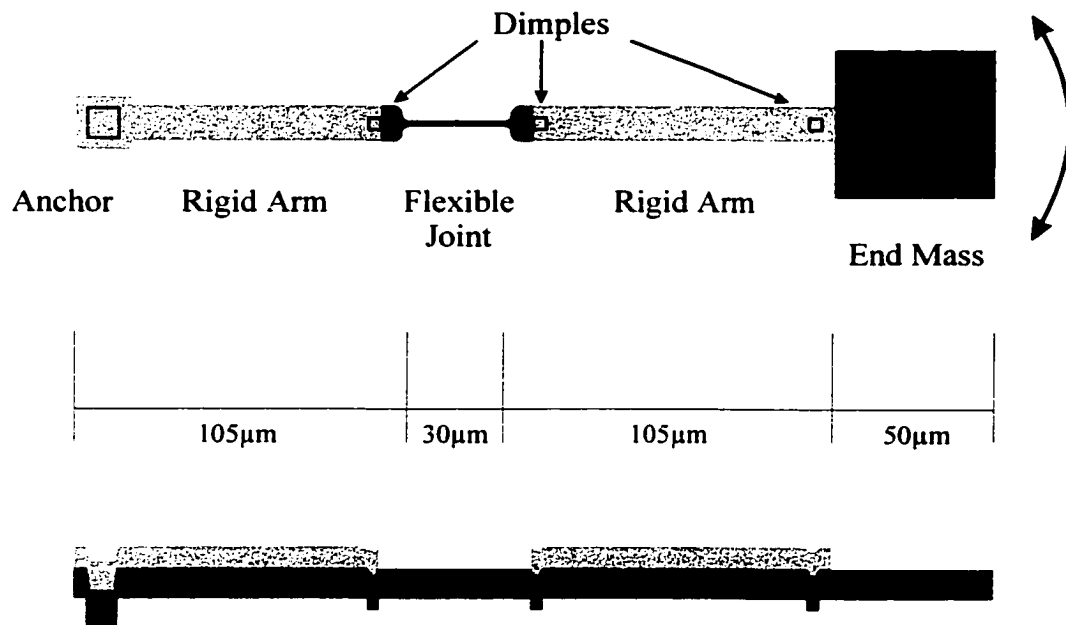


Figure 3-2: Layout Schematic of the Joint-Mass Setup (Top and Side View)

The first fabrication run featured three different joint designs: the I-joint, the H-joint, and the X-joint. The nomenclature originated from the shape of the designs. The H- and X-joints were fabricated with three different arm lengths. Since all joints were fabricated with the two variations of end-masses, the first fabrication run resulted in 14 prototypes. Figure 3-3 on page 19 shows the L-Edit layout schematics for these joints.

The joint shapes first considered, the H- and X-joint, only differ in the angle α that the joint arms form with the joint axis. For the H-joint $\alpha = 0^\circ$ while for the X-joint $\alpha = 45^\circ$. Later, this prompted the design of a joint with $\alpha = 90^\circ$, the S-joint. These joints are all approximately point-symmetric to the centre point of the joint. To examine the difference in behaviour by asymmetric joints, the U-joint and the V-joint were designed. These two joints simply represent half an H-joint (U-joint) and half an X-joint (V-joint).

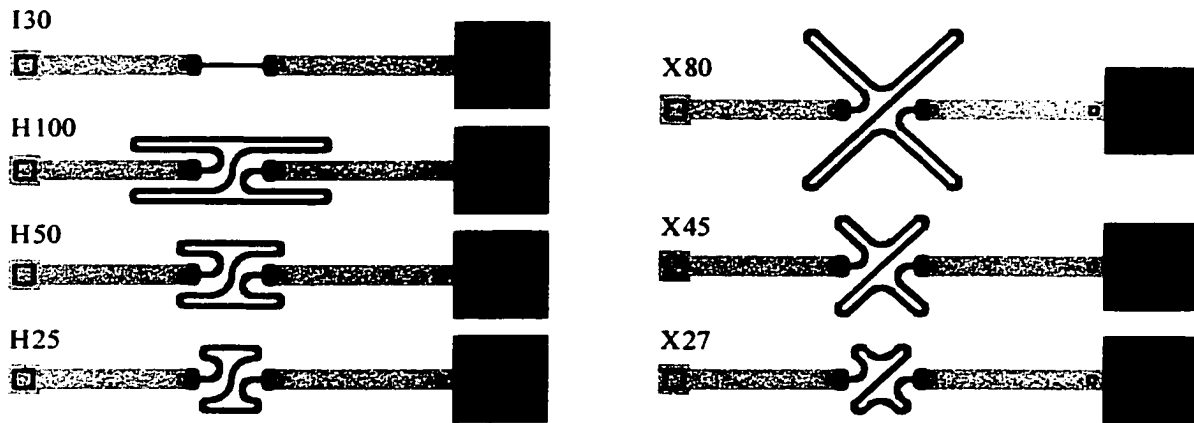


Figure 3-3: The First Seven Prototypes (Small End-Mass)

Table 3-1: Fabricated Standard Joints

Type	Folded Length L_f [μm]	Total Length L [μm]	Angle α	Identifier
I 30	30	30	0°	I_std_01
H 100	100	471	0°	H_std_01
H 50	50	271	0°	H_std_02
H 25	25	171	0°	H_std_03
U 65	65	261	0°	U_std_01
X 80	80	458	45°	X_std_01
X 45	45	260	45°	X_std_02
X 27	27	158	45°	X_std_03
V 55	55	258	45°	V_std_01
S 100	100	232	90°	S_std_01

Table 3-1 on page 19 lists the different standard joints fabricated. A complete list of all joints fabricated and simulated along with exact descriptions of the individual joint designs can be found in Appendix A.1.

The folded length L_f describes the dimensions of the folded joints as shown in Figure 3-4. The total length L describes the length of the unfolded joint.

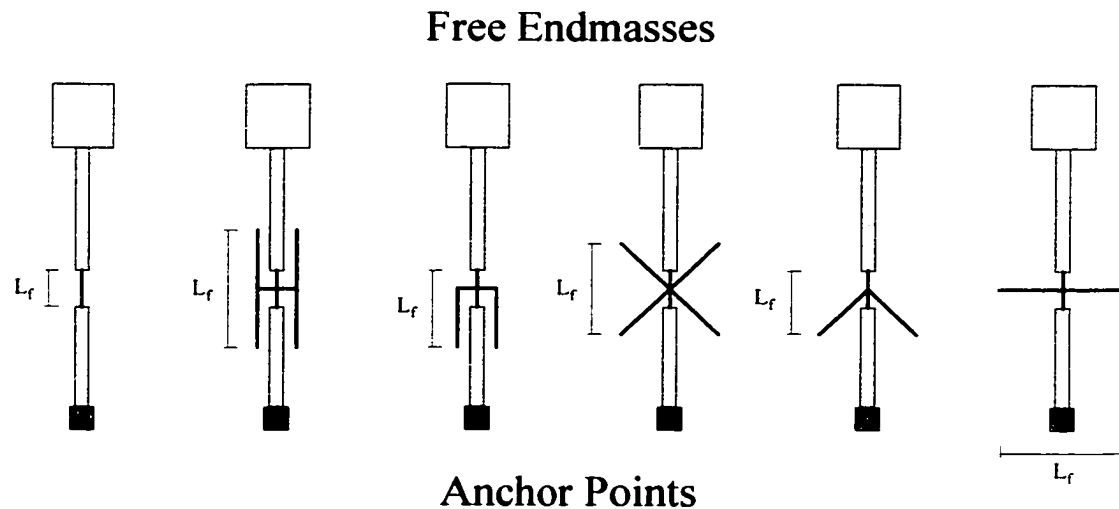


Figure 3-4: Folded Joint Length L_f for Various Joints

3.3 Kinematic Equivalents

One of the goals of this research was to build micro-planar mechanisms without the need for assembly and without kinematic pairs (joints) involving rotating and/or sliding. A planar kinematic pair with a single Degree-Of-Freedom (DOF) and with a form closure can be realised by a slide (S) joint or a rotary (R) joint (see Figure 3-5A on page 21). A two DOF joint can be realised by a rotary-slide that facilitates both sliding and rotating (RS) (see Figure 3-5B & C).

The micro-mechanisms were designed to be self supporting with no other part touching the base but the anchors forming the mechanisms' frames. Simple cantilever beam formulas ($\delta = PL^3/3EI$) show that this is true for the lengths considered.

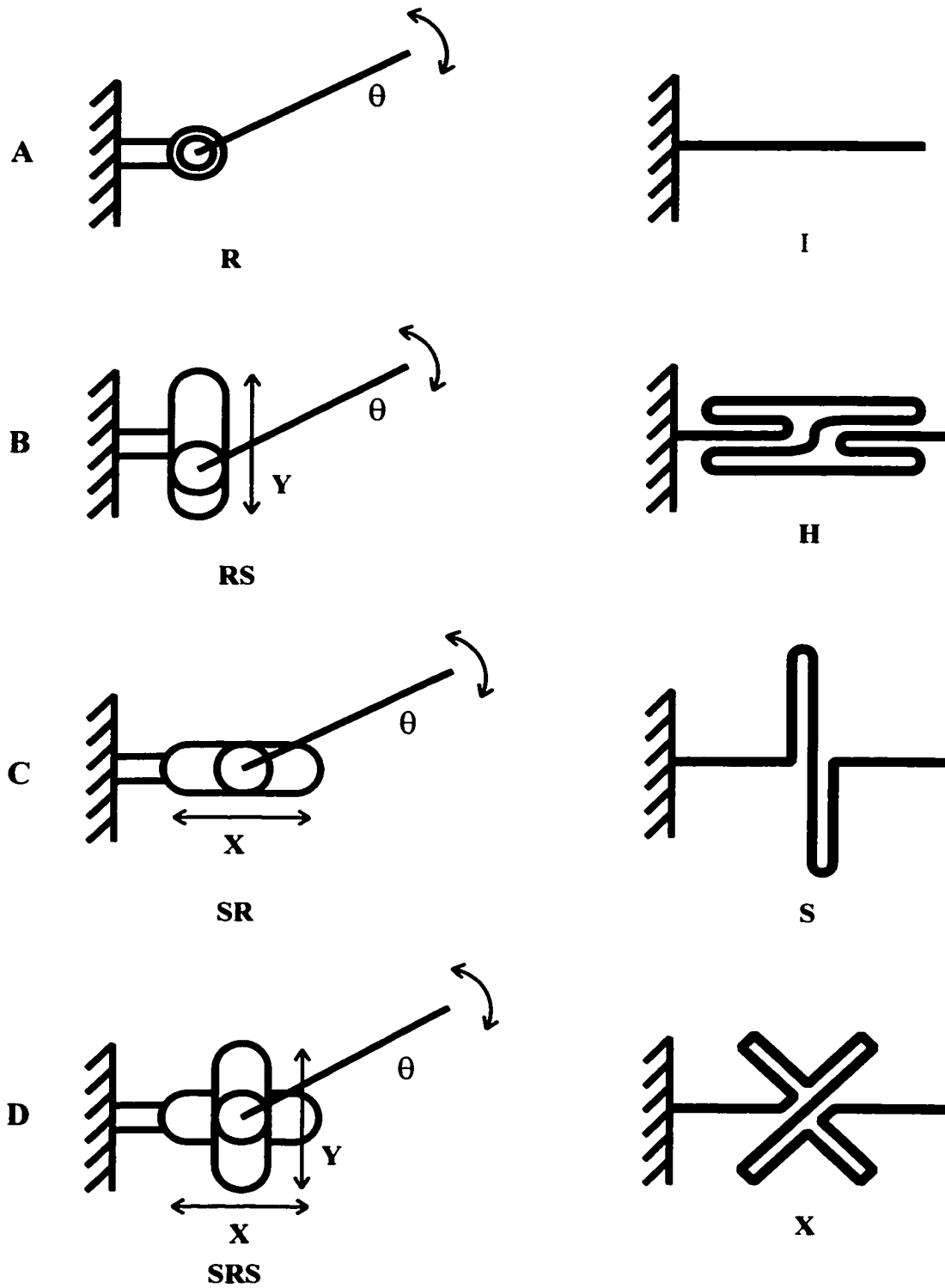


Figure 3-5: Example Diagrams of Rigid Kinematic Pairs and Their Flexure Counterparts

3.4 Fabricated Joints

In general the results were promising although many joints were initially stuck to the ground with part of the end-mass (demonstrating the importance of surface forces such as stiction and surface tension). A little push with a probe needle, however, easily released the joint-mass structure. Figure 3-6 shows SEM micrographs of some of the fabricated joints.

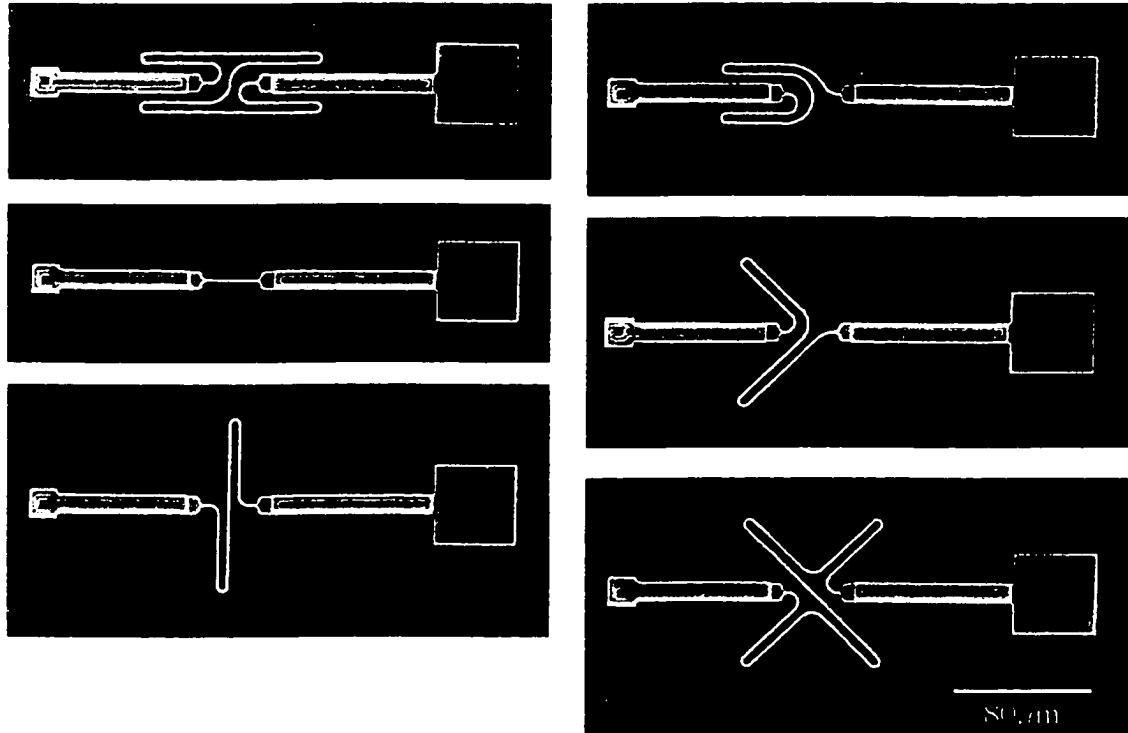


Figure 3-6: SEM Micrographs of the Six Basic Joints (CJ2 chip)

The joints described in the previous sections were fabricated on two different fabrication runs using the Cronos MUMPs process provided to the University through the Canadian Microelectronics Corporation (CMC). CMC's run identifiers consist of the last two digits of the run year *YY*, the number *##* of the run within that year (01, 02, etc.), and *MU* for MUMPs: *YY##MU*, e.g. 9902MU.

Since MUMPs is a multi-user process each fabricated chip has a design designation. It consists of an *I* for implementation (or *D* for design rule check), *MU* for MUMPs, *DT* for

DalTech, and a three letter code ??? for the design. The DalTech MEMS Lab identifier is *IMUDT???*, e.g. IMUDTRT2.

The two chips that featured joint designs used in this thesis were IMUDTRT2 (9902MU, September 1999) and IMUDTCJ2 (0002MU, July 2000). RT2 featured I-, H-, and X-joints with small and large end-masses while CJ2 included all joint designs in a small end-mass and a special double layer version (see Chapter 8). A complete listing of all chips manufactured by the Dalhousie MEMS Lab using the MUMPs process can be found in Appendix E.

The following chapters show results of FEA simulations and experiments conducted with these fabricated joints.

4 Standard Joint FE Analysis

This chapter introduces Finite Element Analysis and the choice of software. It explains the reasoning behind using beam models and describes the calculation methods used in this thesis.

4.1 Introduction

Due to the relatively long turn-around time of the MEMS fabrication process, 14 weeks, a trial and error approach to component design is not very efficient. One way around this time delay is putting a large number of copies of the same component on the same chip, each with slight variations. This way chances are high that at least one of the variations will produce acceptable results.

In addition to this approach finite element analysis can be used to examine the proposed structures prior to the fabrication process, thereby giving the chance of eliminating some flawed design variations and replacing them with variations based on FEA results. This way chip real estate can be used more efficiently.

One major advantage of FEA is the possibility of calculating properties that would be difficult, if not impossible, to find analytically or experimentally. This is especially interesting for micro-scale components since some properties which are easily measured on macro-scale components become difficult to determine, for example stiffnesses. On the micro-scale it is not only difficult to exert a known force on a component but also to exactly measure the resulting displacement.

The objective of this thesis is to determine various mechanical properties of a variety of joint designs using finite element analysis and to verify them by comparison with experimentally determined values.

4.2 The Finite Element Method

The finite element method (FEM) or finite element analysis (FEA) is one of the most popular numerical computing methods in the field of engineering. This can be explained by the versatility of this method, which is applicable to a wide variety of physical problems.

The basic idea behind this method is as follows: using geometrical and numerical division a complex, analytically unsolvable problem is split into small, partly linearised sub-problems. The solutions of these easily solvable sub-problems are then combined to form the general solution.¹

FEA has its origin in statics. Especially in the field of civil engineering shell and bridge constructions were simulated early on. One of the most famous examples is the roof of the olympic stadium in Munich, Germany, shown in Figure 4-1.



Figure 4-1: The Roof of the Olympic Stadium in Munich

It was simulated 30 years ago at the Institute of Statics and Dynamics in Stuttgart with more than 11,000 unknowns.

4.2.1 Areas of Application²

The first application of FEA was probably made in the treatment of linear elastic problems where so-called matrix methods of elasto-statics were used to examine beams, discs, and shells as finite elements. Upgrading of the basic elements by increasing the number of nodes and by introducing higher order displacement approaches resulted in an improvement of this method with regards to computation and in higher accuracy of the results.

1. See [27] p. 1

2. See [10] p. 5f. and [27] p. 2f.

FEA is increasingly used in many research fields. This can be attributed to the rapid development of the available computational power accompanied by drastic price drops. It is now possible to carry out FE calculations on mid-size PCs in an acceptable time frame. Additionally the increase in user-friendliness and power of the FE software played a large role in broadening its acceptance. Results that had to be interpreted by hand using metre-long print-outs can now be graphically evaluated and manipulated in a variety of ways.

In addition to structural analysis the following fields are now common for the application of numerical simulations:

- fluid mechanics,
- acoustics,
- dynamics,
- heat transfer,
- modal analysis,
- contact analysis, as well as
- electric and magnetic field analysis.

However, the research in this thesis only required non-linear structural analysis and modal analysis.

In order to examine interaction effects coupling of different calculation methods is used more and more often. For example fluid mechanics and structural analysis are coupled in order to calculate effects in bearings.

It is one of the objectives of this thesis to show that FEA can be used successfully to study compliant MEMS devices. In addition to its original use to calculate component stress due to specific loads, FEA is increasingly used as an instrument to better understand complex effects. In case of the joints examined in this thesis FE analysis is used to calculate properties of the different joints which are difficult or impossible to determine experimentally.

4.2.2 General Description of FEA¹

The base for the finite element method is to view the examined structure as an arrangement of a finite number of sub-structures. In this case the matrix formulation is especially useful for carrying out the numerical calculations.

Characteristic for FEA is the introduction of plane or spatial elements of suitable size and shape in order to approximately describe a complex continuum. This way a complex problem is reduced to a large number of simple problems.

The solution consists of three parts:

- Idealisation of the continuum by division into finite elements,
- Determination of geometric and elastic element properties,
- Approximate calculation of the idealised total continuum.

It should be emphasised that a crucial difference to the finite difference method is, that only physical approximations are made, namely the division of the real continuum into a discrete system of elements and the displacement functions for these elements. No approximations are necessary during the following mathematical treatment.

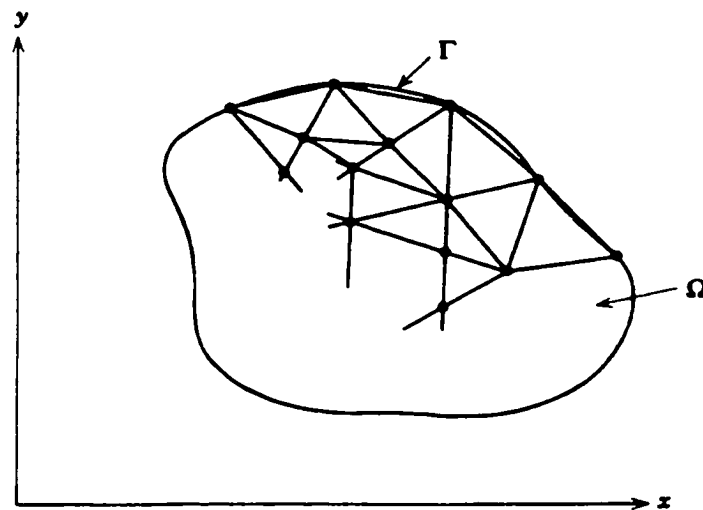


Figure 4-2: Two-Dimensional Continuum Divided Into Triangular Elements^a

a. see [13] p. 79

1. See [10] p. 153

The following section will briefly describe the *displacement or stiffness method* which is the most commonly used solution method.

4.2.3 The Displacement Method¹

Elasticity problems form the most important foundation for a large class of calculations in structural analysis. The approximation treatment using the displacement method of finite elements uses the following steps:

1. The elastic continuum is geometrically discretised by dividing it into simple sub-structures, e.g. pyramid or block elements, in three dimensions.
2. The real continuum is idealised by imagining the connection of the respective elements in discrete nodes, which lie on the element edges. The *displacements* of these nodes are introduced as the basic unknown for the calculations.
3. Within every single element an approximation approach for the displacements is made. Suitable functions are introduced, such that the displacement approach on the element edges is linearly dependent on the displacements of the nodes and thereby clearly described. Since the material properties of the real continuum are also valid inside the element, the stress and strain inside each element can be calculated from the nodal displacements using the shape change law of the theory of elasticity and basic kinematic equations.
4. Equivalent forces are assumed at the nodes in order for the strains inside the elements to be statically equivalent. Only the total equilibrium of the element can be satisfied this way. In certain regions within the element the equilibrium relations might be violated.

This way the most important elastic properties of an element are

1. See [10] p. 153 ff.

expressed by a linear relationship between nodal forces and nodal displacements. This relationship is called the stiffness relation. From the resulting stiffness matrices of the single elements the stiffness matrix of the whole continuum can be constructed by suitable transformation into a global coordinate system.

For the construction of the stiffness matrix of an element the choice of a suitable displacement approach is of crucial importance.

5. The nodal displacements of all elements fulfil the requirement of the consistency of the displacements. From the condition for the approximate fulfilment of the equilibrium in the whole continuum, idealised using finite elements, the following system of equations can be deduced:

$$\mathbf{K} \cdot \vec{u} = \vec{F} \quad (4-1)$$

with the stiffness matrix \mathbf{K} , the nodal displacement vector \vec{u} , and the nodal force vector \vec{F} . Basically the nodal displacements can be calculated for given nodal forces using this system of equations. Normally, however, a few displacements are already given, e.g. constraints, making it necessary to re-order the system of equations.

6. Using the known stiffness properties the distortions inside the elements can be calculated from the actual nodal displacements. Through appropriate averaging the stress and strain distribution of the whole examined elastic component can be approximated using the stresses and strains of the individual elements.

A more in-depth description of the individual steps is not feasible here. The interested reader can find more information in [10, 13, 35].

4.2.4 Coupled Energy Domains

Micro-electro-mechanical (MEM) devices tend to make the FE analysis more difficult as they usually combine two or more of the fields mentioned above. These coupled energy domains require a coupled analysis.

Many MEM devices contains coupled energy domains. For example the coupling in the case of the condenser microphone becomes stronger with smaller distances between backplate an membrane as well as smaller thicknesses of membrane and backplate [25]. This is more likely to occur in a micro-device than in a macro-device.

Other examples are micro-pumps [33], involving a coupling of fluid dynamics with thermodynamics and structural mechanics, and micro-motors, combining structural mechanics with structural dynamics and electro statics [5].

Fortunately the joints examined in this thesis did not required coupled analysis.

4.3 FEA Models

As explained in Chapter 4.2 the finite element method uses a discretised model of the continuum that is examined. Using a software package a model is created using a pre-processor. In this pre-processor the geometry is created and meshed with elements.

4.3.1 FEA Software

In the 1999 winter term a directed study was conducted by the author examining the different available simulation tools for microsystems. The final report recommended the use of ANSYS as the simulation tool of choice due to its being relatively inexpensive and providing most of the necessary functionality. The complete report can be found as Appendix F of this thesis.

Following the recommendation of the report an ANSYS/University High license was acquired in September 1999 which was used for all simulations in this research.

4.3.2 Units

Since ANSYS does not allow the user to specify units it is the users responsibility to make sure that the entered numerical values are in the correct relationship. This can be achieved by simply using standard MKS (SI) units for all input values. For the simulation of MEMS, however, it is more useful to use the μ MKS unit system since all length inputs will be in microns. μ MKS units use 1 μm as the standard unit for length, keeping 1 kg as mass, and 1 s as time unit. The following table lists the basic and derived units in the MKS and the μ MKS system along with multipliers to transfer a value from MKS to μ MKS:

Table 4-1: Mechanical Conversion Factors for MKS to μ MKS^a

Mechanical Parameter	MKS Unit	Dimension	Multiply by This Number	To Obtain μ MKS Unit	Dimension
Length	m	m	10^6	μm	μm
Mass	kg	kg	1	kg	kg
Time	s	s	1	s	s
Force	N	$\text{kg}\cdot\text{m}/\text{s}^2$	10^6	μN	$\text{kg}\cdot\mu\text{m}/\text{s}^2$
Stress	Pa	$\text{kg}/\text{m}\cdot\text{s}^2$	10^{-6}	MPa	$\text{kg}/\mu\text{m}\cdot\text{s}^2$
Young's Modulus	Pa	$\text{kg}/\text{m}\cdot\text{s}^2$	10^{-6}	MPa	$\text{kg}/\mu\text{m}\cdot\text{s}^2$
Density	kg/m^3	kg/m^3	10^{-18}	$\text{kg}/\mu\text{m}^3$	$\text{kg}/\mu\text{m}^3$

a. see [1] ch. 1.3

4.3.3 Material Properties

In order to accurately simulate the behaviour of a component the FEA solver has to be provided with properties of the used materials. The following property values were used in all FE simulations:

$$\text{Young's Modulus: } E = 169 \text{ GPa} = 169 \cdot 10^3 \frac{\mu\text{N}}{\mu\text{m}^2} \quad (4-2)$$

$$\text{Poisson's Ratio: } \nu = 0.22 \quad (4-3)$$

$$\text{Density: } \rho = 2330 \frac{\text{kg}}{\text{m}^3} = 2.33 \cdot 10^{-15} \frac{\text{kg}}{\mu\text{m}^3} \quad (4-4)$$

The values for these material properties vary significantly throughout the literature. For example Sharpe [28] cites Young's Modulus as 169 ± 6 GPa, this value was used as it applies directly to MUMPs layers. Other researchers such as Kahn [15] and Koskinen [18] cite values of 150 ± 30 GPa and 175 ± 25 GPa. Thus there remains a large range of measured values for Young's modulus.

4.3.4 Solid vs Beam Model

ANSYS provides 189 different element types for use in discretising a continuum. The elements used in structural analysis can be divided into five basic types:

LINK elements can be used to simulate spars and trusses. No bending or torsion of the element is considered. Nodes have translational degrees of freedom.

BEAM elements can be used to simulate beams. Bending and torsion of the element are taken into account. Nodes have translational and rotational degrees of freedom. The element shape function is based on the beam theory.

PLANE elements can be used to make 2D models of solid structures. No bending or torsion of the element is considered. Nodes have translational degrees of freedom.

SHELL elements can be used to model thin solid structures (e.g. membranes). The thickness of the element has to be small compared to its lateral dimensions for the underlying theory to be valid. Bending and torsion of the element are taken into account. Nodes have translational and rotational degrees of freedom.

SOLID elements are used to model 3D solid structures. No bending or torsion of the element is considered. Nodes have translational degrees of freedom. Therefore several layers of elements have to be used in order to account for torsion. Linear or higher order shape functions are associated with the elements.

Considering the shape of the examined joints, LINK, PLANE, and SHELL elements are not suitable for their simulation. BEAM and SOLID elements can be used to model the joints accurately. In order to choose the right element, two models of an H-joint were created: one using only SOLID elements, the other only using BEAM elements.

Solid Model

In order to create the solid model the geometric information from the 2.5D layout editor was combined with knowledge of the manufacturing process and an exact three dimensional model was created in the ANSYS pre-processor. The process was very tedious and automation of the process for use with different joint layouts would have been very difficult. The manual creation of the prototype model took about two days.

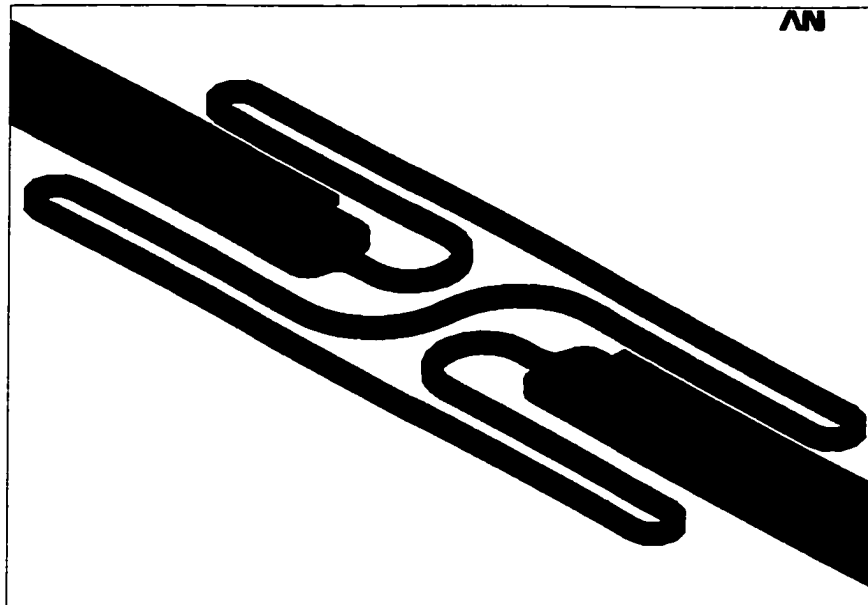


Figure 4-3: Solid Model of an H-Joint (close-up)

The finished geometric model was meshed using SOLID95 - 3D 20-Node Structural Solid - elements. The meshed model consisted of 14,626 elements and 31,390 nodes with a total number of 20,384 degrees of freedom. The standard modal analysis took about 2.5 hours on a Sun SPARC5 with 64MB of RAM.

Figure 4-3 on page 33 shows a close-up of the joint area of the solid model. It can be observed that even the connection area between the arm and the joint is accurately modelled. Note that every black line in the picture represents the boundary of one element. Due to the fine detail of the model all elements have to be relatively small resulting in a very large number of elements.

Beam Model

In contrast to the solid model the beam model takes advantage of the fact that the microstructures to be examined are made up from flat, long, relatively slender parts. Using BEAM189 - 3D Quadratic Finite Strain Beam - elements the structure is first divided into parts, each of which is then assigned a specific beam cross-section and meshed with beam elements.

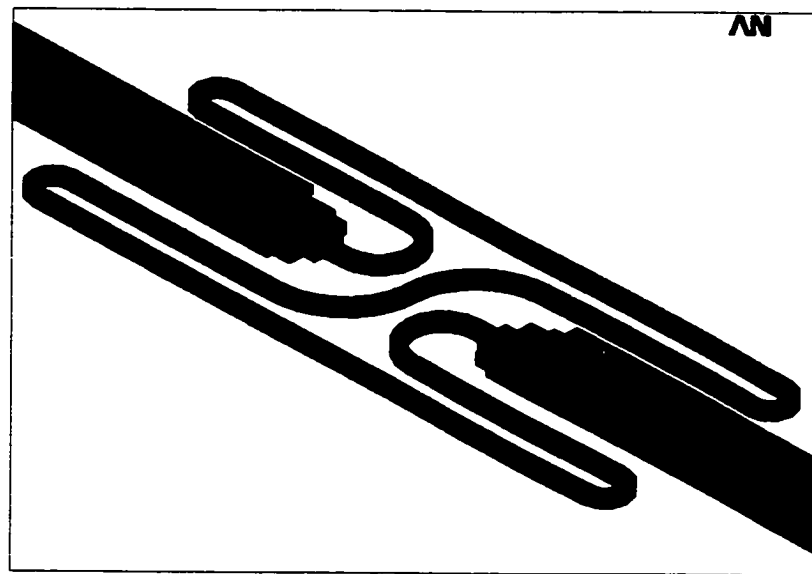


Figure 4-4: Beam Model of an H-Joint (close-up)

Unlike in the solid model only black lines perpendicular to the beam axis represent an element boundary. For example the cross-section of the thin joint section does not consist of four elements but only of one. It can be observed in Figure 4-4 that the areas in which the thin joint is connected to the arms are not as accurately modelled as in the solid model.

This results in a slight inaccuracy in the results but since this area is not crucial for stiffness calculations the influence was considered to be minor.

The meshed model consisted of 292 BEAM189 elements with 877 nodes resulting in a total of 3504 active degrees of freedom. The standard modal analysis on the SPARC5 took 30 seconds for this model to complete.

Comparison

Table 4-2 shows the comparison of the solid and the beam model from the previous sections. It can be seen that for the performed standard modal analysis (first five modes) the reduction of the number of degrees of freedom by a factor of six resulted in a decrease in the solution time by a factor of three hundred. This enormous reduction in solution time can be explained in part by the decrease in matrix size by a factor of 36, which should result in an equal reduction of solution time, but mainly by the ability of the computer to fit the complete model into the main memory and the resulting decrease in necessary slow input-output operations.

Table 4-2: Comparison Solid/Beam Model

	Solid Model	Beam Model	Difference
DOFs	20,000	3,500	÷5.7
Solution Time	9,000sec	30sec	÷ 300
Freq. Mode 1	5.82kHz	5.78kHz	-0.70%
Freq. Mode 2	6.03kHz	6.00kHz	-0.51%
Freq. Mode 3	45.33kHz	45.19kHz	-0.30%
Freq. Mode 4	46.46kHz	46.39kHz	-0.16%
Freq. Mode 5	54.77kHz	54.81 kHz	+0.07%

The resonance frequencies calculated using the two models do not differ significantly. The principal mode is undercalculated by less than one percent using the beam model and the differences are even less for the higher modes. These differences were to be expected since the solid model approximates the prototype structure more closely than the beam model. However, since not even the solid model represents the prototype completely accu-

rately, we can simply accept this 1% error as a systematic error for all results and exploit the huge difference in required solution time.

Since the beam model also proved to be a lot easier to parametrise and adjust, all simulations were made using beam models.

4.4 FEA Methods

Once a FE model has been created it can be used to calculate results to a variety of given problems. In this thesis two different solution methods were used to calculate results: Modal Analysis and non-linear Static Analysis.

4.4.1 Modal Analysis¹

Modal analysis is used to determine the natural frequencies and mode shapes of a structure. As mentioned in Chapter 3.1 the natural frequency is directly related to the stiffness, but far more easily measurable.

For free vibration, the equation of motion for an undamped system with constant stiffness and mass effects can be expressed in matrix notation as

$$\mathbf{M} \cdot \ddot{\vec{u}} + \mathbf{K} \cdot \vec{u} = \vec{0} \quad (4-5)$$

with mass matrix \mathbf{M} , stiffness matrix \mathbf{K} , and displacement vector \vec{u} .

For a linear system, free vibrations will be harmonic of the form

$$\vec{u} = \vec{\phi}_i \cdot \cos(\omega_i t) \quad (4-6)$$

with eigenvector $\vec{\phi}_i$ representing the mode shape of the i^{th} natural frequency and the i^{th} natural circular frequency ω_i .

Thus, equation (4-5) becomes:

$$(-\omega_i^2 \mathbf{M} + \mathbf{K}) \cdot \vec{\phi}_i = \vec{0} \quad (4-7)$$

1. see [3] ch. 17.3

This is an eigenvalue equation. In order to get non-trivial solutions ($\vec{\phi}_i \neq \vec{0}$) the determinant of $(-\omega_i^2 \mathbf{M} + \mathbf{K})$ has to be zero. This means that the basic task of a modal analysis reduces to solving the following equation:

$$|-\omega_i^2 \mathbf{M} + \mathbf{K}| = 0 \quad (4-8)$$

This eigenvalue problem may be solved for up to n values of ω_i^2 and n eigenvectors $\vec{\phi}_i$ which satisfy equation (4-7), where n is the number of DOFs.

Every eigenvalue-eigenvector pair defines a mode of free vibration of the structure. The i^{th} eigenvalue ω_i^2 has the following relationship with the i^{th} natural frequency:

$$f_i = \frac{\omega_i}{2\pi} \quad (4-9)$$

Each eigenvector (or mode shape) is normalised such that:

$$\vec{\phi}_i^T \cdot \mathbf{M} \cdot \vec{\phi}_i = 1 \quad (4-10)$$

ANSYS provides several methods to solve this eigenvalue problem. All have their advantages and disadvantages. Since the beam model used results in relatively small problems it was decided to use the Subspace method to extract the eigenvalues and mode shapes. Details about this and the other offered methods can be found in [3] Chapter 15.10.

4.4.2 Non-Linear Static Analysis¹

If a structure experiences large deformations, its changing geometric configuration can cause the structure to respond non-linearly. An example would be the fishing rod shown in Figure 4-5. During the loading of the rod its geometric configuration and therefore the acting moment arms change, thereby influencing the stiffness of the rod. Geometric non-linearity is characterised by “large” displacements and/or rotations. Any displacement and/or rotation that changes the geometry enough to change the resulting stiffness is considered “large”. For example, during the axial loading of the joints examined in this thesis, their geometry changes causing a change in axial stiffness (see Chapter 6.4).

1. see [2] ch. 8

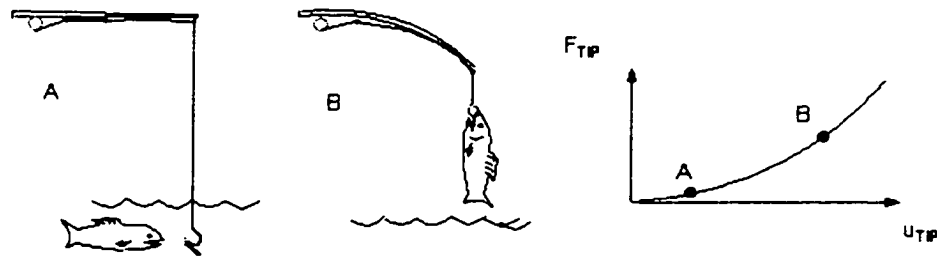


Figure 4-5: A Fishing Rod Demonstrates Geometric Non-Linearities^a

a. see [2] Figure 8-2

ANSYS uses a “Newton-Raphson” approach to solve non-linear problems. In this approach, the load is subdivided into a series of load increments. Before each solution, the Newton-Raphson method evaluates the out-of-balance load vector, which is the difference between the restoring forces (the loads corresponding to the element stresses) and the applied loads. The program then performs a linear solution, using the out-of-balance loads, and checks for convergence. If convergence criteria are not satisfied, the out-of-balance load vector is re-evaluated, the stiffness matrix is updated, and a new solution is obtained. This iterative procedure continues until the problem converges.

In order to take into account any geometric non-linear effects, a specified load is applied gradually in a selected number of substeps. For example, a $100\ \mu\text{N}\mu\text{m}$ moment is applied in ten steps of $10\ \mu\text{N}\mu\text{m}$. Each of these substeps take the result of the previous substep as the starting point.

Figure 4-6 on page 39 shows 16 different loadsteps with their respective loads as used for the stiffness calculations in the following chapters. Eight of the loadsteps are divided into 10 substeps. These represent in-plane and out-of-plane moment loads applied in positive and negative direction first at one end and then at the other end of the joint. They are separated by loadsteps with no load applied. These loadsteps are used to let the system relax and go back into its load free state before applying the next load.

Using this method it was possible to examine in-plane and out-of-plane behaviour in one calculation.

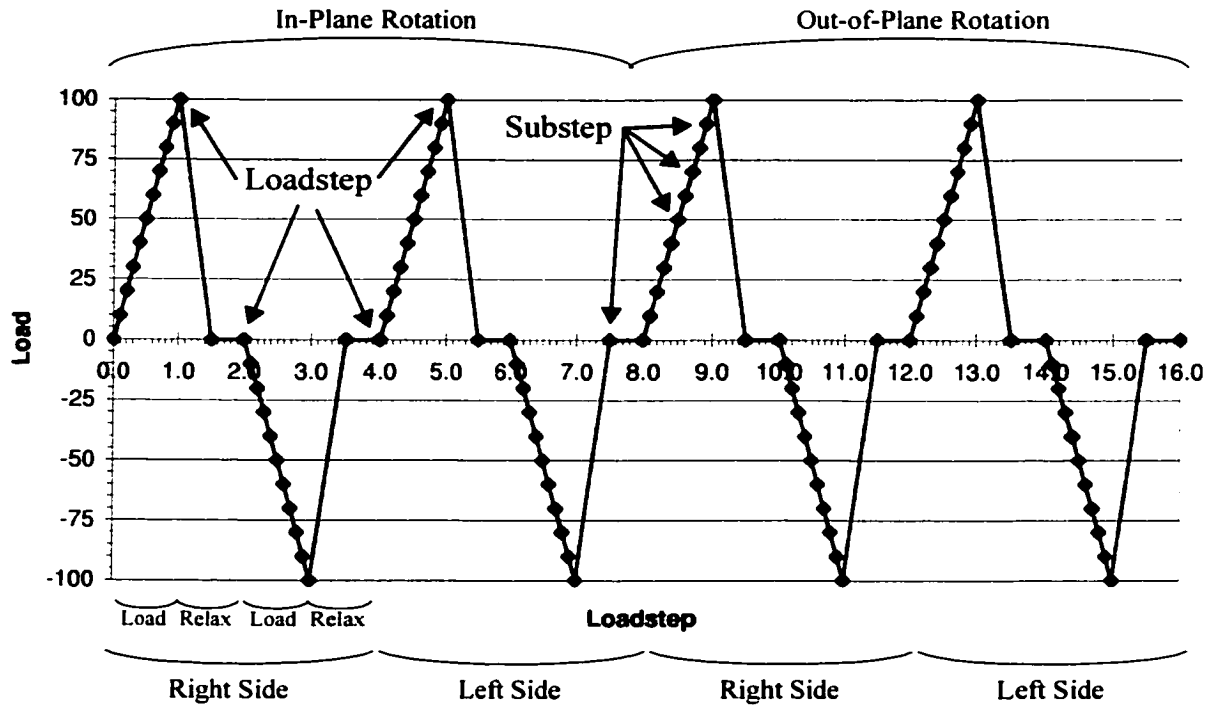


Figure 4-6: Loadsteps for In-Plane and Out-of-Plane Rotational Stiffness Calculations

5 Primary FEA Results

This chapter presents the primary results of the FE analysis. Results for centres of rotation and stiffnesses for the in-plane rotational and in-plane axial directions are presented.

5.1 Introduction

Since the purpose of the joints examined in this thesis is to connect links in planar mechanisms their most interesting properties are the in-plane rotational stiffness and the in-plane axial stiffness. This chapter presents the results for these two properties of “ideal joints” while Chapter 6 will discuss other properties and effects discovered during the FE analysis.

Note that due to the large range of values of Young’s modulus in the literature (see Chapter 4.3.3 on page 31) all FEA results will be presented with two significant figures only. In order to limit the data to a comprehensible amount, only the FEA results for joints actually manufactured are listed in this chapter. The results for all examined models can be found in Appendix A. Note that for the graphs and the regression analyses the results from all models were used.

5.2 Centre of Rotation

Rotational stiffnesses are defined as the quotient of an acting moment M and the resulting angular displacement θ . Since a force F at a distance d from the centre of rotation induces a moment $M = F \cdot d \cdot \sin(\alpha)$, the location of the centre of rotation for the joints is an important property.

Consider a cantilever beam of length L subjected to an applied force F_o or a moment M_o with a deflection δ and an angular deflection θ . The centre of rotation measured from the fixed end can be found by

$$\text{COR}_x = L - \frac{\delta}{\theta} = L - \frac{\iint M dx dx}{\int M dx} \quad (5-1)$$

where M is the total moment given by $M = \int F_o dx + M_o$.

For an I-joint of length L subjected to a pure force load ($M = F_0x$, see Figure 5-1a), the centre of rotation is at $L/3$. For the same beam subjected to a pure moment ($M = M_0$, see Figure 5-1b), the centre of rotation is at the centre of mass $L/2$. As the moment arm is increased the moment acting along the beam approaches a constant value and the centre of rotation approaches the centre of mass. For the I-joint with a test force applied at a distance of $170\mu\text{m}$ the difference between the centre of rotation and the centre of mass is approximately 0.3%.

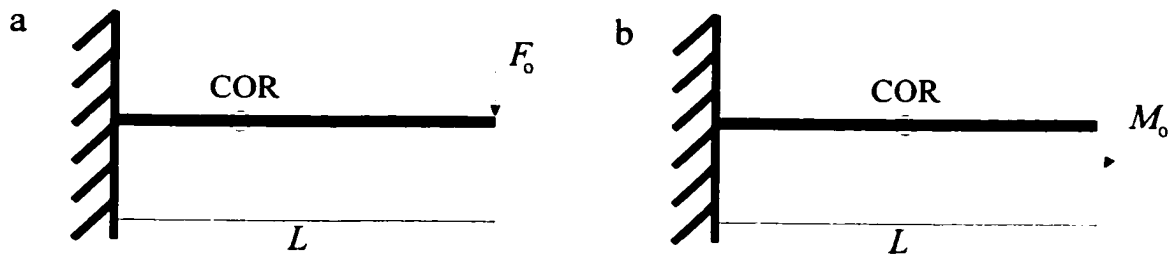


Figure 5-1: Centre of Rotation for a Cantilever Beam

For joints of folded length L_f symmetric to their centre, the centre of rotation for a pure moment input is located at the centre of the joint. For force input the centre of rotation can be approximated by the centre of mass if the force is applied at a distance of at least $3 \cdot L_f$ (see Chapter 6.3) from the centre of rotation. FE simulations and experimental observations support this approximation.

Unlike the other joints, the U- and V-joints are not symmetric to the centre of the joint. The centres of mass and rotation are shifted towards the side of the joint arms (towards the anchor point in case of the examined joint-mass systems). In first approximation the centre of rotation is shifted backwards by $L_a/2$. In order to get a more accurate position of the centre of rotation for all joints it was calculated using FEA.

Figure 5-2 on page 42 shows the geometric calculation of the centre of rotation of the joints between two load steps. The positions of two monitored points at the end of one load-step are labelled A and B. The positions of the respective points after the following loadstep are labelled A' and B'. The point where the perpendicular bisectors to the lines connecting

A with A' and B with B' intersect is the current centre of rotation. All four points lie on the circumference of a circle around this centre of rotation.

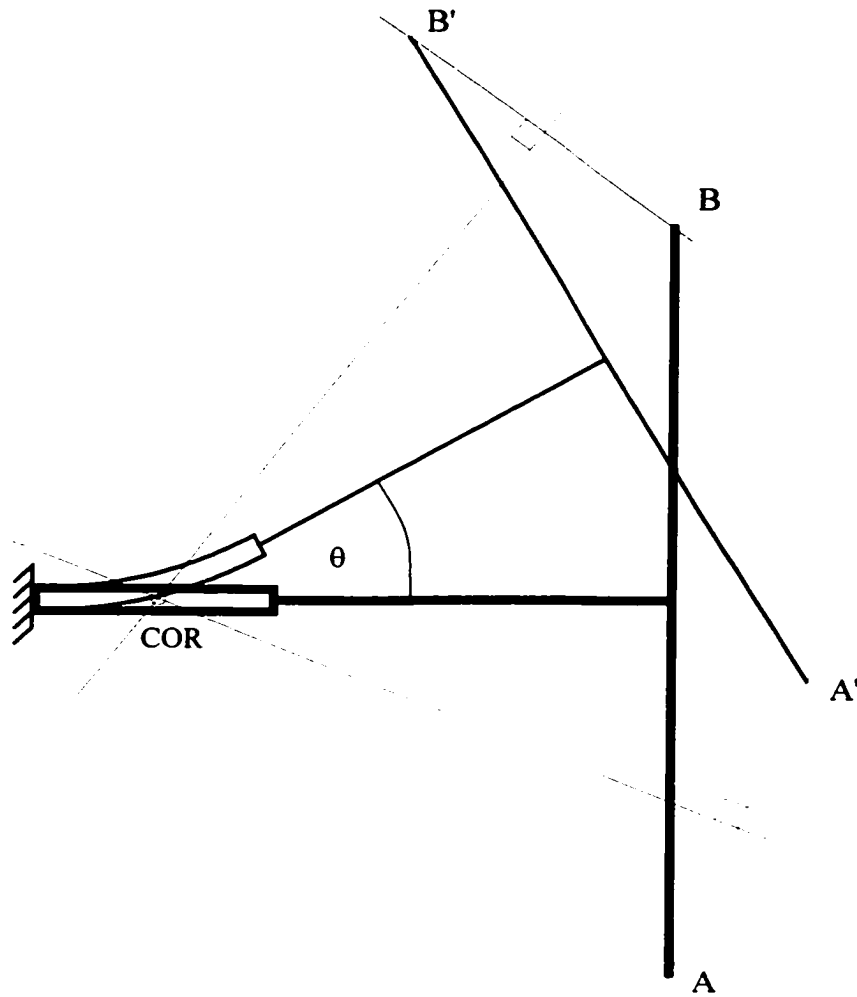


Figure 5-2: Calculation of the Centre of Rotation

This centre of rotation moves during the application of different loads. Chapter 6.5 describes this effect in detail. To calculate the centre of rotation for zero load, an average was taken of the calculated slopes and line centres from the smallest positive and the smallest negative loadstep.

As expected, for pure moment load, the centre of rotation for standard H-, I-, S-, and X-joints was found to be at the centre of the joint. Figure 5-3 on page 43 shows the FEA results found for all joints.

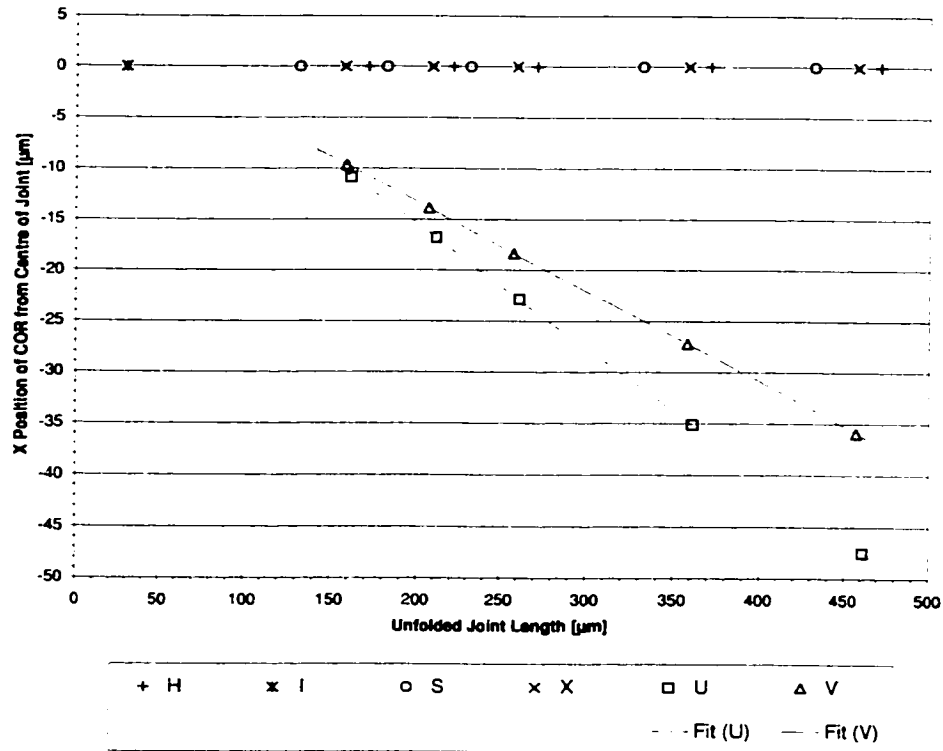


Figure 5-3: Centre of Rotation for U- and V-Joints for Different Joint Length (FEA)

Using linear regression and the respective formulas that relate folded and unfolded joint length from Table A-4 on page 138 the following formulas for the axial distance of the centre of rotation from the centre of the joint for all joints were derived:

$$COR_{H, I, S, X} = 0.000L_f + 0.00 \tag{5-2}$$

$$COR_U = -0.488L_f + 8.87 = -0.488L_a + 1.55 \tag{5-3}$$

$$COR_V = -0.498L_f + 8.90 = -0.498L_a + 1.43 \tag{5-4}$$

It can be seen that the initial assumption of a shift by $0.5L_a$ for U- and V-joints is close to the actual position of the centre of rotation.

5.3 Resonant Modes

As described in Chapter 4.4.1 resonance frequencies and the respective mode shapes for a given structure can be calculated using modal analysis. In this part of the simulation the beam models of all joint variations were analysed using the Subspace method provided by the ANSYS software. The first six modes of the joint-mass systems were extracted.

Table 5-1 shows the types and order of modes found for the various joints. Out-of-plane rotational (OP Rot), in-plane rotational (IP Rot), axial, and torsional (Tors) first and second modes were encountered

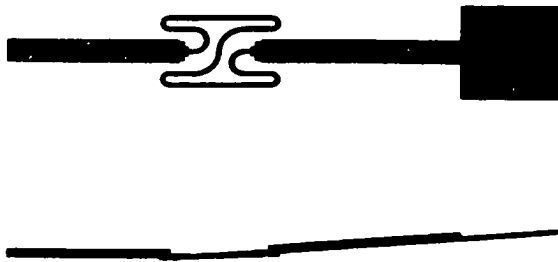
Table 5-1: FEA Predicted First- and Higher-Order Modes for Various Joints

Joint Type and L_f	L [μm]	Mode 1	Mode 2	Mode 3	Mode 4
I 30	30	OP Rot 1	IP Rot 1	Tors 1	OP Rot 2
H 100	471	OP Rot 1	IP Rot 1	OP Rot 2	Axial 1
H 50	271	OP Rot 1	IP Rot 1	Axial 1	Tors 1
H 25	171	OP Rot 1	IP Rot 1	Axial 1	Tors 1
X 80	458	OP Rot 1	IP Rot 1	Axial 1	Tors 1
X 45	260	OP Rot 1	IP Rot 1	Axial 1	Tors 1
X 27	158	OP Rot 1	IP Rot 1	Axial 1	Tors 1
S 100	232	OP Rot 1	IP Rot 1	Axial 1	Tors 1
U 65	261	OP Rot 1	IP Rot 1	Axial 1	Tors 1
V 55	258	OP Rot 1	IP Rot 1	Axial 1	Tors 1

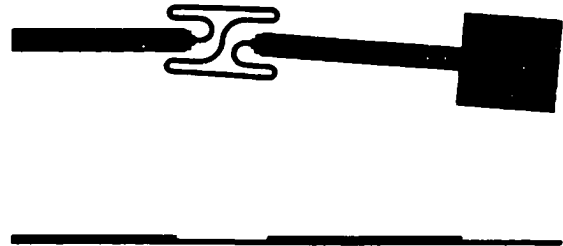
Since these joints will be used in planar mechanisms the interesting modes for this research are the first in-plane rotational mode and the first axial mode. As can be seen from Table 5-1 these are modes two and three for most joints. The rest of this chapter will discuss the stiffnesses for these two modes. The fact that the first out-of-plane rotational mode is mode one for all joints will be discussed in Chapter 6.2. The higher modes are not central to this thesis, were not observed experimentally, and will therefore not be discussed.

Figure 5-4 shows the mode shapes of the first four modes of an H 50 joint as top and side views.

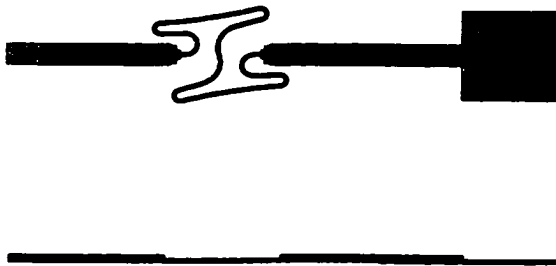
1. OP Rot 1



2. IP Rot 1



3. Axial 1



4. Tors 1

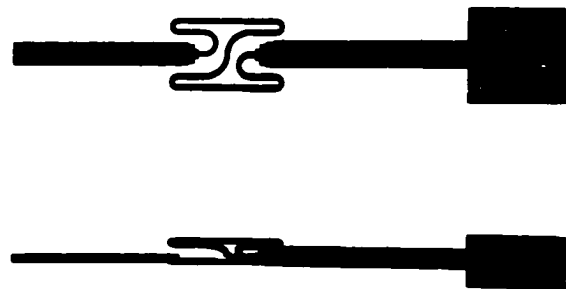


Figure 5-4: Mode Shapes of the First Four Modes of an H 50 Joint

5.4 In-Plane Rotational Stiffness

As mentioned before, the in-plane-rotational stiffness is the key feature of the joints. The softer the joint is in the in-plane rotational direction, the closer it is to a pin-joint (assuming all other stiffnesses are bigger).

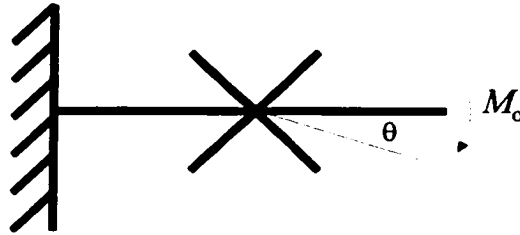


Figure 5-5: In-Plane Rotational Motion

Using non-linear analysis the in-plane rotational stiffness of the joints was calculated by applying a series of moment loads in the in-plane direction and extracting the resulting angular displacements. One end of the joint was fixed and the other end was subjected to a $100\mu\text{N}\mu\text{m}$ moment applied in ten steps in both positive and negative direction. To calculate the stiffness the applied moment was divided by the resulting angular displacement.

Table 5-2: In-Plane Rotational Stiffness K_θ of Various Joints (FEA)

Joint Type and L_f	Unfolded Length L [μm]	In-Plane Rotational Stiffness [$\mu\text{N}\mu\text{m}/\text{rad}$] K_θ
I 30	30	7,500
H 100	471	480
H 50	271	830
H 25	171	1,300
X 80	458	490
X 45	260	870
X 27	158	1,400
S 100	232	970
U 65	261	860
V 55	258	870

Table 5-2 on page 46 shows the calculated stiffnesses of selected standard joints. The complete list of values can be found in Appendix A. It can be observed that the in-plane rotational stiffness decreases with increasing total unfolded joint length. Furthermore the stiffness does seem to depend on the total unfolded joint length only and not on the type of joint, i.e. the shape the joint is folded into.

Since during in-plane rotation all bending moments occur in the plane of the folded joint, all joint segments are subjected to bending only. A pure moment load is constant over the whole joint. Therefore each joint segment is subjected to the same bending moment regardless of its orientation. Consequently the in-plane rotational stiffness should only depend on the total unfolded joint length.

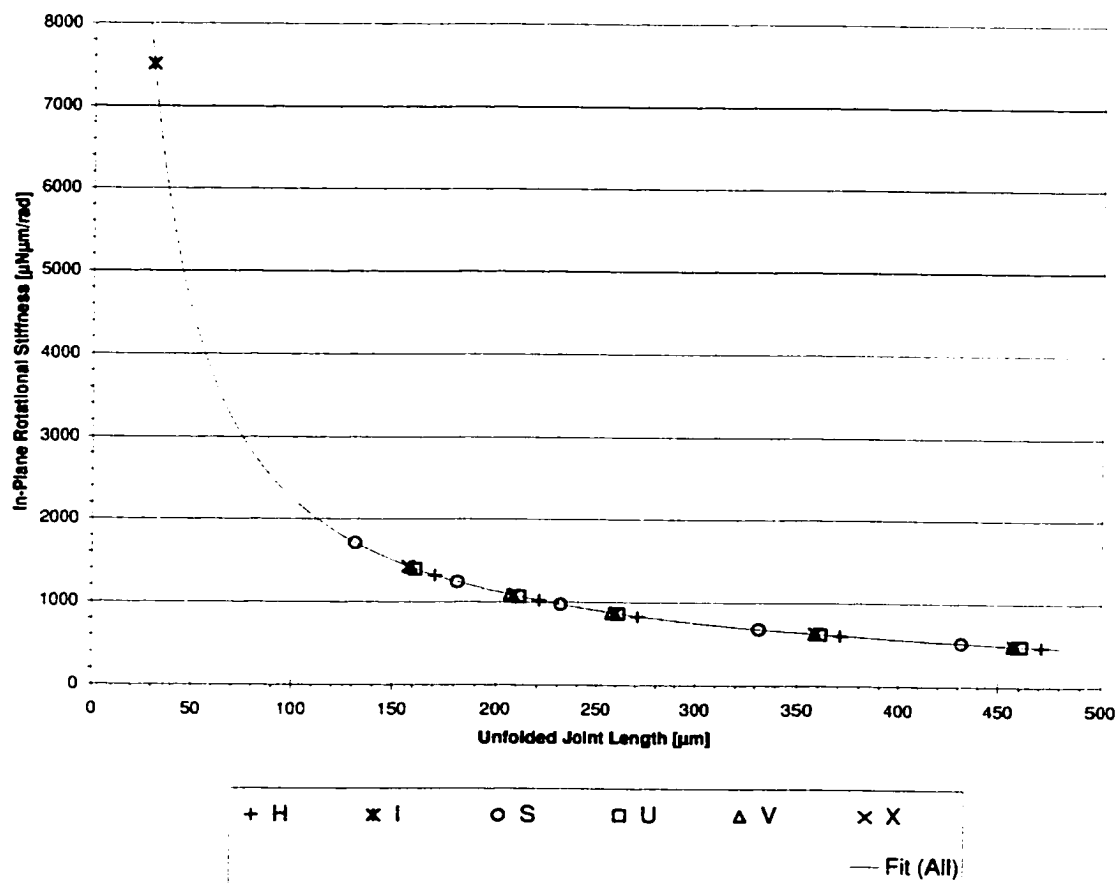


Figure 5-6: In-Plane Rotational Stiffness K_{θ} for Various Joint Types and Lengths (FEA)

Figure 5-6 on page 47 graphs the in-plane rotational stiffnesses of various standard joints over the total joint length. It can be observed that all joints lie on the same curve. Using regression analysis the following equation for the in-plane-rotational stiffness was found with a coefficient of determination $R^2 = 1.00$:

$$K_{\theta} = 900 \frac{\mu\text{N}\mu\text{m}}{\text{rad}} \cdot \left(\frac{250\mu\text{m}}{L} \right)^{1.00} = \frac{EI}{L} \quad (5-5)$$

In order to make the formula more comprehensible it was adjusted to a normal joint length of $250\mu\text{m}$. An analysis of the original formula showed that its coefficient is exactly the product of Young's modulus and cross-sectional moment of inertia. Therefore the formula for the in-plane rotational stiffness can be simplified to $K_{\theta} = EI/L$. This is the formula for the rotational bending stiffness of a cantilever beam. This means that the shape of the joint has no influence on the in-plane rotational stiffness which agrees with the expectations.

The in-plane rotational stiffness was found to be constant over the examined load range ($-100\mu\text{N}\mu\text{m}$ to $+100\mu\text{N}\mu\text{m}$).

Figure 5-7 on page 49 replots the FEA results for the in-plane rotational Stiffness K_{θ} from Figure 5-6 on page 47, multiplying the stiffness by a normalised length ($L/250\mu\text{m}$). As shown in the figure, for all joints: $K_{\theta} \cdot (L/250\mu\text{m}) = \text{constant} = 900\mu\text{N}\mu\text{m}\text{rad}^{-1}$ (for this material and cross-section). This agrees with equation (5-5) that was found using regression analysis.

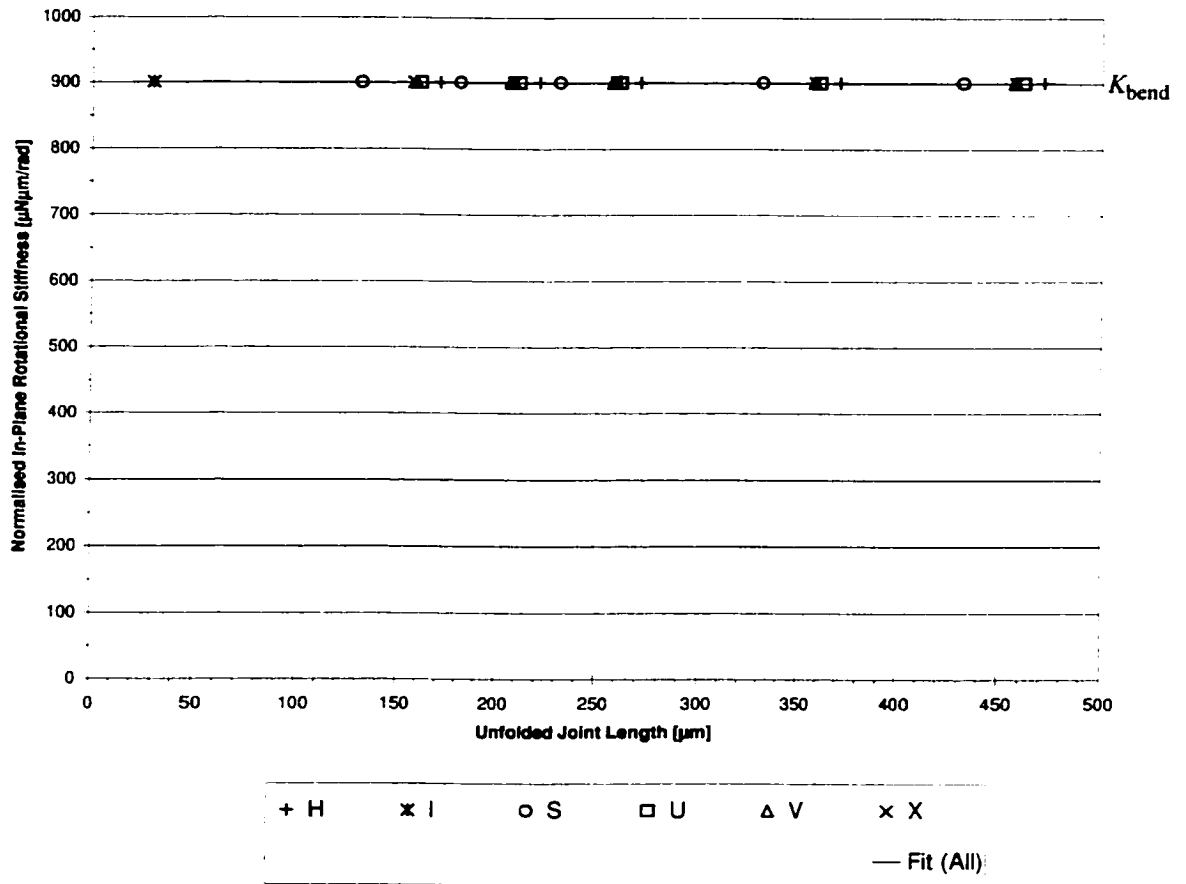


Figure 5-7: Normalised In-Plane Rotational Stiffness $K_{\theta} \cdot (L/250\mu\text{m})$ for Various Joint Types and Lengths (FEA)

5.5 In-Plane Axial Stiffness

Unlike the in-plane rotational stiffness the in-plane axial stiffness is a translational stiffness. Therefore it was calculated by applying a series of forces onto one end of the joint, while holding the other end fixed, and calculating the resulting linear displacement. Only the displacement in axial direction was considered in this section.

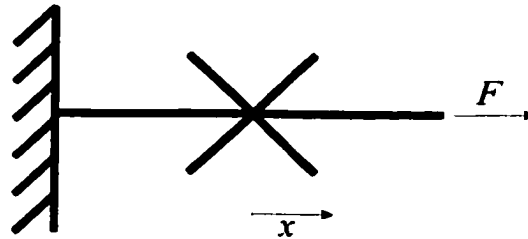


Figure 5-8: In-Plane Axial Motion

Table 5-3: In-Plane Axial Stiffness K_x of Various Joints (FEA)

Joint Type and L_f	Unfolded Length L [μm]	In-Plane Axial Stiffness [$\mu\text{N}/\mu\text{m}$] K_x
I 30	30	23,000
H 100	471	2.2
H 50	271	4.2
H 25	171	7.5
X 80	458	0.63
X 45	260	2.8
X 27	158	9.1
S 100	232	1.0
U 65	261	4.6
V 55	258	1.3

As expected, for each joint, shorter means stiffer.

Since the resulting stiffnesses proved not to be constant for the applied forces, the resting stiffness was calculated as an average of the stiffnesses from the smallest applied

force in compression and tension. Chapter 6.4 discusses the geometric non-linearities causing these stiffness variations.

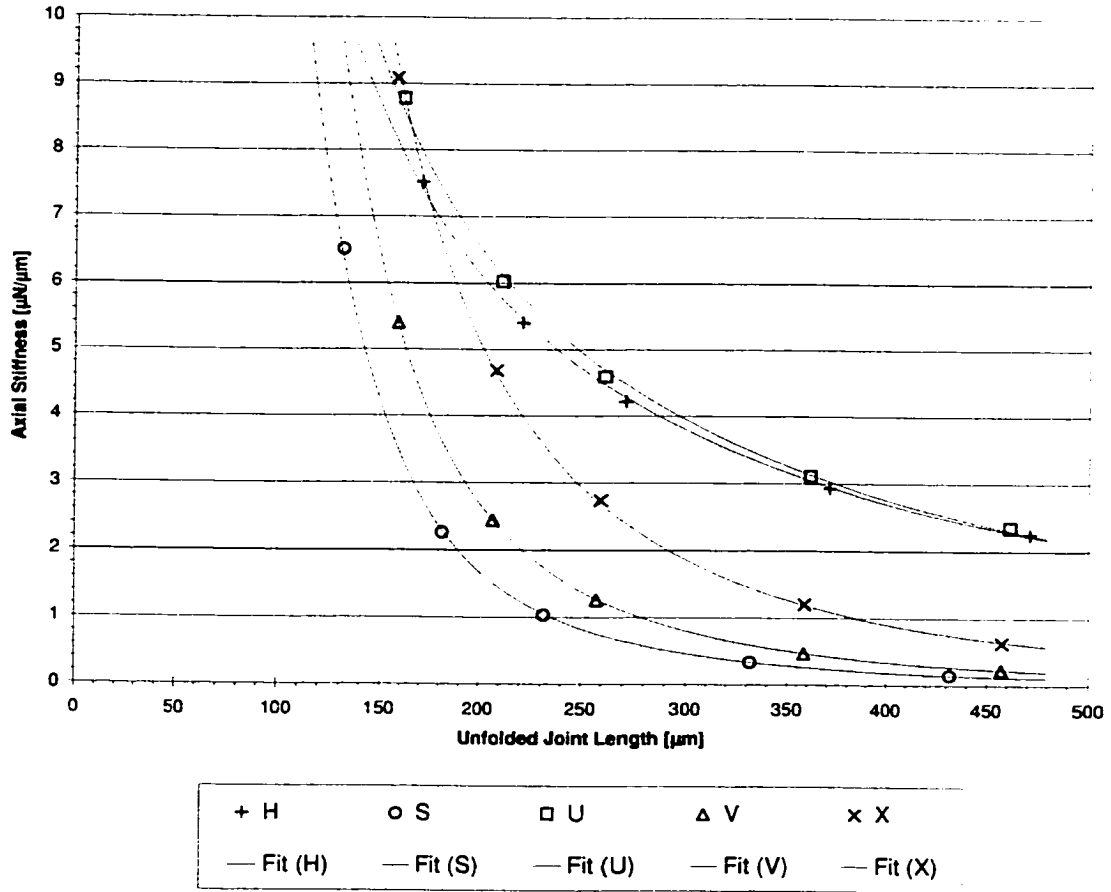


Figure 5-9: Axial Stiffness K_x for Various Joint Types and Lengths (FEA)

For long joints the stiffness can be expected to be highest for joints with most joint segments oriented in axial direction (H, U). The lowest can be expected for the S-joint with most of its segments perpendicular to the direction of motion.

Figure 5-9 shows a plot of the resting in-plane axial stiffnesses over the total joint length. H- and U-joints are axially stiffest since most of the joint segments are oriented in the same direction as the applied force. The H- and U-joint's axial stiffnesses are almost

identical for large joint lengths with an increasing difference towards shorter joints where the curved joint segments, which differ between the joints, gain more influence.

X- and V-joints have intermediate axial stiffnesses since most of their joint segments are at a 45° angle with the acting force. Since the X-joint has more curved joint segments in line with the acting force its stiffness is higher than that of the V-joint.

The S-joint is softest in axial direction since most of its joint segments are perpendicular to the acting axial force.

Table 5-4 lists the in-plane axial stiffness of five long joints with approximately equal total joint lengths. It can be observed that the stiffness is lower for higher joint arm angles.

Table 5-4: Long Joints: Axial Stiffness K_x Governed by Joint Arm Angle

Joint Type	Unfolded Length L [μm]	Joint Arm Angle α	In-Plane Axial Stiffness [$\mu\text{N}/\mu\text{m}$] K_x
U 115	461	0°	2.4
H 100	472	0°	2.3
X 80	458	45°	0.63
V 90	457	45°	0.23
S 200	432	90°	0.15

For shorter joints the curved segments of the joints tend to dominate the behaviour. Table 5-5 on page 53 lists the lengths of the curved parts of five short joints with approximately equal total joint length. It can be observed that the in-plane axial stiffness is higher the longer the curved segments of the joint are. This means that the stiffness no longer dependent on the angle of the joint arms.

Table 5-5: Short Joints: Axial Stiffness K_x Governed by Curved Joint Length

Joint Type	Unfolded Length L [μm]	Curved Length L_c [μm]	In-Plane Axial Stiffness [$\mu\text{N}/\mu\text{m}$] K_x
X 27	158	94.8	9.1
U 40	161	84.8	8.8
H 25	171	81.4	7.5
V 37	159	65.0	5.4
S 38	182	43.7	2.3

The following equations for in-plane axial stiffness were calculated with a coefficient of determination $R^2 = 1.00$ using regression analysis. In order to make the formulas more comprehensible they were adjusted to a normal joint length of $250\mu\text{m}$:

$$\text{U-joint:} \quad K_x = 5.0 \frac{\mu\text{N}}{\mu\text{m}} \cdot \left(\frac{250\mu\text{m}}{L} \right)^{1.25} \quad (5-6)$$

$$\text{H-joint:} \quad K_x = 4.7 \frac{\mu\text{N}}{\mu\text{m}} \cdot \left(\frac{250\mu\text{m}}{L} \right)^{1.19} \quad (5-7)$$

$$\text{X-joint:} \quad K_x = 2.9 \frac{\mu\text{N}}{\mu\text{m}} \cdot \left(\frac{250\mu\text{m}}{L} \right)^{2.50} \quad (5-8)$$

$$\text{V-joint:} \quad K_x = 1.4 \frac{\mu\text{N}}{\mu\text{m}} \cdot \left(\frac{250\mu\text{m}}{L} \right)^{2.99} \quad (5-9)$$

$$\text{S-joint:} \quad K_x = 0.83 \frac{\mu\text{N}}{\mu\text{m}} \cdot \left(\frac{250\mu\text{m}}{L} \right)^{3.19} \quad (5-10)$$

According to these equations the axial stiffnesses for H- and U-joints are approximately inversely proportional to the total joint length. This is consistent with a straight beam subjected to tension or compression ($K \propto \frac{AE}{L}$). The S-, V-, and X-joints are approximately proportional to $1/L^3$. This is consistent with a cantilever beam loaded at the end ($K \propto \frac{EI}{L^3}$).

Figure 5-10 on page 54 plots the in-plane axial stiffness normalised to a joint length of $250\mu\text{m}$ ($K_x \cdot (L/250\mu\text{m})$) versus the total joint length. It can be seen that the normalised

stiffness for H- and U-joints is approximately constant, which confirms the equations above. X-, V-, and S-joints, however, do not show a constant normalised stiffness, which is also reflected in the equations above.

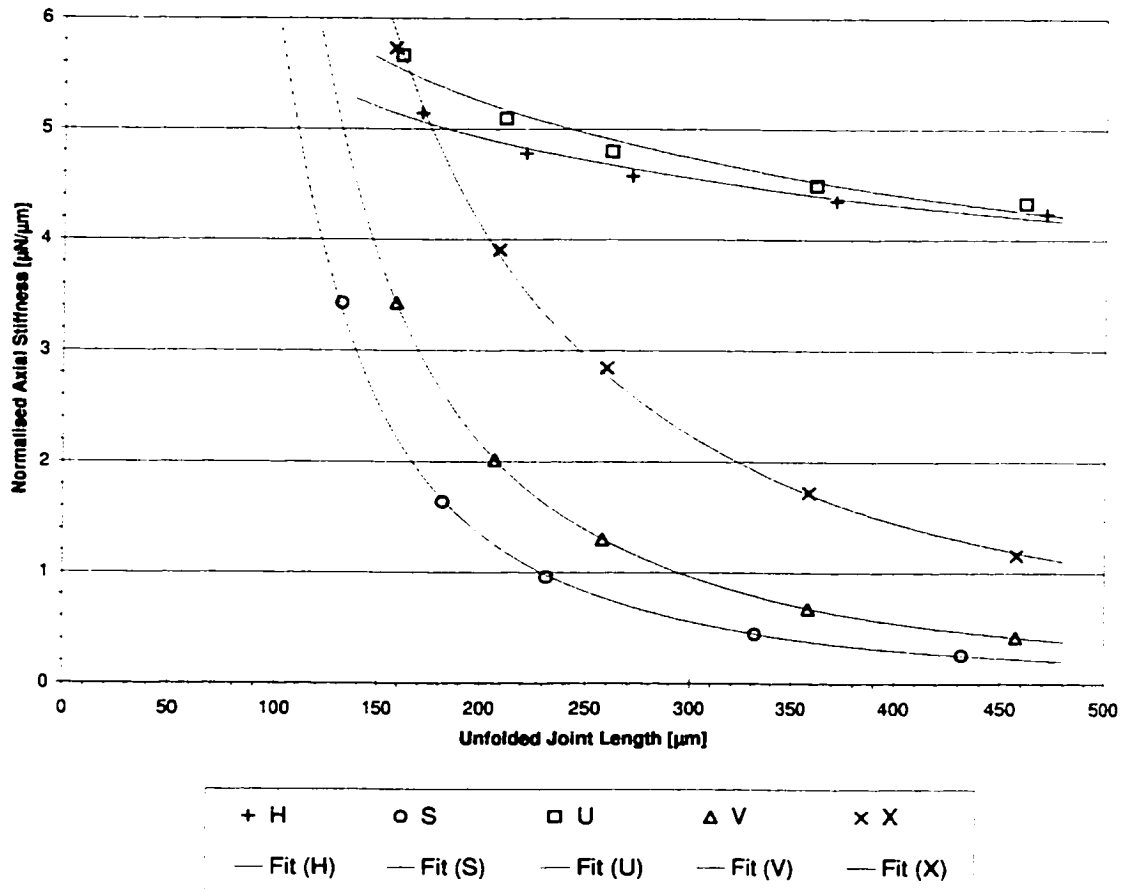


Figure 5-10: Normalised Axial Stiffness $K_x \cdot (L/250\mu\text{m})$ for Various Joint Types and Lengths (FEA)

6 Secondary FEA Results

This chapter presents FEA results for joint properties that exist along with the desired stiffnesses presented in the previous chapter. It discusses out-of-plane motion, reaction to force loading, and non-linear joint behaviour. It introduces centrodes and procedures to calculate the radii of curvature of the centrodes.

6.1 Introduction

While the previous chapter focused on the results for the “ideal” joint, the in-plane rotational and axial stiffnesses, this chapter describes the other properties present, which define a “real” joint:

- Joint motion in out-of-plane rotational direction
- Lateral joint response to force (instead of moment) loads
- Non-linear behaviour of the joints
- Motion of the centre of rotation during loading

6.2 Out-of-Plane Rotational Stiffness

As can be seen in Table 5-1 on page 44 the lowest mode for all joints is the out-of-plane rotational mode. Table 6-1 shows the calculated out-of-plane stiffnesses for various joints.

Table 6-1: Out-of-Plane Rotational Stiffnesses K_ϕ of Various Joints (FEA)

Joint Type and L_f	Unfolded Length L [μm]	Out-of-Plane Rotational Stiffness [$\mu\text{N}\mu\text{m}/\text{rad}$] K_ϕ	Stiffness Ratio K_ϕ/K_θ
I 30	30	7,500	1.00
H 100	471	460	0.95
H 50	271	760	0.92
H 25	171	1,200	0.88
X 80	458	410	0.83
X 45	260	720	0.83
X 27	158	1,200	0.84
S 200	432	370	0.71
S 100	232	710	0.72
S 50	132	1,300	0.74

A comparison between the in-plane rotational stiffnesses (Table 5-2 on page 46) and the out-of-plane rotational stiffnesses (Table 6-1) shows that they are close, with the out-of-plane stiffness being 5-30% lower than the in-plane stiffness. Two trends can be observed within this relationship:

1. With decreasing joint length the ratio of the out-of-plane to the in-plane rotational stiffness seems to decrease for H-joints, stay approximately constant for X-joints, and increase for S-joints.
2. The ratio between the out-of-plane and in-plane rotational stiffnesses is closest to 1 for H-joints, intermediate for X-joints, and smallest for S-joints.

Both phenomena are caused by the different shapes of the joints. During in-plane rotational motion the joints are subjected to an in-plane bending moment. Since this bending moment is acting in the same plane as the shaped beam is situated in, all parts of the joint are subjected to bending (Figure 6-1a). During out-of-plane rotational motion, however, the bending moment is acting in a plane that is perpendicular to the joint plane and to the joint axis. Therefore only joint elements parallel to the joint axis are subjected to bending, while joint elements perpendicular to the joint axis are subjected to torsion (Figure 6-1b).

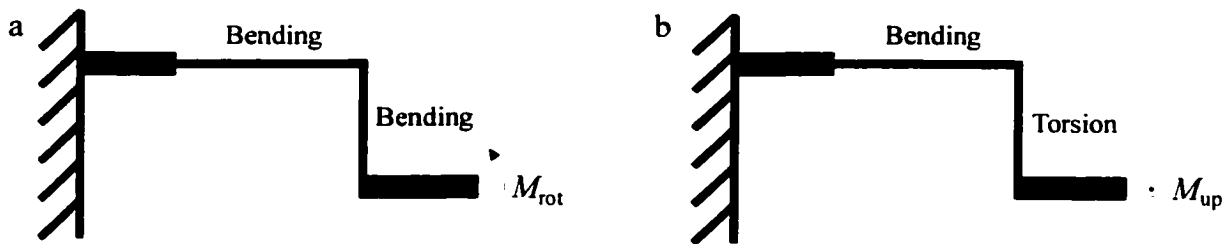


Figure 6-1: In-Plane Versus Out-of-Plane Motion (Top View)

The bending stiffness K_{bend} and torsional stiffness K_{tors} of a cantilevered beam with a square cross-section are given by:

$$K_{\text{bend}} = \frac{EI}{L} \quad \text{with } I = \frac{a^4}{12} \quad (\text{square cross-section}) \quad (6-1)$$

$$K_{\text{tors}} = \frac{GK}{L} \quad \text{with } K = 0.1406a^4 \quad (\text{square cross-section}) \quad (6-2)$$

where a is the width of the square beam. For a cantilevered beam of $250 \mu\text{m}$ length and a square cross-section of $2 \mu\text{m} \times 2 \mu\text{m}$ this yields $K_{\text{bend}} = 900 \mu\text{N}\mu\text{m}/\text{rad}$ and $K_{\text{tors}} = 620 \mu\text{N}\mu\text{m}/\text{rad}$. Note that K is the torsional section property of the beam not a stiffness.

Therefore the joint stiffness can be expected to be lower the more joint segments are subjected to torsion during the motion. Consequently the H- and U-joints should show the smallest difference between the in-plane and out-of-plane rotational stiffnesses, while the S-joint should show the largest difference (approx. $0.69 = K_{\text{tors}} / K_{\text{bend}}$).

For H- and U-joints the decrease in length increases the ratio of joint segment lengths that are subjected to torsion to those subjected to bending during the out-of-plane motion, thereby decreasing the stiffness ratio. The opposite effect can be observed for the S-joint. For X- and V-joints the ratio stays approximately constant.

Figure 6-2 on page 58 shows the out-of-plane rotational stiffnesses plotted versus the total unfolded joint length. It can be seen that the H- and U-joints show the highest out-of-plane rotational stiffness, followed by the X- and V-joints, and the S-joint.

Since the H- and the U-joint have approximately the same ratio of joint segments subjected to bending versus torsion their out-of-plane rotational stiffness were expected to be roughly the same. This is confirmed in Figure 6-2. The same effect can be observed for the X- and the V-joint. The difference between the stiffnesses become smaller with increasing joint length. This can be explained with the part of the joints that differ between H and U, and X and V respectively, becoming short compared to the total joint length, thereby decreasing its influence on the stiffness. The S-joint shows the lowest stiffnesses. This is con-

sistent with the fact that most of its joint segments are subjected to torsion rather than bending.

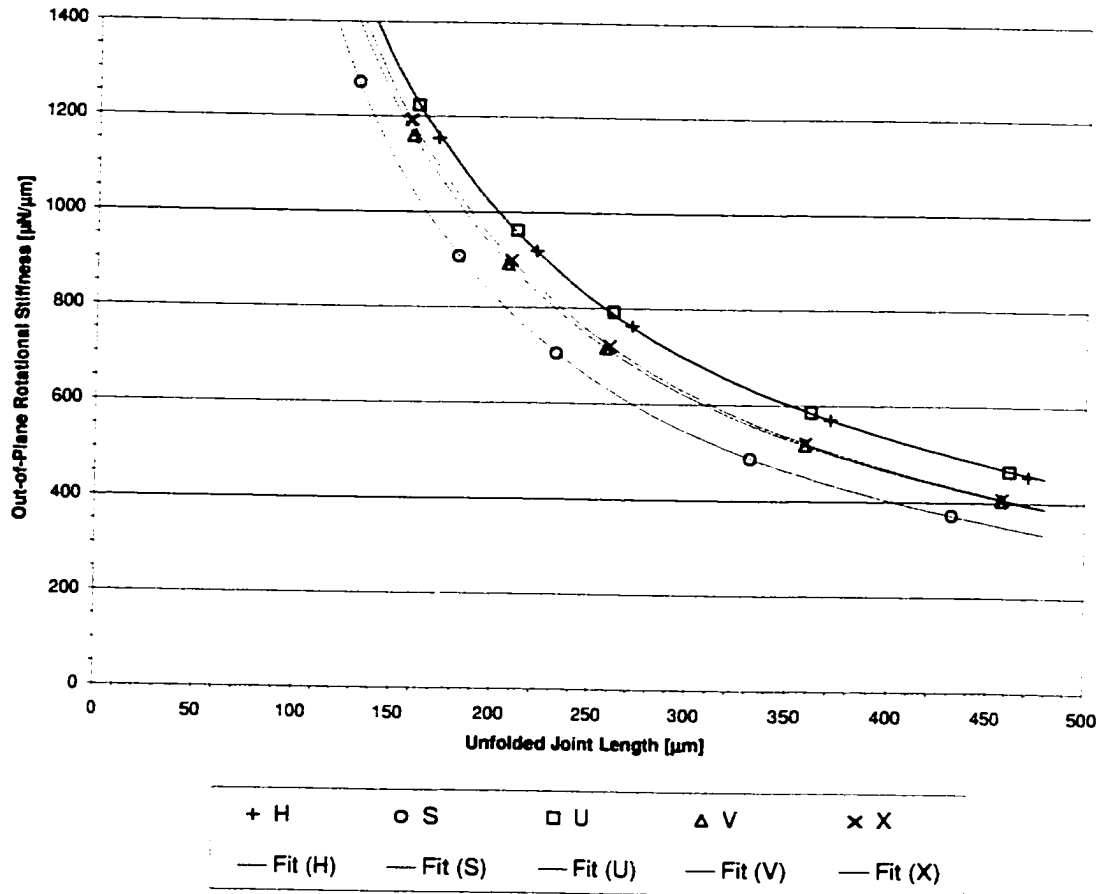


Figure 6-2: Out-of-Plane Rotational Stiffness K_ϕ for Various Joint Types and Lengths (FEA)

Over a range from $-100\mu\text{N}\mu\text{m}$ to $+100\mu\text{N}\mu\text{m}$ the out-of-plane rotational stiffnesses of the joints were found to be constant.

Using regression analysis the following formulas for the out-of-plane rotational stiffnesses were found with a coefficient of determination $R^2 = 1.00$. In order to make the formulas more comprehensible they were adjusted to a normal joint length of $250\mu\text{m}$:

$$\text{H-joint:} \quad K_{\phi} = 820 \frac{\mu\text{N}\mu\text{m}}{\text{rad}} \cdot \left(\frac{250\mu\text{m}}{L} \right)^{0.92} \quad (6-3)$$

$$\text{U-joint:} \quad K_{\phi} = 820 \frac{\mu\text{N}\mu\text{m}}{\text{rad}} \cdot \left(\frac{250\mu\text{m}}{L} \right)^{0.92} \quad (6-4)$$

$$\text{X-joint:} \quad K_{\phi} = 750 \frac{\mu\text{N}\mu\text{m}}{\text{rad}} \cdot \left(\frac{250\mu\text{m}}{L} \right)^{1.01} \quad (6-5)$$

$$\text{V-joint:} \quad K_{\phi} = 740 \frac{\mu\text{N}\mu\text{m}}{\text{rad}} \cdot \left(\frac{250\mu\text{m}}{L} \right)^{1.00} \quad (6-6)$$

$$\text{S-joint:} \quad K_{\phi} = 650 \frac{\mu\text{N}\mu\text{m}}{\text{rad}} \cdot \left(\frac{250\mu\text{m}}{L} \right)^{1.03} \quad (6-7)$$

$$\text{All joints:} \quad K_{\theta} = 900 \frac{\mu\text{N}\mu\text{m}}{\text{rad}} \cdot \left(\frac{250\mu\text{m}}{L} \right)^{1.00} \quad (6-8)$$

The exponent in the equations above is approximately 1 for all joints. The coefficients are between $K_{\text{bend}} = 900 \mu\text{N}\mu\text{m}/\text{rad}$ and $K_{\text{tors}} = 620 \mu\text{N}\mu\text{m}/\text{rad}$ for a $250\mu\text{m}$ cantilever beam with the S-joint closest to K_{tors} and the H- and U-joints closest to K_{bend} . This backs up the previous assumption that the separation of the out-of-plane rotational stiffnesses is caused by different amounts of the joints subjected to bending versus torsion. Note that the equation (6-8) for in-plane-rotational stiffness has K_{bend} as the coefficient. This results from all joint segments being subjected to bending during in-plane rotation.

Figure 6-3 on page 60 plots the out-of-plane rotational stiffness normalised to a joint length of $250\mu\text{m}$ ($K_{\phi} \cdot (L/250\mu\text{m})$) versus the total joint length. A linear relationship can be observed for all joints. All normalised stiffnesses are lower than the pure bending stiffness K_{bend} and higher than the pure torsional stiffness K_{tors} (also shown in Figure 6-3).

H- and U-joints show the highest normalised stiffness, X- and V-joints intermediate, and S-joints the lowest. This is in good agreement with the predictions.

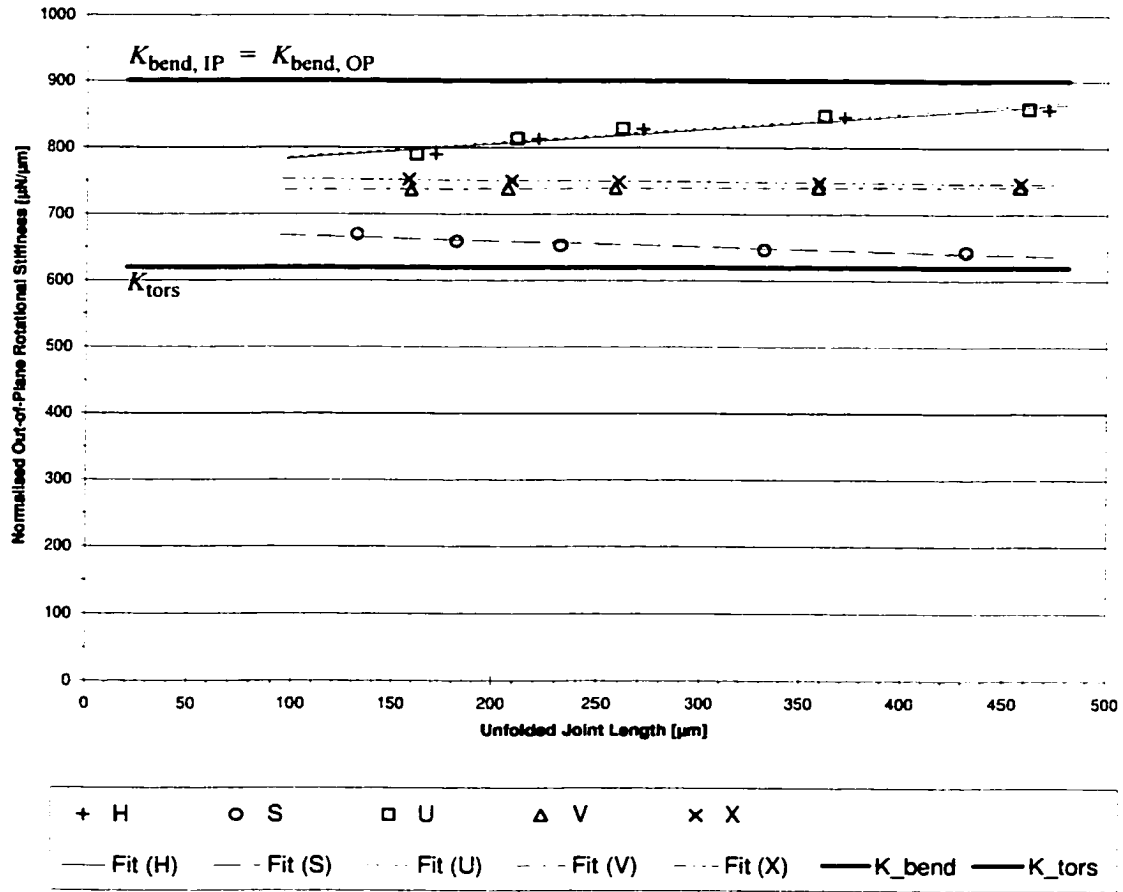


Figure 6-3: Normalised Out-of-Plane Rotational Stiffness $K_{\phi} \cdot (L/250 \mu\text{m})$ for Various Joint Types and Lengths (FEA)

The fact that the proposed use for the examined joints is within in-plane mechanisms makes the closeness of the out-of-plane and in-plane rotational stiffnesses undesirable. Especially since the joints appear to be softer in out-of-plane direction than in the in-plane. Unfortunately this is the direct result of the layer thickness and minimum feature size of the Poly 1 layer in the MUMPs process which result in a square cross-section.

The MUMPs process offers an unsupported method to create structures with a higher aspect ratio by combining the Poly 1 and Poly 2 layers. Using this process joints with a thickness to width aspect ratio of 3.5:2 were created. Since this process is unsupported and difficult to combine with regular structures, the results for these joints will be discussed in Chapter 8.

6.3 In-Plane Lateral Stiffness

Chapter 5.4 described the reaction of the joints to a pure moment load. It resulted in a rotational displacement. If the load is a force F_o applied at a distance d from the centre of rotation of the joint in the in-plane lateral direction, the resulting displacement is a combination of the rotational displacement due to the moment $M_o = F_o d$ induced by the force and the translational displacement due to the force itself. Thus, the resulting motion is actually a two DOF motion.

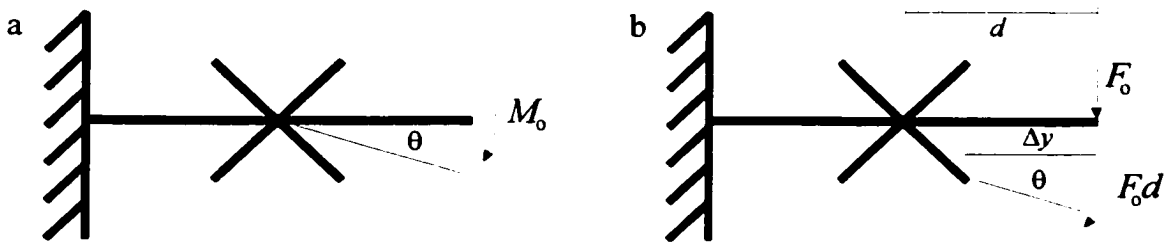


Figure 6-4: In-Plane Rotational Motion Due to Pure Moment (a) and Pure Force (b)

Figure 6-5 shows the resulting two degree of freedom displacement of an H 100 joined due to a force load of $F_o = 1 \mu\text{N}$ at a distance $d = 150 \mu\text{m}$ from the centre of rotation (in this case the centre of the joint). The force results in a rotational displacement $\theta = F_o d / K_\theta$ and a translational displacement $\Delta y = F_o / K_y$.

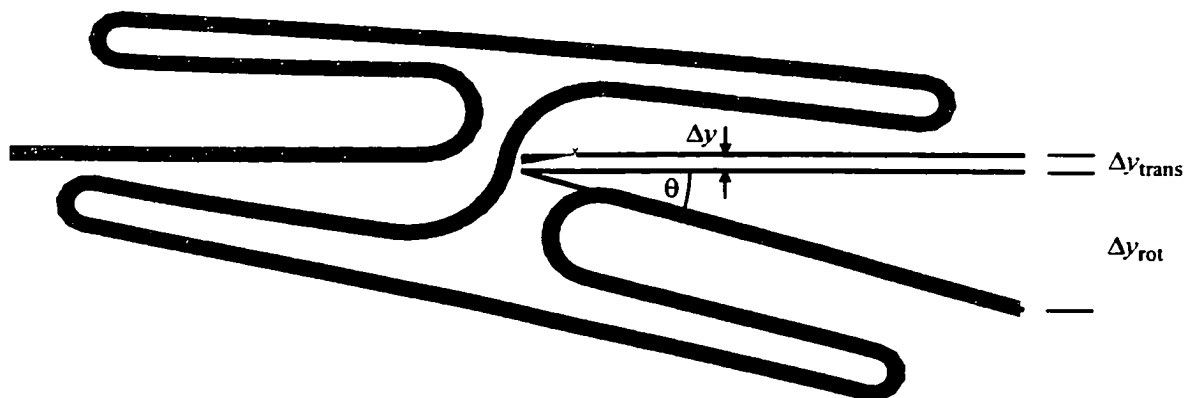


Figure 6-5: Two Degree of Freedom Motion

In order to find the in-plane lateral stiffnesses K_y of the various joints a series of forces ($-10\mu\text{N} \leq F_o \leq 10\mu\text{N}$) was applied at the ends of the joints ($d = 15\mu\text{m}$). Using the in-plane rotational stiffness K_θ calculated in Chapter 5.4 the angular displacement θ due to the force induced moment was calculated. The linear displacement of the joint end point in lateral direction due to this angular displacement was calculated as $\Delta y_{\text{rot}} = d \sin \theta$. Subtracting this distance from the total displacement in lateral direction calculated by ANSYS yielded the displacement due to translation $\Delta y_{\text{trans}} = \Delta y_{\text{tot}} - \Delta y_{\text{rot}}$. The in-plane lateral stiffness K_y was then calculated using $K_y = F_o / \Delta y_{\text{trans}}$.

By applying the force load at different distances from the centre of rotation it was verified that the value of K_y does not depend on the position of the applied force. However, since the induced moment is linearly dependent on the distance of the inducing force from the centre of rotation the relative importance of the resulting translational displacement becomes smaller the further away the force is applied. In first approximation the relative importance can be described by

$$\frac{\Delta y_{\text{rot}}}{\Delta y_{\text{trans}}} = \frac{K_y}{K_\theta / d^2} \quad (6-9)$$

Table 6-2: “Safe” Distance d_o for Various Joints (FEA)

Joint Type	“Safe” Distance d_o	
I	$3.0 \cdot L_f$	$3.0 \cdot L$
H	$3.5 \cdot L_f$	$0.60 \cdot L$
U	$3.0 \cdot L_f$	$0.70 \cdot L$
X	$3.5 \cdot L_f$	$0.55 \cdot L$
V	$2.5 \cdot L_f$	$0.50 \cdot L$
S	$50\mu\text{m}$	$50\mu\text{m}$

Using this formula a “safe” distance d_o can be found for which the translational displacement is only 1% of the rotational displacement, i.e. for which the load can be treated as pure moment. For H-, U-, V-, and X-joints this distance is between $2.5L_f$ and $3.5L_f$ or

between 50% and 70% of the total joint length. For the S-joint the distance is constant at approximately $d_o = 50\mu\text{m}$.

Figure 6-6 plots the in-plane lateral stiffness over the total unfolded joint length. H-, U-, V-, and X-joints show similar stiffnesses with H- and U-joints being softer than X- and V-joints. This is a result of the force acting perpendicular to the majority of the joint segments for H and U while acting under a 45° angle for X and V. The S-joint was calculated as being much stiffer than the other joints. This results from the fact that most joint segments of the S-joint are in parallel to the applied force.

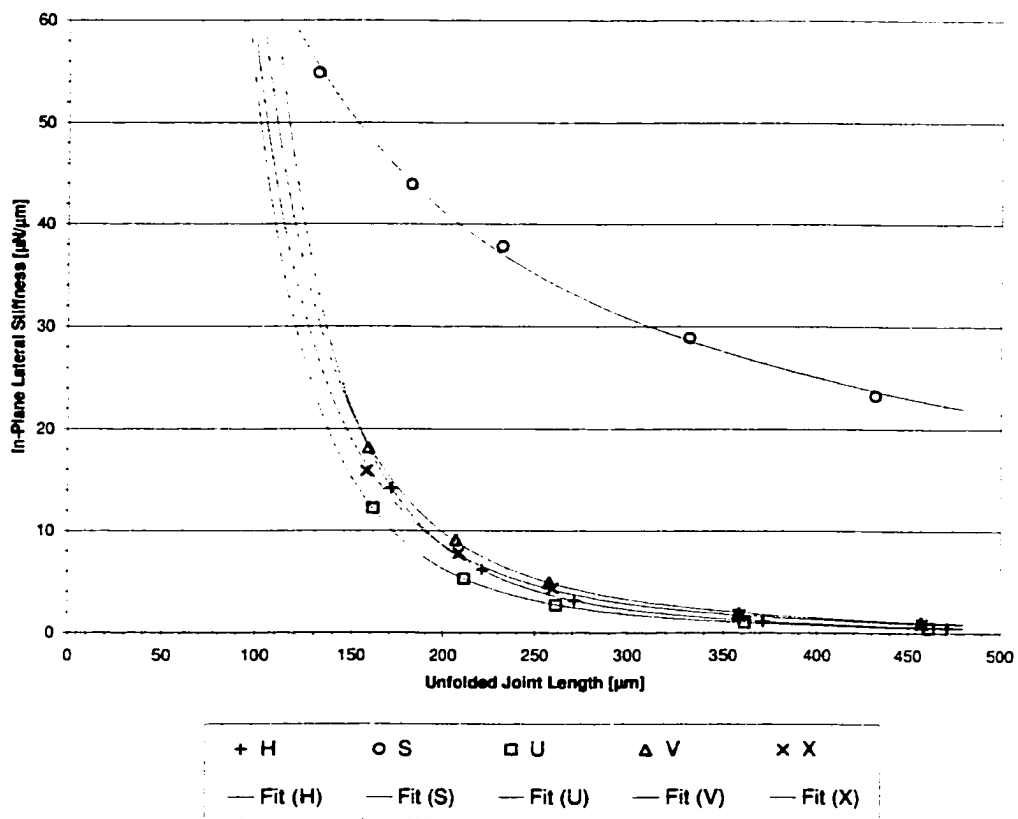


Figure 6-6: In-Plane Lateral Stiffness K_y for Various Joint Types and Lengths (FEA)

Using regression analysis the following equations for the in-plane lateral stiffnesses of the various joints were calculated with coefficients of determination $R^2 = 1.00$. In order to make the formulas more comprehensible they were adjusted to a normal joint length of $250\mu\text{m}$.

$$\text{U-joint:} \quad K_y = 3.1 \frac{\mu\text{N}}{\mu\text{m}} \cdot \left(\frac{250\mu\text{m}}{L} \right)^{3.09} \quad (6-10)$$

$$\text{H-joint:} \quad K_y = 4.1 \frac{\mu\text{N}}{\mu\text{m}} \cdot \left(\frac{250\mu\text{m}}{L} \right)^{3.28} \quad (6-11)$$

$$\text{X-joint:} \quad K_y = 4.6 \frac{\mu\text{N}}{\mu\text{m}} \cdot \left(\frac{250\mu\text{m}}{L} \right)^{2.75} \quad (6-12)$$

$$\text{V-joint:} \quad K_y = 5.3 \frac{\mu\text{N}}{\mu\text{m}} \cdot \left(\frac{250\mu\text{m}}{L} \right)^{2.75} \quad (6-13)$$

$$\text{S-joint:} \quad K_y = 35 \frac{\mu\text{N}}{\mu\text{m}} \cdot \left(\frac{250\mu\text{m}}{L} \right)^{0.72} \quad (6-14)$$

It can be observed that in the equations for the H-, U-, V-, and X-joints the exponents are approximately 3. This is consistent with a cantilever beam loaded at the end ($K \propto \frac{EI}{L^3}$). The equation for the S-joint, however, has an exponent close to 1. This is consistent with a straight beam in tension or compression ($K \propto \frac{AE}{L}$).

The high in-plane lateral stiffness of the S-joint allows the treatment of a force load as a pure moment load making it closest to an “ideal joint”.

6.4 Non-Linear Joint Stiffness

As mentioned in Chapter 5.5, the calculated axial stiffnesses were not constant but varied with the magnitude of the applied force. Figure 6-7 shows how the stiffness of an H 100 joint changes with the magnitude of the applied force. Compression is described with a negative force magnitude, tension with a positive one. For the H 100 joint the axial stiffness varies by more than 50% between largest applied forces in tension and compression:

$$\text{Stiffness variation equals } \frac{K_{\text{comp}} - K_{\text{tens}}}{K_{\text{tens}}}$$

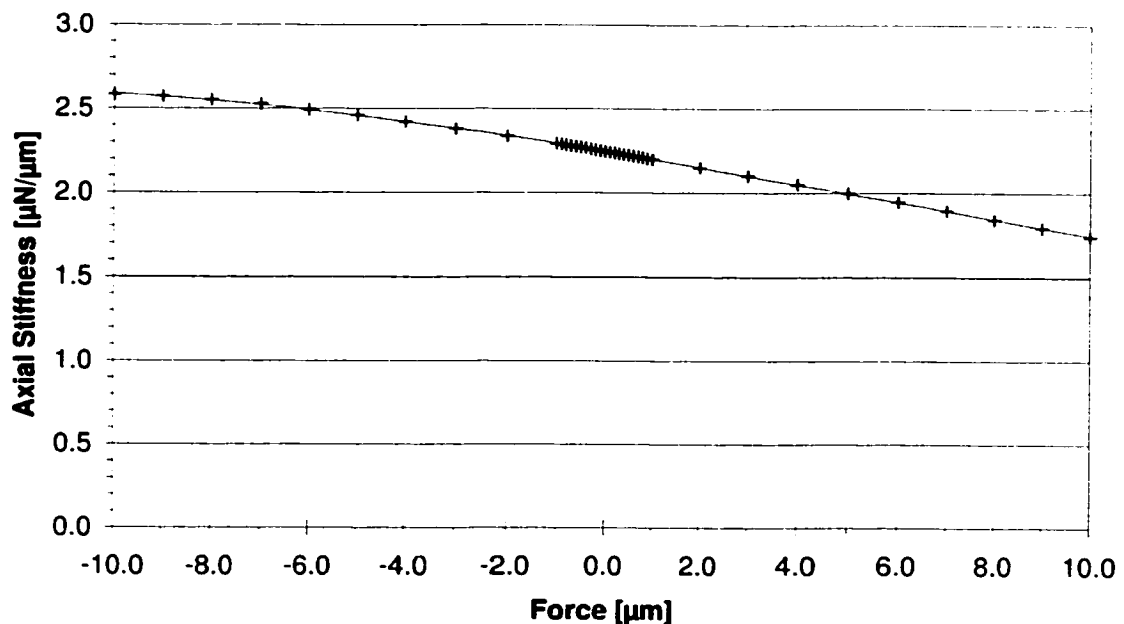


Figure 6-7: Stiffness Non-Linearity in Applied Force for an H 100 joint

Figure 6-8 on page 67 shows the reason for the stiffness change. The pictures on the left side show an H 100 joint in compression (exaggerated). The top picture shows the unloaded joint. The two pictures below show the joint with axial compression loads of 5 μN (centre) and 10 μN (bottom) as calculated by ANSYS. The pictures on the right show the joints with axial tension loads of 5 μN (centre) and 10 μN (bottom). The change of the joint shape during the loading sequence changes moment arms and therefore the moments induced by the applied force. Just like for the fishing rod in Figure 4-5 on page 38 these geometric non-linearities cause the axial stiffness to change with the applied load.

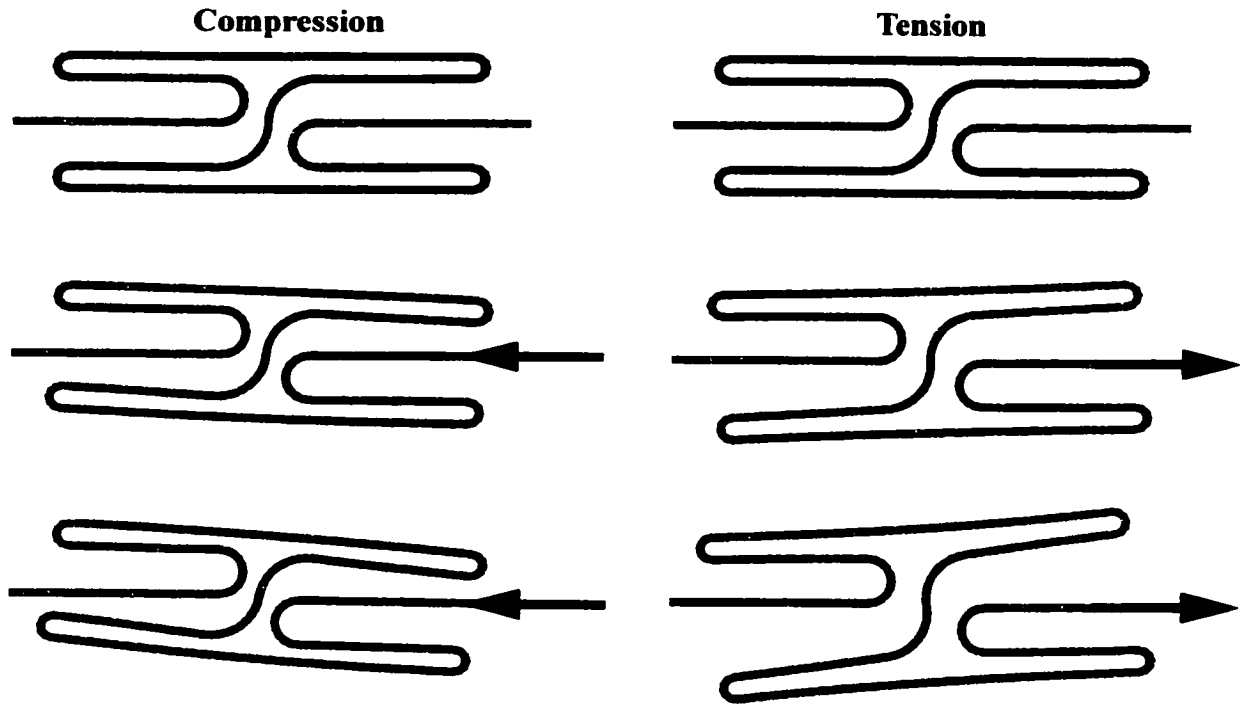


Figure 6-8: Shape Change of an H-Joint During Axial Loading (FEA, exaggerated)

This effect is larger for longer joints. It also varies greatly with joint shape. The largest variation in stiffness can be examined for the H-joint (see Table 6-3). This was to be expected since even a slight change of orientation in the long joint arms of the H-joint causes a significant change in axial stiffness.

Table 6-3: Stiffness Variation for Various Joints Between a 10 μ N Compression and a 10 μ N Tension Load (FEA)

Joint Type and L_f	Unfolded Length L [μ m]	Stiffness Variation
		$\frac{K_{comp} - K_{tens}}{K_{tens}}$
H 100	471	50%
V 90	457	39%
X 80	458	36%
U 115	461	18%
S 200	432	12%

Figure 6-9 shows the same effect observed in an experimental setup. The left pictures show an H 100 in compression by a probe needle while the right pictures show an H 100 joint in tension.

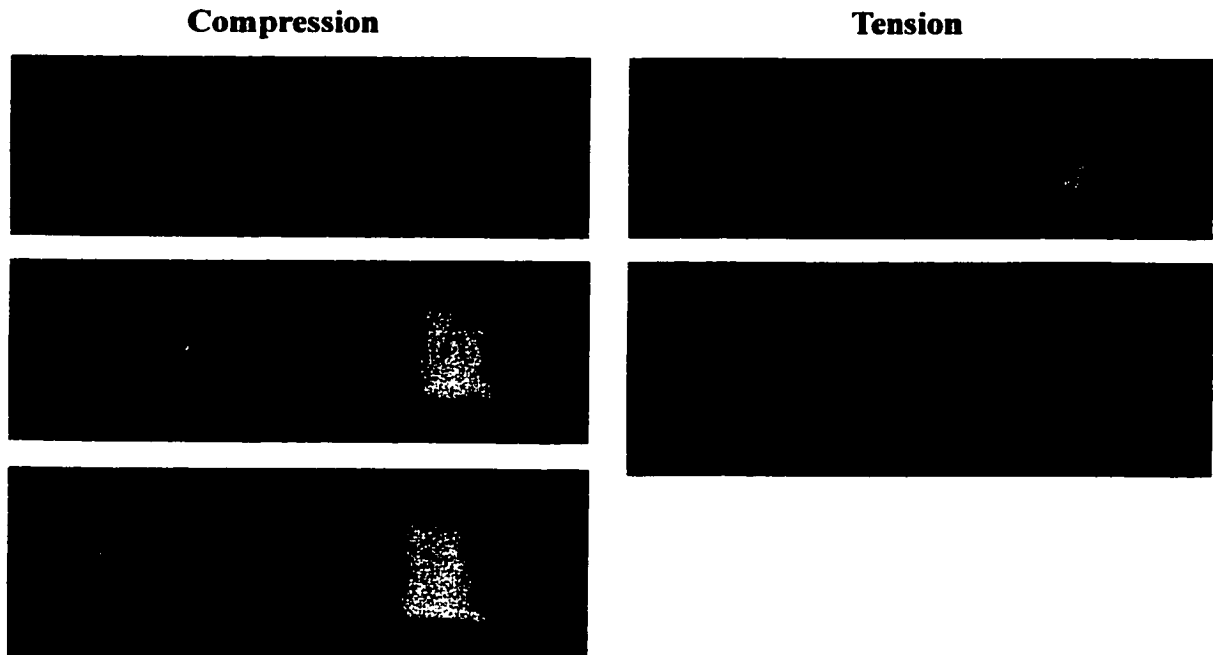


Figure 6-9: Shape Change of an H-Joint During Axial Loading by a Probe Needle
(Large Force Used for Demonstration)

6.5 Centroides

Chapter 5.2 calculated the centre of rotation (COR) for the joints in the resting position using finite element analysis. It was observed that as the load changed the location of the COR changed. The path of the COR during loading is called the centroide. The centroides can be used to make an accurate kinematic model of the joint.

Introduction¹

For a pure rotary (pin) joint the centre of rotation is independent of the load. It is fixed at the position of the pin.

Since compliant joints cannot be pure rotary joints, the position of the centre of rotation can be expected to move during loading. The successive positions of the COR form a path called the centroide.

Since a compliant joint connects two links, there will be two centroides associated with any one centre of rotation (one for each link). These are formed by fixing one link and rotating the other, then swapping the links.

Figure 6-10a on page 70 shows the location of the COR $I_{2,2}$ (between two loads applied to link 2) while keeping link 1 anchored. Because link 1 is stationary, or fixed, the path formed by the CORs is called the fixed centroide. By temporarily inverting the mechanism and fixing link 2, as shown in Figure 6-10b, link 1 can be moved and the location of COR $I_{1,1}$ (between two loads applied to link 1) can be determined. Since in the original linkage link 2 was the moving link this is called the moving centroide. Figure 6-10c shows the original linkage with both fixed and moving centroides superimposed.

If the joint is replaced by two cams with the fixed and moving centroide as contacting surfaces, rolling the moving centroide against the fixed centroide produces motion identical to the motion produced by the original joint (see Figure 6-10d).

1. see [24] p. 207f.

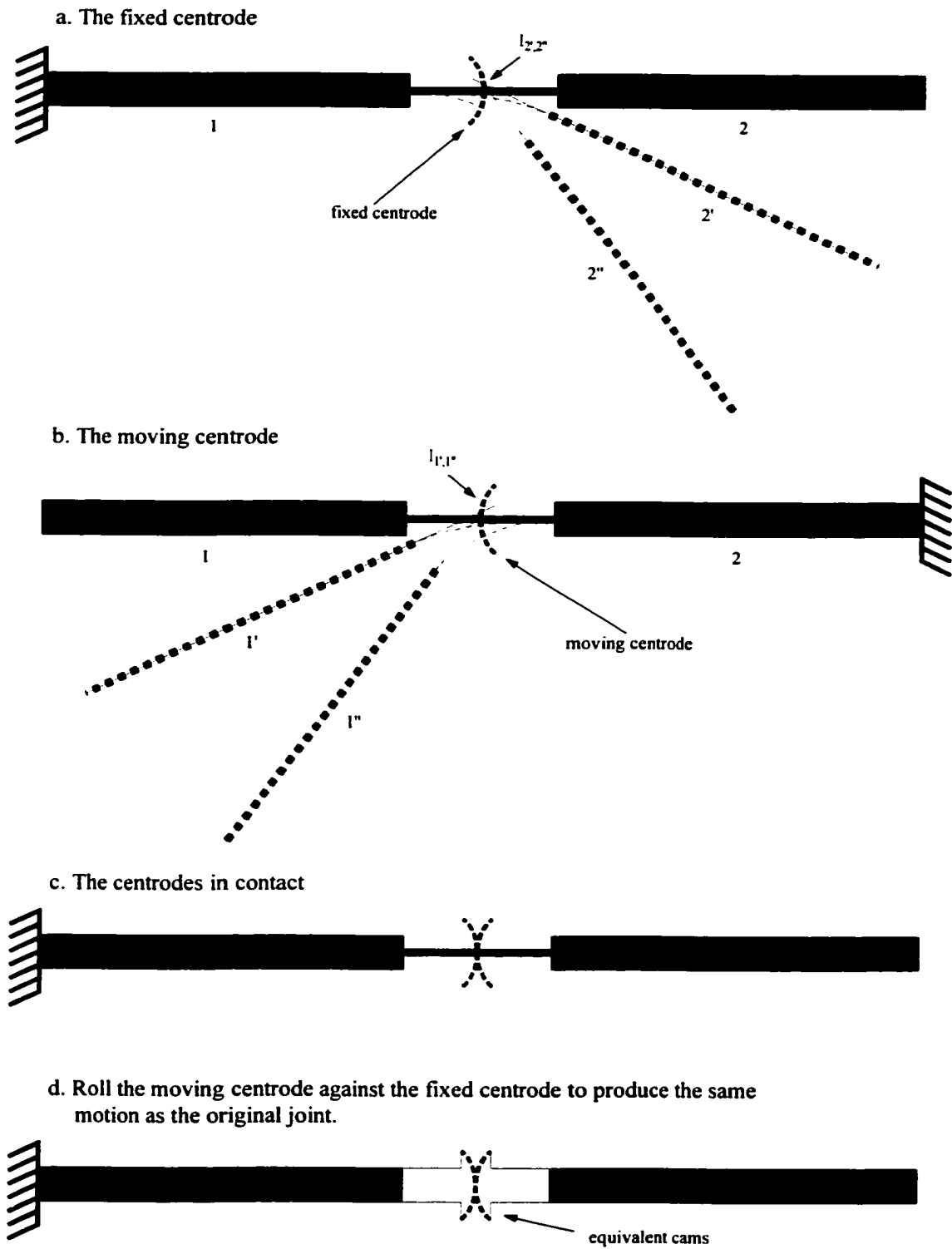


Figure 6-10: Fixed and Moving Centroides of a Joint Link System

FEA Results

Figure 6-11 shows the centrodes for the four symmetric joint types. Each marker (\times or $+$) indicates the position of the current centre of rotation in 1° rotation steps for the links. The underlying grey areas show the position of the actual joint.

The locations of the centres of rotation were calculated by loading the joints with pure moment loads in 20 steps for each centrode. The loads were chosen so as to cause a 1° angular displacement per load step. Due to the pure moment loading the lateral stiffness K_y has no effect on the location of the COR.

The centrodes of the U- and V-joint are shifted towards the anchor point and are therefore located in the link, outside the actual joint. The centrode is located at the position of the resting COR presented in Chapter 5.2. This makes kinematic models of the U- and V-joints more difficult. Otherwise the shape of the centrodes are similar to the shape of the H- and X-joints' centrodes.

Considering only symmetric joints (I, H, X, S) the distance that the centre of rotation moves in axial direction during loading seems to be related to the axial stiffness K_x of the joints. For the axially stiffest joint, the I-joint, the COR moves less than $0.1 \mu\text{m}$ in the axial direction during loading. For the axially softest joint, the S-joint, the COR moves the furthest of all joints. Note that even for the S-joint the COR only moves $\pm 2 \mu\text{m}$ in axial direction between the -10° and $+10^\circ$ position. For a bridged gap size of $30 \mu\text{m}$ and a total joint length of over $200 \mu\text{m}$ this is not a large change.

The combination of the axial and lateral travel of the centre of rotation results in a variation of the angle of the centrode with the lateral axis. As the in-plane axial stiffness of the joints decreases the angle of the centrode with the lateral axis increases.

Table 6-4: Angle of Centrodes for Various Joints

Joint Type and L_f	Unfolded Length [μm]	Centrode Angle
I 30	30	0°
H 50	271	59°
X 45	260	66°
S 100	232	78°

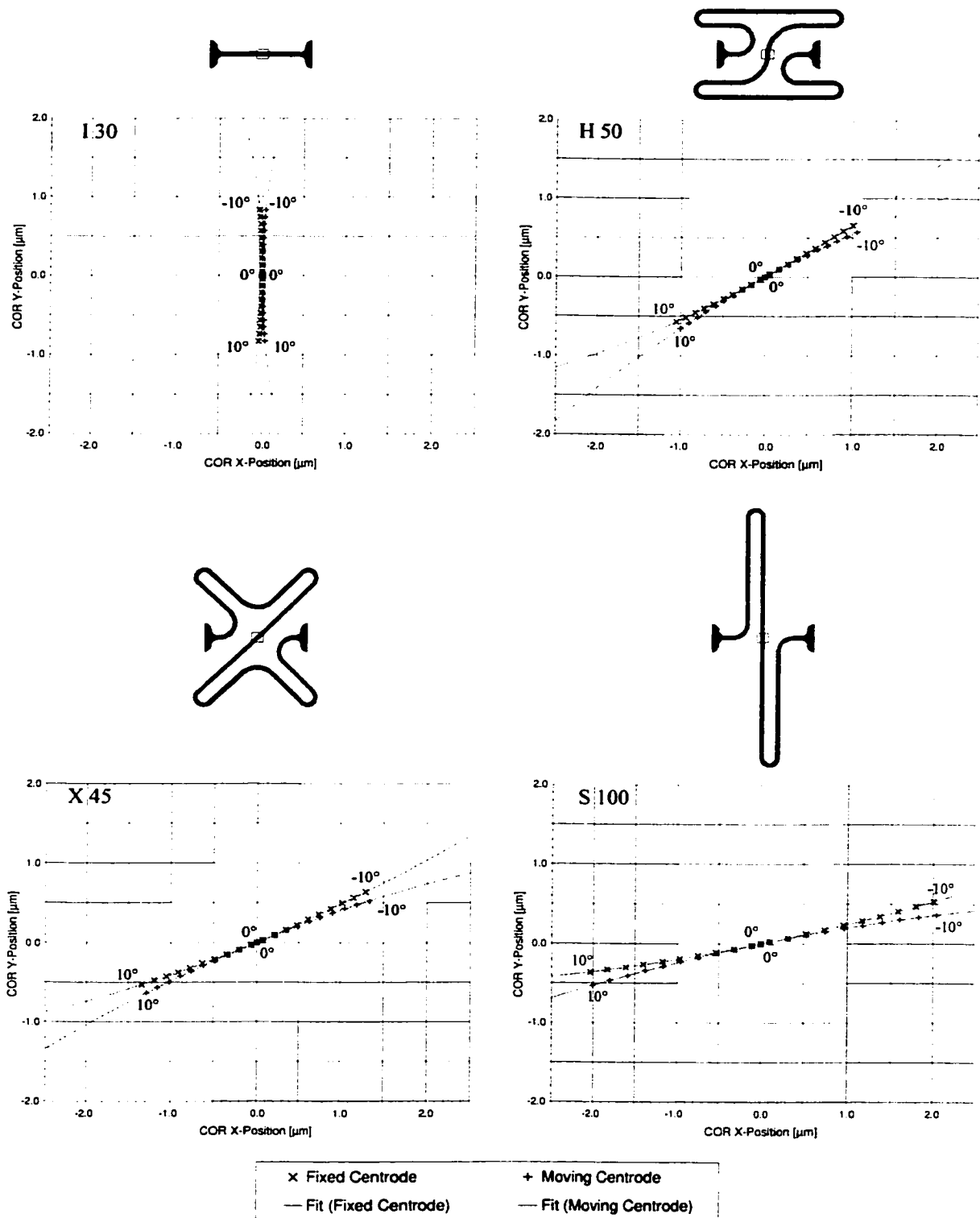


Figure 6-11: Centroid of I 30, H 50, X 45, S 100 (Shaded Area Represents Joint Beam)

Radius of Curvature

In order to be able to numerically compare the influence of the joint shape on the centres the radius of curvature of the centrodes at the 0° location was calculated. This was achieved by taking the COR locations at 1° , 0° , and -1° and fitting a circle through them.

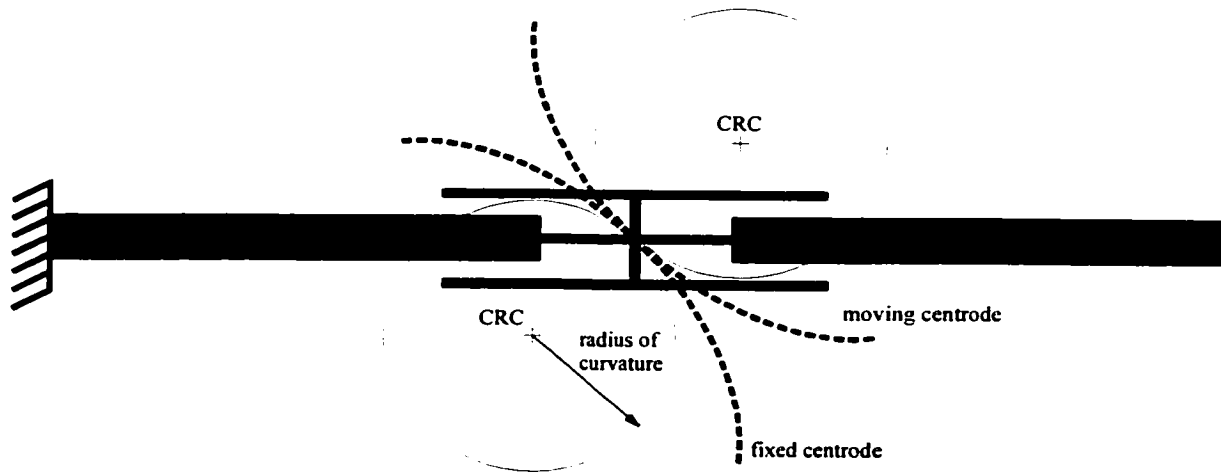


Figure 6-12: Radius of Curvature of a Centrod at Location of 0° COR

Note that since all three points are located close to each other on the same side of the circle, a small change in location of the points can result in a large change in result for the circle. Therefore the results (Radius of Curvature and CRC = Centre of Radius of Curvature) are given as integer values only. Note results for the fixed and the moving centrodes are similar but slightly different.

Table 6-5: Radii of Curvature of Centrodes for Various Joints

Joint Type and L_f	Unfolded Length [μm]	Fixed Centrod [μm]			Moving Centrod [μm]		
		Radius	CRC _x	CRC _y	Radius	CRC _x	CRC _y
I 30	30	9	-9	0	9	9	0
H 50	271	15	-8	-13	15	8	13
X 45	260	18	-7	-17	17	7	16
S 100	232	25	-6	25	25	5	24

The radius of curvature of the centrode seems to be related to the axial stiffness of the joint. The axially softest joint, the S-joint, has the largest radius of curvature, while the axially stiffest joint, the H-joint, has the smallest radius of curvature. The H-joint is closest to a pure rotary joint which has zero radius of curvature.

Figure 6-13 shows the radii of curvature of various joint types graphed versus the total unfolded joint length.

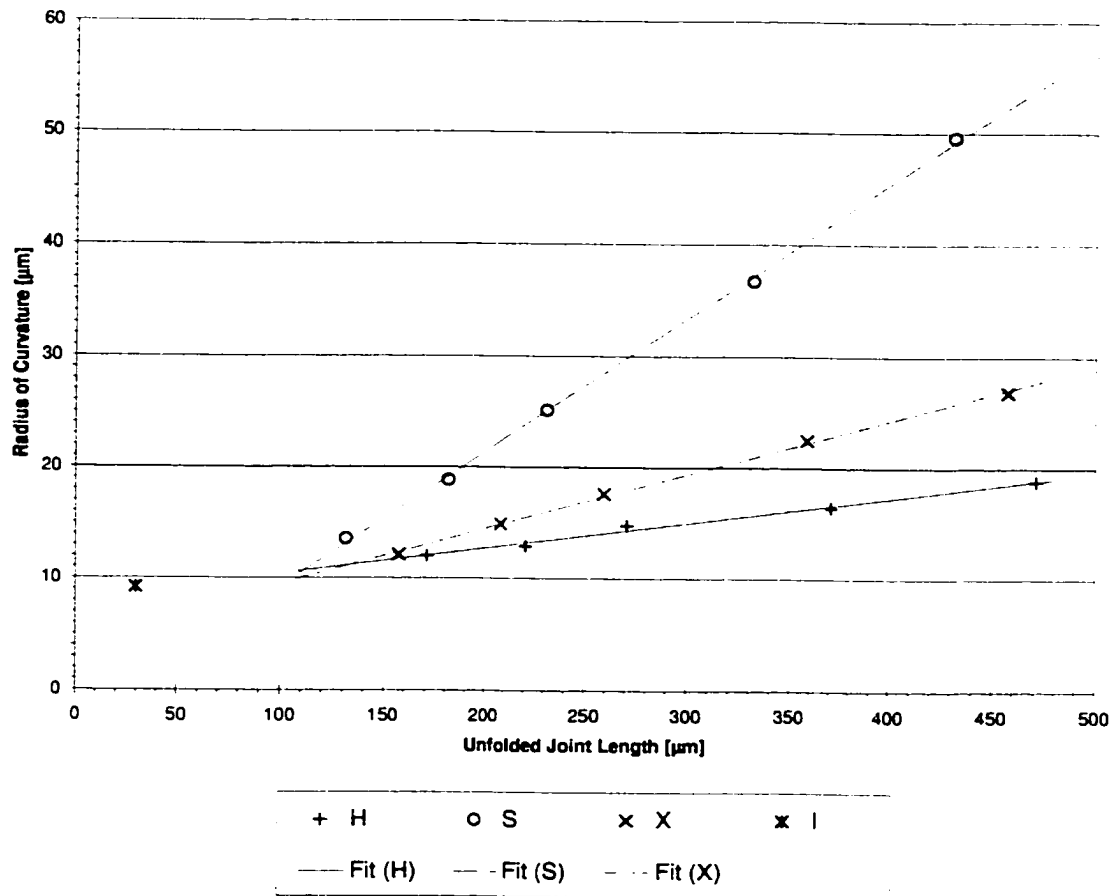


Figure 6-13: Radii of Curvature for Various Joint Types

7 Standard Joint Experiments

This chapter introduces the experimental methods used to measure the resonance frequencies of fabricated joints. It presents experimental results found using two different methods and compares them to FEA results.

7.1 Introduction

As mentioned before, the desired properties of the joints to be measured were their stiffnesses in different directions. At the present time, direct stiffness measurements of micro-joints are not easily attainable in the Dalhousie MEMS Lab due to the difficulty to apply a known force or to measure the reaction force to a known displacement. Stiffness, however, can be measured indirectly via a resonance test. To facilitate such tests oscillating joint-mass systems were fabricated (see Figure 3-2 on page 18). A typical resonating system consisted of a joint bridging a $30\ \mu\text{m}$ gap connecting two rigid $105\ \mu\text{m}$ long arms and a large square pendulum mass ($50\ \mu\text{m} \times 50\ \mu\text{m}$). One arm was stationary and its end anchored to the substrate, the other arm was free to oscillate. The arms and end-masses were $2\ \mu\text{m}$ or $3.5\ \mu\text{m}$ thick. The cross-section of the beam forming the joints was approximately $2\ \mu\text{m} \times 2\ \mu\text{m}$.

7.2 Experimental Methods

A series of tests was performed on surface micro-machined polysilicon micro-joints to experimentally measure the stiffness and range of motion of the joints. A static test of deflection was performed using a probe manipulator with the deflected device viewed through a CCD camera and video monitor. The I-joint was very stiff and showed little range of motion. The H-joint had a larger range of motion but was limited by the closely spaced joint loops. The X-joint had the largest range of motion. The other joints had intermediate ranges.

7.2.1 Non-Contacting Laser Reflectance System

Due to the small size of the structures, classical macro-scale measurement techniques are not possible. The measurement of the natural frequencies of the joints was carried out using a non-contacting laser reflectance system (see Figure 7-1 on page 76).

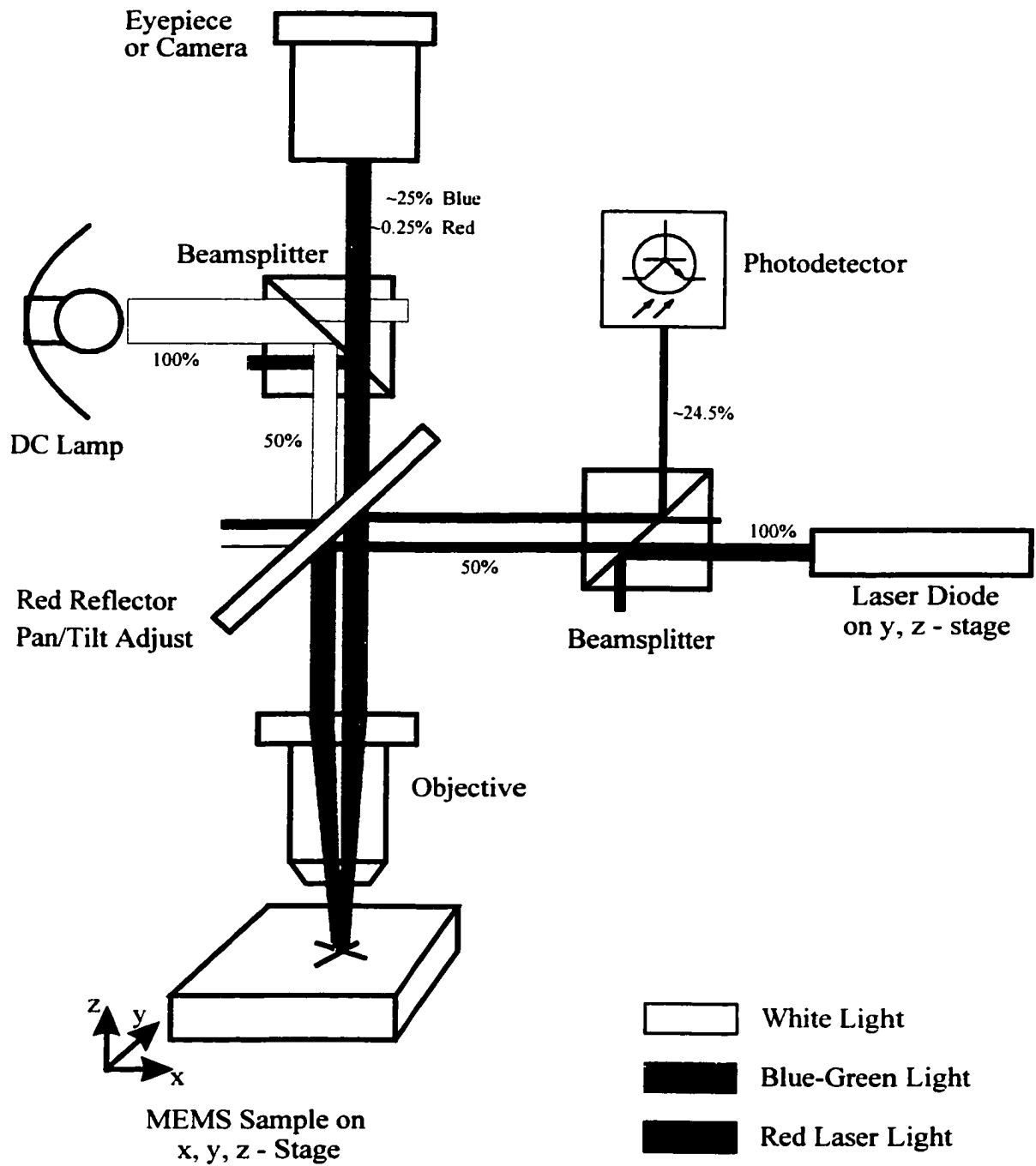


Figure 7-1: Schematic of the Non-Contacting Laser Probe Microscope System

A modified microscope with a co-axial laser probe allowed simultaneous observation of the device and optical testing. By moving a micromachined sample on an x - y table, different parts of the micro-device can be moved under and sampled by the fixed laser beam. There is a difference in the reflectance of the light as the arm or end-mass passes through the beam, hence the frequency of vibration can be measured by noting the change in intensity of the reflected light received by a photo detector. Resonance frequencies above 200kHz can be measured with this apparatus, although the frequencies discussed here ranged from 2 to 20kHz.

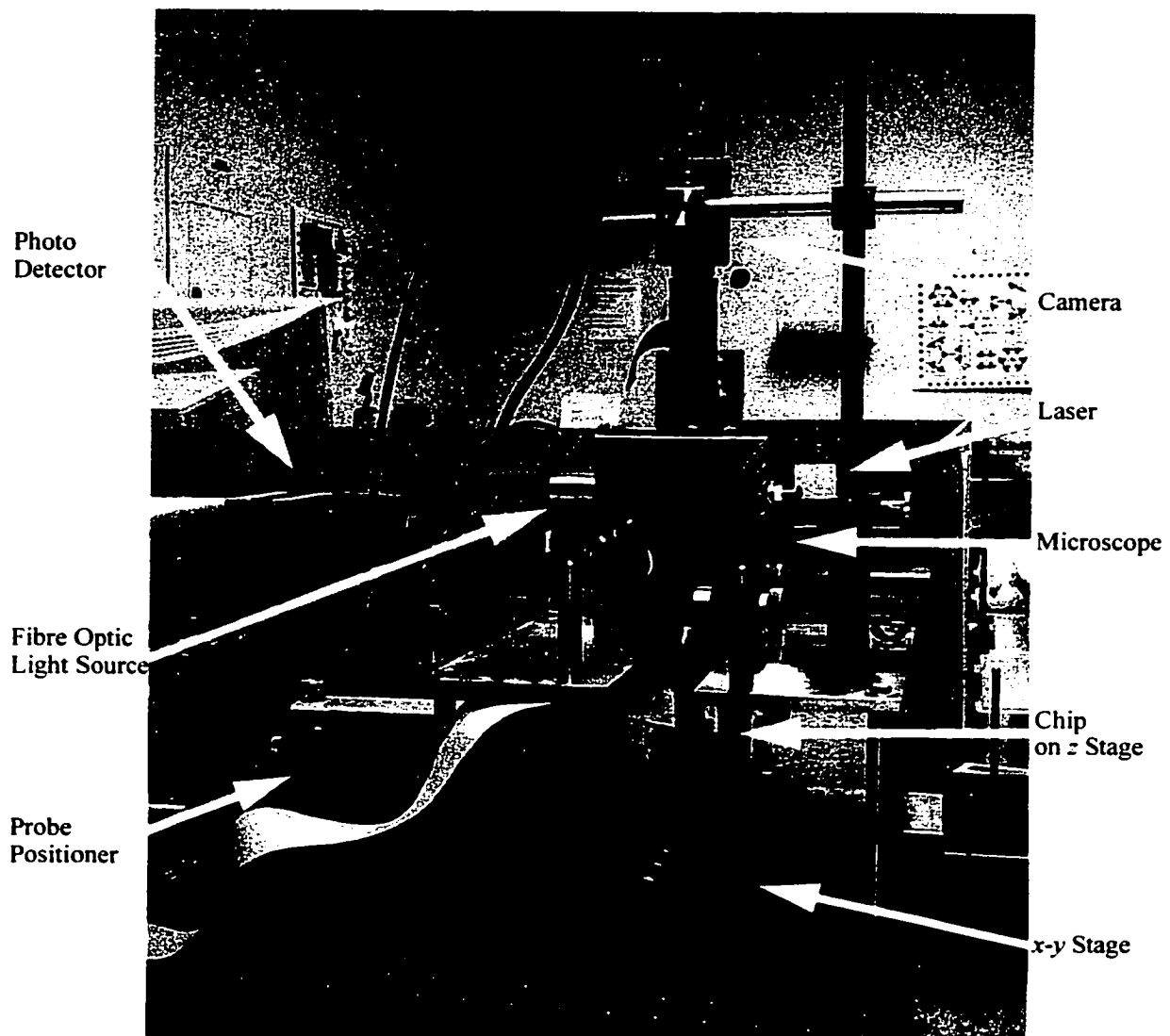


Figure 7-2: Photograph of the Non-Contacting Laser Probe Microscope System

The apparatus was originally designed by Ted Hubbard and James Wylde and later improved by Ralph Wilke (see [31]).

The joint-mass systems were excited using one of two methods: 1) Aerodynamic excitation using compressed air through a hypodermic needle (forced dynamic behaviour). The compressed air excitation was found to provide a white noise source up to approximately 200 kHz. 2) Micro-probes were used to ‘flick’ the joints. The probes were used to deflect the end-mass and then moved axially until the end-mass was released suddenly, thereby exciting the joint (transient dynamic behaviour).

7.2.2 Aerodynamic Excitation

The principle behind aerodynamic excitation is that of forced dynamic behaviour. A structure subjected to an excitation force spectrum consisting of white noise (all frequencies present with same amplitude) will start vibrating at its natural frequency. This phenomenon is the basis for wind instruments and referred to as the ‘reed’ effect. In the case of aerodynamic excitation the white noise excitation force spectrum is provided by directing a stream of compressed air flowing through a hypodermic needle onto the joint-mass system.

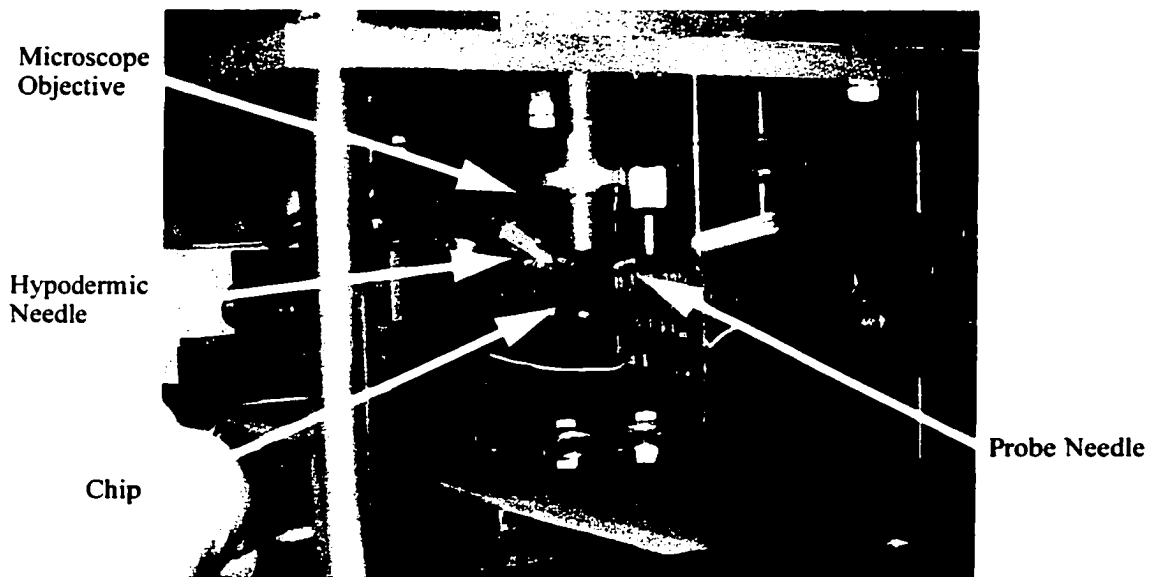


Figure 7-3: The Hypodermic Needle Air Excitation Setup

Through a series of pressure gauges and valves the university compressed air supply is connected to a hypodermic needle mounted on one of the probe manipulators. Shortly after exiting the hypodermic needle the airflow becomes turbulent and provides a white noise excitation source¹. Figure 7-3 on page 78 shows a photograph of the setup.

The position of the needle and the strength of the air flow strongly influence the quality of the excitation. Best results were achieved by positioning the needle on the anchor side of the joint-mass setup and directing the flow towards the end-mass. The exact position and height of the needle has to be determined using a trial and error approach since it differs from joint to joint. The air flow should be set to the minimum strength that still excites vibration. If the flow is too strong, the end-mass touches the ground during vibration.



**Figure 7-4: Photograph of Resonating X-Joint with Laser Reflection
(Aerodynamic Excitation)**

Figure 7-4 on page 79 shows a resonating X 80 joint-mass system with the laser spot. Since the camera records 30 frames per second and the joint-mass system vibrated at 6kHz, the image is blurred and shows part of the path of the vibrating system.

1. see [32]

While the joint-mass system completes one physical vibration cycle the arm passes the laser spot twice. Therefore the measured optical frequency is twice the actual mechanical frequency. This can be taken into account by measuring the frequency using every second peak in the recorded spectrum. Figure 7-5 on page 80 shows the recorded trace of a resonating X 45 joint-mass system.

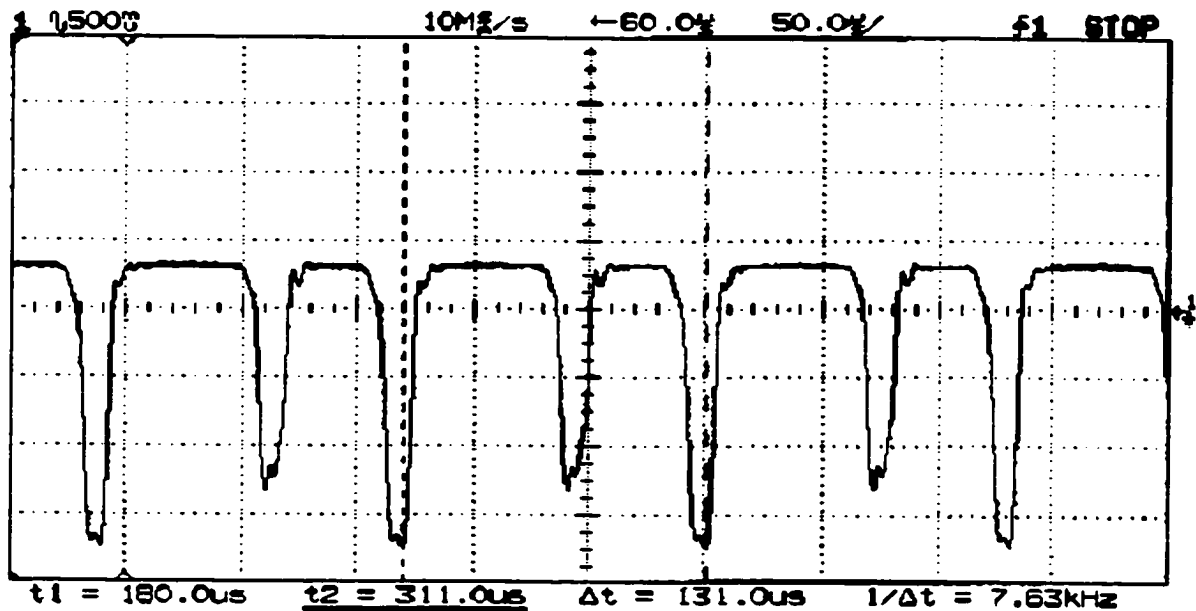


Figure 7-5: Oscilloscope Trace of a Resonating X-Joint (Aerodynamic Excitation)

7.2.3 The 'Flick'-Test

When a spring-mass system is excited by a suddenly applied non periodic excitation $F(t)$, the response to such an excitation is called transient response, since steady-state oscillations are generally not produced. Such oscillations take place at the natural frequencies of the system with the amplitude varying in a manner dependent on the type of excitation.¹

This is the basis for the 'flick'-test which records the response of the system to an impulsive excitation force. Using a probe needle the free end-mass is displaced in the direction of horizontal rotational motion and then suddenly released. Figure 7-6 on page 81 shows a displaced system just before release. While returning to its rest state the joint-mass

1. see [30] p. 89

system oscillates around the resting position. Due to damping the amplitudes of these oscillations get rapidly smaller and cannot be seen with the human eye. The oscillations die out after approximately 4 ms.

In order to record the frequency of these oscillations, the laser probe microscope introduced in Chapter 7.2.1 was used. The output of the photo detector was connected to an oscilloscope and a spectrum analyser. The oscilloscope was used to record the decaying oscillations while the spectrum analyser recorded the frequency spectrum of the oscillations.



Figure 7-6: Manually Displaced Joint-Mass System

Figure 7-7 on page 82 shows the oscilloscope trace of the decaying oscillation of a U-joint in response to a 'flick' excitation. It can be observed, that after 3 ms the oscillation amplitude has decayed enough to disappear in the background noise. This poses a problem for the spectrum analyser. In order to get a better frequency resolution of the recorded spectrum, the sampling time has to be increased. For a frequency span of 0 to 12.5kHz a FFT resolution of 100 bins results in a frequency resolution of 0.125kHz with a required sampling time of 8s. Increasing the number of bins to 200 increases the frequency resolution to 0.0625kHz but also increases the required sampling time to 16s.¹

1. see [23] p. 2-9 ff.

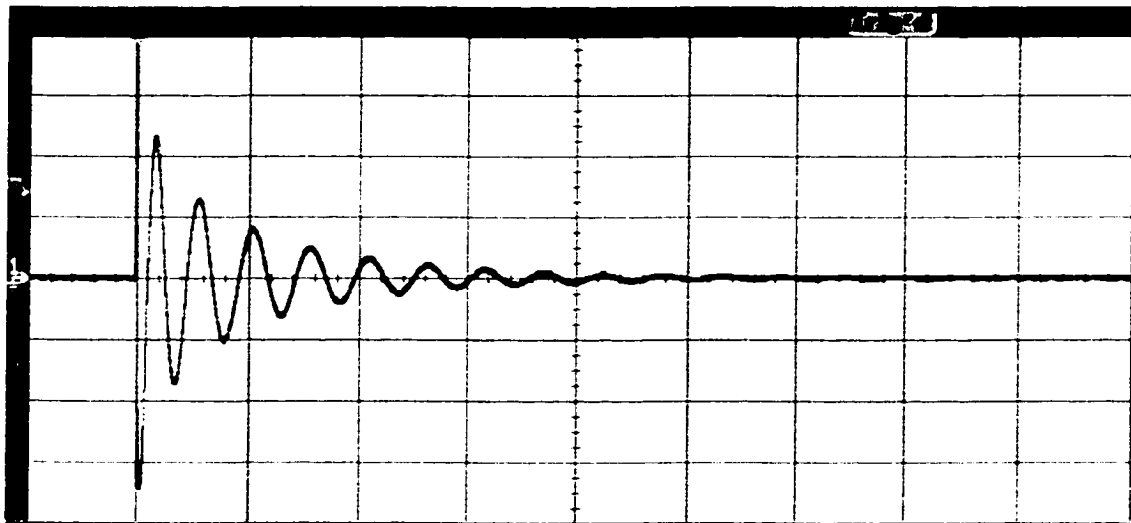


Figure 7-7: Recorded Oscilloscope Trace of a Decaying Oscillation of a U-Joint ('Flick'-Test)

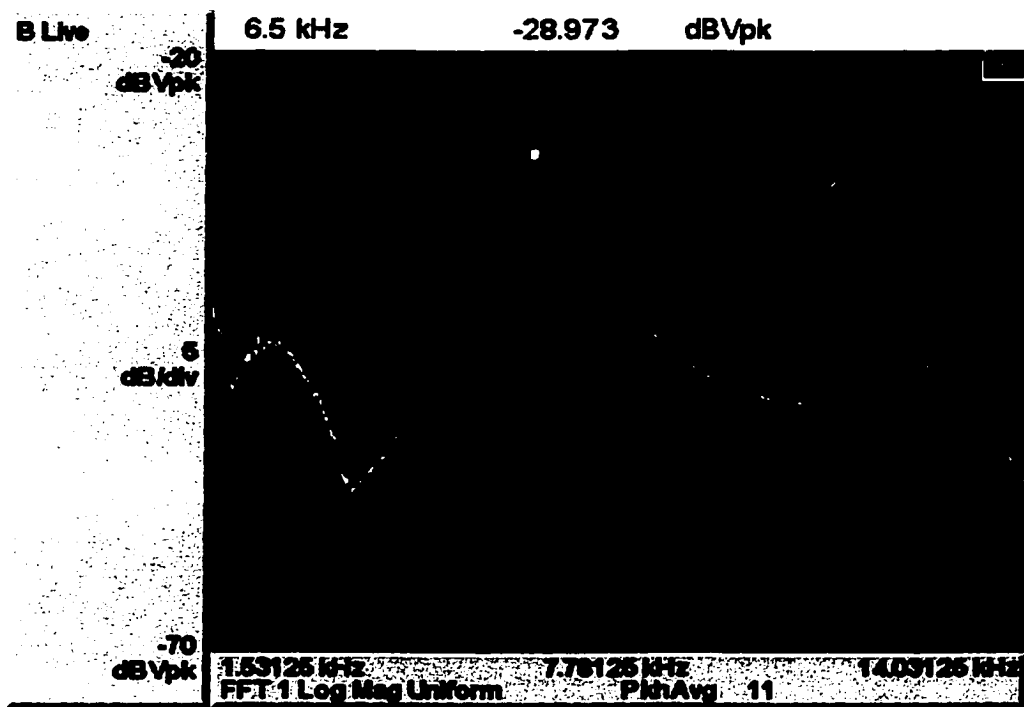


Figure 7-8: Recorded Spectrum Analyser Trace of the Transient Response of a U-Joint ('Flick'-Test)

Since the actual signal is only present for 3 or 4ms the recorded frequency spectrum is contaminated during the rest of the sampling time. This results in a broadening of the frequency peak in the spectrum. Reducing the sample time, however, results in a lower frequency resolution, broadening the frequency peak due to the larger bin size. A test of all the different settings found the 200 bin setting with a 12.5kHz frequency span to work best. Figure 7-8 on page 82 shows a frequency spectrum recorded with these settings.

In practise, it proved to be more accurate to get the frequencies from time based measurements off the oscilloscope rather than the spectrum analyser.

A set of step-by-step instructions for the 'flick'-test can be found in Appendix D.2 on page 174.

7.2.4 Calculation of Corresponding Stiffnesses

Once resonance frequency of a joint is measured, the corresponding rotational stiffness can be calculated using the following formula:

$$f = \frac{1}{2\pi} \cdot \sqrt{\frac{K_{\theta}}{I_{yy}}} \quad (7-1)$$

which yields to

$$K_{\theta, \text{exp}} = (2\pi f_{\text{exp}})^2 \cdot I_{yy} \quad (7-2)$$

with the in-plane rotational stiffness $K_{\theta, \text{exp}}$, the measured resonance frequency f_{exp} , and the mass moment of inertia I_{yy} about the out-of-plane axis.

The free arm and the free end-mass of the joint-mass system combined are much heavier than the actual joint itself (21.4ng vs. 4.4ng, H 100). Therefore, in first approximation, only those two are considered in the calculation of the mass moment of inertia.

7.3 Experimental Results

The seven joints fabricated on the RT2 chip were measured using aerodynamic excitation. All 24 joints on CJ2 were only tested using the ‘flick’-test since this proved to be the less invasive and less time consuming method.

7.3.1 Aerodynamic Excitation

Using aerodynamic excitation the resonance frequencies of the seven joints fabricated on RT2 were measured in the large end-mass variation. The method provided good results but was very tedious in execution. The position of the hypodermic needle as well as the magnitude of the air flow greatly influenced the vibration of the joint-mass systems.

For every joint five measurements were made and the average and standard deviation were taken. Figure 7-5 on page 80 shows a typical trace of a vibrating joint. Table 7-1 lists the measured result along with the corresponding FEA calculated frequencies. It also shows the stiffnesses calculated from the experimental frequencies using equation (7-2), as well as the corresponding stiffness calculated using FEA.

Table 7-1: Measured and FEA In-Plane Rotational Resonance Frequencies and Stiffnesses for Various Joints (Large End-Mass, Aerodynamic Excitation)

Joint Type and L_f	Unfolded Length L [μm]	Frequency [kHz]		Stiffness [$\mu\text{N}\mu\text{m}/\text{rad}$]	
		Exp.	FEA	Exp.	FEA
I 30	30	16 ± 1	18	5000 ± 600	7500
H 100	471	4.2 ± 0.1	4.5	340 ± 20	480
H 50	271	5.2 ± 0.2	6.0	530 ± 40	830
H 25	171	6.5 ± 0.2	7.6	820 ± 50	1300
X 80	458	4.5 ± 0.1	4.6	390 ± 20	490
X 45	260	5.9 ± 0.2	6.2	680 ± 50	870
X 27	158	7.6 ± 0.2	7.9	1100 ± 60	1400

It can be observed that the measured frequencies and stiffnesses are fairly close to the predicted frequencies and stiffnesses. The measured values appear all to be lower than the predicted values. Reasons for that will be discussed in Chapter 7.4 on page 89.

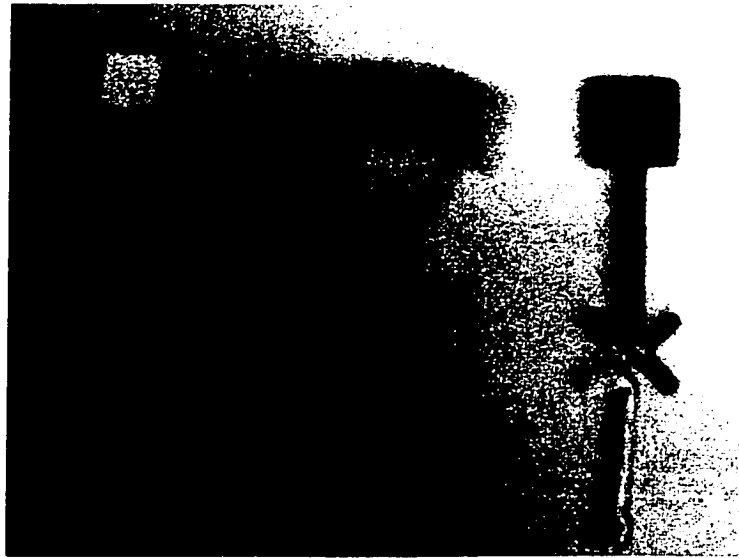


Figure 7-9: Two Joints Vibrating Side-by-Side

In general the aerodynamic excitation method proved to deliver good results but also to be rather destructive. Since the joint-mass systems on the chip were spaced relatively close in order to fit a large number of them onto the limited space available, it was never possible to excite only one joint alone. Figure 7-9 shows an X 80 joint vibrating between an I 30 and an X 45 joint. The X 45 joint appears black because it is lifting off the surface due the air flow. Just a slight change in air flow could cause the X 45 joint to vibrate as well.

Because different joints also required different magnitudes of air flow for excitation it happened fairly often that the air flow needed to excite one joint proved to be too large for its neighbour, which was destroyed in the process. Figure 7-10 on page 86 shows the result of a misguided air-flow. The rotor of a torsional comb-drive was displaced approximately $400\mu\text{m}$. Since it is connected to the substrate by a very soft spring it was not destroyed. Due to their higher stiffness the joints examined in this thesis were usually destroyed upon contact with misguided or overly strong air-flows.

Since this destructive side effect was highly undesired due to the small number of chips (fifteen) that were available for testing, an alternative method was sought and found in the 'flick'-test which proved a lot less invasive and also faster to conduct.

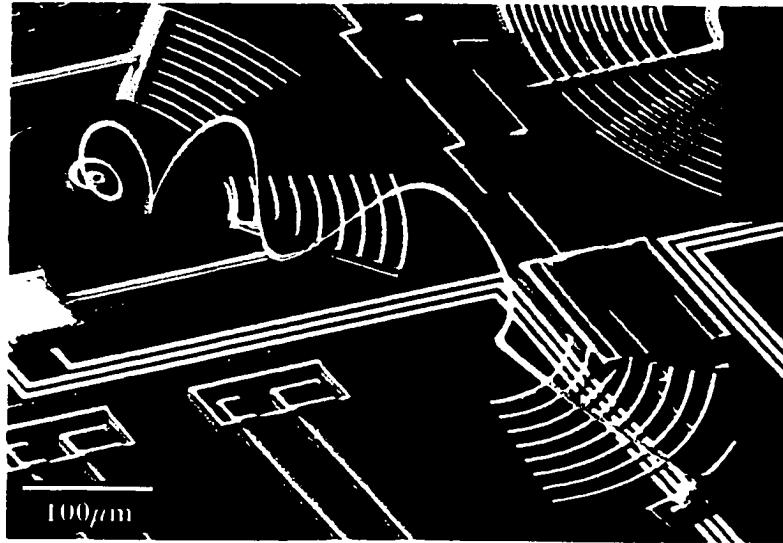


Figure 7-10: Destructive Power of Aerodynamic Excitation

7.3.2 The ‘Flick’-Test

As described in Chapter 7.2.3 the ‘flick’-test is based on the response of a joint-mass system to the manual displacement and sudden release of the end-mass using a probe needle (see Figure 7-6 on page 81). The ‘flick’-test proved to be much easier in execution than the aerodynamic excitation. It also was much less invasive. Joints could be excited one at a time.

In order to get accurate measurements the resonance frequency was calculated by measuring the period of ten oscillations using the digital oscilloscope, dividing it by ten and taking the inverse. This was done for five independent measurements and an average value along with a standard deviation was calculated. The spectrum analyser proved to be too inaccurate for the reasons described in Chapter 7.2.3 and was therefore only used for comparison.

The measurements proved to be very well reproducible resulting in small standard deviations. The resolution of the digital oscilloscope was taken into account as a systematic error. Table 7-2 lists the measured frequencies along with the calculated stiffness values and the corresponding FEA predicted values.

Table 7-2: Measured and FEA In-Plane Rotational Resonance Frequencies and Stiffnesses for Various Joints (Small End-Mass, 'Flick'-Test)

Joint Type and L_f	Unfolded Length L [μm]	Frequency [kHz]		Stiffness [$\mu\text{N}\mu\text{m}/\text{rad}$]	
		Exp.	FEA	Exp.	FEA
I 30	30	20 ± 1	24	4800 ± 500	7500
H 100	471	5.4 ± 0.1	6.1	350 ± 10	480
H 50	271	7.4 ± 0.1	8.2	660 ± 20	830
H 25	171	9.5 ± 0.1	10	1100 ± 20	1300
X 80	458	5.4 ± 0.1	6.2	350 ± 10	490
X 45	260	7.5 ± 0.1	8.4	680 ± 20	870
X 27	158	9.8 ± 0.2	11	1200 ± 50	1400
S 100	232	7.7 ± 0.1	8.9	720 ± 20	970
U 65	261	6.4 ± 0.1	7.0	690 ± 20	860
V 55	258	6.4 ± 0.1	7.3	650 ± 20	880

Just like in the aerodynamic excitation measurements it can be observed that all the measured values are lower than the values predicted using FEA. Nevertheless they are still close to the predicted values.

7.3.3 Damping

The resonance frequency is decreased by damping:

$$\omega_{\text{damped}}^2 = (1 - \zeta^2)\omega_n^2 \quad (7-3)$$

where $\omega_n = 2\pi f_n$ is the undamped circular resonance frequency and ζ is the damping factor. ζ was measured from the exponential decay of the experimental measurements as shown in Figure 7-11 on page 88, and found to be approximately 0.06 to 0.08. Note that the laser beam is gaussian (non-linear) which means that the recorded signal amplitude is not the exact amplitude of the motion. Therefore ζ is only an approximation. Measurements of the frequency spectrum half-width yielded similar results. While this high value of ζ will have a significant effect on the amplitude of the signal as shown in Figure 7-11, it has little effect on the resonance frequency. From equation (7-3), $f_{\text{damped}}/f_n = 0.994$, and damping will be ignored in f and K calculations.

The quality factor Q is related to ζ by

$$Q = \frac{1}{2\zeta} \quad (7-4)$$

Thus the quality factor for the joint-mass systems ranged from 6 to 8. This is a relatively low value of Q , however it is similar to values reported in the literature [11, 34]. For example Zhang reported micro-resonators vibrating in air with Q 's of 16-18.

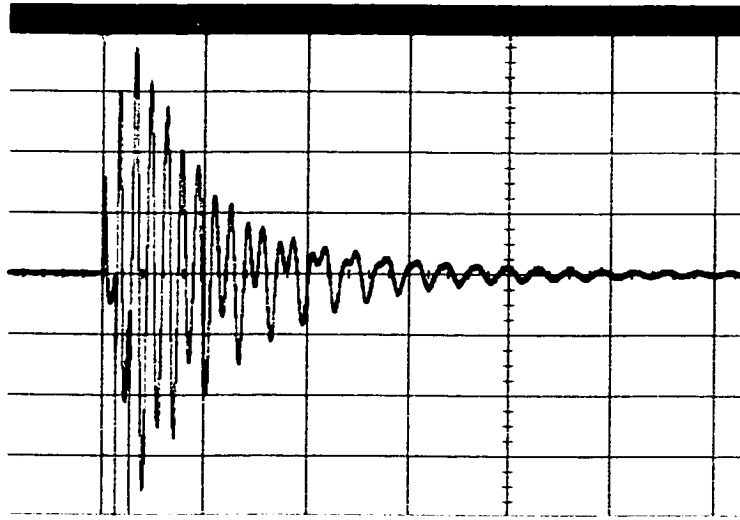


Figure 7-11: Exponential decay of transient response: $\zeta = 0.06$ and $Q = 8$.

7.4 Discussion

Figure 7-12 shows both experimental and FEA in-plane rotational stiffness values. Figure 7-13 on page 90 graphs the experimental and FEA stiffness values normalised to a joint length of 250µm.

Error bars were omitted in the graphs since the encountered errors were too small to register in the graphs (see Table 7-2 on page 87). Note that the given errors are only statistical errors and the systematical error encountered in reading the time for 10 cycles off the oscilloscope.

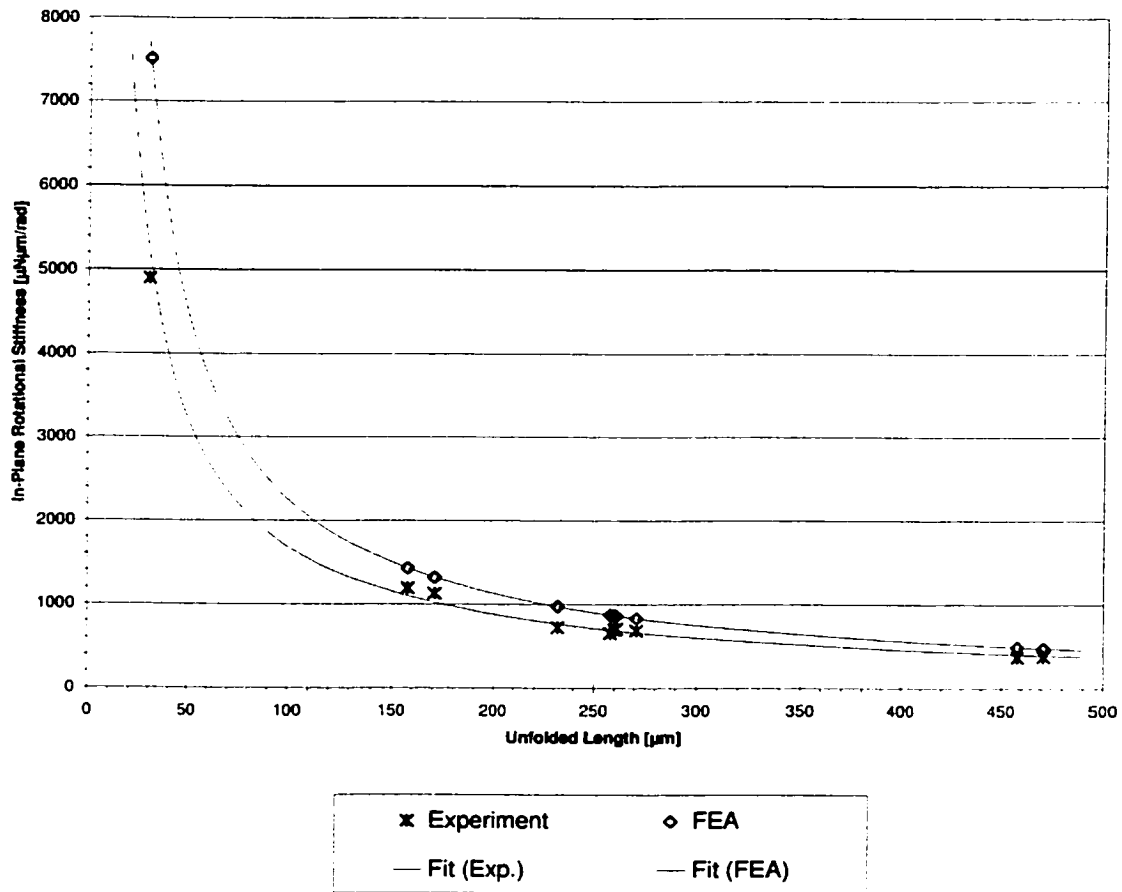


Figure 7-12: In-Plane Rotational Stiffness K_{θ} for Various Joints ('Flick'-Test and FEA)

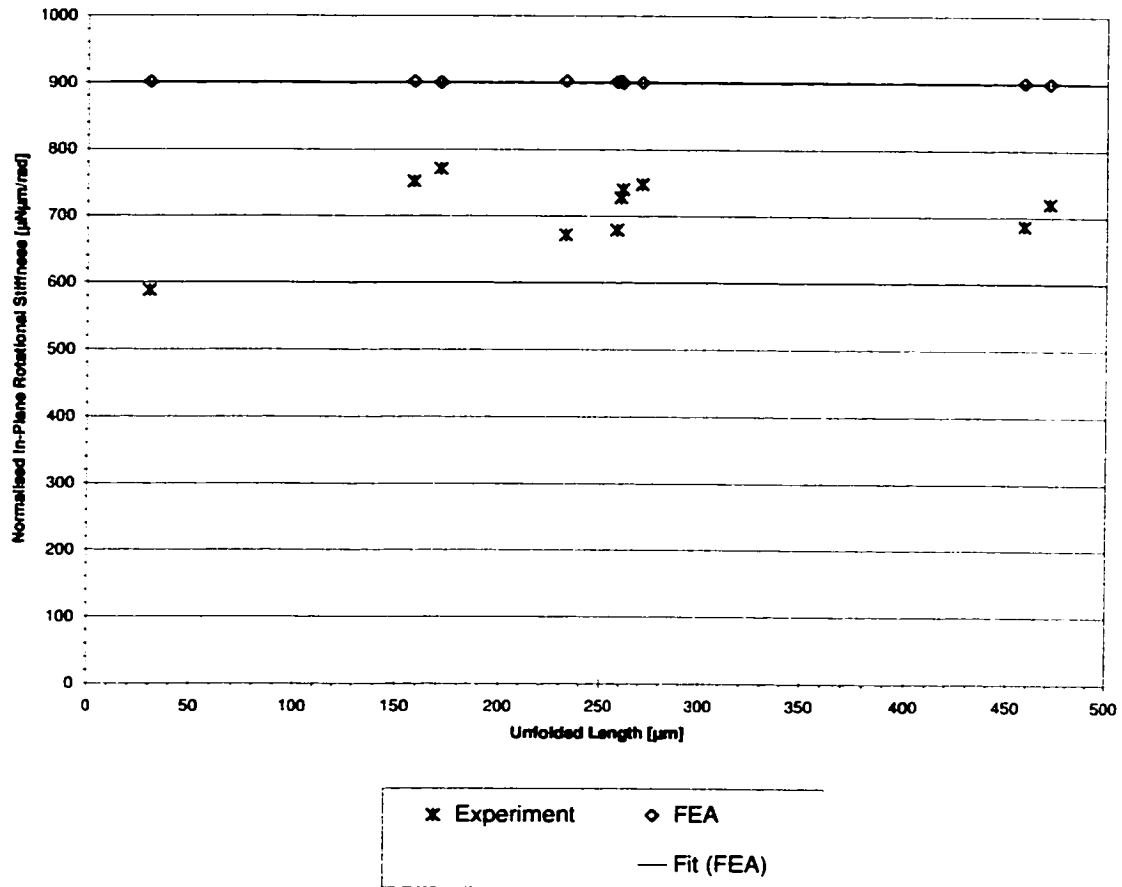


Figure 7-13: Normalised In-Plane Rotational Stiffness $K_{\theta} \cdot (L/250 \mu\text{m})$ for Various Joints ('Flick'-Test and FEA)

The experimentally measured stiffnesses agree well with those from the FEA simulations, consistently underestimating them to within approximately 10% for shorter joints and to within approximately 20% for longer joints.

This is predominantly due to three factors:

1. The beams were vibrating in air, not a vacuum as simulated, and thus were subjected to a small amount of damping (see Chapter 7.3.3).
2. The joint anchors (attachments to the substrate) are not infinitely stiff, thus adding compliance to the system, which was not accounted for in

the FEA simulation. This will decrease the measured resonance frequencies of the joints (see [9] and [16]).

3. A likely contributor to the stiffness variation is a mismatch between the value of Young's modulus used in the FE simulations and that of the actual material used in the devices. As mentioned in Chapter 4.3.3 a large range of measured values for Young's modulus can be found in the literature. For example Sharpe [28] cites Young's modulus as 169 ± 6 GPa, this value was used as it applies directly to MUMPs layers. Other researchers such as Kahn [15] and Koskinen [18] cite values of 150 ± 30 GPa and 175 ± 25 GPa.

The natural frequency is related to Young's modulus by $f \propto \sqrt{K/I}$ and $K \propto E$, thus $f \propto \sqrt{E}$. A given offset in E will return a corresponding offset in f^2 and K. The observed values of the in-plane rotational stiffness in Figure 7-12 were well fit using 146 GPa for Young's modulus of polysilicon.

7.5 External Measurements

Some of the joints designed for this thesis were also measured by two other groups in April of 2001. A group of senior undergraduate mechanical engineering students used joints on the RT2 chip to test their compact micro-positioner design project. Dr. Manfred Jericho from the Department of Physics measured the stiffnesses of some joints on the RT2 chip using atomic force microscopy.

7.5.1 Compact Micro-Positioner

For their final year design project Creelman et al. [4] designed a compact micro-positioner (CMP) that can be used to directly measure forces and therefore stiffnesses of MEMS devices. In order to test their design they measured the in-plane axial stiffnesses of a series of H- and X-joints. Table 7-3 lists the measured values along with the predicted stiffness using FEA. The measured stiffnesses are in good agreement with the predicted values.

Table 7-3: Measured and FEA Axial Stiffness of Various H- and X-joints (CMP)

Joint Type and L_f	Unfolded Length L [μm]	Stiffness [$\mu\text{N}/\mu\text{m}$]	
		Exp. ^a	FEA
H 100	471	1.9 ± 0.4	2.3
H 50	271	3.0 ± 0.6	4.2
H 25	171	9.4 ± 1.9	7.5
X 80	458	0.59 ± 0.12	0.63
X 45	260	2.3 ± 0.5	2.7

a. see [4] p. 61

7.5.2 Atomic Force Microscopy

Dr. Manfred Jericho from the Department of Physics at Dalhousie University uses atomic force microscopy (AFM) to measure osmotic pressure of bacteria. In order to capture live bacteria a MEMS device was designed for this purpose. During the design process an RT2 chip was lent to Dr. Jericho for preliminary testing. He also measured the in-plane axial stiffnesses of a series of H-joints. Table 7-4 list the measured stiffnesses along with the predicted FEA values.

Table 7-4: Measured and FEA Axial Stiffness of Various H-joints (AFM)

Joint Type and L_f	Unfolded Length L [μm]	Stiffness [$\mu\text{N}/\mu\text{m}$]	
		Exp. ^a	FEA
H 100	471	2.8 ± 0.1	2.25
H 50	271	4.5 ± 0.4	4.22
H 25	158	6.6 ± 0.4	7.51

a. see [14]

The measured values are in good agreement with the predicted values. Note that the predicted stiffness is the resting stiffness, i.e. when no force is acting. As described in Chapter 6.4 geometric non-linearities cause the in-plane axial stiffness to vary with the applied force. Especially for long joints higher experimental stiffness values can be expected for a compressive load. This is in good agreement with the measured values.

8 Joint Layout Variations

This chapter presents variations of the standard joint layout and their influence on the joint behaviour. Double layer joints, joints with non-constant width, and the paper-clip joint are introduced.

8.1 Introduction

The results from Chapters 5 and 6 brought up a question: Can the ratios between the stiffnesses be influenced by means other than the joint shape? First to be considered was the fact that all joints turned out to be softest in out-of-plane direction, which was undesirable for their use in planar mechanisms. An unsupported process for the production of double layer joints was tested with mixed results. Secondly the effect of increasing the widths of selected joint segments was examined. Thirdly, the possibility of decreasing the arm spacing for the H-joint was examined.

8.2 Double Layer Joints

As mentioned in Chapter 6.2, the fact that the out-of-plane stiffness turned out to be the lowest stiffness for all joints is undesirable for their use in planar mechanisms. The low out-of-plane stiffness makes it easier for elements of large mechanisms like the micro-stages introduced in Chapter 9.3 to touch the substrate and stick to it, thereby negatively influencing the behaviour of the mechanisms. Note that these surface contacts are normally initiated by impact forces on the chip and not by gravity.

The only way to make the joints stiffer in out-of-plane than in the in-plane direction is to increase their thickness to width ratio by either increasing their thickness or decreasing their width. Unfortunately the layer thickness in the MUMPs process is fixed to $2\mu\text{m}$ for the Poly 1 layer and $1.5\mu\text{m}$ for the Poly 2 layer. Furthermore, the minimum feature size of the MUMPs process is $2\mu\text{m}$. This allows for a maximum thickness to width ratio of 1:1, which is the aspect ratio of the discussed standard joints.

However, in its design handbook for the MUMPs process Cronos introduces a process for the creation of double thickness structures by stacking the Poly 1 and Poly 2 layers.¹

In order to do this, first a continuous sheet is drawn on the POLY1 level. Next a continuous sheet is drawn on the POL1_POLY2_VIA enclosing the POLY1 sheet by $5\mu\text{m}$. Finally the desired double layer structure is drawn on the POLY2 level on top of the other sheets. During the etch process the unprotected Poly 1 will be etched away together with the undesired Poly 2 in the same etch step, thereby creating a double layer structure with smooth walls. This way structures with a maximum thickness to width aspect ratio of 1.75:1 can be created. Unfortunately, Cronos does not guarantee this process to work. Figure 8-1 shows the layout of a double layer H 100 joint.

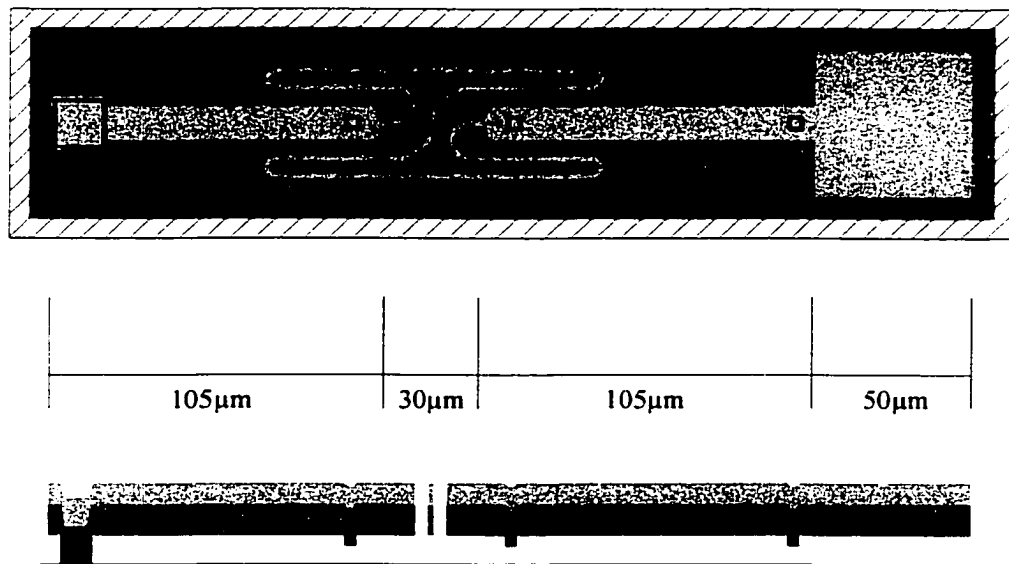


Figure 8-1: Layout of a Double Layer H 100 Joint (Top View and Cross-Section)

In order to test this unsupported process and to examine a possible solution for the out-of-plane stiffness problem, all joints on CJ2 were also fabricated as double layer versions.

1. see [17] p.34

8.2.1 FEA Results

Using the same methods as in Chapters 5 and 6, the in-plane rotational, in-plane axial, and out-of-plane rotational stiffnesses were calculated for the double layer joints.

Table 8-1 lists the calculated stiffnesses for various double layer joints. A comparison with the corresponding values for the single layer joints (Table 5-2 on page 46, Table 5-3 on page 50, and Table 6-1 on page 55) shows similar behaviour for the double layer joints: shorter joints are stiffer.

Table 8-1: Stiffnesses K_θ , K_x , K_ϕ of Various Double Layer Joints (FEA)

Joint Type and L_f	Unfolded Length L [μm]	In-Plane Rotational Stiffness [$\mu\text{N}\mu\text{m}/\text{rad}$] K_θ	In-Plane Axial Stiffness [$\mu\text{N}/\mu\text{m}$] K_x	Out-of-Plane Rotational Stiffness [$\mu\text{N}\mu\text{m}/\text{rad}$] K_ϕ
I 30	30	13,000	39,000	40,000
H 100	471	840	3.9	2,100
H 50	271	1,500	7.4	3,200
H 25	171	2,300	13	4,400
X 80	458	860	1.1	1,400
X 45	260	1,500	4.8	2,500
X 27	158	2,500	16	4,100
S 100	232	1,700	1.8	2,000
U 65	261	1,500	8.0	3,400
V 55	258	1,500	2.2	2,400

A comparison of the in-plane rotational stiffness for single (SL) and double layer (DL) joints (see Figure 8-2) shows identical behaviour. The only difference is that the rotational stiffnesses for the double layer joints are larger by a factor of 1.75. This was to be expected since the in-plane rotational stiffness is governed by $K_{\theta} = EI/L$. Because the cross-sectional moment of inertia for in-plane rotation of the double layer joints is increased by a factor equal to the thickness ratio ($I = \frac{bh^3}{12} \rightarrow \frac{(1.75)bh^3}{12}$) during the step to double layer joints, the in-plane rotational stiffness can be expected to increase by a factor 1.75 as well. This agrees with the observed behaviour.

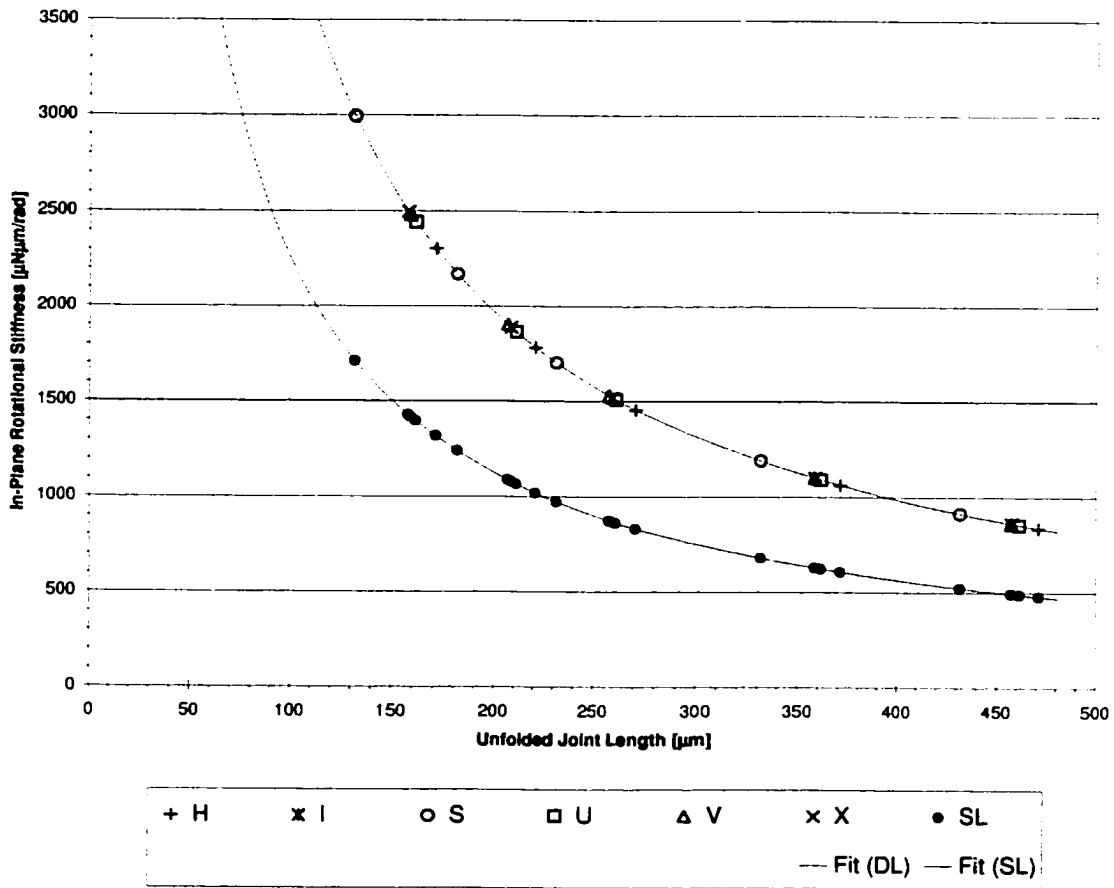


Figure 8-2: In-Plane Rotational Stiffness K_{θ} for Various Double Layer (DL) and Single Layer (SL) Joint Types and Lengths (FEA)

The same behaviour can be observed for the in-plane axial stiffness. Figure 8-3 shows the results for single layer (H1, S1) and double layer (H2, S2) H- and S-joints, the H-joint being the stiffest and the S-joint the softest in both cases. The only difference is, again, that the axial stiffnesses for double layer joints are larger by a factor of 1.75 due to the increased thickness. This can be explained by the increase in the cross-sectional moment of inertia for the S-joint ($K \propto \frac{EI}{L^3} \rightarrow \frac{E(1.75I)}{L^3}$) and a change in the cross-section for the H-Joint ($K \propto \frac{EA}{L} \rightarrow \frac{E(1.75A)}{L}$).

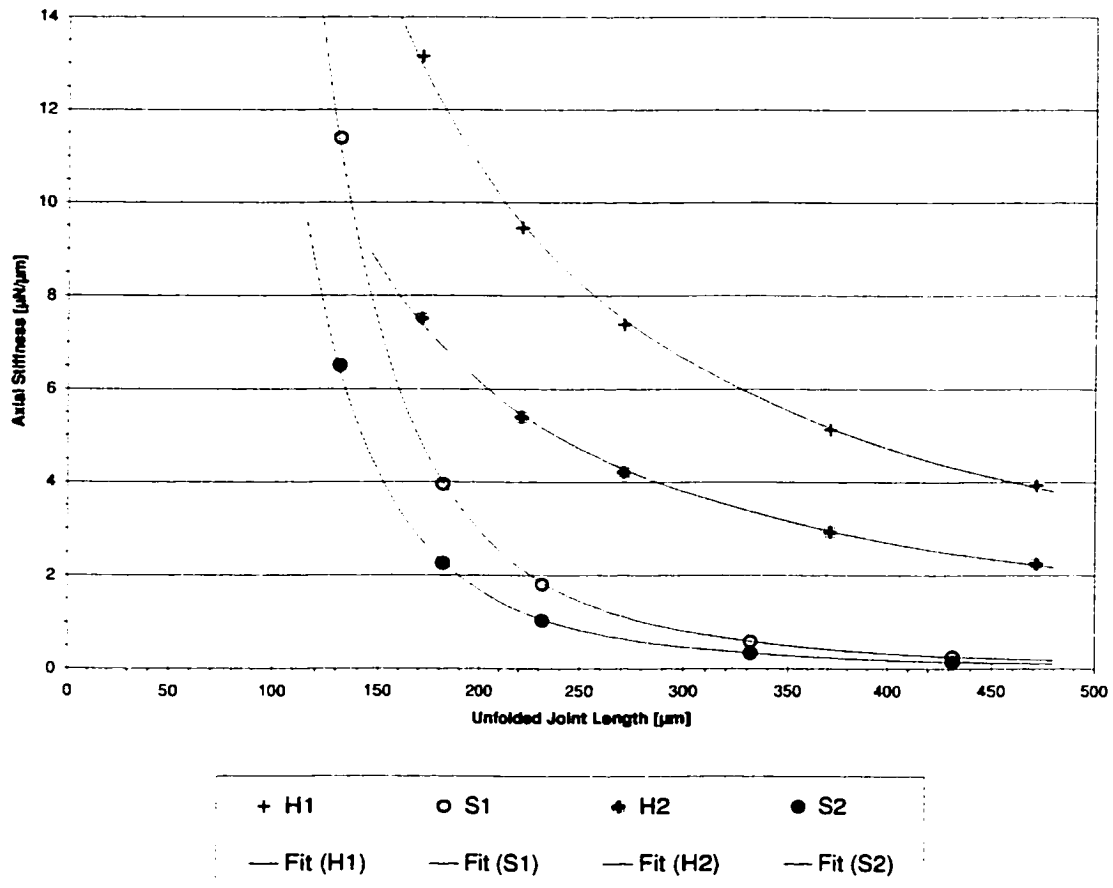


Figure 8-3: Axial Stiffness K_x for Various Double Layer (2) and Single Layer (1) Joint Types and Lengths (FEA)

Figure 8-4 graphs the out-of-plane stiffness for double (H2, S2) and single layer (H1, S1) joints over the total unfolded joint length. A comparison reveals identical joint behaviour. In this case, however, the stiffness for double layer joints is larger by a factor of 4.1 for H-joints and 2.8 for S-joints. The reason for this difference in stiffness increase is the different stress modes in these two joints.

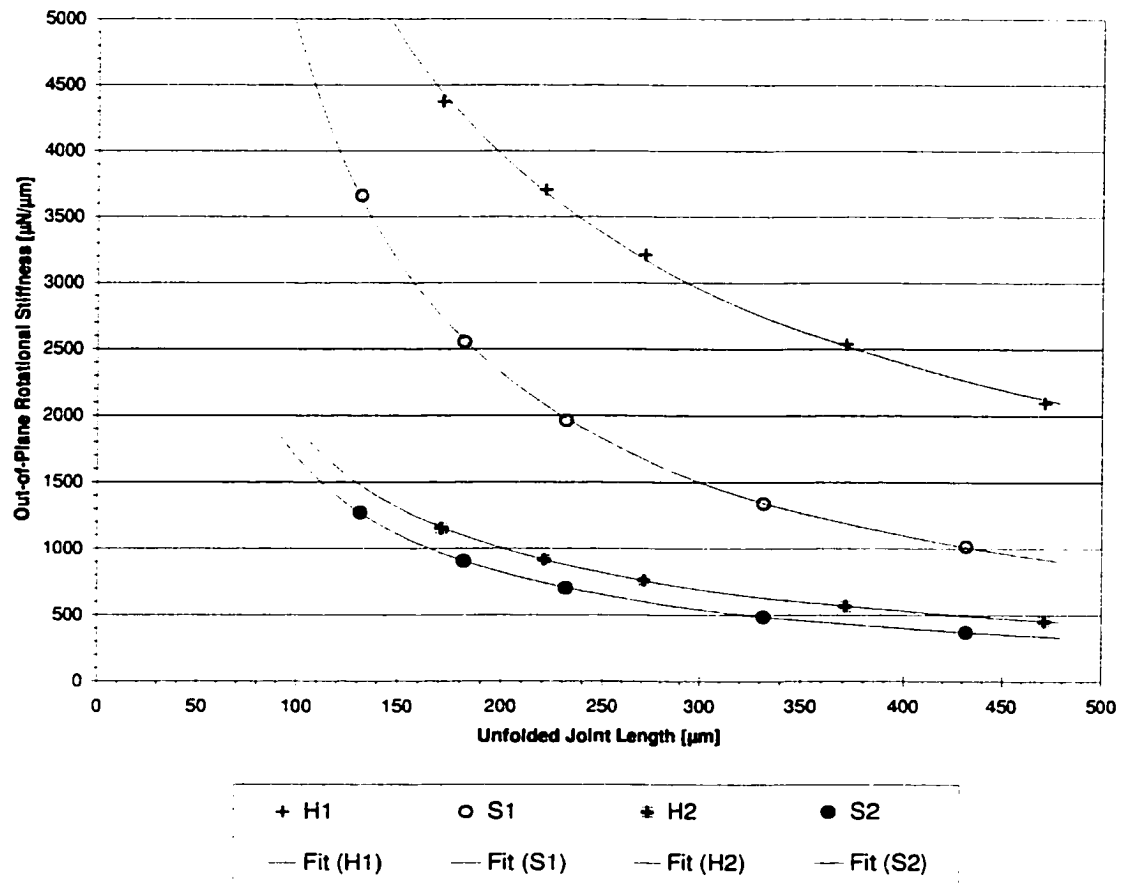


Figure 8-4: Out-of-Plane Rotational Stiffness K_ϕ for Various Double Layer (2) and Single Layer (1) Joint Types and Lengths (FEA)

As explained in Chapter 6.2, during out-of-plane rotational motion some joint segments are subjected to bending while others are subjected to torsion. Since the rotational bending stiffness of a cantilever beam is given by $K_{\text{bend}} = EI/L$ and its torsional stiffness by $K_{\text{tors}} = GK'/L$, an increase in thickness will affect I and K' differently. An increase in

thickness by a factor of 1.75 increases the cross-sectional moment of inertia for out-of-plane rotation ($I = \frac{bh^3}{12} \rightarrow \frac{b(1.75h)^3}{12}$) and therefore the bending stiffness by a factor of 5.4. The torsional stiffness, however, is only increased by a factor of 2.7 through the change of the torsional section property ($K = 0.1406a^4 \rightarrow 0.3752a^4$, square to rectangle with 1.75:1 aspect ratio).

The increase in stiffness (4.1) for H-joints, most of whose joint segments are subjected to bending, is close to the factor of 5.4. The S-joint, with most of its segments subjected to torsion, shows a stiffness increase (2.8) close to 2.7.

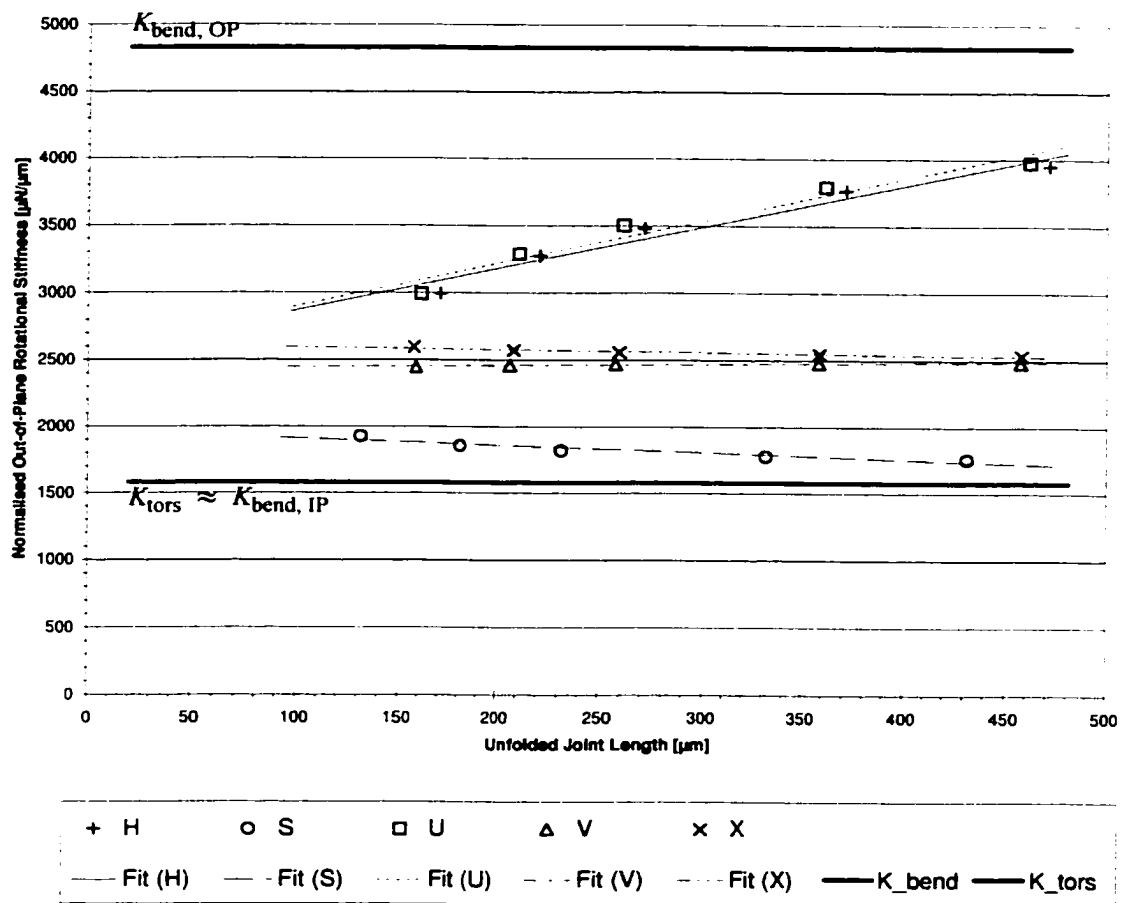


Figure 8-5: Normalised Out-of-Plane Rotational Stiffness $K_\phi \cdot (L/250 \mu\text{m})$ for Various Double Layer Joint Types and Lengths (FEA)

Figure 8-5 on page 100 shows the out-of-plane rotational stiffness for various double layer joints normalised to a joint length of $250 \mu\text{m}$. As in Figure 6-3 on page 60, the corre-

sponding graph for standard joints, it can be seen that the out-of-plane stiffness is approximately constant for all joints with different values for different joints.

Note that in this case the bending stiffnesses are different for out-of-plane ($K_{\text{bend,OP}} = 4830 \mu\text{N}\mu\text{m}/\text{rad}$) and in-plane bending ($K_{\text{bend,IP}} = 1583 \mu\text{N}\mu\text{m}/\text{rad}$). This has the effect that for double layer joints the out-of-plane rotational stiffness is generally higher than the in-plane rotational stiffness. This was the motivation for the use of double layer joints.

The out-of-plane rotational stiffnesses of the H- and U-joints are closest to $K_{\text{bend,OP}}$ since their out-of-plane motion involves mostly bending.

For this particular aspect ratio, but not in general, the in-plane bending stiffness is approximately equal to the torsional stiffness ($K_{\text{tors}} = 1577 \mu\text{N}\mu\text{m}/\text{rad}$). Therefore the out-of-plane rotational stiffness of the S-joint, whose out-of-plane motion involves mostly torsion, is very close to its in-plane rotational stiffness.

8.2.2 Experimental Results

The double layer joints were only fabricated on CJ2. Therefore all measurements were taken on CJ2. However, although two copies of each joint were fabricated on CJ2, it took three chips in order to complete ‘flick’-test measurements on all 24 double layer joint layout variations. This was not due to an invasive measurement procedure but rather due to the fact that many of the joints were already destroyed before the chip was opened in the lab for the first time. Figure 8-6 shows the debris of some destroyed double layer joints. All of them broke off at the joint part.

Note that only the in-plane rotational stiffness can be measured using the ‘flick’-test. The desired property in this case is the out-of-plane rotational stiffness. However, if the measured in-plane stiffnesses agree with the respective FEA calculations, the same agreement can be deduced for the out-of-plane stiffness.

In addition to many of the double layer joints being destroyed even before the start of testing, the joints turned out to be rather brittle, snapping off at the joint part much easier

than the single layer joints, especially while trying to release joints that were stuck to the substrate.

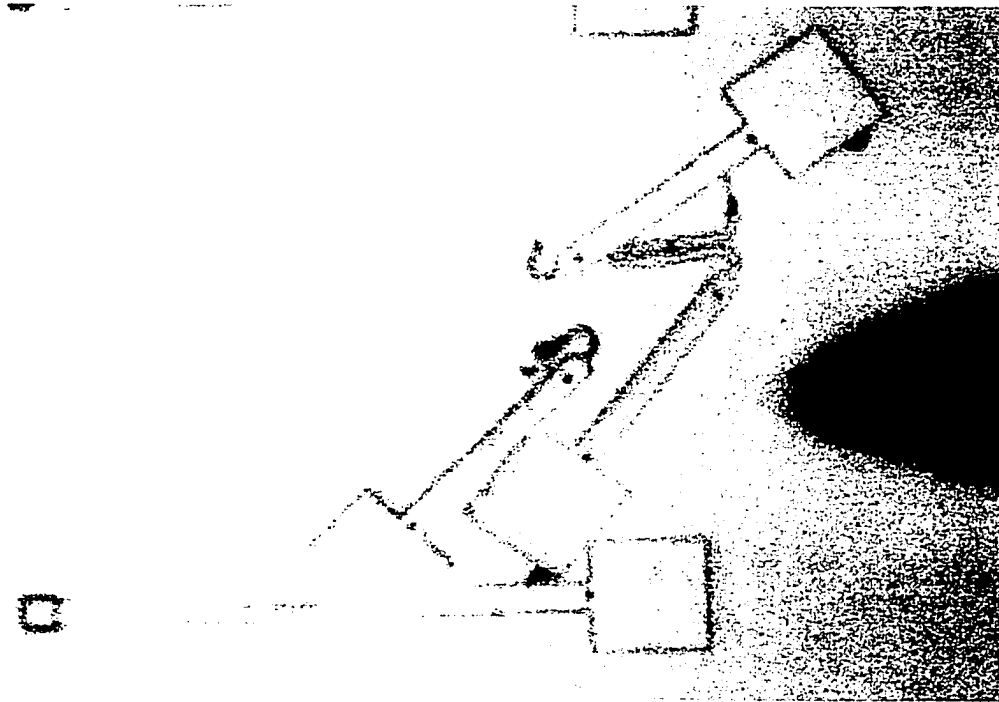


Figure 8-6: Destroyed Double Layer Joints as Delivered from Foundry

Table 8-2: Measured and FEA In-Plane Rotational Resonance Frequencies and Stiffnesses for Various Double Layer Joints ('Flick'-Test)

Joint Type and L_f	Unfolded Length L [μm]	Frequency [kHz]		Stiffness [$\mu\text{N}\mu\text{m}/\text{rad}$]	
		Exp.	FEA	Exp.	FEA
I 30	30	20 ± 1	25	7400 ± 100	13,000
H 100	471	5.9 ± 0.1	6.4	680 ± 40	840
H 50	271	7.4 ± 0.1	8.6	1100 ± 60	1,500
H 25	171	9.5 ± 0.1	11	1800 ± 100	2,300
X 80	458	5.9 ± 0.1	8.8	680 ± 30	860
X 45	260	7.5 ± 0.1	8.8	1100 ± 40	1,500
X 27	158	10 ± 1	11	2000 ± 100	2,500
S 100	232	8.4 ± 0.1	9.3	1400 ± 80	1,700
U 65	261	6.5 ± 0.1	7.5	1100 ± 70	1,500
V 55	258	6.4 ± 0.1	7.7	1000 ± 60	1,500

One possible explanation for this behaviour is the fact, that, although they are etched in one step, the joints consist of two layers laid down at different times. If these two layers have different residual stresses the double layer structure could be subjected to large internal stresses making it more vulnerable to external impacts.

Nevertheless, measurements for all double layer joints were made and are listed in Table 8-2 on page 102. As in the single layer joint measurements, the double layer experimental values are generally lower than the corresponding FEA values. The amount of underestimation is slightly larger than for the single layer joints.

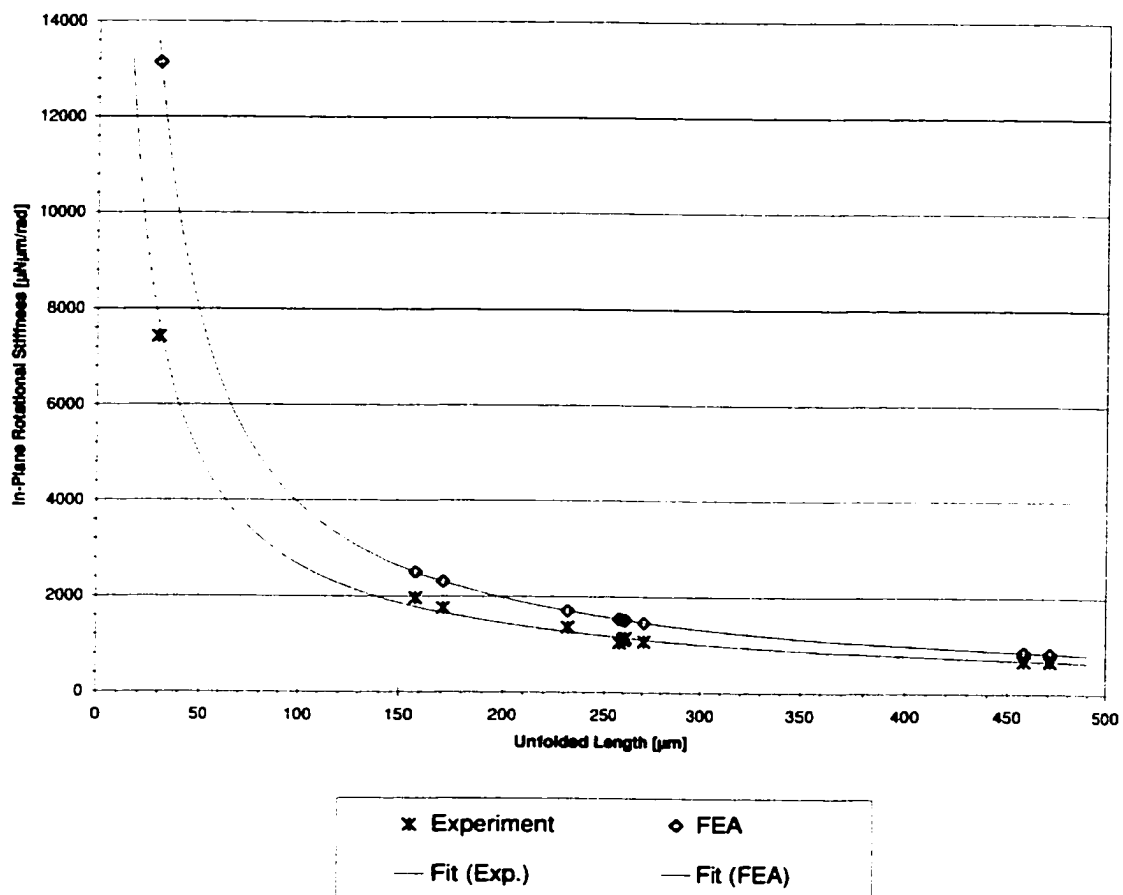


Figure 8-7: In-Plane Rotational Stiffness K_{θ} for Various Double Layer Joints ('Flick'-Test and FEA)

Figure 8-7 on page 103 shows the experimental values for the in-plane rotational stiffness calculated from the frequency values measured using the ‘flick’-test plotted over the total unfolded joint length, along with the corresponding FEA values. It can be observed that the experimental values are lower than the FEA values for all joints.

Figure 8-8 graphs the experimental and FEA stiffness values normalised to a joint length of 250µm. Like in the previous graph the experimental values are lower than the FEA values for all joints.

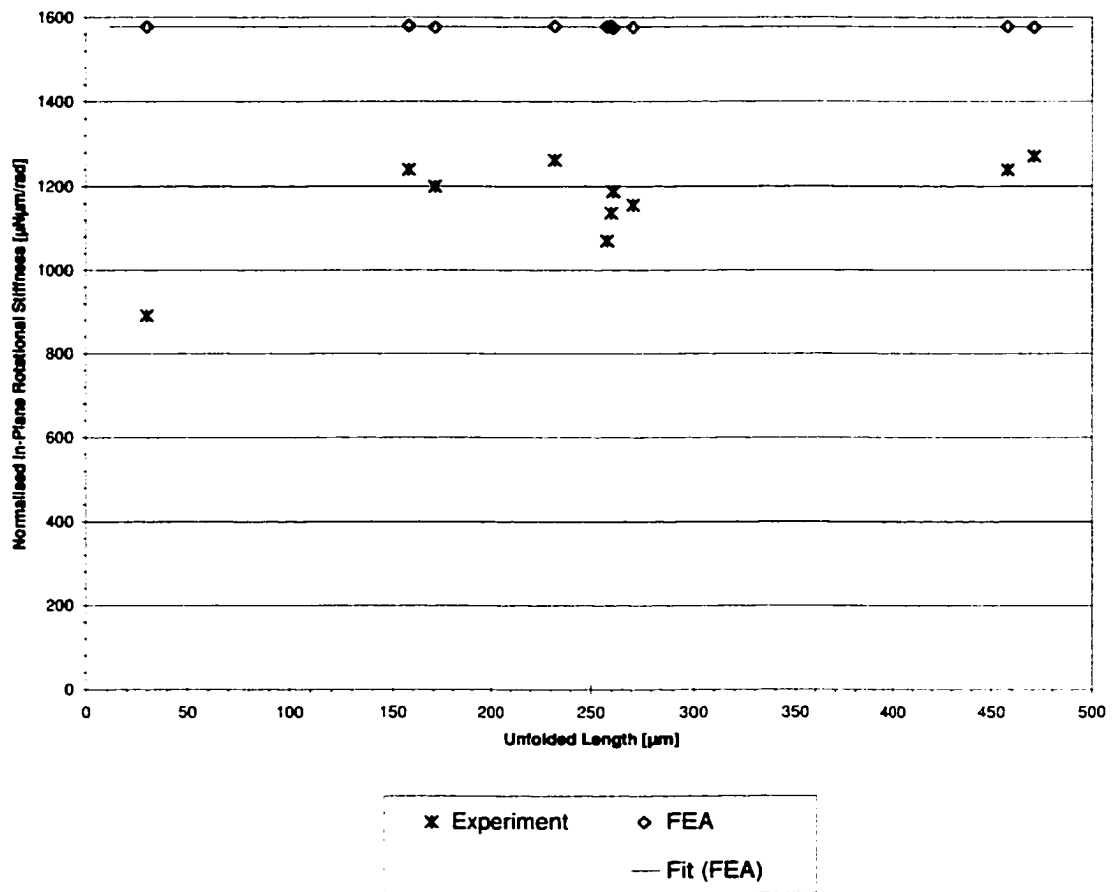


Figure 8-8: Normalised In-Plane Rotational Stiffness $K_{\theta} \cdot (L/250\mu\text{m})$ for Various Double Layer Joints (‘Flick’-Test and FEA)

8.2.3 Discussion

FEA calculations showed that the use of double layer joints has the desired effect on the out-of-plane stiffness, making it larger than the in-plane stiffness, while having no effect on the in-plane rotational and axial stiffnesses, other than increasing them by a factor of 1.75. Experimental observations, however, revealed an increased brittleness of the fabricated joints. This resulted in a more difficult handling and an increased fabrication failure rate.

These observations along with the difficult process to connect double layer to single layer structures and the not guaranteed fabrication process make the double layer joints impractical and unreliable for the use in planar mechanisms.

8.3 Joint Width Variations

In a discussion with Dr. Guy Kember the question arose as to whether the ratio of in-plane rotational to in-plane axial stiffness, the two key properties of the joints, could be influenced by selectively widening segments of the joints in order to increase either the in-plane rotational or the axial stiffness. Figure 8-9 shows the H 100 and the X 80 joint along with four variations each.

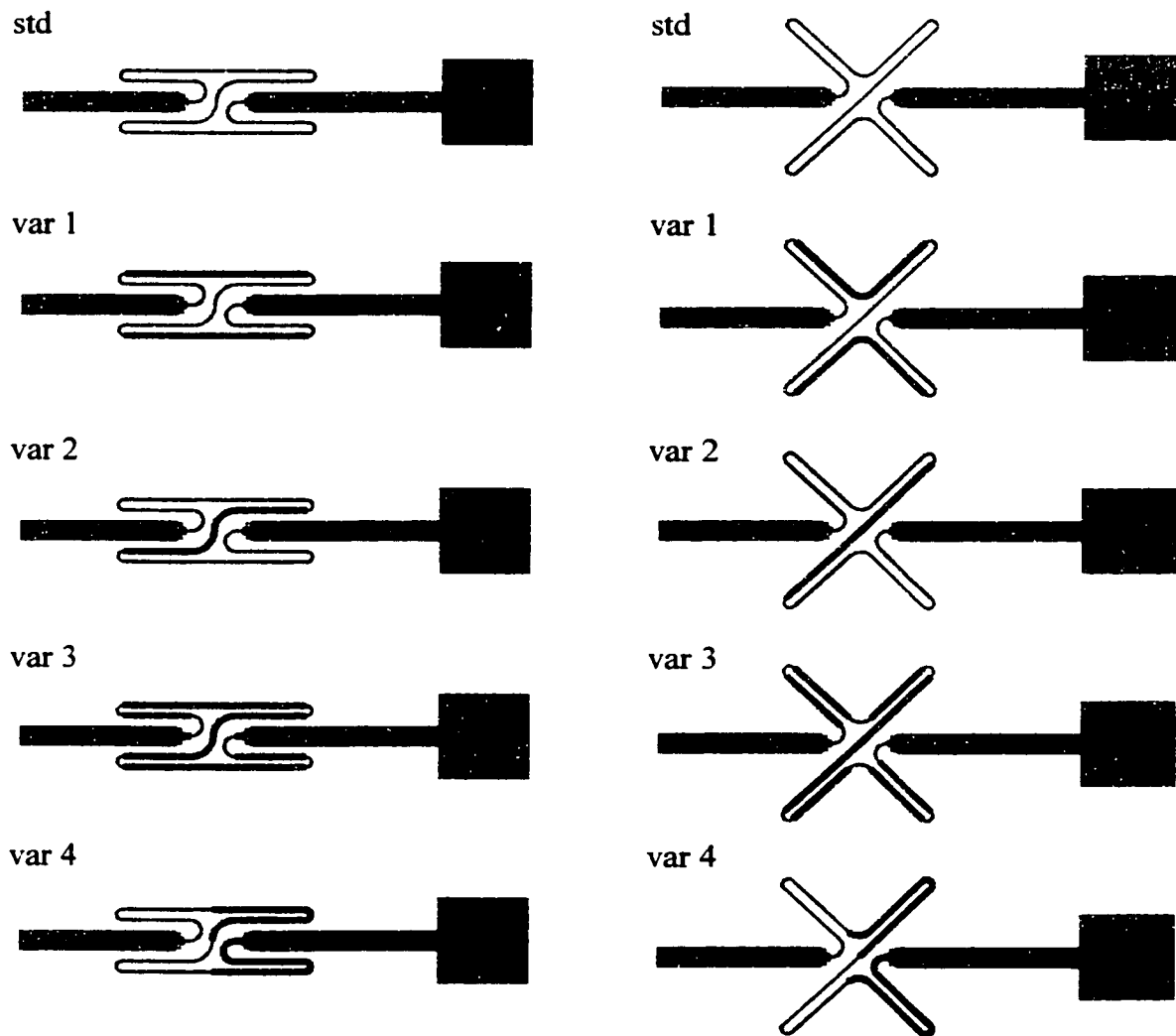


Figure 8-9: H 100 and X 80 Along with Four Layout Variations

Variation 1 shows widened top and bottom segments while variation 2 has a widened centre segment. Variation 3 consists of widened linear joint segments, leaving only the curved segments at the original width. Variation 4 presents a joint whose right hand side segments are widened. All widened segments are $4\mu\text{m}$, twice the width of the regular segments.

Table 8-3 list the FEA results for in-plane rotational and axial stiffness for H- and X-joint variations. It also list the ratio of those stiffnesses normalised to the stiffnesses of the standard joints.

Table 8-3: In-Plane Rotational and Axial Stiffnesses of Various H- and X-Joint Variations (FEA)

Joint Type and L_f	Unfolded Length L [μm]	In-Plane Rotational Stiffness [$\mu\text{N}\mu\text{m}/\text{rad}$] K_θ	In-Plane Axial Stiffness [$\mu\text{N}/\mu\text{m}$] K_x	Stiffness Ratio $\frac{K_{x, \text{var}} / K_{x, \text{std}}}{K_{\theta, \text{var}} / K_{\theta, \text{std}}}$
H 100 std	471	480	2.2	1.0
H 100 var 1	471	760	5.2	1.5
H 100 var 2	471	610	2.6	0.93
H 100 var 3	471	1800	10	1.2
H 100 var 4	471	850	4.0	1.0
X 80 std	458	490	0.63	1.0
X 80 var 1	458	780	1.1	1.1
X 80 var 2	458	630	0.74	0.91
X 80 var 3	458	1600	2.0	0.97
X 80 var 4	458	910	1.1	0.94

It can be seen that the only two variations that cause an increase in the stiffness ratio of 20% or more are Variation 1 and 3 of the H-joint. The widening of the top and bottom segments seems to increase the stiffness ratio while the widening of the centre segment seems to decrease it. All other variations increase or decrease the stiffness ratio by less than 10% while sometimes increasing the stiffnesses themselves by up to three times.

Variation 1 of the H-joint increases the in-plane rotational stiffness of the joint by 60% while increasing its in-plane axial stiffness by 140%. This results in an overall increase of the stiffness ratio by 50%.

The increase in rotational stiffness can be compensated by an increase in overall joint length of approximately 60%. Since for the H-joint both in-plane axial and rotational stiffness are approximately proportional to the inverse of the total joint length, this increase in length will not affect the stiffness ratio. However, a 60% increase in total length causes a 70% increase in the folded joint length for the H 100 joint. This results in a decrease of the maximum angle of rotation by 40%.

If only the stiffness ratio of the joint but not the rotational stiffness itself is important for the design then variation 1 (thickening long, straight arms) provides moderate improvement.

8.4 Joint Spacing Variation: The Paper-Clip Joint

The previous section found that the only width variation that could significantly increase the axial stiffness of the H-joint was to widen the top and bottom arm of the joint. Even then this resulted only in a 50% improvement in axial stiffness.

For the given gap size of $30\mu\text{m}$ the H-joint proved to be the axially stiffest joint possible. Without changing its cross-section the H-joint's axial stiffness could only be improved by a tighter spacing of its arms. This, however, would severely limit its range of motion.

If the size of the gap bridged by the joint is adjustable a variation of the H-joint, the paper-clip joint (PC-joint) can be constructed. Figure 8-10 shows the transformation of an H 25 joint into an PC 25 joint. By increasing the gap size room is created for the top and bottom arms to move towards the joint axis. At the same time the centre arm is straightened out. While the H 25 joint bridges the standard $30\mu\text{m}$ gap with an unfolded joint length of $171\mu\text{m}$, the PC 25 joint bridges a gap of $54\mu\text{m}$ with an unfolded joint length of $126\mu\text{m}$.

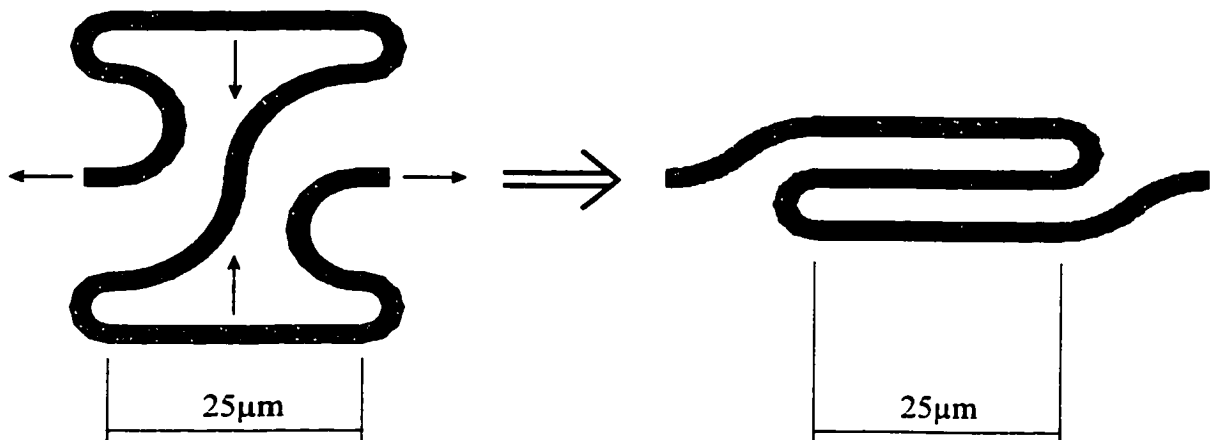


Figure 8-10: Transformation from H 25 to PC 25 Joint

In the same way other H-joints can be transformed into PC-joints. Figure 8-11 on page 110 shows the H 100, H 50, and H 25 joints with their respective PC-joints. Note that the corresponding PC-joint has a shorter overall length (L) than the H-joint.

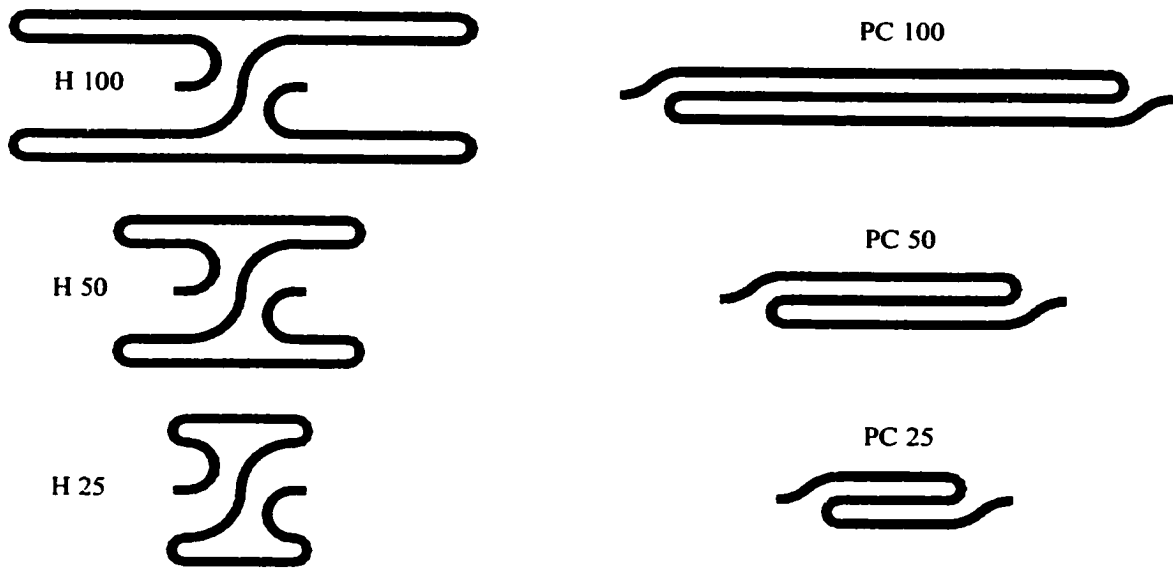


Figure 8-11: Various H-Joints and the Corresponding PC-Joints

Table 8-4 lists FEA results for various PC-joints. The results for H-joints of same total length are given in brackets. Note that for the same total joint length the folded length (L_f) of the H-joint is shorter than that of the PC-joint. As expected, the FEA results show very high in-plane axial stiffnesses for the paper-clip joints.

Table 8-4: In-Plane Stiffnesses of Various PC-Joints and (H-joints) of Same Length (FEA)

Joint Type and L_f	Unfolded Length L [μm]	Gap Width Bridged L_g [μm]	Rotational Stiffness K_θ [$\mu\text{N}\mu\text{m}/\text{rad}$]	Axial Stiffness K_x [$\mu\text{N}/\mu\text{m}$]	Lateral Stiffness K_y [$\mu\text{N}/\mu\text{m}$]
PC 100 (H 70)	351	129 (30)	640	28 (3.1)	0.062 (1.3)
PC 50 (H 33)	201	79 (30)	1,100	52 (6.1)	0.24 (8.4)
PC 25 (H 14)	126	54 (30)	1,800	89 (11)	0.84 (39)

Using regression analysis the following equation for the axial stiffness can be found:

$$\text{PC-joint:} \quad K_x = 41 \frac{\mu\text{N}}{\mu\text{m}} \cdot \left(\frac{250\mu\text{m}}{L} \right)^{1.13} \quad (8-1)$$

$$\text{H-joint:} \quad K_x = 4.7 \frac{\mu\text{N}}{\mu\text{m}} \cdot \left(\frac{250\mu\text{m}}{L} \right)^{1.19} \quad (8-2)$$

A comparison with the respective equation of the H-joint shows that the PC-joint is approximately 8.7 times stiffer in axial direction than an H-joint of the same unfolded joint length.

$$\frac{K_{x, \text{PC}}}{K_{x, \text{H}}} = 8.7 \cdot \left(\frac{250\mu\text{m}}{L} \right)^{0.06} \approx 8.7 \quad (8-3)$$

This large increase in axial stiffness can be explained with the paper-clip joint having three parallel arms with one arm in the centre. Also the arms are spaced at $6\mu\text{m}$. An H-joint has two long arms (top and bottom) and two arms that are broken up into four short arms closer to the axis. The major difference, however, is that the long arms are $18\mu\text{m}$ from the joint axis and the shorter arms are $12\mu\text{m}$ from the axis.

Therefore the arm spacing is much closer for the PC-joint which results in a much higher stiffness in axial direction.

A major disadvantage of the PC-joint is the fact that in order to get a longer and therefore rotationally softer joint the gap between the links it connects has to be increased. The length of the gap required can be calculated using the following formula:

$$L_g = (L - 51\mu\text{m}) / 3 + 29\mu\text{m} = L_f + 29\mu\text{m} \quad (8-4)$$

Another disadvantage is the fact that the paper-clip joint is also much softer in lateral direction (K_y) than the corresponding H-joint (see Table 8-4 on page 110). In order to be able to neglect the lateral compliance with respect to the rotational compliance as discussed in Chapter 6.3 eventual force loads have to be applied at a distance greater than $13 \cdot L_f$ from the centre of the joint ($3.5 \cdot L_f$ for H-joint).

Therefore the paper-clip joint is a good choice if a large axial stiffness is required and the gap size and the lateral compliance are not important.

9 Joint Design Guidelines

This chapter derives rules from the previously presented results and presents guidelines for designing joints for use in planar mechanisms. It also introduces two example mechanisms that use flexible micro-joints discussed in this thesis.

9.1 Joint Observations

Before presenting guidelines for the selection of the proper joint for given requirements some observations made during the examinations in the previous chapters will be presented.

9.1.1 In-Plane Rotational Stiffness (K_θ)

The in-plane rotational stiffness of the joints examined in this thesis depends only on the total unfolded joint length. The shape of the joint has no influence on the in-plane rotational stiffness.

If the desired in-plane rotational stiffness K_θ is known, the necessary joint length L can be found using the following equation:

$$\frac{L_{\text{required}}}{250\mu\text{m}} = \frac{900\frac{\mu\text{N}\mu\text{m}}{\text{rad}}}{K_{\theta, \text{desired}}} \quad (9-1)$$

9.1.2 Out-of-Plane Rotational Stiffness (K_ϕ)

In Chapter 6.2 the problem of the joints actually being softest in the out-of-plane direction was discussed. It was found to be a characteristic of the MUMPs process imposed by the design rules of the process. Furthermore, changing the length does not significantly change the stiffness ratio K_ϕ/K_θ . The joint shape has a minor effect on the stiffness ratio. Since the joints examined in this thesis were designed for use in planar mechanisms this is an undesirable property. The only alternative MUMPs method, creating double layer joints, was examined in Chapter 8.2 and found to be impractical and unreliable.

For joints of the same layout manufactured using a different foundry process this problem might not occur due to different layer thicknesses and design rules. Silicon on in-

sulator (SOI) processes, for example, can feature structural layers with thicknesses of $50\mu\text{m}$. Using such processes the out-of-plane stiffness can be addressed and improved.

For these reasons the following design guidelines will ignore the out-of-plane stiffness and just accept the fact that for the MUMPs process the joints will always be softest in out-of-plane direction ($K_\phi \approx 70 - 95\% K_\theta$).

9.1.3 Angular Range of Motion

The only joint with a strongly limited range of motion is the H-joint. All H-joints with a folded joint length $L_f > 30\mu\text{m}$ ($L > 190\mu\text{m}$) suffer from the fact that at a certain angular deflection one of the joint arms touches one of the rigid links. At this point the joint becomes instantaneously stiffer¹ and loses its usefulness. The range of motion decreases with increasing joint length. It could be improved by increasing the distance of the joint arms from the joint axis. This, however, would lead to a decrease in axial stiffness. For an H 100 joint the useful range of motion is approximately $\pm 10^\circ$ whereas the X- and S-joints have useful ranges of motions of approximately $\pm 45^\circ$.

If a larger range of motion is required the X-joint can be used to replace an H-joint. It is softer in axial direction than the H-joint but still much stiffer axially than the S-joint.

9.1.4 Degrees of Freedom

The joints examined in this thesis, designed by folding long slender beams into various shapes, generally possess three degrees of freedom in the plane: a rotational, an axial, and a lateral degree of freedom. Examination of these three degrees of freedom in Chapters 5.4, 5.5, and 6.3, however, revealed that, depending on the shape, joints are stiffer in certain directions than in others. Therefore the compliance in some of the directions can be neglected depending on the joint shape. This effectively reduces the degrees of freedom for some joints to two or even one.

One degree of freedom joints, namely, rotating pin joints or translating slider joints, are typically referred to as “full joints”. Two degree of freedom joints are usually referred

1. Experimentally observed by Creelman et al in [4].

to as “half joints”. The half joint is sometimes also called a rotary-slide joint because it allows both rotating (angular motion) and sliding (linear motion). Note that if the motion of a half joint in one of the two directions can be constrained one freedom can be “locked out” and the half joint can be made to behave as a full joint. It can therefore be a pure rotary, pure slide, or rotary-slide joint.¹

The joints examined in this thesis are three degree of freedom joints. They cannot be pure rotary or pure slide joints. However, due to high stiffness or high compliance in some directions they can be separated into three DOF, rotary-slide, pseudo rotary, and pseudo slide joints.

9.1.5 I-Joint

The I-joint is much stiffer than any of the other joints in axial and lateral direction. For the lateral stiffness this is mostly due to its shorter length. The extreme stiffness in axial direction on the other hand is caused by its shape. It is simply the stiffness of a straight rod in tension or compression. Therefore it can be reduced to one effective degree of freedom, rotation.

The I-joint is closest in behaviour to a pin-joint. However, due to its shorter length it is also more than eight times stiffer in the in-plane rotational direction than the other joints. This and its unadjustable length make the I-joint useless for most applications.

9.1.6 Asymmetric Joints

The rationale for examining asymmetric joints arose by observing in FE simulations that only two of the four joint arms of H- and X-joints are subjected to high stresses during rotational motion. Therefore the U- and V-joints were designed by omitting the unstressed arms. However, the asymmetry did not improve the joint performance.

The U-joint turned out to be very close in performance to the H-joint. For the same joint length both joint types possess the same in-plane rotational and approximately the same axial stiffness. In lateral direction the U-joint is slightly softer than the H-joint.

1. see [24] p. 22 f.

The V-joint, although designed as half an X-joint, turned out to possess an axial stiffness closer to that of the S-joint. This can be explained by one of the added curved segments being approximately perpendicular to the axial direction, thereby reducing the axial stiffness. Its lateral stiffness, however, is approximately the same as that of the X-joint, as is the in-plane rotational stiffness.

Since both the U- and the V-joint only possess two arms, their footprint for a joint of equal rotational stiffness, i.e. total length, is larger than the footprint of the respective H- and X-joints. This also decreases the maximum possible angular deflection for the U-joint as compared to the respective H-joint.

The use of U- and V-joints in mechanisms is more inconvenient since their shifted centres of rotation have to be taken into account during the design of the mechanism.

For these reasons there is no advantage in using the U- and V-joints instead of the H- and X-joints.

9.2 Joint Selection Guide

The process of selecting the proper joint for given requirements can be broken down into two questions:

- Which joint should be used?
- What effect does a change in length have on the joint?

Table 9-1 lists the in-plane stiffnesses for the examined symmetric joint types. For uniform comparison, joints of a total unfolded joint length 250 μm were used. The corresponding stiffnesses were calculated using the formulas found by regression analysis, which were introduced in Chapters 5, 6, and 8. The shorter I-joint is listed for comparison. Note that the PC-joint bridges a larger gap than the other joints.

Table 9-1: In-Plane Stiffnesses for Standard Joints (FEA, Regression)

Joint Type	Unfolded Length L [μm]	Rotational Stiffness K_{θ} [$\mu\text{N}\mu\text{m}/\text{rad}$]	Axial Stiffness K_x [$\mu\text{N}/\mu\text{m}$]	Lateral Stiffness K_y [$\mu\text{N}/\mu\text{m}$]
I 30	30	7,500	23,000	99
PC 66	250	900	41	0.16
H 45	250	900	4.7	4.1
X 43	250	900	2.9	4.6
S 109	250	900	0.83	35

Since the in-plane rotational stiffness only depends on the total joint length, all joints in Table 9-1 (except for the shorter I-joint) have the same rotational stiffness. In axial direction the H-joint is stiffest, about six times stiffer than the softest joint, the S-joint. In lateral direction the S-joint is stiffest, about eleven times stiffer than the softest joint, the H-joint. The PC-joint is even more axially selective than the H-joint, but is listed separately due to its greater gap width ($L_g = 95 \mu\text{m}$).

Table 9-2 list in-plane stiffness trends for the various joints, namely the length dependence of the stiffnesses as well as the stiffness ratios. These were taken from the regression formulas derived in previous chapters.

Table 9-2: In-Plane Stiffness Trends for Standard Joints (FEA, Regression)

Joint Type	Rotational Stiffness K_θ	Axial Stiffness K_x	Lateral Stiffness K_y	$\frac{K_x}{K_\theta}$	$\frac{K_y}{K_\theta}$	$\frac{K_y}{K_x}$
PC	$\propto 1/L$	$\propto 1/L^{1.13}$	$\propto 1/L^{3.28}$	$\propto 1/L^{0.13}$	$\propto 1/L^{2.28}$	$\propto 1/L^{2.15}$
H	$\propto 1/L$	$\propto 1/L^{1.19}$	$\propto 1/L^{3.28}$	$\propto 1/L^{0.19}$	$\propto 1/L^{2.28}$	$\propto 1/L^{2.09}$
X	$\propto 1/L$	$\propto 1/L^{2.50}$	$\propto 1/L^{2.75}$	$\propto 1/L^{1.50}$	$\propto 1/L^{1.75}$	$\propto 1/L^{0.25}$
S	$\propto 1/L$	$\propto 1/L^{3.19}$	$\propto 1/L^{0.72}$	$\propto 1/L^{2.19}$	$\propto L^{0.28}$	$\propto L^{2.47}$

9.2.1 Designing a Pseudo Slide (Slider) Joint

A pure slide joint is a one degree of freedom joint (full joint) with only a translational freedom. A pure slide joint cannot be achieved with flexible joints but by maximising K_θ/K_x and K_y/K_x a pseudo slide joint can be achieved.

Suitable Joint(s)

Table 9-1 on page 116 shows that the S-joint is best suited for this situation. It is the joint softest in axial direction (K_x) and the joint stiffest in lateral direction (K_y). This makes it effectively a two degree freedom rotary-slide joint with a translational freedom (axial direction) and a rotational freedom.

Effect of Joint Length

Table 9-2 on page 117 shows that the axial stiffness of the S-joint is strongly dependent on the total joint length. During axial loading most joint segments are subjected to beam bending ($K \propto \frac{EI}{L^3}$). The lateral stiffness, on the other hand, is not strongly dependent on the total unfolded joint length. During lateral loading most joint segments are subjected to compression or tension ($K \propto \frac{AE}{L}$).

Relative to the axial stiffness both the rotational stiffness ($\frac{K_\theta}{K_x} \propto L^{2.19}$) and the lateral stiffness ($\frac{K_y}{K_x} \propto L^{2.47}$) increase rapidly with increasing total joint length. This means that for long joints the S-joint becomes a pseudo slide joint, since the rotational and lateral compliance become negligible compared to the axial compliance.

Recommendations

For a pseudo slide joint, choose a long S-joint. It should be as long as possible in order to minimise the K_x/K_θ ratio. Note that for long joints sagging of the arms will become a problem. This can be counteracted by attaching small platforms with dimples at locations along the joint.

If a rotary-slide joint is required, choose an S-joint. The relative importance of rotating versus sliding can be adjusted by varying the total joint length.

The distance at which lateral forces are applied has little effect on the joint performance since its lateral stiffness (K_y) is very big.

9.2.2 Designing a Pseudo Rotary (Pin) Joint

A pure rotary joint is a one degree of freedom joint (full joint) with only a rotational freedom. A pure rotary joint cannot be achieved with flexible joints but by maximising K_x/K_θ and K_y/K_θ a pseudo rotary joint can be achieved.

Suitable Joint(s)

Table 9-1 on page 116 shows that both the H-joint and the PC-joint are suited for this situation. Both are stiff in axial direction (K_x). However, they are also soft in lateral direction (K_y). The PC-joint is more axially selective than the H-joint but limited by its adjustable gap width. This makes both joints effectively two degrees of freedom rotary-slide joints with a rotational freedom and a translational freedom (lateral direction).

Effect of Joint Length

Table 9-2 on page 117 shows that the axial stiffness of both joints is not strongly dependent on the total joint length. During axial loading most joint segments are subjected to compression or tension ($K \propto \frac{AE}{L}$). The lateral stiffness, on the other hand, is strongly dependent on the total unfolded joint length. During lateral loading most joint segments are subjected to beam bending ($K \propto \frac{EI}{L^3}$).

Relative to the rotational stiffness the axial stiffness slowly increases with decreasing total joint length ($\frac{K_x}{K_\theta} \propto \frac{1}{L^{0.19}}$ for H, $\frac{K_x}{K_\theta} \propto \frac{1}{L^{0.13}}$ for PC) while the lateral stiffness rapidly increases ($\frac{K_y}{K_\theta} \propto \frac{1}{L^{2.28}}$ for both). This means that for short joints the H-joint and the PC-joint become a pseudo rotary joints, since the lateral and axial compliance become negligible compared to the rotational compliance.

Recommendations

If a pseudo rotary joint (“pin” joint) is required, choose an H-joint or a PC-joint.

Choose an H-joint if lateral forces are being applied close to the joint or if the gap size is important. The H-joint is stiffer in lateral direction than the PC-joint and therefore has a greater resistance to lateral forces. It is also designed for a gap size of 30 μm and its length can therefore be adjusted without adjusting the gap size.

Choose a PC-joint if predominantly moment loads or large axial force loads are present. The PC-joint is about nine times stiffer in axial direction than the H-joint and therefore has a greater resistance to axial forces. Due to its design, an adjustment in total joint length also results in a change of the size of the bridged gap.

Since both joints are relatively soft in lateral direction they have to be made as short as possible in order to minimise the K_y/K_θ ratio. Note that a decrease in length also causes an increase in rotational stiffness. Therefore a compromise has to be found.

The distance at which lateral forces are applied has a large effect on the joint performance, especially for the PC-joint. The safe distance for which the lateral motion caused by a force becomes negligible to the rotational motion caused by the induced moment is $3.5 \cdot L_f$ for the H-joint and $13 \cdot L_f$ for the PC-joint.

9.3 Examples for Joints as Part of Mechanisms

To show the use of the examined joints in mechanisms, flexural motion amplifiers and micro-stages are presented at this point. Note that these mechanisms were not the focus of this thesis. These mechanisms are only introduced as examples of joint use.

9.3.1 Flexural Motion Amplifiers

This section examines the extension of the linear range of motion of micromachined thermal actuators. Thermal actuators are commonly used in MEMS technology. Unfortunately their range of motion is limited to about 5-10 μm . A flexure mechanism is used to increase this range of motion without using rotating geared transmissions.

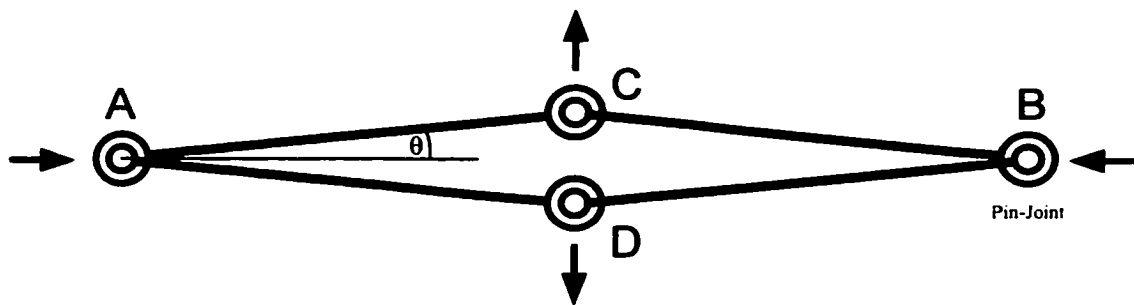


Figure 9-1: Schematic of a Flexural Motion Amplifier

Two opposing sets of thermal actuators compress or extend a toggle mechanism (a kinematic dyad). The bars are fabricated at a small angle θ relative to the line of action of the actuators. The output transverse force developed at the bar pivot point is reduced by a factor of $\tan(\theta)$ and the transverse motion is amplified by a factor of $1 / \tan(\theta)$. The amplification ratio varies with angle, being greatest for smaller angles. Figure 9-1 shows the layout of a toggle mechanism with an angle of six degrees between the bars. If points A and B of the mechanism are displaced by equal small amounts towards the centre, points C and D will be displaced approximately ten times that distance away from the centre.

The schematic of the flexural motion amplifier shown in Figure 9-1 calls for pure rotary joints (“pin” joints) to connect the links. Chapter 9.2.2 suggests short H-joints or short PC-joints as the joints of choice. Since the footprint of the H-joint was too big for this ap-

plication and large, predominantly axial forces were involved, PC-joints were used to connect the bars.

Several variations of this mechanism with different angles were fabricated; see Figure 9-2 for a typical layout. Figure 9-3 on page 123 shows the movement of a mechanism fabricated from surface micromachined polysilicon. The mechanism is approximately $500\mu\text{m}$ across and the flexure joints are $2\mu\text{m}\times 2\mu\text{m}$ in cross section. Two sets of parallel thermal actuators displace horizontally, compressing two symmetric toggle mechanisms and the amplified motion is perpendicular. Using a detailed FE model of the mechanism, the joints and the thermal actuators, a series of temperature loads was applied to the thermal actuators and the resulting displacement calculated and found to agree with experimental measurements.

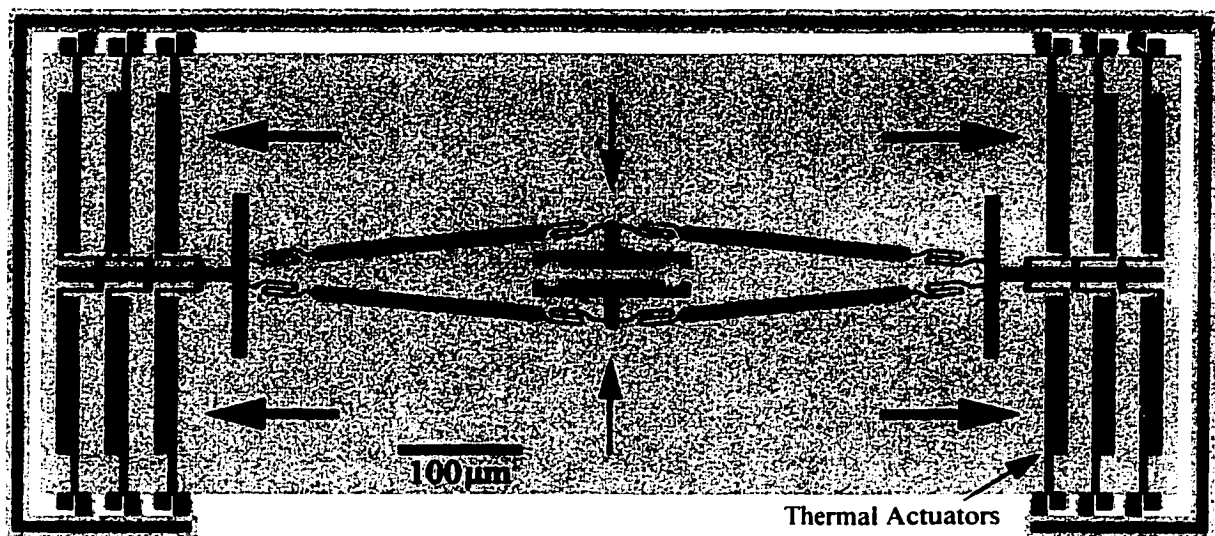


Figure 9-2: Flexural Motion Clamping Mechanism (PS1 chip)

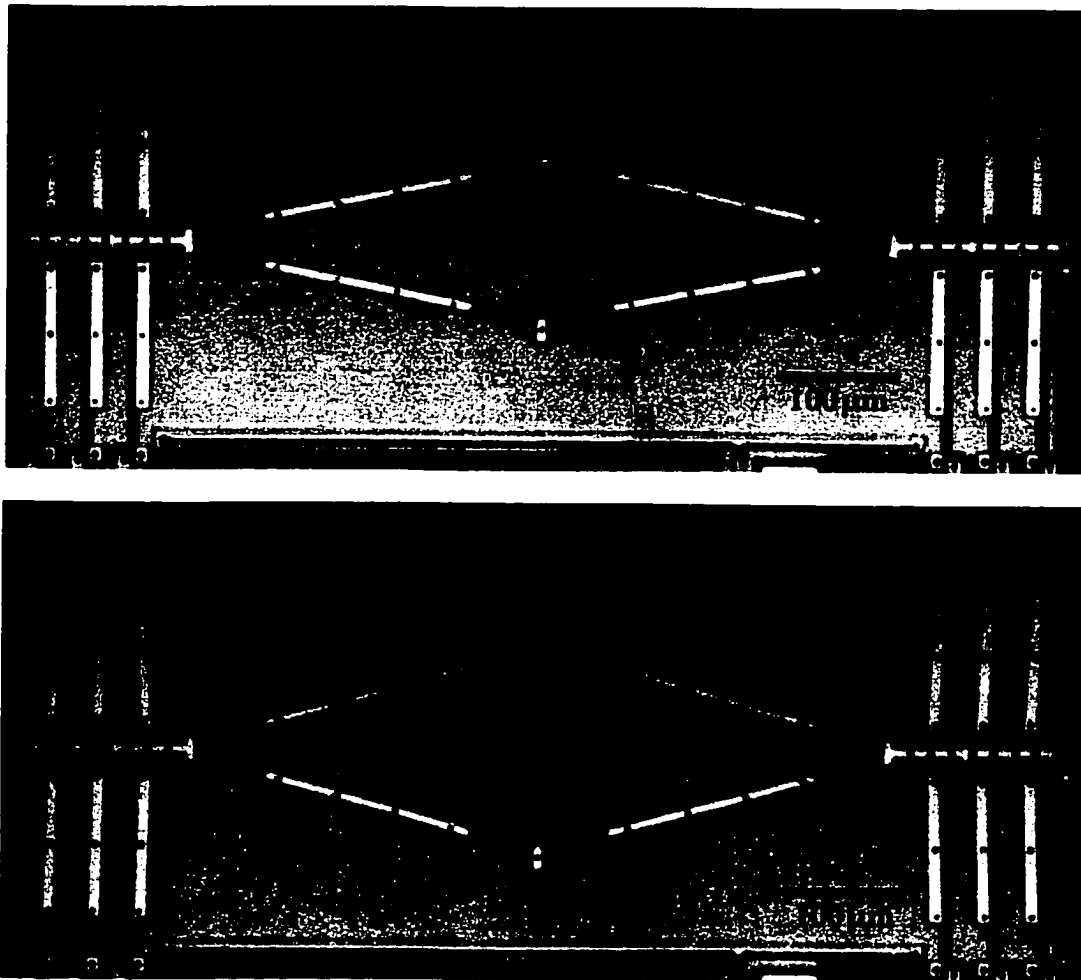


Figure 9-3: Motion of a Flexural Motion Amplifier (top: 0V, bottom: 6V, CJ2 chip)

9.3.2 Three Degrees of Freedom Micro-Stage

Using pure rotary joints and rotary-slide joints a parallel manipulator mechanism, resembling a three legged spider, was designed. It provides three degrees of freedom: x , y , and θ .

Figure 9-4 shows a kinematic diagram for the manipulator. Kinematically it has 3 pure rotary joints J_1 with 1 DOF each, 3 rotary-slide joints J_2 with 2 DOF, and 5 rigid links L : the frame, 3 legs, 1 platform. The well known Kutzbach's criterion for planar motion provides the mechanism's mobility M (DOF): $M = 3(L - 1) - 2 \cdot J_1 - 1 \cdot J_2 = 3$. The 3 DOF mobility accounts for x , y , and θ motion.

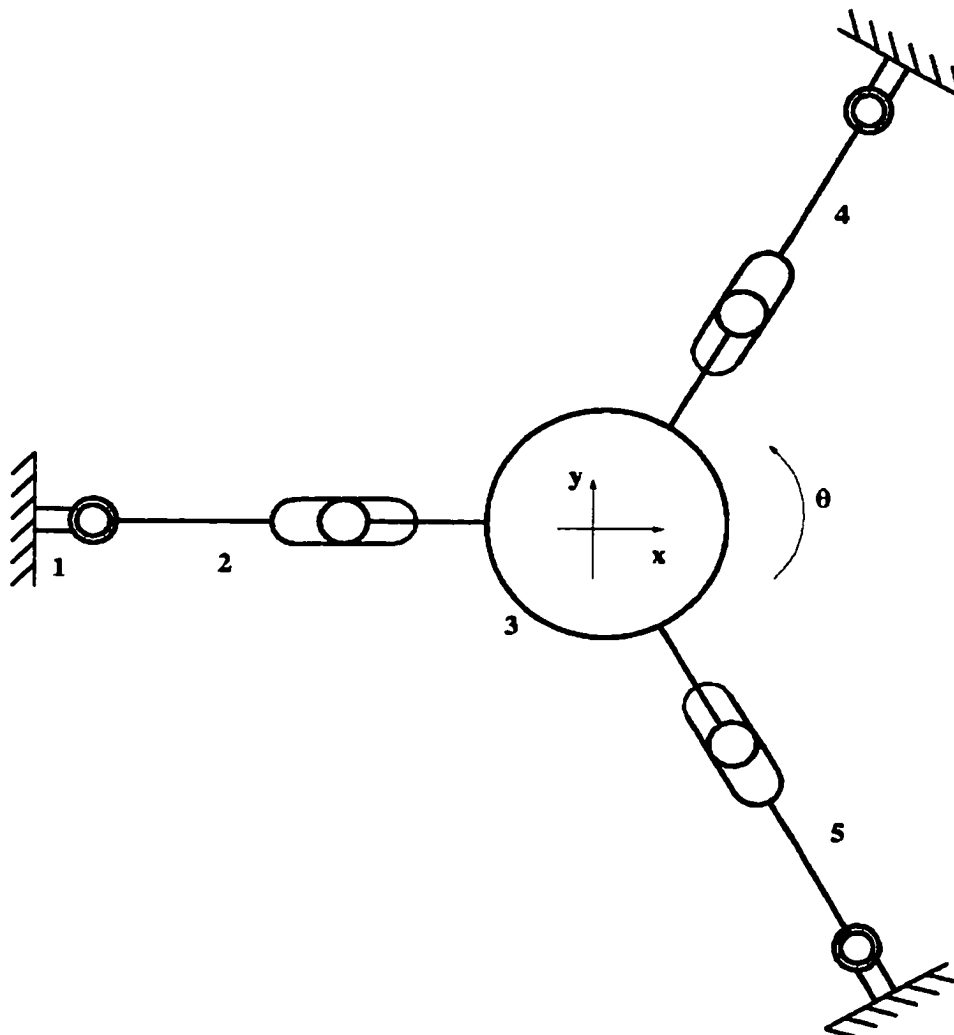


Figure 9-4: 3 DOF Parallel Manipulator Mechanism (Kinematic Representation)^a

a. see [6]

A micro-scale version (Figure 9-5) of the above platform has been designed and fabricated commercially through the MUMPs process. S-joints were used for the rotary-slide joints as suggested in Chapter 9.2.1. In order to provide the necessary compliance in axial direction a relatively long version of the S-joint was used. Small Poly 1 squares with dimples were attached to the curvatures of the joints to avoid stiction of the joints to the surface.

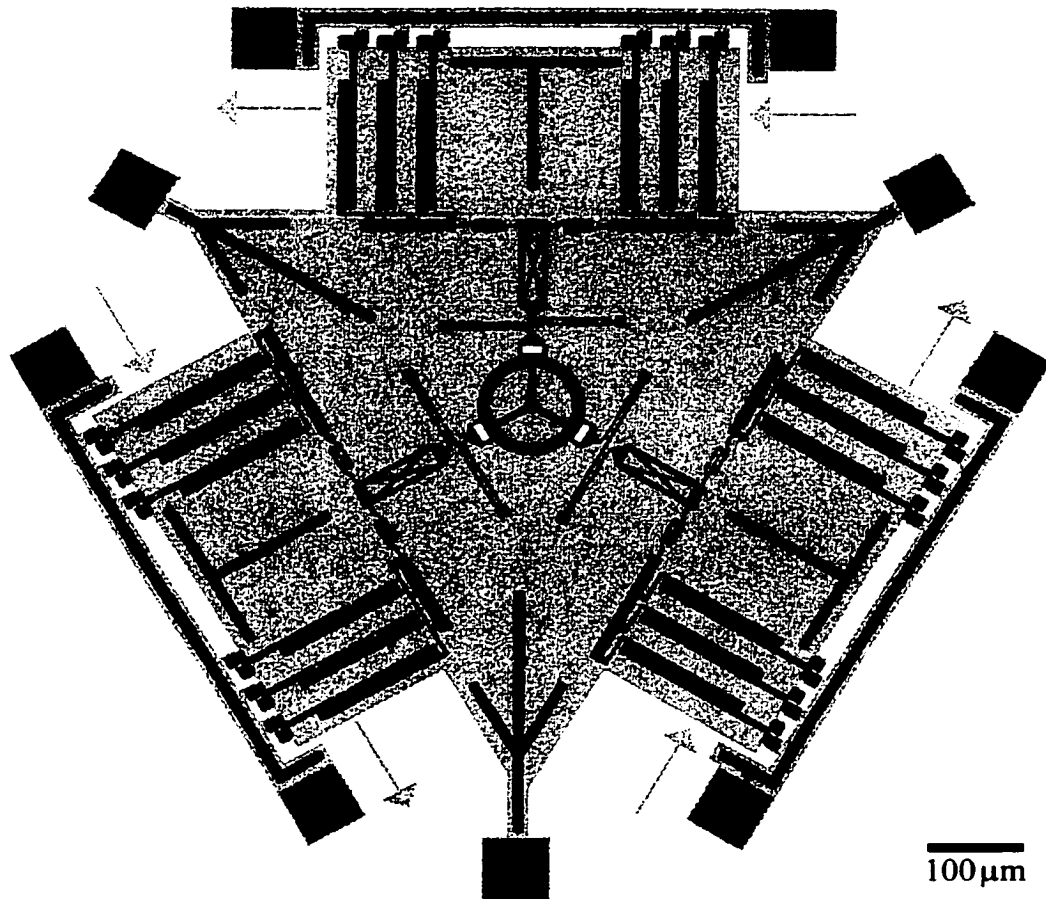


Figure 9-5: Uni-Directional 3 DOF Micro-Stage with Long S-Joints
(Layout, CM2 chip)

The design shown in Figure 9-5 uses the flexures of two banks of three thermal actuators in parallel as the rotary joint. In order to de-couple the two actuator banks PC-joints were used. This allows the transfer of large forces in axial direction while providing compliance in rotational direction.

Figure 9-6 shows a photograph of a micro-stage fabricated with the MUMPs process. Figure 9-7 shows a close-up of the platform and the joints used in the micro-stage.

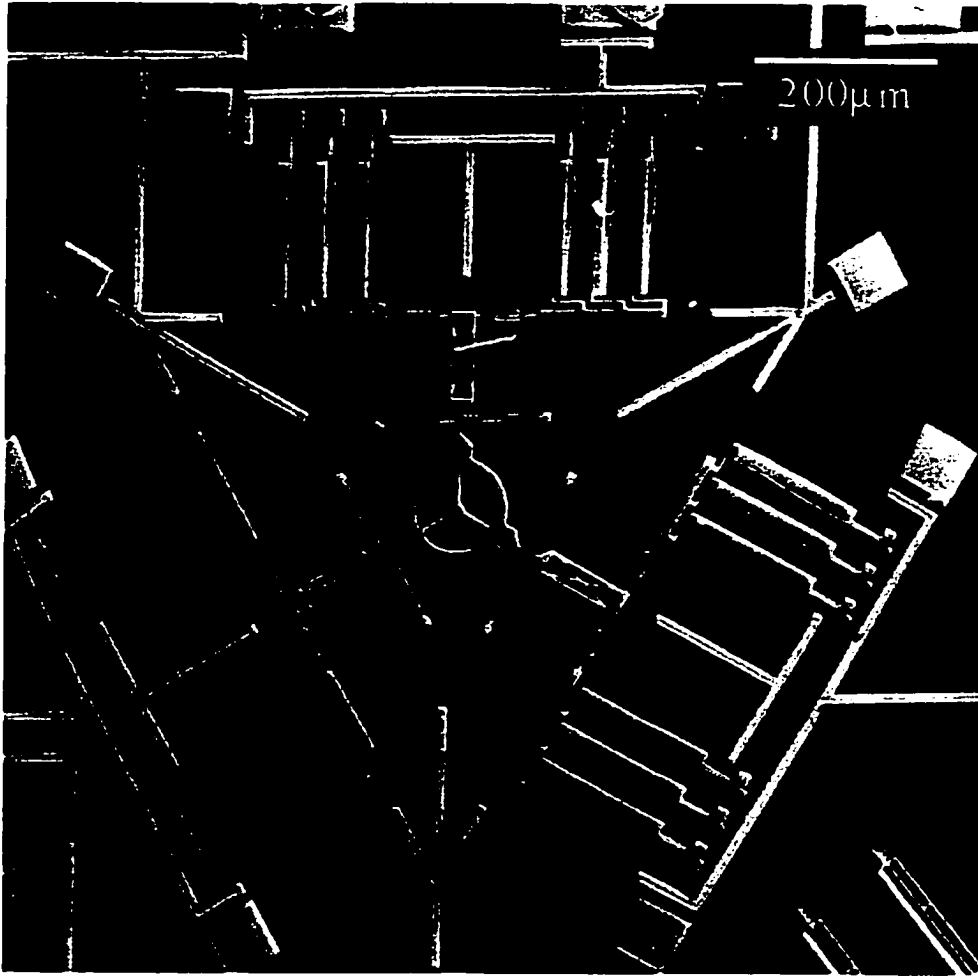


Figure 9-6: Uni-Directional 3 DOF Micro-Stage with Long S-Joints
(SEM Micrograph, CM2 chip)

Tests of the fabricated mechanism showed that it does work in the way it was design to, however, yielding lower linear and angular displacements of the platform than expected. The tests also showed that this can be attributed to the low forces provided by the thermal actuators. By increasing the force output of the thermal actuators or reducing the stiffness of the mechanism the range of motion of the platform could be increased.

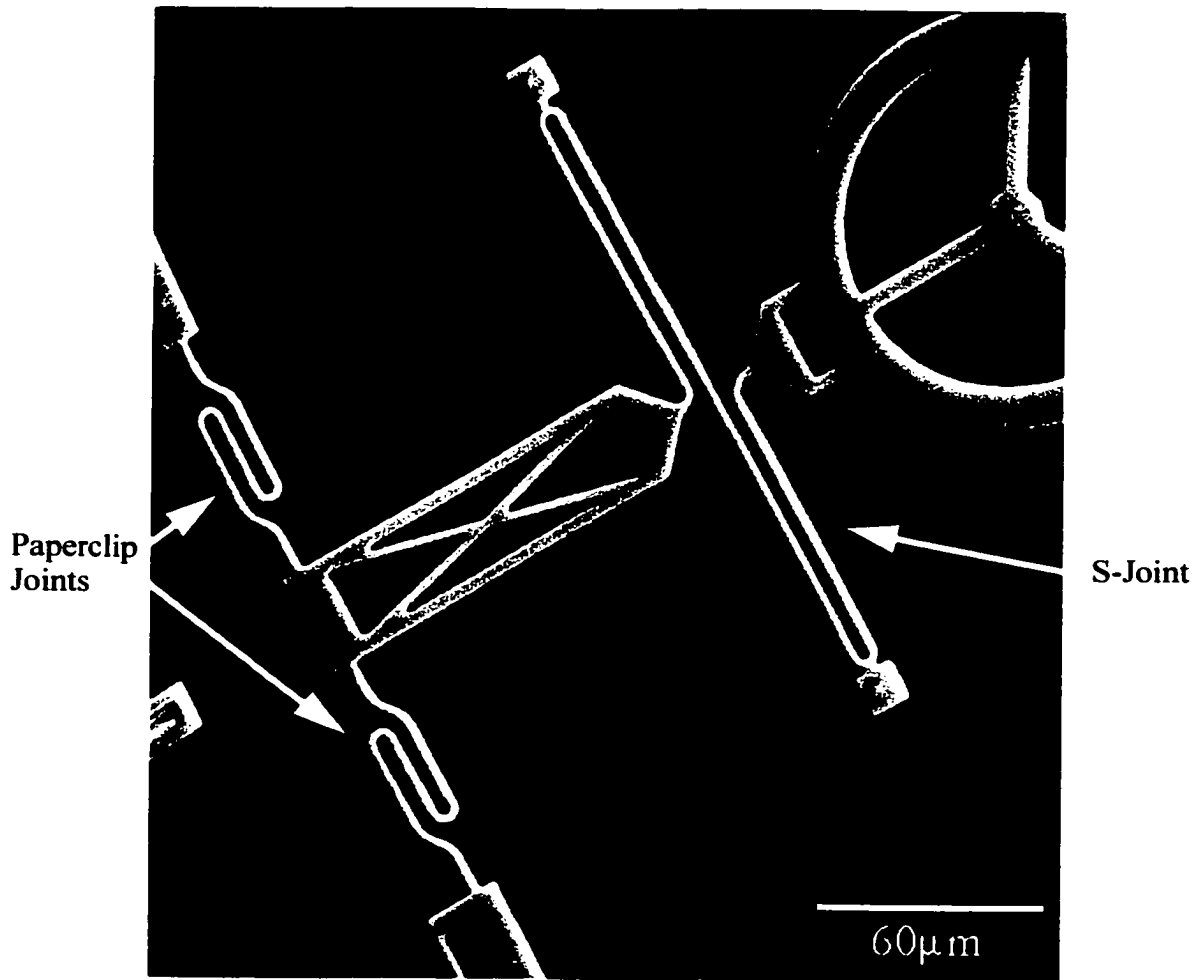


Figure 9-7: SEM Micrograph of Polysilicon Micro-Stage (Close-Up, CM2 chip)

10 Conclusion

This research presented the first attempt to systematically examine flexible micro-joints using finite element analysis. It examined the possibility of taking long slender beams and folding them into a variety of shapes to connect two links at a fixed distance: ‘I’, ‘H’, ‘X’, ‘S’, ‘U’ and ‘V’ shaped joints were considered. Using finite element analysis models of 93 variations of joints were analysed. The models were used to calculate joint stiffnesses in various directions as well as resonant modes and frequencies.

The in-plane rotational stiffness K_θ of the joints was found to depend only on the total joint length L . During in-plane rotational motion all joint segments are subjected to bending only for all joint types. Therefore the shape of the joint has no influence on the in-plane rotational stiffness ($K_\theta = \frac{EI}{L}$).

The in-plane axial K_x and lateral stiffnesses K_y were found to depend on how much of the joint is subjected to bending ($K \propto \frac{EI}{L^3}$) and how much is subjected to tension or compression ($K \propto \frac{AE}{L}$) during the translational motion. Joints with most segments parallel to the joint axis are axially stiffest and laterally softest, joints with most segments perpendicular are axially softest and laterally stiffest. The H-joint was found to be axially stiffest, the S-joint axially softest.

All out-of-plane rotational stiffnesses K_ϕ were found to be 5-30% lower than the respective in-plane rotational stiffnesses ($K_\phi \approx 70 - 95\% K_\theta$). For out-of-plane rotational motion joint segments parallel to the joint axis are subjected to bending while segments perpendicular to the axis are subjected to torsion. Because the torsional stiffness is lower than the bending stiffness, the joint shape has an influence on the out-of-plane rotational stiffness. The H-joint with most segments subjected to bending has the highest K_ϕ , the S-joint with most segments subjected to torsion the lowest K_ϕ .

Dynamic optical tests of joint-mass systems were carried out and experimental values for resonant frequencies (2-20kHz) and rotational stiffnesses were found to agree with FEA predictions to within 10-20%. Quality factors of 6-8 were measured. The observed values were well fit by a polysilicon Young’s modulus of 146GPa.

In order to increase the out-of-plane rotational stiffness of the joints double layer joints were examined. The increased joint thickness had the desired effect and experimental results confirmed the FEA results. However, increased brittleness and fabrication failure rate led to the recommendation of not using double layer joints.

Variation of the width of selected joint segments for the H- and X-joints yielded only one scenario in which the in-plane axial stiffness of the joint was increased significantly relative to the in-plane rotational stiffness. Doubling the width of the top and bottom arm of the H-joint yielded a 50% increase.

Decreasing the lateral spacing of the arms of an H-joint led to the design of the paper-clip (PC) joint. The PC-joint proved to be approximately nine times stiffer in axial direction than the H-joint. To make room for the closer spaced arms, however, the size of the gap between the connected links had to be enlarged. This limits the usefulness of the PC-joint.

Design guidelines were derived from the simulation results. The recommendations included not to use I-, U-, or V-joints. A long S-joint was found to be the choice for the use as a pseudo slide joint. The choice for the use as a pseudo rotary joint was found to be a short H- or PC-joint.

Two examples of joint use in planar mechanisms were presented: flexural motion amplifiers and 3 DOF micro-stages.

Recommendations for Future Work

In order to increase the out-of-plane rotational stiffness of the joints a Poly 2 joint on top of a Poly 1 joint could be used. Separated by the $0.75\ \mu\text{m}$ gap of the removed second oxide layer the two joints would only be connected to the links but not to each other. This would increase the out-of-plane stiffness without the increased brittleness experienced with the double layer joints.

Joints in mechanisms were only presented as examples for joint use in this thesis. Building on the results of this research the performance of the joints in various mechanisms could be investigated.

11 References

- [1] *ANSYS Coupled-Field Analysis Guide*. 4th ed. 1999. Canonsburg, PA: ANSYS.
- [2] *ANSYS Structural Analysis Guide*. 5th ed. 1999. Canonsburg, PA: ANSYS.
- [3] *ANSYS Theory Reference*. 11th ed. 1999. Canonsburg, PA: ANSYS.
- [4] Creelman, Laura, Paul Dandurand, Robert Ewing, and Gavin Tweedie. 2001. *Report on Design Project #3: Compact Micro Positioner*. Halifax, NS: Department of Mechanical Engineering, Dalhousie University.
- [5] Beerschwinger, U., N. G. Milne, S. J. Yang, R. L. Reuben, A. J. Sangster, and H. Ziad. 1994. Coupled Electrostatic and Mechanical FEA of a Micromotor. *Journal of Microelectromechanical Systems*. 3 (4): 162-171.
- [6] Fettig, Heiko, Ted Hubbard, and Marek Kujath. 2000. Simulation and Modeling of Compliant Micro-Mechanisms. In *Proceedings of SEM IX International Congress, Microscale Systems Symposium, Orlando, FL, June 2000*. Bethel, CT: SEM. 12-18.
- [7] Feynman, Richard P. 1992. There is Plenty of Room on the Bottom. *Journal of Microelectromechanical Systems*. 1 (1): 60-66.
- [8] Feynman, Richard P. 1993. Infinitesimal Machinery. *Journal of Microelectromechanical Systems*. 2 (1): 4-14.
- [9] Gill, J. J.-Y., L. V. Ngo, P. R. Nelson, and Kim Chang-Jin. 1998. Elimination of Extra Spring Effect at the Step-Up Anchor of Surface-Micromachined Structure. *Journal of Microelectromechanical Systems*. 7 (1): 114-121.
- [10] Hahn, Hans Georg. 1982. *Methode der finiten Elemente in der Festigkeitslehre* (Finite Element Method in Structural Design). 2nd ed. Wiesbaden, Germany: Akademische Verlagsgesellschaft.
- [11] Hosaka, H., K. Itao, and S. Kuroda. 1994. Evaluation of Energy Dissipation Mechanisms in Vibrational Microactuators. In *Proceedings of MEMS'94 - IEEE Seventh Workshop on MicroElectroMechanical Systems, Oiso, Japan, January, 1994*. San Diego, CA: IEEE. 193-198.
- [12] Hubbard, Ted. 1998. *MECH 6325 Micro-Electro-Mechanical Systems*. Unpublished Classnotes. Dalhousie University. Halifax, NS.
- [13] Huebner, Kenneth H., Earl A. Thornton, and Ted G. Byron. 1995. *The Finite Element Method for Engineers*. New York: John Wiley & Sons.

- [14] Jericho, Manfred. (April 2001). Unpublished Stiffness Measurements. Department of Physics, Dalhousie University. Halifax, NS.
- [15] Kahn, H., S. Stemmer, K. Nandakumar, A. H. Heuer, R. L. Mullen, R. Ballarini, and M. A. Huff. 1996. Mechanical Properties of Thick, Surface Micromachined Polysilicon Films. In *Proceedings of MEMS'96 - IEEE Ninth Workshop on MicroElectro-Mechanical Systems, San Diego, CA, January 1996*. San Diego, CA: IEEE. 343-353.
- [16] Kobrinsky, M. J., E. R. Deutsch, and S. D. Senturia. 2000. Effect of Support Compliance and Residual Stress on the Shape of Doubly Supported Surface-Micromachined Beams. *Journal of Microelectromechanical Systems*. 9 (3): 361-369.
- [17] Koester, David A., et al. 2001. *MUMPs™ Design Handbook, Rev. 6.0*. Research Triangle Park, NC: Cronos Integrated Microsystems.
- [18] Koskinen, J., S. E. Steinwall, R. Soave, and H. H. Johnson. 1993. Microtensile Testing of Free-Standing Polysilicon Fibers of Various Grain Sizes. *Journal of Micromechanics and Microengineering*. 3 (1): 13-17.
- [19] Kota, S. 1995. Designing Compliant Mechanisms. *Mechanical Engineering*. 117 (11): 93-96.
- [20] Kota, S. 1999. Designing Compliant Mechanisms with Applications to MEMS and Smart Structures. In *Proceedings of the Tenth IFToMM Congress on the theory of machines and mechanisms, Oulu, Finland, June 1999*. Montreal: IFToMM. 2722-2728.
- [21] Kota, S., J. Hetrick, Li Zhe, S. Rodgers, and T. Krygowski. 2000. Synthesizing High-Performance Compliant Stroke Amplification Systems for MEMS. In *Proceedings of MEMS'00 - IEEE Thirteenth workshop on MicroElectroMechanical Systems, Miyazaki, Japan, January 2000*. San Diego, CA: IEEE. 164-169.
- [22] Larson, U., O. Sigmund, and S. Bouwstra. Design and Fabrication of Compliant Micromechanisms and Structures with Negative Poisson's Ratio. *Journal of Microelectromechanical Systems*. 6 (2): 99-106.
- [23] *Model SR785 Dynamic Signal Analyzer: Operating Manual and Programming Reference*. 1998. Rev 1.0. Sunnyvale, CA: Stanford Research Systems.
- [24] Norton, Robert L. 1992. *Design of Machinery: An Introduction to the Synthesis and Analysis of Mechanisms and Machines*. New York: McGraw-Hill.

- [25] Pedersen, M., W. Olthuis, and P. Bergveld. 1995. On the Simulation of Subminiature Condenser Microphones Using Finite Differences. In *Simulation and Design of Microsystems and Microstructures*. Billerica, MA: Computational Mechanics. 185-192
- [26] Petersen, Kurt E. 1982. Silicon as a Mechanical Material. *Proceedings of the IEEE*. 79 (8): 420-457.
- [27] Sauter, Jürgen, and Puchinger, Martin. 1991. *Finite-Elemente-Seminar für den Konstrukteur (Finite Element Seminar for the Designer)*. Karlsruhe: Institute for Machine and Automotive Design - University of Karlsruhe.
- [28] Sharpe, W. N., Yuan Bin, R. Vaidyanathan, and R. L. Edwards. 1997. Measurement of Young's Modulus, Poisson's ratio, and Tensile Strength of Polysilicon. In *Proceedings of MEMS'97 - IEEE Tenth Workshop On MicroElectroMechanical Systems, Nagoya, Japan, January 1997*. San Diego, CA: IEEE. 424-429.
- [29] Suzuki, K., I. Shimoyana, and H. Miura. 1994. Insect Model Based Microrobot with Elastic Hinges. *Journal of Microelectromechanical Systems*. 3 (1): 4-10.
- [30] Thomson, William T., and Marie D. Dahleh. 1998. *Theory of Vibration with Applications*. 5th ed. Upper Saddle River, NJ: Prentice-Hall.
- [31] Wilke, Ralph, James Wylde, and Ted Hubbard. 2000. Frequency Changes in Aerodynamically Excited Resonating Micro-machined Beams. In *Proceedings of IEEE Canadian Conference of Electrical and Computer Engineering, Halifax, NS, May 2000*. San Diego, CA: IEEE. WM 5.2.
- [32] Wylde, James. 1999. *Dynamic Testing and Characterization of Micro-machined Beams*. Unpublished Ph.D. Thesis. Faculty of Engineering - Dalhousie University. Halifax, NS.
- [33] Zengerle, R., M. Richter, F. Brosinger, A. Richter, and H. Sandmaier. 1993. Performance Simulation of Microminiaturized Membrane Pumps. In *Proceedings of Transducers '93, Yokohama, Japan, 1993*. 106-111.
- [34] Zhang, Xia, and W. C. Tang. 1994. Viscous Air Damping in Laterally Driven Microresonators. In *Proceedings of MEMS'94 - IEEE Seventh Workshop on MicroElectro-Mechanical Systems, Oiso, Japan, January 1994*. San Diego, CA: IEEE. 199-204.
- [35] Zienkiewicz, O. C., and Taylor, R. L. 1997. *The Finite Element Method - Vol. 1: Basic Formulation and Linear Problems*. 4th ed. London: McGraw-Hill.

A Summary of Joint Properties

A.1 Joint Variation Identifiers

In order to distinguish the wide variety of joints, 93 FEA models and 55 fabricated joints, that were examined, they were given a characteristic identifier. This identifier was used in the layout files of the fabricated chips, as well as in the ANSYS simulations. Table A-1 on page 135 and Table A-2 on page 136 list the identifiers grouped by joint along with the respective folded and unfolded lengths and state whether they were fabricated or not.

The complete identifier for any given variation is:

$$Type_Variation_Layers \quad (A-1)$$

Here *Type* stands for the type of joint, H, I, S, U, V, or X. *Variation* stands for the variation identifier. Identifiers including ‘std’ have a $2\mu\text{m} \times 2\mu\text{m}$ cross-section for the whole joint, while ‘var’ joints feature varying cross-sections and joint shape. The type of setup the joint is fabricated in is described by the *Layers* identifier: ‘sm’ stands for a single layer joint with a small end-mass, ‘lm’ for a single layer joint with a large end-mass, and ‘dl’ for a double layer joint.

A standard single layer H-joint with a folded length of $100\mu\text{m}$ and a small end-mass is therefore identified by *H_std_01_sm*.

All joint layouts in IMDTCJ2 and all FE simulations were organised using these identifiers. For the sake of simplicity all standard joints are also referred to by *Type L_f*, e.g. H 100.

Table A-1: Identifiers of Examined Joint Variations (H, X, S)

Type	Variation	Layers			Fabricated	Folded Length L_f [μm]	Unfolded Length L [μm]	Simple Standard Identifier	
		dl	sm	lm					
H	std_01	dl	sm	lm	yes (CJ2, RT2)	100	471	H 100	
	std_02	dl	sm	lm	yes (CJ2, RT2)	50	271	H 50	
	std_03	dl	sm	lm	yes (CJ2, RT2)	25	171	H 25	
	std_04	dl	sm		no	75	371	H 75	
	std_05	dl	sm		no	37.5	221	H 38	
	var_01	dl	sm		yes (CJ2)	100	471		
	var_02	dl	sm		yes (CJ2)	100	471		
	var_03	dl	sm		yes (CJ2)	100	471		
	var_04	dl	sm		yes (CJ2)	100	471		
	var_05	dl	sm		yes (CJ2)	75	371		
	X	std_01	dl	sm	lm	yes (CJ2, RT2)	79.5	458	X 80
		std_02	dl	sm	lm	yes (CJ2, RT2)	44.5	260	X 45
		std_03	dl	sm	lm	yes (CJ2, RT2)	26.5	158	X 27
		std_04	dl	sm		no	62	359	X 62
		std_05	dl	sm		no	35.5	209	X 36
var_01		dl	sm		yes (CJ2)	79.5	458		
var_02		dl	sm		yes (CJ2)	79.5	458		
var_03		dl	sm		yes (CJ2)	79.5	458		
var_04		dl	sm		yes (CJ2)	79.5	458		
var_05		dl	sm		yes (CJ2)	35.5	359		
S		std_01	dl	sm		yes (CJ2)	100	232	S 100
		std_02	dl	sm		no	50	132	S 50
		std_03	dl	sm		no	200	432	S 200
		std_04	dl	sm		no	150	332	S 150
		std_05	dl	sm		no	75	182	S 75
	var_01	dl	sm		yes (CJ2)	100	232		
	var_02	dl	sm		yes (CJ2)	100	232		

Table A-2: Identifiers of Examined Joint Variations (I, U, V, PC)

Type	Variation	Layers			Fabricated	Folded Length L_f (μm)	Unfolded Length L (μm)	Simple Standard Identifier
		dl	sm	lm				
I	std_01	dl	sm	lm	yes (CJ2, RT2)	30	30	I 30
U	std_01	dl	sm		yes (CJ2)	65	261	U 65
	std_02	dl	sm		no	115	461	U 115
	std_03	dl	sm		no	40	161	U 40
	std_04	dl	sm		no	90	361	U 90
	std_05	dl	sm		no	52.5	211	U 53
	var_01	dl	sm		yes (CJ2)	65	471	
V	std_01	dl	sm		yes (CJ2)	54.75	258	V 55
	std_02	dl	sm		no	90	457	V 90
	std_03	dl	sm		no	37.25	159	V 38
	std_04	dl	sm		no	72.5	358	V 73
	std_05	dl	sm		no	45.75	207	V 46
	var_01	dl	sm		yes (CJ2)	54.75	258	
PC	std_01		sm		yes (CJ2)	25	126	PC 25
	std_02		sm		no	50	201	PC 50
	std_03		sm		no	75	276	PC 75
	std_04		sm		no	100	351	PC 100
	std_05		sm		no	125	426	PC 125
	std_06		sm		no	1	54	PC 1

A.2 The ANSYS Co-Ordinate System

By default the plot control options of ANSYS provide a number of pre-defined views. Unfortunately these can be a little confusing. For example, the *Top* view shows the X - Z plane, while the *Front* view shows the X - Y plane. This is contrary to the “world” co-ordinate system, which has a top view showing the x - y plane and the front view showing the x - z plane.

To distinguish the co-ordinate systems ANSYS co-ordinates are given in capital letters, “world” co-ordinates in lower case letters. Table A-3 lists the differences in co-ordinates and conversion factors.

Table A-3: Relation Between ANSYS and “World” Co-Ordinate System

Direction	“World” Co-Ordinate	Multiply by This Number	To Obtain ANSYS Co-Ordinate
In-Plane Axial	x	1	X
In-Plane Lateral	y	-1	Z
Out-of-Plane Lateral	z	1	Y

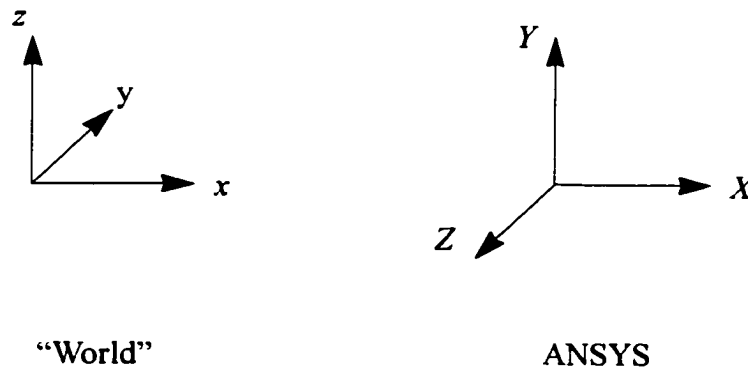


Figure A-1: The “World” and the ANSYS Co-Ordinate System

All results and graphs in this thesis are presented in the “world” co-ordinate system. The descriptions of the joint segments in the following sections, however, are given in the ANSYS co-ordinate system.

A.3 Total Unfolded Joint Length

For all joints an increase in total joint length affects only the length of straight segments. The segments that do not change make up the static length L_s . Table A-4 list the static lengths for the various joint types and equations to calculate the total unfolded joint length L from the folded joint length L_f .

Table A-4: Total Unfolded Joint Length

Joint Type	Static Length L_s [μm]	Total Unfolded Length L [μm]		
H	119.1	$4L_f + L_s - 48$	$4L_f + 71.1$	$4(L_a + L_b) + 71.1$
I	0.0	L_f	L_f	
S	43.7	$2L_f + L_s - 12$	$2L_f + 31.7$	$4L_a + 31.7$
U	122.5	$4L_f + L_s - 121.2$	$4L_f + 1.3$	$4L_a + 61.3$
V	65.0	$5.657L_f + L_s - 116.9$	$5.657L_f - 51.9$	$5.657L_a + 33.0$
X	94.8	$5.657L_f + L_s - 87.0$	$5.657L_f + 7.8$	$5.657(L_a + L_b) + 7.8$
PC	51.1	$3L_f + L_s$	$3L_f + 51.1$	$6L_a + 51.1$

A.4 H-Joints

A.4.1 Layout Schematics

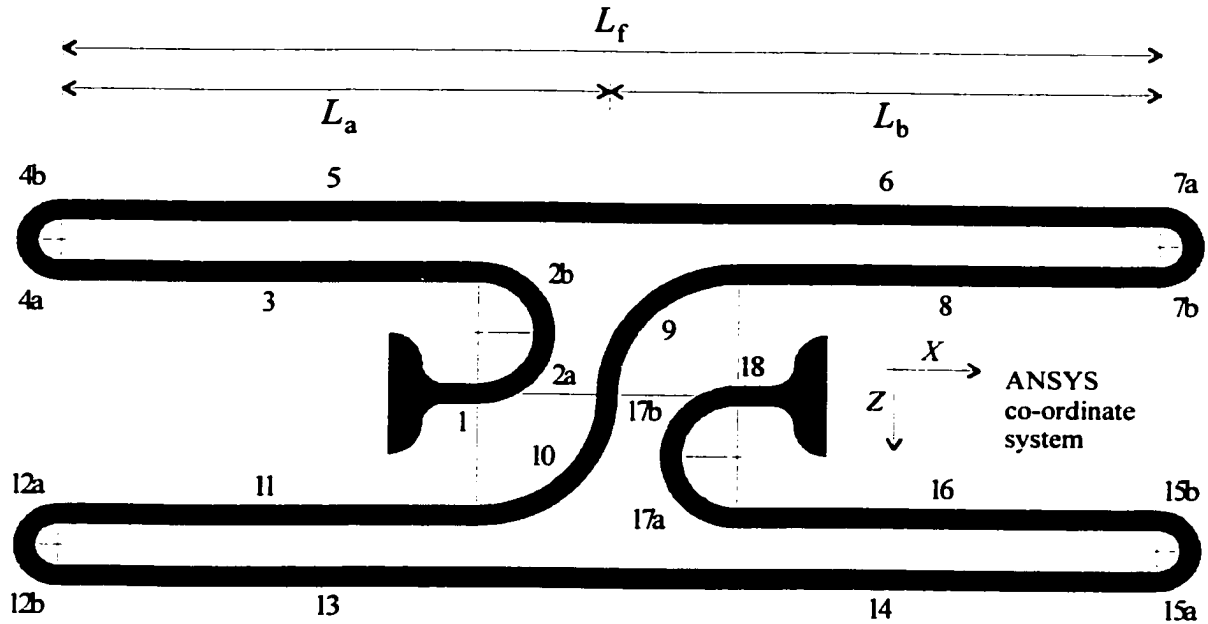


Figure A-2: Geometric Layout of an H-Joint

Table A-5: H-Joint Variations

Variation	Folded Length [μm]			Unfolded Length [μm]	Segments $2\mu\text{m}$ wide	Segments $4\mu\text{m}$ wide
	L_f	L_a	L_b			
H_std_01	100	50	50	471	1-18	
H_std_02	50	25	25	271	1-18	
H_std_03	25	12.5	12.5	171	1-18	
H_std_04	75	37.5	37.5	371	1-18	
H_std_05	37.5	18.75	18.75	221	1-18	
H_var_01	100	50	50	471	1-4, 7-12, 15-18	5, 6, 13, 14
H_var_02	100	50	50	471	1-7, 12-18	8-11
H_var_03	100	50	50	471	2, 4, 7, 12, 15, 17	1, 3, 5, 6, 8-11, 13, 14, 16, 18
H_var_04	100	50	50	471	1-5, 10-13	6-9, 14-18
H_var_05	75	50	25	371	1-18	

Table A-6: Joint Segments of an H-Joint

Joint Segment	Point (X, Z) [μm]			Angle		Radius [μm]
	Start	End	Centre	Start	End	
1	-15, 0	-12, 0				
2a	-12, 0	-6, -6	-12, -6	-90°	0°	6
2b	-6, -6	-12, -12	-12, -6	0°	90°	6
3	-12, -12	$-L_a, -12$				
4a	$-L_a, -12$	$-L_a-3, -15$	$-L_a, -15$	-90°	-180°	3
4b	$-L_a-3, -15$	$-L_a, -18$	$-L_a, -15$	180°	90°	3
5	$-L_a, -18$	0, -18				
6	0, -18	$L_b, -18$				
7a	$L_b, -18$	$L_b+3, -15$	$L_b, -15$	90°	0°	3
7b	$L_b+3, -15$	$L_b, -12$	$L_b, -15$	0°	-90°	3
8	$L_b, -12$	12, -12				
9	12, -12	0, 0	12, 0	90°	180°	12
10	0, 0	-12, 12	-12, 0	0°	-90°	12
11	-12, 12	$-L_a, 12$				
12a	$-L_a, 12$	$-L_a-3, 15$	$-L_a, 15$	90°	180°	3
12b	$-L_a-3, 15$	$-L_a, 18$	$-L_a, 15$	-180°	-90°	3
13	$-L_a, 18$	0, 18				
14	0, 18	$L_b, 18$				
15a	$L_b, 18$	$L_b+3, 15$	$L_b, 15$	-90	0	3
15b	$L_b+3, 15$	$L_b, 12$	$L_b, 15$	0	90	3
16	$L_b, 12$	12, 12				
17a	12, 12	6, 6	12, 6	-90	-180	6
17b	6, 6	12, 0	12, 6	180	90	6
18	12, 0	15, 0				

A.4.2 FEA Results

Table A-7: H-Joint-Mass Resonance Frequencies (FEA)

Variation	Unfolded Length [μm]	Resonance Frequency [kHz]			Frequency Ratios	
		Out-of-Plane Rotational	In-Plane Rotational	In-Plane Axial	<u>Axial</u> <u>In-Plane</u>	<u>Out-of-Plane</u> <u>In-Plane</u>
H_std_01_sm (H 100)	471	5.84	6.05	46.4	7.7	0.97
H_std_04_sm (H 75)	371	6.61	6.91	54.8	7.9	0.96
H_std_02_sm (H 50)	271	7.70	8.16	67.2	8.2	0.94
H_std_05_sm (H 38)	221	8.46	9.06	76.7	8.5	0.93
H_std_03_sm (H 25)	171	9.47	10.3	91.1	8.8	0.92
H_var_01_sm	471	6.53	7.61	48.4	6.4	0.86
H_var_02_sm	471	6.25	6.80	46.1	6.8	0.92
H_var_03_sm	471	7.60	11.6	53.1	4.6	0.65
H_var_04_sm	471	6.37	7.03	52.6	7.5	0.91
H_var_05_sm	371	6.11	6.36	54.8	8.6	0.96
H_std_01_lm (H 100)	471	4.33	4.48	38.4	8.6	0.97
H_std_02_lm (H 75)	271	5.68	6.01	54.5	9.1	0.95
H_std_03_lm (H 25)	171	6.99	7.60	70.5	9.3	0.92
H_std_01_dl (H 100)	471	9.71	6.36	51.2	8.1	1.5
H_std_04_dl (H 75)	371	10.7	7.25	60.8	8.4	1.5
H_std_02_dl (H 50)	271	12.1	8.55	75.0	8.8	1.4
H_std_05_dl (H 38)	221	13.0	9.49	85.8	9.0	1.4
H_std_03_dl (H 25)	171	14.0	10.8	102	9.4	1.3
H_var_01_dl	471	10.7	7.99	69.3	8.7	1.3
H_var_02_dl	471	10.5	7.14	53.2	7.5	1.5
H_var_03_dl	471	12.3	12.2	83.0	6.8	1.0
H_var_04_dl	471	10.7	7.42	61.2	8.2	1.4
H_var_05_dl	371	10.1	6.70	60.9	9.1	1.5

Table A-8: H-Joint Stiffnesses (FEA)

Variation	Unfolded Length [μm]	Rotational Stiffnesses [μN μm/rad]		Translational Stiffnesses [μN/μm]	
		In-Plane K_{θ}	Out-of-Plane K_{ϕ}	In-Plane Axial K_x	In-Plane Lateral K_y
H_std_01_sm (H 100)	471	478	455	2.24	0.515
H_std_04_sm (H 75)	371	607	570	2.93	1.11
H_std_02_sm (H 50)	271	831	763	4.22	3.13
H_std_05_sm (H 38)	221	1,020	919	5.40	6.17
H_std_03_sm (H 25)	171	1,320	1,160	7.51	14.2
H_var_01_sm	471	761	570	5.17	0.772
H_var_02_sm	471	606	525	2.55	0.618
H_var_03_sm	471	1,810	782	10.3	1.54
H_var_04_sm	471	850	620	3.99	1.63
H_var_05_sm	371	607	570	2.93	1.09
H_std_01_lm (H 100)	471	478	455	2.24	0.515
H_std_02_lm (H 75)	271	831	763	4.22	3.13
H_std_03_lm (H 25)	171	1,320	1,160	7.51	14.2
H_std_01_dl (H 100)	471	837	2,100	3.93	0.90
H_std_04_dl (H 75)	371	1,060	2,540	5.13	1.95
H_std_02_dl (H 50)	271	1,460	3,210	7.38	5.48
H_std_05_dl (H 38)	221	1,780	3,700	9.46	10.8
H_std_03_dl (H 25)	171	2,310	4,380	13.2	24.8
H_var_01_dl	471	1,330	2,540	9.05	1.35
H_var_02_dl	471	1,060	2,480	4.46	1.08
H_var_03_dl	471	3,160	3,490	17.93	2.70
H_var_04_dl	471	1,490	2,950	6.98	2.85
H_var_05_dl	371	1,060	2,540	5.13	1.91

A.4.3 Derived Equations

$$K_{\theta} = 900 \frac{\mu\text{N}\mu\text{m}}{\text{rad}} \cdot \left(\frac{250\mu\text{m}}{L} \right)^{1.00} \quad (\text{A-2})$$

$$K_x = 4.7 \frac{\mu\text{N}}{\mu\text{m}} \cdot \left(\frac{250\mu\text{m}}{L} \right)^{1.19} \quad (\text{A-3})$$

$$K_y = 4.1 \frac{\mu\text{N}}{\mu\text{m}} \cdot \left(\frac{250\mu\text{m}}{L} \right)^{3.28} \quad (\text{A-4})$$

$$K_{\phi} = 820 \frac{\mu\text{N}\mu\text{m}}{\text{rad}} \cdot \left(\frac{250\mu\text{m}}{L} \right)^{0.92} \quad (\text{A-5})$$

$$\frac{K_x}{K_{\theta}} \propto \frac{1}{L^{0.19}}; \quad \frac{K_y}{K_{\theta}} \propto \frac{1}{L^{2.28}} \quad \frac{K_{\phi}}{K_{\theta}} \propto L^{0.08} \quad (\text{A-6})$$

A.5 I-Joints

A.5.1 Layout Schematics

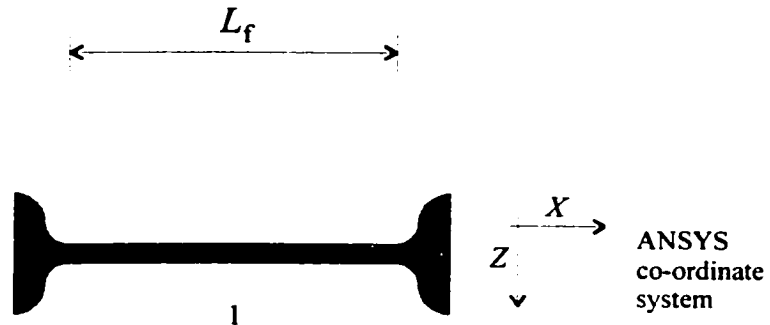


Figure A-3: Geometric Layout of an I-Joint

Table A-9: I-Joint Variations

Variation	Folded Length [μm]			Unfolded Length [μm]	Segments 2 μm wide	Segments 4 μm wide
	L_f	L_a	L_b			
I_std_01	30			30	1	

Table A-10: Joint Segments of an I-Joint

Joint Segment	Point (X, Z) [μm]			Angle		Radius [μm]
	Start	End	Centre	Start	End	
1	-15, 0	15, 0				

A.5.2 FEA Results

Table A-11: I-Joint-Mass Resonance Frequencies

Variation	Unfolded Length [μm]	Resonance Frequency [kHz]			Frequency Ratios	
		Out-of-Plane Rotational	In-Plane Rotational	In-Plane Axial	$\frac{\text{Axial}}{\text{In-Plane}}$	$\frac{\text{Out-of-Plane}}{\text{In-Plane}}$
I_std_01_sm (I 30)	30	22.1	24.4	206	8.4	0.91
I_std_01_lm (I 30)	30	16.3	17.9	150	8.3	0.91
I_std_01_dl (I 30)	30	30.4	25.4	251	9.9	1.2

Table A-12: I-Joint Stiffnesses (FEA)

Variation	Unfolded Length [μm]	Rotational Stiffnesses [μNμm/rad]		Translational Stiffnesses [μN/μm]	
		In-Plane K_{θ}	Out-of-Plane K_{ϕ}	In-Plane Axial K_x	In-Plane Normal K_y
I_std_01_sm (I 30)	30	7,510	7,510	22,500	98.9
I_std_01_lm (I 30)	30	7,510	7,510	22,500	98.9
I_std_01_dl (I 30)	30	13,100	40,300	39,400	173

A.6 S-Joints

A.6.1 Layout Schematics

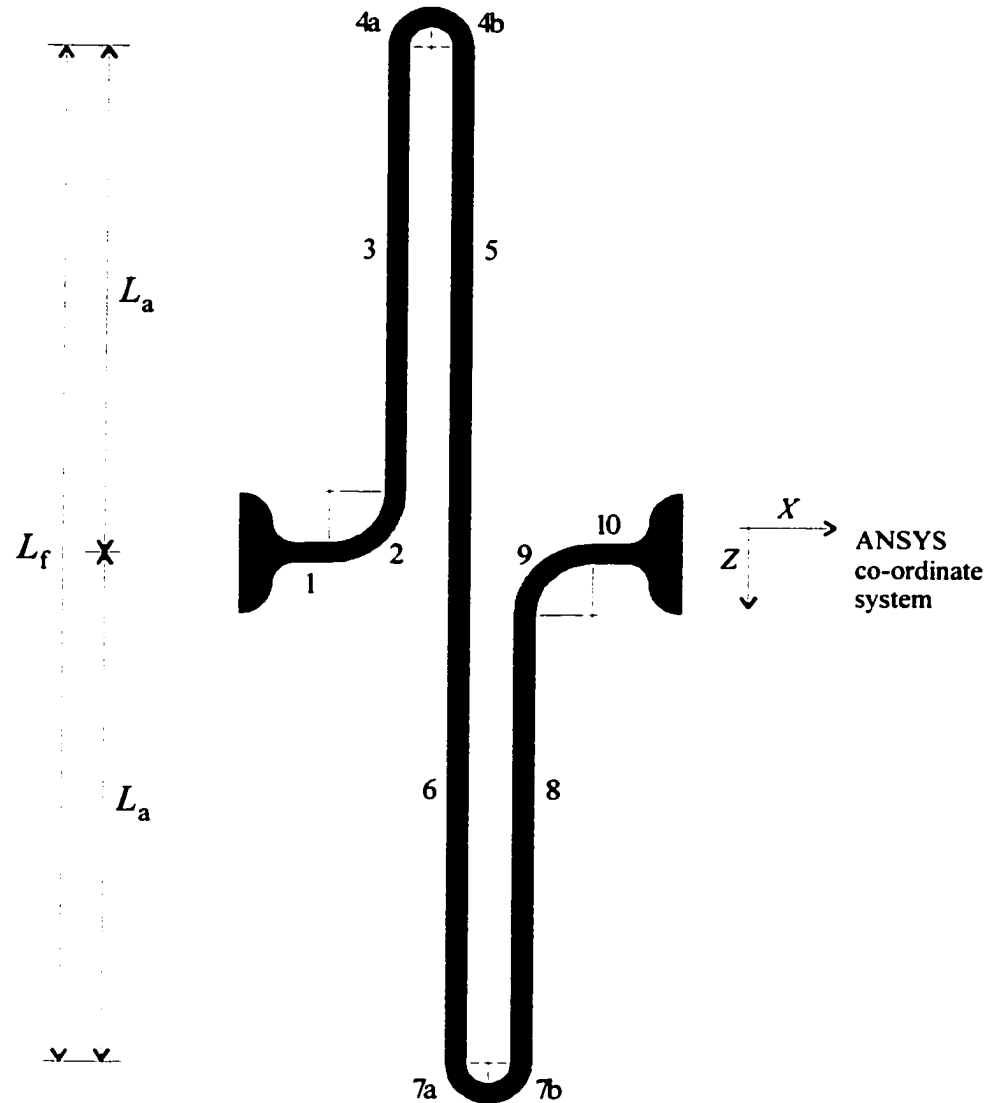


Figure A-4: Geometric Layout of an S-Joint

Table A-13: S-Joint Variations

Variation	Folded Length [μm]			Unfolded Length [μm]	Segments 2 μm wide	Segments 4 μm wide
	L_f	L_a	L_b			
S_std_01	100	50		232	1-10	
S_std_02	50	25		132	1-10	
S_std_03	200	100		432	1-10	
S_std_04	150	75		332	1-10	
S_std_05	75	37.5		182	1-10	
S_var_01	100	50		232	3, 5, 6, 8	1, 2, 4, 7, 9, 10
S_var_02	100	50		232	1, 2, 4, 7, 9, 10	3, 5, 6, 8

Table A-14: Joint Segments of an S-Joint

Joint Segment	Point (X, Z) [μm]			Angle		Radius [μm]
	Start	End	Centre	Start	End	
1	-15, 0	-12, 0				
2	-12, 0	-6, -6	-12, -6	-90°	0°	6
3	-6, -6	-6, $-L_a$				
4a	-6, $-L_a$	-3, $-L_a-3$	-3, $-L_a$	180°	90°	3
4b	-3, $-L_a-3$	0, $-L_a$	-3, $-L_a$	90°	0°	3
5	0, $-L_a$	0, 0				
6	0, 0	0, L_a				
7b	3, L_a+3	3, L_a+3	3, L_a	-180°	-90°	3
7b	3, L_a+3	6, L_a	3, L_a	-90°	0°	3
8	6, L_a	6, 6				
9	6, 6	12, 0	12, 6	180°	90°	6
10	12, 0	15, 0				

A.6.2 FEA Results**Table A-15: S-Joint-Mass Resonance Frequencies (FEA)**

Variation	Unfolded Length [μm]	Resonance Frequency [kHz]			Frequency Ratios	
		Out-of-Plane Rotational	In-Plane Rotational	In-Plane Axial	<u>Axial</u> <u>In-Plane</u>	<u>Out-of-Plane</u> <u>In-Plane</u>
S_std_03_sm (S 200)	432	5.09	6.45	12.5	1.9	0.79
S_std_04_sm (S 150)	332	6.00	7.40	19.0	2.6	0.81
S_std_01_sm (S 100)	232	7.36	8.88	33.7	3.8	0.83
S_std_05_sm (S 75)	182	8.39	10.0	49.9	5.0	0.84
S_std_02_sm (S 50)	132	9.94	11.8	85.1	7.2	0.84
S_var_01_sm	232	7.75	9.71	37.6	3.9	0.80
S_var_02_sm	232	11.1	16.4	57.7	3.5	0.68
S_std_03_dl (S 200)	432	6.87	6.75	13.9	2.1	1.0
S_std_04_dl (S 150)	332	7.97	7.75	21.2	2.7	1.0
S_std_01_dl (S 100)	232	9.67	9.30	37.7	4.1	1.0
S_std_05_dl (S 75)	182	11.0	10.5	56.0	5.3	1.0
S_std_02_dl (S 50)	132	13.0	12.3	95.6	7.8	1.1
S_var_01_dl	232	10.1	10.2	42.0	4.1	1.0
S_var_02_dl	232	16.0	17.1	64.4	3.8	0.93

Table A-16: S-Joint Stiffnesses (FEA)

Variation	Unfolded Length [μm]	Rotational Stiffnesses [μNμm/rad]		Translational Stiffnesses [μN/μm]	
		In-Plane K_{θ}	Out-of-Plane K_{ϕ}	In-Plane Axial K_x	In-Plane Normal K_y
S_std_03_sm (S 200)	432	520	370	0.15	23.3
S_std_04_sm (S 150)	332	680	490	0.33	28.9
S_std_01_sm (S 100)	232	970	710	1.04	37.9
S_std_05_sm (S 75)	182	1,240	910	2.26	43.9
S_std_02_sm (S 50)	132	1,710	1,270	6.51	54.9
S_var_01_sm	232	1,170	780	1.30	64.6
S_var_02_sm	232	3,350	1,690	3.13	71.9
S_std_03_dl (S 200)	432	910	1,020	0.26	41.1
S_std_04_dl (S 150)	332	1,190	1,340	0.58	50.6
S_std_01_dl (S 100)	232	1,700	1,960	1.81	66.3
S_std_05_dl (S 75)	182	2,170	2,560	3.95	78.5
S_std_02_dl (S 50)	132	2,990	3,660	11.4	96.1
S_var_01_dl	232	2,040	2,150	2.28	106
S_var_02_dl	232	5,870	6,130	5.49	126

A.6.3 Derived Equations

$$K_{\theta} = 900 \frac{\mu\text{N}\mu\text{m}}{\text{rad}} \cdot \left(\frac{250\mu\text{m}}{L}\right)^{1.00} \quad (\text{A-7})$$

$$K_x = 0.83 \frac{\mu\text{N}}{\mu\text{m}} \cdot \left(\frac{250\mu\text{m}}{L}\right)^{3.19} \quad (\text{A-8})$$

$$K_y = 35 \frac{\mu\text{N}}{\mu\text{m}} \cdot \left(\frac{250\mu\text{m}}{L}\right)^{0.72} \quad (\text{A-9})$$

$$K_{\phi} = 650 \frac{\mu\text{N}\mu\text{m}}{\text{rad}} \cdot \left(\frac{250\mu\text{m}}{L}\right)^{1.03} \quad (\text{A-10})$$

$$\frac{K_x}{K_{\theta}} \propto \frac{1}{L^{2.19}}; \quad \frac{K_y}{K_{\theta}} \propto L^{0.28} \quad \frac{K_{\phi}}{K_{\theta}} \propto \frac{1}{L^{0.03}} \quad (\text{A-11})$$

A.7 U-Joints

A.7.1 Layout Schematics

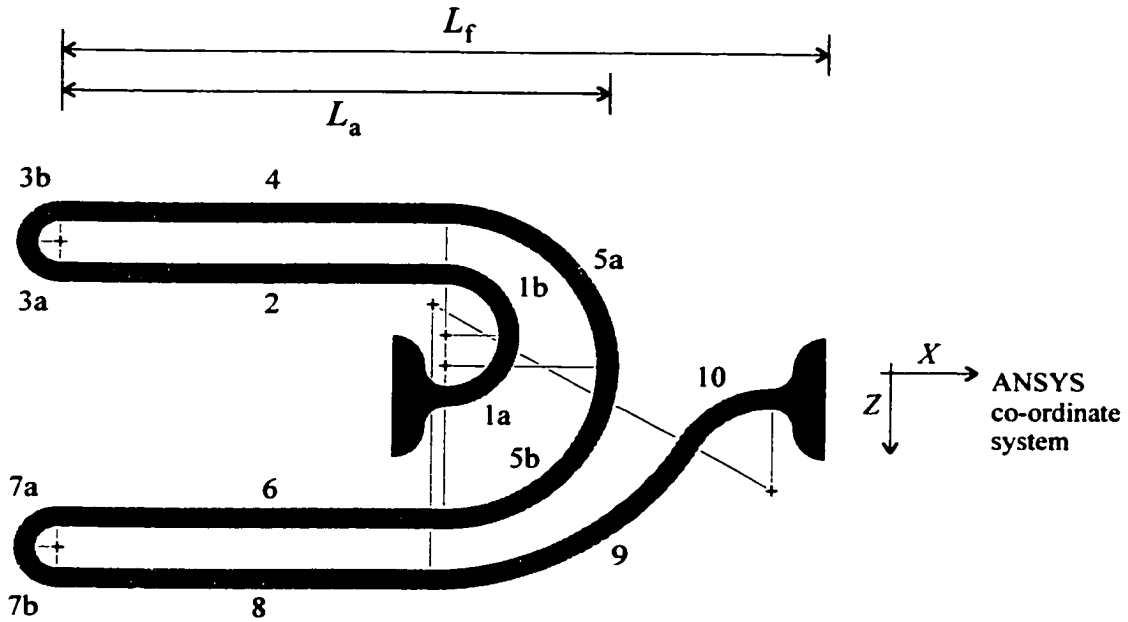


Figure A-5: Geometric Layout of an U-Joint

Table A-17: U-Joint Variations

Variation	Folded Length [μm]			Unfolded Length [μm]	Segments 2 μm wide	Segments 4 μm wide
	L_f	L_a	L_b			
U_std_01	65	50		261	1-10	
U_std_02	115	100		461	1-10	
U_std_03	40	25		161	1-10	
U_std_04	90	75		361	1-10	
U_std_05	52.5	37.5		211	1-10	
U_var_01	65	50		261	2, 4, 6, 8	1, 3, 5, 7, 9, 10

Table A-18: Joint Segments of an U-Joint

Joint Segment	Point (X, Z) [μm]			Angle		Radius [μm]
	Start	End	Centre	Start	End	
1a	-15, 0	-9, -6	-15, -6	-90°	0°	6
1b	-9, -6	-15, -12	-15, -6	0°	90°	6
2	-15, -12	$-L_a$, -12				
3a	$-L_a$, -12	$-L_a-3$, -15	$-L_a$, -15	-90°	-180°	3
3b	$-L_a-3$, -15	$-L_a$, -18	$-L_a$, -15	180°	90°	3
4	$-L_a$, -18	-15, -18				
5a	-15, -18	0, -3	-15, -3	90°	0°	15
5b	0, -3	-15, -12	-15, -3	0°	-90°	15
6	-15, 12	$-L_a$, 12				
7a	$-L_a$, 12	$-L_a-3$, 15	$-L_a$, 15	90°	180°	3
7b	$-L_a-3$, 15	$-L_a$, 18	$-L_a$, 15	0°	-90°	3
8	$-L_a$, 18	-16.18, 18				
9	-16.18, 18	7.21, 4.5	-16.18, -9	-90°	-30°	27
10	7.21, 4.5	15, 0	15, 9	150°	90°	9

A.7.2 FEA Results**Table A-19: U-Joint-Mass Resonance Frequencies (FEA)**

Variation	Unfolded Length [μm]	Resonance Frequency [kHz]			Frequency Ratios	
		Out-of-Plane Rotational	In-Plane Rotational	In-Plane Axial	$\frac{\text{Axial}}{\text{In-Plane}}$	$\frac{\text{Out-of-Plane}}{\text{In-Plane}}$
U_std_02_sm (U 115)	461	4.39	4.49	47.6	11	0.98
U_std_04_sm (U 90)	361	5.33	5.50	56.5	10	0.97
U_std_01_sm (U 65)	261	6.74	7.04	70.1	10	0.96
U_std_05_sm (U 53)	211	7.74	8.18	81.0	9.9	0.95
U_std_03_sm (U 40)	161	9.08	9.79	98.5	10	0.93
U_var_01_sm	261	7.72	8.59	81.2	9.45	0.90
U_std_02_dl (U 115)	461	7.64	4.79	52.6	11	1.6
U_std_04_dl (U 90)	361	9.05	5.84	62.8	11	1.5
U_std_01_dl (U 65)	261	11.0	7.45	78.3	11	1.5
U_std_05_dl (U 53)	211	12.2	8.64	90.7	10	1.4
U_std_03_dl (U 40)	161	13.7	10.3	111	11	1.3
U_var_01_dl	261	13.3	9.11	90.2	9.91	1.5

Table A-20: U-Joint Stiffnesses (FEA)

Variation	Unfolded Length [μm]	Rotational Stiffnesses [μN μm/rad]		Translational Stiffnesses [μN/μm]	
		In-Plane K_{θ}	Out-of-Plane K_{ϕ}	In-Plane Axial K_x	In-Plane Normal K_y
U_std_02_sm (U 115)	461	490	470	2.35	0.469
U_std_04_sm (U 90)	361	620	590	3.11	0.982
U_std_01_sm (U 65)	261	860	790	4.59	2.70
U_std_05_sm (U 53)	211	1,070	960	6.03	5.25
U_std_03_sm (U 40)	161	1,400	1,220	8.78	12.2
U_var_01_sm	261	1,420	1,130	6.39	8.35
U_std_02_dl (U 115)	461	855	2,150	4.11	0.810
U_std_04_dl (U 90)	361	1,090	2,620	5.44	1.71
U_std_01_dl (U 65)	261	1,510	3,350	8.03	4.70
U_std_05_dl (U 53)	211	1,870	3,890	10.6	9.17
U_std_03_dl (U 40)	161	2,440	4,640	15.4	21.3
U_var_01_dl	261	2,490	5,660	11.2	14.5

A.7.3 Derived Equations

$$COR_U = -0.488L_f + 8.87 = -0.488L_a + 1.55 \quad (\text{A-12})$$

$$K_{\theta} = 900 \frac{\mu\text{N}\mu\text{m}}{\text{rad}} \cdot \left(\frac{250\mu\text{m}}{L}\right)^{1.00} \quad (\text{A-13})$$

$$K_x = 5.0 \frac{\mu\text{N}}{\mu\text{m}} \cdot \left(\frac{250\mu\text{m}}{L}\right)^{1.25} \quad (\text{A-14})$$

$$K_y = 3.1 \frac{\mu\text{N}}{\mu\text{m}} \cdot \left(\frac{250\mu\text{m}}{L}\right)^{3.09} \quad (\text{A-15})$$

$$K_{\phi} = 820 \frac{\mu\text{N}\mu\text{m}}{\text{rad}} \cdot \left(\frac{250\mu\text{m}}{L}\right)^{0.92} \quad (\text{A-16})$$

$$\frac{K_x}{K_{\theta}} \propto \frac{1}{L^{0.25}}; \quad \frac{K_y}{K_{\theta}} \propto \frac{1}{L^{2.09}} \quad \frac{K_{\phi}}{K_{\theta}} \propto L^{0.08} \quad (\text{A-17})$$

A.8 V-Joints

A.8.1 Layout Schematics

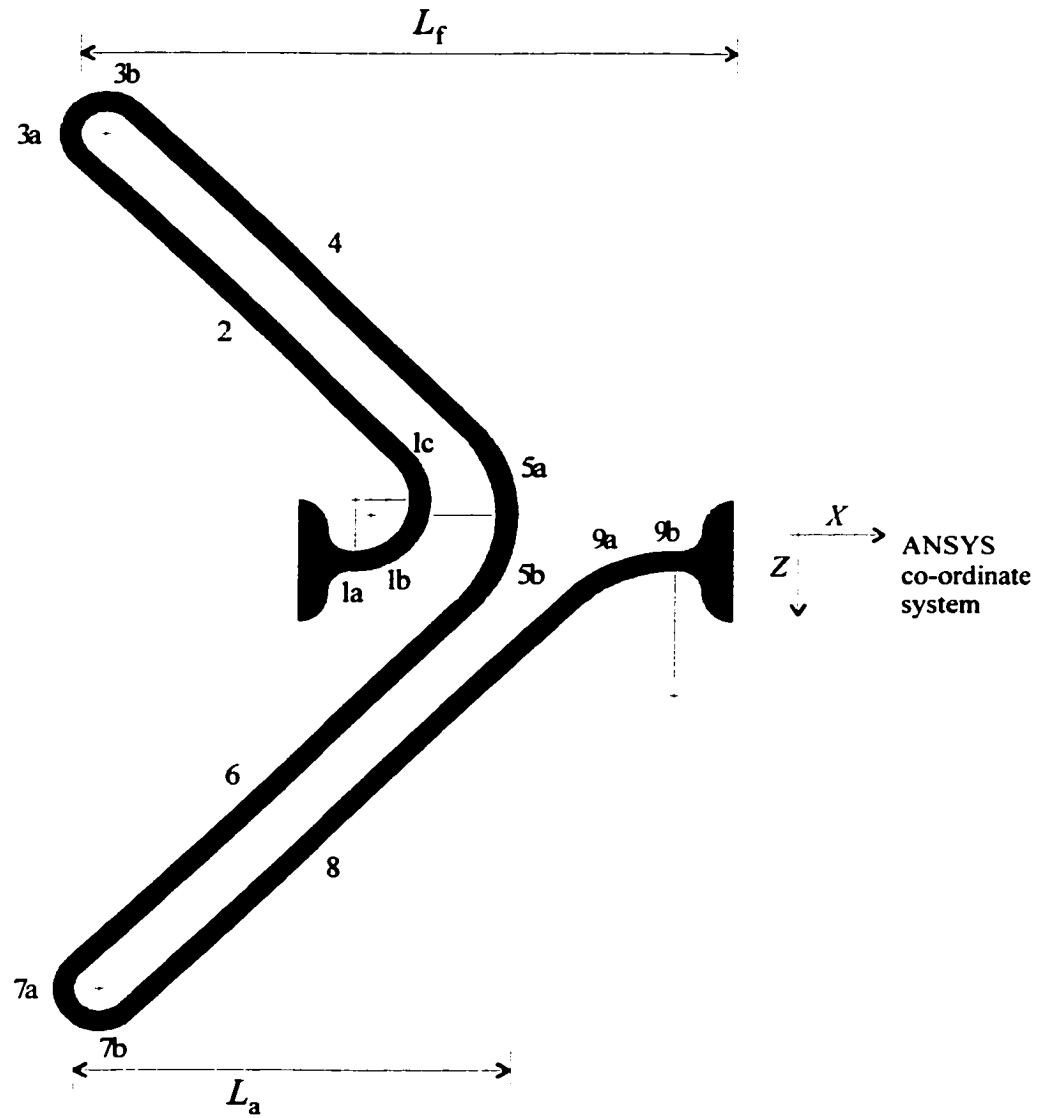


Figure A-6: Geometric Layout of an V-Joint

Table A-21: V-Joint Variations

Variation	Folded Length [μm]			Unfolded Length [μm]	Segments 2 μm wide	Segments 4 μm wide
	L_f	L_a	L_b			
V_std_01	54.75	39.75		258	1-9	
V_std_02	90	75		457	1-9	
V_std_03	37.25	22.25		159	1-9	
V_std_04	72.5	57.5		371	1-9	
V_std_05	45.75	30.75		221	1-9	
V_var_01	54.75	39.75		258	2, 4, 6, 8	1, 3, 5, 7, 9

Table A-22: Joint Segments of an V-Joint

Joint Segment	Point (X, Z) [μm]			Angle		Radius [μm]
	Start	End	Centre	Start	End	
1a	-15, 0	-14.5, 0				
1b	-14.5, 0	-9.5, -6	-14.5, -6	-90°	0°	6
1c	-9.5, -6	-10.25, -10.25	-14.5, -6	0°	45°	6
2	-10.25, -10.25	$-L_a, -L_a$				
3a	$-L_a, -L_a$	$-L_a, -L_a-4.5$	$-L_a+2.25, -L_a-2.25$	225°	135°	3.18
3b	$-L_a, -L_a-4.5$	$-L_a+4.5, -L_a-4.5$	$-L_a+2.25, -L_a-2.25$	135°	45°	3.18
4	$-L_a+4.5, -L_a-4.5$	-4.25, -13.25				
5a	-4.25, -13.25	-0.63, -4.5	-13, -4.5	45°	0°	12.37
5b	-0.63, -4.5	-4.25, 4.25	-13, -4.5	0°	-45°	12.37
6	-4.25, 4.25	$-L_a, L_a$				
7a	$-L_a, L_a$	$-L_a, L_a+4.5$	$-L_a+2.25, L_a+2.25$	135°	225°	3.18
7b	$-L_a, L_a+4.5$	$-L_a+4.5, L_a+4.5$	$-L_a+2.25, L_a+2.25$	225°	315°	3.18
8	$-L_a+4.5, L_a+4.5$	5.11, 3.89				
9a	-5.11, 3.89	14.5, 0	14.5, 13.28	135	90	13.28
9b	14.5, 0	15, 0				

A.8.2 FEA Results**Table A-23: V-Joint-Mass Resonance Frequencies (FEA)**

Variation	Unfolded Length [μm]	Resonance Frequency [kHz]			Frequency Ratios	
		Out-of-Plane Rotational	In-Plane Rotational	In-Plane Axial	Axial In-Plane	Out-of-Plane In-Plane
V_std_02_sm (V 90)	457	4.41	4.85	15.4	3.2	0.91
V_std_04_sm (V 73)	358	5.31	5.83	22.4	3.8	0.91
V_std_01_sm (V 55)	258	6.66	7.33	37.0	5.1	0.91
V_std_05_sm (V 46)	207	7.65	8.46	51.7	6.1	0.90
V_std_03_sm (V 37)	159	8.95	9.96	77.3	7.8	0.90
V_var_01_sm	258	7.23	8.23	40.9	5.0	0.88
V_std_02_dl (V 90)	457	6.96	5.16	17.1	3.3	1.3
V_std_04_dl (V 73)	358	8.16	6.18	25.0	4.0	1.3
V_std_01_dl (V 55)	258	9.93	7.74	41.4	5.4	1.3
V_std_05_dl (V 46)	207	11.2	8.91	57.9	6.5	1.3
V_std_03_dl (V 37)	159	12.8	10.5	86.7	8.3	1.2
V_var_01_dl	258	11.0	8.69	45.7	5.3	1.3

Table A-24: V-Joint Stiffnesses (FEA)

Variation	Unfolded Length [μm]	Rotational Stiffnesses [μNμm/rad]		Translational Stiffnesses [μN/μm]	
		In-Plane K_{θ}	Out-of-Plane K_{ϕ}	In-Plane Axial K_x	In-Plane Normal K_y
V_std_02_sm (V 90)	457	493	405	0.23	1.02
V_std_04_sm (V 73)	358	629	517	0.47	1.93
V_std_01_sm (V 55)	258	874	717	1.26	4.94
V_std_05_sm (V 46)	207	1,090	892	2.44	9.10
V_std_03_sm (V 37)	159	1,419	1,160	5.40	18.2
V_var_01_sm	258	1,121	853	1.56	9.15
V_std_02_dl (V 90)	457	862	1,360	0.40	1.63
V_std_04_dl (V 73)	358	1,100	1,730	0.82	3.31
V_std_01_dl (V 55)	258	1,530	2,400	2.21	8.53
V_std_05_dl (V 46)	207	1,910	2,970	4.27	15.8
V_std_03_dl (V 37)	159	2,480	3,850	9.45	31.6
V_var_01_dl	258	1,960	2,950	2.73	15.7

A.8.3 Derived Equations

$$\text{COR}_V = -0.498L_f + 8.90 = -0.498L_a + 1.43 \quad (\text{A-18})$$

$$K_{\theta} = 900 \frac{\mu\text{N}\mu\text{m}}{\text{rad}} \cdot \left(\frac{250\mu\text{m}}{L}\right)^{1.00} = \frac{EI}{L} \quad (\text{A-19})$$

$$K_x = 1.4 \frac{\mu\text{N}}{\mu\text{m}} \cdot \left(\frac{250\mu\text{m}}{L}\right)^{2.99} \quad (\text{A-20})$$

$$K_y = 5.3 \frac{\mu\text{N}}{\mu\text{m}} \cdot \left(\frac{250\mu\text{m}}{L}\right)^{2.75} \quad (\text{A-21})$$

$$K_{\phi} = 740 \frac{\mu\text{N}\mu\text{m}}{\text{rad}} \cdot \left(\frac{250\mu\text{m}}{L}\right)^{1.00} \quad (\text{A-22})$$

$$\frac{K_x}{K_{\theta}} \propto \frac{1}{L^{1.99}}; \quad \frac{K_y}{K_{\theta}} \propto \frac{1}{L^{1.75}} \quad \frac{K_{\phi}}{K_{\theta}} \propto 1 \quad (\text{A-23})$$

A.9 X-Joints

A.9.1 Layout Schematics

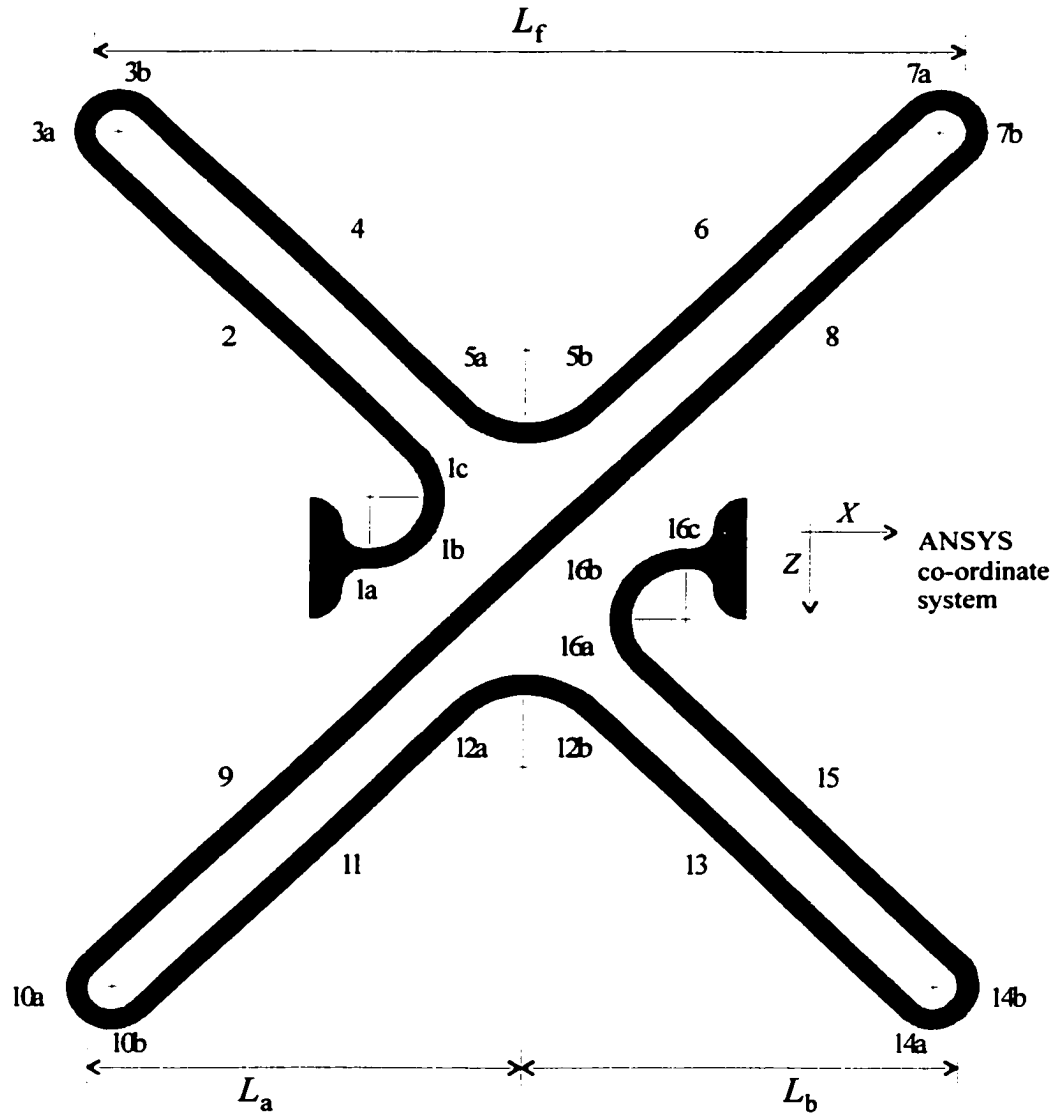


Figure A-7: Geometric Layout of an X-Joint

Table A-25: X-Joint Variations

Variation	Folded Length [μm]			Unfolded Length [μm]	Segments 2 μm wide	Segments 4 μm wide
	L_f	L_a	L_b			
X_std_01	79.5	39.75	39.75	458	1-16	
X_std_02	44.5	22.25	22.25	260	1-16	
X_std_03	26.5	13.25	13.25	158	1-16	
X_std_04	62	31	31	359	1-16	
X_std_05	37.5	17.75	17.75	209	1-16	
X_var_01	79.5	39.75	39.75	458	1-3, 7-10, 14-16	4-6, 11-13
X_var_02	79.5	39.75	39.75	458	1-7, 10-16	8-9
X_var_03	79.5	39.75	39.75	458	1, 3, 5, 7, 10, 12, 14, 16	2, 4, 6, 8, 9, 11, 13, 15
X_var_04	79.5	39.75	39.75	458	1-5, 10-13	5-8, 12-16
X_var_05	62	39.75	22.25	359	1-16	

Table A-26: Joint Segments of an X-Joint

Joint Segment	Point (X, Z) [μm]			Angle		Radius [μm]
	Start	End	Centre	Start	End	
1a	-15, 0	-14.5, 0				
1b	-14.5, 0	-9.5, -6	-14.5, -6	-90°	0°	6
1c	-9.5, -6	-10.25, -10.25	-14.5, -6	0°	45°	6
2	-10.25, -10.25	$-L_a, -L_a$				
3a	$-L_a, -L_a$	$-L_a, -L_a-4.5$	$-L_a+2.25, -L_a-2.25$	225°	135°	3.18
3b	$-L_a, -L_a-4.5$	$-L_a+4.5, -L_a-4.5$	$-L_a+2.25, -L_a-2.25$	135°	45°	3.18
4	$-L_a+4.5, -L_a-4.5$	-5.75, -14.75				
5a	-5.75, -14.75	0, -12.37	0, -20.5	225°	270°	8.13
5b	0, -12.37	5.75, -14.75	0, -20.5	270°	315°	8.13
6	5.75, -14.75	$L_b-4.5, -L_b-4.5$				
7a	$L_b-4.5, -L_b-4.5$	$L_b, -L_b-4.5$	$L_b+2.25, -L_b-2.25$	135°	45°	3.18
7b	$L_b, -L_b-4.5$	$L_b, -L_b$	$L_b+2.25, -L_b-2.25$	45°	-45°	3.18
8	$L_b, -L_b$	0, 0				
9	0, 0	$-L_a, L_a$				
10a	$-L_a, L_a$	$-L_a, L_a+4.5$	$-L_a+2.25, L_a+2.25$	135°	225°	3.18
10b	$-L_a, L_a+4.5$	$-L_a+4.5, L_a+4.5$	$-L_a+2.25, L_a+2.25$	225°	315°	3.18
11	$-L_a+4.5, L_a+4.5$	-5.75, 14.75				
12a	-5.75, 14.75	0, 12.37	0, 20.5	135°	90°	8.13
12b	0, 12.37	5.75, 14.75	0, 20.5	90°	45°	8.13
13	5.75, 14.75	$L_b-4.5, L_b+4.5$				
14a	$L_b-4.5, L_b+4.5$	$L_b, L_b+4.5$	$L_b+2.25, L_b+2.25$	225°	315°	3.18
14b	$L_b, L_b+4.5$	L_b, L_b	$L_b+2.25, L_b+2.25$	-45°	45°	3.18
15	L_b, L_b	10.25, 10.25				
16a	10.25, 10.25	9.5, 6	14.5, 6	225	180	6
16b	9.5, 6	14.5, 0	14.5, 6	180	90	6
16c	14.5, 0	15, 0				

A.9.2 FEA Results

Table A-27: X-Joint-Mass Resonance Frequencies (FEA)

Variation	Unfolded Length [μm]	Resonance Frequency [kHz]			Frequency Ratios	
		Out-of-Plane Rotational	In-Plane Rotational	In-Plane Axial	Axial In-Plane	Out-of-Plane In-Plane
X_std_01_sm (X 80)	458	5.54	6.20	25.6	4.1	0.89
X_std_04_sm (X 62)	359	6.33	7.06	35.7	5.1	0.90
X_std_02_sm (X 45)	260	7.50	8.35	54.4	6.5	0.90
X_std_05_sm (X 38)	209	8.38	9.33	71.6	7.7	0.90
X_std_03_sm (X 27)	158	9.64	10.7	100	9.3	0.90
X_var_01_sm	458	6.37	7.77	32.3	4.2	0.82
X_var_02_sm	458	6.00	6.99	27.5	3.9	0.86
X_var_03_sm	458	7.63	11.1	43.5	3.9	0.69
X_var_04_sm	458	6.37	7.48	33.0	4.4	0.85
X_var_05_sm	359	5.99	6.61	32.9	5.0	0.91
X_std_01_lm (X 80)	458	4.10	4.58	20.9	4.6	0.90
X_std_02_lm (X 45)	260	5.53	6.15	44.1	7.2	0.90
X_std_03_lm (X 27)	158	7.11	7.91	75.1	9.5	0.90
X_std_01_dl (X 80)	458	8.09	6.51	28.5	4.4	1.2
X_std_04_dl (X 62)	359	9.17	7.41	39.8	5.4	1.2
X_std_02_dl (X 45)	260	10.8	8.75	60.9	7.0	1.2
X_std_05_dl (X 38)	209	12.0	9.78	80.1	8.2	1.2
X_std_03_dl (X 27)	158	13.7	11.3	112	10	1.2
X_var_01_dl	458	9.45	8.15	35.8	4.4	1.2
X_var_02_dl	458	8.84	7.33	30.5	4.2	1.2
X_var_03_dl	458	11.8	11.7	48.0	4.1	1.0
X_var_04_dl	458	9.67	7.89	36.4	4.6	1.2
X_var_05_dl	359	8.88	6.96	36.7	5.3	1.3

Table A-28: X-Joint Stiffnesses (FEA)

Variation	Unfolded Length [μm]	Rotational Stiffnesses [$\mu\text{N}\mu\text{m}/\text{rad}$]		Translational Stiffnesses [$\mu\text{N}/\mu\text{m}$]	
		In-Plane K_{θ}	Out-of-Plane K_{ϕ}	In-Plane Axial K_x	In-Plane Normal K_y
X_std_01_sm (X 80)	458	492	408	0.63	0.853
X_std_04_sm (X 62)	359	628	521	1.20	1.73
X_std_02_sm (X 45)	260	868	721	2.74	4.32
X_std_05_sm (X 38)	209	1,080	899	4.68	7.79
X_std_03_sm (X 27)	158	1,430	1,190	9.08	15.9
X_var_01_sm	458	779	545	1.05	1.18
X_var_02_sm	458	627	481	0.74	1.06
X_var_03_sm	458	1,610	798	1.95	2.52
X_var_04_sm	458	914	599	1.14	2.92
X_var_05_sm	359	629	521	1.03	1.74
X_std_01_lm (X 80)	458	492	408	0.63	0.853
X_std_02_lm (X 45)	260	868	721	2.74	4.32
X_std_03_lm (X 27)	158	1,430	1,190	9.08	15.86
X_std_01_dl (X 80)	458	862	1,390	1.11	1.49
X_std_04_dl (X 62)	359	1,100	1,770	2.11	3.03
X_std_02_dl (X 45)	260	1,520	2,470	4.80	7.55
X_std_05_dl (X 38)	209	1,890	3,080	8.19	13.7
X_std_03_dl (X 27)	158	2,500	4,110	15.9	27.8
X_var_01_dl	458	1,360	1,940	1.84	2.06
X_var_02_dl	458	1,100	1,680	1.30	1.86
X_var_03_dl	458	2,810	3,210	3.42	4.41
X_var_04_dl	458	1,600	2,180	1.99	5.10
X_var_05_dl	359	1,100	1,770	1.80	3.04

A.9.3 Derived Equations

$$K_{\theta} = 900 \frac{\mu\text{N}\mu\text{m}}{\text{rad}} \cdot \left(\frac{250\mu\text{m}}{L} \right)^{1.00} \quad (\text{A-24})$$

$$K_x = 2.9 \frac{\mu\text{N}}{\mu\text{m}} \cdot \left(\frac{250\mu\text{m}}{L} \right)^{2.50} \quad (\text{A-25})$$

$$K_y = 4.6 \frac{\mu\text{N}}{\mu\text{m}} \cdot \left(\frac{250\mu\text{m}}{L} \right)^{2.75} \quad (\text{A-26})$$

$$K_{\phi} = 750 \frac{\mu\text{N}\mu\text{m}}{\text{rad}} \cdot \left(\frac{250\mu\text{m}}{L} \right)^{1.01} \quad (\text{A-27})$$

$$\frac{K_x}{K_{\theta}} \propto \frac{1}{L^{1.50}}; \quad \frac{K_y}{K_{\theta}} \propto \frac{1}{L^{1.75}} \quad \frac{K_{\phi}}{K_{\theta}} \propto \frac{1}{L^{0.01}} \quad (\text{A-28})$$

A.10 PC-Joints

A.10.1 Layout Schematics

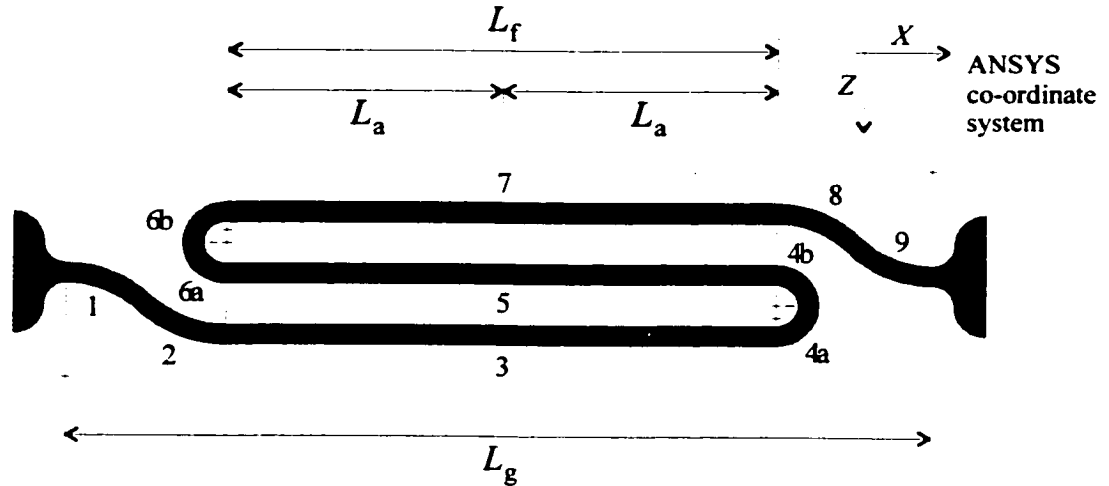


Figure A-8: Geometric Layout of a PC-Joint

Table A-29: PC-Joint Variations

Variation	Folded Length [μm]			Unfolded Length [μm]	Gap Width [μm]	Segments 2 μm wide	Segments 4 μm wide
	L_f	L_a	L_b				
PC_std_01_sm	25	12.5		126	54	1-9	
PC_std_02_sm	50	25.5		201	79	1-9	
PC_std_03_sm	75	37.5		276	104	1-9	
PC_std_04_sm	100	50		351	129	1-9	
PC_std_05_sm	125	62.5		426	154	1-9	
PC_std_06_sm	1	0.5		54	30	1-9	

Table A-30: Joint Segments of an PC-Joint

Joint Segment	Point (X, Z) [μm]			Angle		Radius [μm]
	Start	End	Centre	Start	End	
1	$-L_a-14.5, 0$	$-L_a-7.25, 3$	$-L_a-14.5, 10.25$	90°	45°	10.25
2	$-L_a-7.25, 3$	$-L_a, 6$	$-L_a, -4.25$	225°	270°	10.25
3	$-L_a, 6$	$L_a, 6$				
4a	$L_a, 6$	$L_a+3, 3$	$L_a, 3$	270°	0°	3
4b	$L_a+3, 3$	$L_a, 0$	$L_a, 3$	0°	90°	3
5	$L_a, 0$	$-L_a, 0$				
6a	$-L_a, 0$	$-L_a-3, -3$	$-L_a, -3$	270°	180°	3
6b	$-L_a-3, -3$	$-L_a, -6$	$-L_a, -3$	180°	90°	3
7	$-L_a, -6$	$L_a, -6$				
8	$L_a, -6$	$L_a+7.25, -3$	$L_a, 4.25$	90°	45°	10.25
9	$L_a+7.25, -3$	$L_a+14.5, 0$	$L_a+14.5, -10.25$	225°	270°	10.25

A.10.2 FEA Results**Table A-31: PC-Joint Stiffnesses (FEA)**

Variation	Unfolded Length [μm]	Rotational Stiffnesses [$\mu\text{N}\mu\text{m}/\text{rad}$]		Translational Stiffnesses [$\mu\text{N}/\mu\text{m}$]	
		In-Plane K_θ	Out-of-Plane K_ϕ	In-Plane Axial K_x	In-Plane Normal K_y
PC_std_05_sm (PC 125)	426	529	521	22.0	0.0393
PC_std_04_sm (PC 100)	351	642	630	28.2	0.0620
PC_std_03_sm (PC 75)	276	816	797	36.4	0.111
PC_std_02_sm (PC 50)	201	1120	1090	51.6	0.244
PC_std_01_sm (PC 25)	126	1790	1700	88.5	0.841
PC_std_06_sm (PC 1)	54	4170	3720	283	38.8

A.10.3 Derived Equations

$$K_{\theta} = 900 \frac{\mu\text{N}\mu\text{m}}{\text{rad}} \cdot \left(\frac{250\mu\text{m}}{L} \right)^{1.00} \quad (\text{A-29})$$

$$K_x = 41 \frac{\mu\text{N}}{\mu\text{m}} \cdot \left(\frac{250\mu\text{m}}{L} \right)^{1.13} \quad (\text{A-30})$$

$$K_y = 0.16 \frac{\mu\text{N}}{\mu\text{m}} \cdot \left(\frac{250\mu\text{m}}{L} \right)^{3.18} \quad (\text{A-31})$$

$$K_{\phi} = 876 \frac{\mu\text{N}\mu\text{m}}{\text{rad}} \cdot \left(\frac{250\mu\text{m}}{L} \right)^{0.97} \quad (\text{A-32})$$

$$\frac{K_x}{K_{\theta}} \propto \frac{1}{L^{1.50}}; \quad \frac{K_y}{K_{\theta}} \propto \frac{1}{L^{2.18}} \quad \frac{K_{\phi}}{K_{\theta}} \propto L^{0.03} \quad (\text{A-33})$$

$$L_g = (L - 51 \mu\text{m}) / 3 + 29 \mu\text{m} = L_f + 29 \mu\text{m} \quad (\text{A-34})$$

B ANSYS Macros

Due to the large number of joint variations examined in this thesis most FE simulations were carried out in batch mode using ANSYS macros. This appendix gives a brief introduction in the preparation of an ANSYS macro.

The easiest way to create a simple ANSYS macro is to carry out the analysis in the interactive mode and use the log-file of the interactive session as a starting point for the creation of a macro. All commands executed during the interactive session using menus and dialogue boxes are recorded in their command language version in the log-file. To create a parameterised macro the respective fixed values have to be substituted by variables in the macro. After erasing all unnecessary code (e.g. from errors made in the interactive session, recorded in the log-file) the macro can be save as a ANSYS macro file by giving it the extension `.mac`.

B.1 Interactive Session

As an example the following steps will create a cantilever beam and calculate its first three resonant modes.

- Start an ANSYS interactive session
 - Enter the *Working Directory* where all files of your model will be stored, e.g. `C:\temp\beam`.
 - Enter the *Initial Jobname*. This is the base-name for all the files related to your model, e.g. `beam1`.
 - For standard models all other settings in this dialogue can be kept at their default entries.
- Enter the preprocessor by selecting Preprocessor from *ANSYS Main Menu*
 - Choose an element type:
Element Type > Add/Edit/Delete... > Add...
 - + Choose element type Structural Beam > 3D elastic 4
 - + Close the dialogue box
 - Specify real constants:
Real Constants > Add/Edit/Delete... > Add...
 - + Choose element type: Type 1 BEAM4
 - + Enter beam properties: area, cross-sectional moment of inertia, etc.

- + Only enter the properties necessary for the type of analysis intended.
- Specify material properties:
 - Material Props > Constant - Isotropic ...
 - + Specify *Material number: 1*
 - + Enter material properties: Young's modulus, Poisson's ratio, etc.
 - + Only enter the properties necessary for the type of analysis intended.
- Create keypoints:
 - Modeling - Create > Keypoints > In Active CS ...
 - + Enter *Keypoint number*
 - + Enter keypoint co-ordinates
 - + Repeat for second keypoint
- Create a straight line:
 - Modeling - Create > Lines - Lines > Straight Line
 - + Pick keypoints 1 and 2 and click *OK*
- Define line attributes:
 - Attributes - Define > All Lines ...
 - + Choose *Material number, Real constant set number, and Element type number*
 - + In this case choose 1 for all.
- Select number of elements:
 - Meshing - Size Cntrl > ManualSize - Lines - All Lines ...
 - + Set *No. of element divisions to 10*
- Mesh the line:
 - Meshing - Mesh > Lines
 - + Pick line 1 and click *OK*
- Switch on element shape display
 - PlotCtrls > Style > Edge Options ...
 - + Set *Display of element to On*
 - + Set *Real constant multiplier to 1*
- Enter the solver by selecting Solution from *ANSYS Main Menu*
 - Specify Constraints:
 - Loads - Apply > Structural - Displacement > On Key-points
 - + Pick keypoint at left end of beam and click *OK*
 - + Select DOFs to be constraint > All DOF
 - + Set *Displacement value to 0*

- **Select Analysis Type:**
Analysis Type - New Analysis...
 - + *Set Type of analysis to Modal*
- **Set analysis options:**
Analysis Options..
 - + *Set Mode extraction method to Subspace*
 - + *Set No. of modes to extract to 3*
 - + *Set Expand mode shapes to Yes*
 - + *Set No. of modes to expand to 3*
 - + *Set Calculate elem results? to Yes*
 - + *Select OK*
 - + *Leave all entries at default values on Subspace Modal Analysis dialogue and select OK*
- **Start the solver:**
Solve - Current LS
 - + *Check Solution Options in pop-up window and close window*
 - + *Select OK to start solution*
- **Enter the postprocessor by selecting General Postproc from ANSYS Main Menu**
 - **Check results:**
Results Summary...
 - + *The first three resonance frequencies are displayed.*
 - **Display mode shapes:**
 - + **Read results:**
Read Results - Next Set
 - + **Plot mode shape:**
Plot Results > Deformed Shape ... > Def shape only
 - + *Repeat for other modes*
- **Exit the Program by selecting Exit ... from File**
 - **Save geometry and loads:**
Save Geom+Loads

B.2 Creating an ANSYS Macro

Using the log-file of the interactive session from the previous section a simple macro can be created.

- Open the log-file, e.g. beam1.log, with a text editor
 - Check commands:
Help on all commands can be found in the *ANSYS Command Manual* in the on-line help
 - Erase unnecessary commands, e.g. commands specifying defaults or mistakes that were entered during the interactive session.
 - Check the commands that involved picking entities during the interactive session.
 - + Replace all P51X entries in the commands with the respective entity numbers:
ANSYS uses P51X as an identifier for picked entities.
 - Add comments:
All lines starting with ! are treated as comments
- Save the macro as an ANSYS macro file, e.g. beam1.mac.

B.3 Using an ANSYS Macro

If the macro file is in the job directory it can be executed like a regular command by just entering beam1 in the command line of ANSYS.

Macros have to be used to do ANSYS analyses in batch mode. In batch mode the model is created and the solution is calculated without any graphical output. This greatly decreases calculation times and makes the successive calculation of a large number of models without supervision possible.

C L-Edit Macros for Joint Creation

The layouts of the joints examined in this thesis were created using a macro module containing five L-Edit macros. The module can be found in the MEMS Pro Workdir under MUMPS\Joints and is called `joints.c`. Once loaded into L-Edit, the macros can be started by pressing *F12* to create an X-joint, *F11* for an H-joint, *F10* for an S-joint, *F9* for a V-joint, and *F8* for a U-joint.

Each macro starts a number of dialogue boxes to enter the properties of the respective joint. Input properties are the location of the joint centre, the folded length, the widths of the joint sections described in Appendix A, as well as the cell name for the created joint and the lithography level it will be created on.

The joints are created from wires with 100 vertices and rounded ends. The division into 100 vertex pieces was necessary to make file export to GDSII files possible. The GDSII file format only supports elements with up to 200 vertices.

D Experimental Procedures

The following sections present step-by-step descriptions of the experimental procedures used in this thesis.

D.1 Aerodynamic Excitation

The following is a step-by-step description of the aerodynamic excitation. Background and motivation for this method can be found in Chapter 7.2.2.

- Make sure that the structure is not stuck to the ground by poking it with the probe needle. Normally axial compression releases the structure, but sometimes the folded joint arms have to be released as well.
- Connect the photo-detector to the oscilloscope.
- Use the following settings on the oscilloscope:
 - Input: AC coupling
 - Trigger: Rising edge, AutoLvl mode
 - Run control: Run
- Load a probe manipulator with a hypodermic needle:
 - Use a 26G 1/2 hypodermic needle
- Connect the on-table air supply to the hypodermic needle:
 - Connect the needle valve to the on-table air supply hose.
 - Connect the needle valve and the hypodermic needle using a thin plastic hose. The hose has to be dry!
- Test the air flow:
 - Make sure the on-table air supply valve is closed.
 - Open the valve that lets compressed air flow into the backup air tank and the on-table air supply.
 - Open the on-table air supply valve.
 - Adjust the air flow using the needle valve and the on-table air flow regulator.
 - Close the on-table air supply valve.
 - Close the needle valve.
- Excite joint into resonance:
 - Position the hypodermic needle so the air flow comes from the anchor side of the joint, originating in the area of the joint anchor.
 - Slowly open the on-table air supply valve.

- Slowly open the needle valve.
- Adjust the position of the hypodermic needle (x, y, z) to yield best excitation.
- Measure the resonance frequency:
 - Position the laser in the path of the resonating joint.
 - Adjust photo-detector to yield maximum signal.
 - Adjust ranges on oscilloscope to show a number of oscillations.
 - Be aware of frequency doubling.
 - Take a snapshot by pressing the *Stop* button on the oscilloscope.
 - Use the cursors of the oscilloscope to calculate the resonance frequency using a number of oscillations to get an average value.
- Print the oscilloscope screen.

D.2 The 'Flick'-Test

The following is a step-by-step description of the 'flick'-test. Background and motivation for this method can be found in Chapter 7.2.3.

- Make sure that the structure is not stuck to the ground by poking it with the probe needle. Normally axial compression releases the structure, but sometimes the folded joint arms have to be released as well.
- Connect the photo-detector to the oscilloscope and to the spectrum analyser.
- Use the following settings on the oscilloscope:
 - Input: DC coupling
 - Trigger: Falling edge, normal mode
 - Trigger level: Just under Poly 0 level
 - Run control: Single
- Use the following settings on the spectrum analyser:
 - Display setup
 - + Measure Group: FFT
 - + Measurement: FFT 1/2 (depending on input channel)
 - Trigger
 - + Trigger Mode: Auto Arm
 - + Trigger Level: Same as on Oscilloscope
 - + Trigger Slope: Falling
 - Frequency
 - + Span: 12.5kHz
 - + Acquisition Time: 16s
 - + FFT lines: 200
 - + Base freq: 100kHz
 - Average
 - + # of Averages: 5
 - + Display Avg: Peak Hold
- Use the probe to displace the end-mass and release it for at least five times.
- Print both screens

E MUMPs Chips Fabricated

Table E-1 lists the chips that were designed by members of the Dalhousie MEMS Lab and fabricated by Cronos with the generous support of the Canadian Microelectronics Corporation (CMC).

Table E-1: MUMPs Chips Designed by the Dalhousie MEMS Lab

Chip Code	Run Code	Submission Date	Designers
RTM	9901MU	March 1999	HF, TH
RT2	9902MU	September 1999	HF, TH
CJS	0001MU	March 2000	HF, MK, TH
CM1	0001MU	March 2000	JW, MK
MF1	0001MU	March 2000	TH, MK, RB
MT1	0001MU	March 2000	TH, MK
BC1	0002MU	July 2000	SB, JW, MJ, TH
CJ2	0002MU	July 2000	HF, TH
TA1	0002MU	July 2000	RH, MK, TH
CM2	0003MU	November 2000	RH, YL, VR, DY, TH, MK
YC2	0101MU	April 2001	YL, MK, TH
PS1	0101MU	April 2001	YL, MK, TH

Table E-2: Complete Chip Design Names

Chip Code	Chip Name	Chip Code	Chip Name
RTM	Ratcheting Torsional Motors	BC1	Bacteria Clamp 1
RT2	Ratcheting Torsional Motors 2	CJ2	Compliant Joints 2
CJS	Compliant Joint Systems	TA1	Thermal Actuators 1
CM1	Compliant Mechanisms 1	CM2	Compliant Mechanisms 2
MF1	Micro-Flyer 1	YC2	Yeast Clamp 2
MT1	Micro-Tools 1	PS1	Protein Sampler 1

Table E-3: Chip Designers

Initials	Name		Initials	Name
TH	Dr. Ted Hubbard		RB	Dr. Robert Bauer
MK	Dr. Marek Kujath		MJ	Dr. Manfred Jericho
JW	James Wylde		SB	Sarah Burke
HF	Heiko Fettig		JW	Jane Walters
RH	Ryan Hickey		VR	Vincent Roy
YL	Yongjun Lai		DY	Dong-Hiu Yang

F Finite Element Analysis of MEMS Devices

This chapter is the report of a directed study conducted during the winter term 1999 which lead to the acquiring of an ANSYS license in September 1999. Some of the facts are now outdated but the comparison of the different applications is still valid and the whole report is included at this point for reference.

F.1 Introduction

The DalTech MEMS Group is conducting on-going research into the design and evaluation of micro-electro-mechanical systems (MEMS). As the cost for manufacturing facilities are very high these MEMS chips are designed on site and manufactured off site. This keeps the manufacturing costs low but has the downside of a rather long turn around time.

With a time period of 12 to 16 weeks between the submission of a design and the reception of the fabricated chip along with a spacing of two or four months between fabrication runs (depending on the process) efficient work on a trial and error basis is very difficult. This is one of the reasons that prompted the decision of the MEMS Group to expand their area of interest to the simulation of MEMS devices.

After the successful development of an etch simulator for the prediction of etch shapes in bulk micromachining the new focus will be on performance simulation of surface micromachined devices.

Simulation of those devices during the design and the layout process will help preventing layout mistakes and increase the performance of the manufactured device. After the fabrication simulation can be used as a verification tool for both the manufactured device and the simulation itself.

As many of the common MEMS devices include coupled energy domains, e. g. electro-mechanical interaction within a combdrive, the simulation of those devices can become rather difficult. Chapter F.2 presents those difficulties along with a number of different approaches that can be taken.

Since the whole simulation area is new to the MEMS group new software will have to be acquired. Chapter F.3 introduces some of the most common commercially available analysis packages. Chapter F.3.1 deals with packages specifically designed to work with MEMS whereas Chapter F.3.2 gives an overview of two general simulation packages.

In addition to comments about the individual programs given in Chapter F.3 Chapter F.4 summarizes the presented programs and gives some advice about acquiring a suitable program.

F.2 Modelling MEMS

Finite Element Analysis (FEA) is one of today's most utilised numerical solution process in engineering. Originally developed for the solution of structural mechanics problems it is now used in a wide variety of fields including structural dynamics, fluid dynamics, thermodynamics and electrostatics. Basically every process that can be described by a differential equation can be solved with FEA.

The general idea behind FEA is to geometrically split up a complex structure into a number of simple shapes. A complex problem is split up into a number of simple problems. The partial solutions of these problems are then combine to form the general solution.

F.2.1 Coupled Energy Domains

Micro-electro-mechanical (MEM) devices tend to make the FE analysis more difficult as they usually combine two or more of the fields mentioned above. These coupled energy domains require a coupled analysis.

A classic case of coupled energy domains is the condenser microphone. A membrane is mounted above a backplate and a voltage is applied between them. Considering only a small deflection of the membrane this setup can be seen as a parallel plate capacitor. Its capacitance is directly proportional to the distance of the two plates. So a deflection of the membrane results in a change of capacitance. But the application of a voltage the system causes an electrostatic force between the plates which results in a deflection of the membrane. A clear coupling of the electro static and the structural energy domain. This results

in two coupled fourth order differential equations. These considerations do consider neither the coupling of the sound waves to the membrane nor its dynamical behaviour. This would only complicate the model much further.

This small example shows that a simple application can result in large problems that have to be overcome in order to do a simulation.

Almost every MEMS device contains coupled energy domains. For example the coupling in the case of the condenser microphone becomes stronger with smaller distances between backplate and membrane as well as smaller thicknesses of membrane and backplate. This is more likely to occur in a micro-device than in a macro-device.

Other examples are micro-pumps, involving a coupling of fluid dynamics with thermodynamics and structural mechanics, and combdrives, combining structural mechanics with structural dynamics and electro statics.

There are different approaches to solve this problem.

F.2.2 Approaches

There are basically three possible approaches to solving the problem of coupled energy domains:

1. Find the underlying differential equations and write a special program to solve them.
2. Use one of the hundreds of programs that other researchers have written for special problems.
3. Use commercially available simulation software.

F.2.3 Do It Yourself

This approach requires a lot of background and mathematical knowledge as well as a lot of man power. Nevertheless it might sometimes be the only possible way to do simulation at all, e. g. if the problem is so specific that none of the commercially available programs and none of the programs written by other researchers can do the simulation.

As an example, at the MESA Research Institute of the University of Twente in Enschede, The Netherlands researchers did simulations on subminiature condenser micro-

phones by setting up the differential equations, transferring them into a finite differences system and solving it with a self written C program. The results they obtained proved to have higher detail, than what could be achieved with analytical models. Due to the complexity and non-linearity of the model, however, they were not able to attain a general solution, meaning that the simulation has to be repeated if a parameter is changed. Nevertheless the method appeared easier and more flexible to them in comparison with finite element packages (i. e. ANSYS), since for these programs an external routine have to be developed to support the application of non-linear electrostatic forces. Therefore, they also believed that the model based on finite differences gave a better trade-off between precision and calculation time. [F9]

F.2.4 Specific Programs¹

Due to the wide variety of possible applications in the MEMS area and the specific problems arising therefrom many research groups have developed their own programs tailored to their specific needs. In most cases these simulation tools run on workstations or PC systems.

The tools were primarily developed for sensor applications. SENSIM [F6], CAPSIM [F10], CAEMENS-D [F15], SENSOR [F2] and NM/SEES [F12] use analytical approaches and/or the more general finite element method (FEM) to simulate the output characteristics of sensors for mechanical, thermal or magnetic quantities. Most of the above-mentioned tools concentrate on the simulation of capacitive or piezoresistive pressure sensors.

In the field of actuators of tool for the simulation of micro-pumps was developed. PUSI [F14] can simulate and optimise the complex dynamic behaviour of a micro-pump.

Other codes have been developed for the simulation of the production process, dynamical simulation of electrostatic actuators, handling of nonlinearities, temperature dependent behaviour and many other fields.

The main problem with these codes is that they are usually so specific that they can only be used for the problem they were designed for. One of the major problems is that as

1. See [F11]

of now there are almost no standard design components for micro-systems. There are components like linear and torsional combdrives as well as other very common parts but as the optimal design for those parts has yet to be found even these common components differ in shape from device to device. So if a simulation code was designed for one specific combdrive it is not necessarily applicable to every combdrive. Therefore, in most cases, it is easier to either write a new program or use one of the more general simulation packages.

F.2.5 Commercial Simulation Packages

In recent years responding to the growing interest in MEMS more commercial simulation packages have become available. These can be divided into two groups.

The first group consists of programs that have been specifically design for the use with MEMS. Most of these programs were first developed as a solver for a specific program. During the years these programs have been constantly expanded and/or combined with other programs to increase their functionality

Chapter F.3 provides an in-depth look at the most interesting programs of this group:

- MEMCAD
- IntelliSuite
- MEMS Pro

The members of the second group are general simulation packages that were designed for FEA of a large number of applications. Although not specifically designed for the use with MEMS they are frequently used for the simulation of MEMS components. In fact some are being extended to make the use with MEMS easier.

Chapter F.3 provides an in-depth look at the two programs of this group that are frequently used for the simulation of MEMS:

- ANSYS
- ABAQUS

As our MEMS group at DalTech neither has the time nor the experience to follow approaches one or two, one of these commercial packages will have to be chosen.

F.3 Analysis Packages

There are many analysis packages commercially available. They can be divided into packages that were specifically designed for analysis of MEMS and into general packages that can be used for analysing MEMS.

F.3.1 MEMS Packages

Of the available package a closer look is taken at two packages which are very powerful but also rather expensive. Also a MEMS product by Tanner EDA, the developer of L-Edit is introduced.

F.3.1.1 MEMCAD¹

MEMCAD is probably the most powerful MEMS simulation package available at the moment. Unfortunately it is also the most expensive. It was developed at the Massachusetts Institute for Technology in Cambridge, Massachusetts and is now distributed by Microcosm.

The latest version is MEMCAD 4.5 which is divided into four major components:

1. Construction
2. Device Modelling
3. Managed Simulation
4. Visualizer

Device Creation

In addition to a basic integrated 2D layout editor designs can be imported in either CIF or GDSII format. After defining the mask layers the process editor allows the creation of a flow simulating the fabrication process. Materials, mask dimensions, and etch profiles are entered into the process flow using a sequence of deposit and etch steps. All material properties can be taken from a database. Although MEMCAD is generally used with surface mi-

1. See [F8]

cromachining the correct specification of the fabrication process also allows for its use with bulk etching.

By importing the file into MemBuilder a 3D model is automatically rendered. It can be further modified if desired. Alternatively the complete layout can be defined in MemBuilder.

MemBuilder produces finite element mesh geometries for all problems involving mechanical deformation, thermal mechanics, fluidics, and fluid mechanics. Electrostatic problems are supported by boundary element methods.

Device Modelling

MEMCAD comes with an extensive set of solvers for all different types of problems. Not all of these solvers have to be purchased. Only the ones needed can be chosen.

The solvers are rich in features and allow many different types of solutions to be computed. Examples include:

- Capacitance and charge calculations
- Deformations from applied pressures or forces
- Coupled electromechanical solutions
- Solutions using full contact boundary conditions
- Modal analysis of the vibration frequencies of mechanical devices

Computed solutions can be viewed either in table matrix format or can be visualised using MEMCAD Visualizer.

Managed Simulation

The Simulation Manager allows the creation of batch run iterations by defining parameters to be varied during the simulation. Hereby model dimensions, temperature or voltage values or other boundary conditions can be varied without modifying the original base model. The complete set of solutions can be animated in Visualizer to clearly define trends and variations.

Other possible managed simulations include simulation of package models used to house MEMS devices and the extraction of spring constant parameters from a non-linear spring model.

Visualizer

The solver output for most MEMS models includes a significant amount of data for analysis and post-processing. With the Visualizer tool this data can easily be displayed in a variety of different 2D and 3D plots. Also the results data can be mapped graphically onto the original model and analyse the solution.

The Visualizer allows viewing of several different types of stresses, thermal variations, temperature gradients, pressures, current densities, and many other parameters, as well as electrostatic fields and mechanical deformations. An adjustable slice plane allows for a complete volume visualization.

After adjusting lighting and other parameters the results can be captured to a file in a variety of resolutions and formats.

Summary

MEMCAD seems to be the tool of choice for the simulation of MEMS devices. It features all the standard tools of good simulation packages for pre- and post-processing which have been enhanced for the simulation of MEMS. Especially the tool for defining the fabrication process simplifies the creation of the model tremendously. Its power, however, comes from the wide variety of solvers featured. Although they can only be coupled in specific combinations they allow for the simulation of a wide variety of problems.

However, the complexity of the program also makes it more difficult to get results without acquiring some level of experience first. In fact Microcosm Technologies even requires that potential customers attend a 3 to 5 day training course before demo requests are honoured. Due to this steep learning curve MEMCAD is probably not the tool to enter the field of simulation with. It might be better to start off with a standard simulation package and wait until the specific requirements of the project are determined to see if they could be fulfilled easier with MEMCAD.

F.3.1.2 IntelliSuite¹

IntelliSuite is a software package developed by the IntelliSense corporation for the design and the simulation of MEMS. It consists of the following parts:

- Mask Layout Editor
- Process Simulation
- Anisotropic Etch Simulator
- Material Database
- Device Analysis

Comprehensive Mask Layout Editor

The mask layout editor allows import and export of GDSII and DXF files as well as other standard vendor formats. It features local and global mask editing (cells) as well as the visualization of multiple mask layers while operating on a certain vendor. It runs on UNIX and Windows NT and is available as a stand-alone package.

Process Simulation and Visualization

In IntelliSuite MEMS structures are created by using process information, mask layouts and by defining the process steps used for manufacturing the devices in a fabrication facility IntelliSuite provides 3D visualizations of the structure at any process step to aid in detailed device design.

In addition to the process visualization, a fabrication simulation is automatically performed which is able to predict fabrication-induced effects often playing a significant role in the functionality of the built device.

AnisE

The AnisE module in IntelliSuite can simulate 3D bulk silicon anisotropic etching. It is capable of predicting the effects of etchant temperature, concentration, and etch time on the final geometry. It also allows for the modelling and visualization of corner compensation

1. See [F5]

and process tolerances with its graphical user interface. Results can be exported in DXF and VRML format. AnisE is also available as a stand-alone product.

MEMaterial

MEMaterial was the first module of the IntelliSuite. It was developed to address the issue of lack of thin-film material information. It features an extensive thin-film material database, a multi-dimensional estimation routine, 2D and 3D visualization as well as unit conversion.

Device Performance Analysis

After performing fabrication simulation, IntelliSuite performs fully-automatic creation of the 3D meshed structure based on the fabrication steps and mask layouts. After the creation of the preliminary mesh users can locally refine the mesh in areas of interest. A special feature is the ability to refine the mechanical and electrostatic mesh separately.

In addition to the automatic meshing engines the model can also be generated and meshed using an interactive mouse and menu driven interface.

After the creation of the 3D numerical models and mesh the analysis modules provide fully coupled thermoelectromechanical analysis of the structure. The following types of analyses can be performed:

- Electrostatic
- Thermo-Mechanical
- Coupled-Thermoelectromechanical
- Fluidic
- Electromagnetic

Summary

IntelliSuite certainly is an interesting tool for MEMS simulation. It provides all necessary features without being as huge as MEMCAD. One of the key features for modelling and simulation of MEMS is the process simulation which definitely would make everything

much easier. Also very positive is the capability of the device performance analysis which features everything the DalTech MEMS Group would require but nothing more.

On the other hand, two parts of the suite already exist at DalTech in similar form. The mask layout editor is certainly comparable to L-Edit. And although our on-line etch simulator might not have as many features as AnisE it is sufficient for our purposes.

F.3.1.3 MEMS Pro¹

MEMS Pro is a MEMS design package by Tanner EDA. It is not really a simulation package. But as it is basically an add-on to L-Edit, the layout editor that is used in the MEMS Group here at DalTech, a short description of some of its interesting features follows.

While L-Edit has many good features and is rather easy to use it was clearly designed for the creation of microchips not micromachines. Many features that would be very helpful for designing micromachines are missing.

One major example is the cross-section tool. It only allows to view cross-sections in one direction. If any other direction is desired the whole cell has to be rotated until the desired direction equals the one direction L-Edit can handle. On top of that the cross-section tool can only display boxes, rectangular polygons. Angular polygons as well as circular layouts are completely ignored. As micromachines usually involve a high number of angular polygons and circular layouts the cross-sectional tool is more or less useless for the designing MEMS. The design of micromachines would be much easier with a tool that allowed for 3D vision of the design.

Also the export features of L-Edit are clearly aimed toward the creation of microelectronics. The only formats it supports are CIF and GDSII, both formats for the definition of microchip designs. Export to analysis software such as ANSYS is not possible as this is not necessary for microelectronics.

To overcome these shortcomings Tanner EDA developed MEMS Pro. After a disappointing first release the just released version 2 looks very promising.

1. See [F13]

Drag and Drop from Schematic to Layout

In the new release 2 of MEMS Pro that was released in April 1999 Tanner EDA added S-Edit to its MEMS Pro package. S-Edit provides the ability to draw schematics of MEMS devices by using a library of standard parts. Further more these can be transferred into L-Edit by drag and drop for automatic layout creation.

Fully Integrated Solid Modeller

Also version 2 introduces a new solid modelling feature that allows the creation of three dimensional models. It uses the MEMS device layout geometry from L-Edit and one of the supported foundry process descriptions to create this model. The foundry process description is also customizable. Surface and bulk micromachining steps such as deposit, etch, mechanical polish, etc. can be viewed without the need for any other visualization software.

MEMS Block Place and Route

Another new feature is the block place and route feature. Amongst other features it includes:

- Performance-driven automatic routing
- Connectivity-driven manual routing
- On-line signal integrity analysis

Built-In Optimiser

According to Tanner EDA new optimization algorithms incorporated in MEMS Pro V2 automatically determine device or process parameters that will optimise the design performance. With the new Optimization Wizard parameters are defined, optimization criteria are set up and optimization algorithms are chosen.

Link to Ansys

After the creation of the three dimensional model it is possible to mesh it and pass it on to ANSYS for further analysis. This feature is supposed to be further improved during the co-operation between Tanner EDA and Ansys, Inc. (See F.3.2.1).

Summary

If Tanner EDA can keep the promises made for release 2 of MEMS Pro it would certainly be worth taking a closer look at. Unfortunately a demo version will not be available until June and the current demo version of release 1 is a rather boring self running demo of L-Edit and T-Spice. The only interesting part of release 1 was a few macros for the automatic creation of common MEMS elements (combdrives, etc.) similar to the MUMPs CAMEL library.

Nevertheless a closer look should be taken at the demo of release 2 when it becomes available in June. It might actually make the designing with L-Edit a lot more comfortable. If it is sold for a reasonable price it might be worth buying.

F.3.2 General Packages

While the previous section gave a description of various simulation programs specifically designed for the use with MEMS this section introduces two general simulation packages. Of the numerous general simulation packages a closer look is taken at ANSYS and ABAQUS. Two packages that are frequently mentioned in articles about MEMS simulation.

F.3.2.1 ANSYS¹

ANSYS is one of the worlds leading finite element analysis packages. Especially at universities it is a very common analysis tool. This is further encouraged by the fairly cheap price packages for universities which consist of the complete program with a limitation of nodal points.

Although ANSYS was not specifically design for the use with MEMS the flagship product ANSYS/Multiphysics features tools for coupled-field analyses in its latest version ANSYS 5.5.

1. See [F1]

Multiphysics

The ANSYS/Multiphysics package combines all the features of the single packages ANSYS/Mechanical, ANSYS/FLOTRAN, and ANSYS/Emag. It also includes the ANSYS/PrepPost package which provides with good tools for pre- and post-processing.

In addition to the features of those packages in the fields of structural, thermal, acoustic, fluid, magnetic and electrostatic analysis it features several coupled-field capabilities. Also the data of all analyses is stored in a single database file (physics file) which simplifies the interaction of the different solvers.

Unfortunately for the simulation of MEMS, one very important coupled-field analysis is not yet supported by ANSYS. This is the electromechanical coupling. But although no official announcements have been made there is hope that this feature will be included in the next version. This is due to cooperation agreements that Ansys, Inc., signed with leading companies in the MEMS field, Tanner EDA, MEMSCAP and Mentor Graphics, earlier this year.

Ansys and Tanner

In January this year Ansys, Inc., and Tanner EDA, the market leader in PC-based design software for MEMS announced their forming of a strategic partnership. With the goal of accelerating the growth of microsystem product design, the two companies signed a joint marketing and development agreement to deliver “a new generation of design and analysis capabilities”.

In its announcement of version 2 of MEMS Pro Tanner EDA states:

... Responding to the petitions of the MEMS design community, Tanner EDA has joint forces with ANSYS to deliver an unparalleled combination of the leading mechanical and electrical CAE tools for a complete microsystems design solution. You will be able to design your MEMS component in L-Edit, create a solid model, mesh the model and then seamlessly pass the model to the powerful ANSYS engine for finite element analysis. [F13]

Ansys, MEMSCAP and Mentor Graphics

In April this year Ansys, Inc., MEMSCAP, S.A. and Mentor Graphics Corporation announced a partnership to “create a complete and easy-to-use engineering environment for design of micro-electro-mechanical systems (MEMS)”. Furthermore the announcement states:

The three partners will work to fully integrate all tools and intellectual property into a complete MEMS design environment, expected to be available by third quarter. The products will enable design teams to seamlessly move from system design to layout, layout to finite elements modelling with ANSYS/Multiphysics, and then translate results into hardware description languages (HDLs) to permit detailed simulation. The environment will support industry-specific intellectual property packages from MEMSCAP for rapid development of applications in telecommunications and other arenas. [F1]

Licensing Options

The following Table shows the different licensing options:

Table F-1: ANSYS Licensing Options^a

	University Low	University High	Research Faculty/Student
Description/Limitations (see notes below)	The program is to be used for educational and research purposes.	The program is to be used for educational and research purposes.	This option is Only for research that is in direct support of acquiring a degree. The program is to be used for research in the public domain and requires submission of annual and final reports to ANSYS, Inc.
License Fee (per year)	C\$1100	C\$1800	C\$4200
Maximum Node Number	8,000 (A) 8,000 (E) 16,000 (F)	16,000 (A) 16,000 (E) 32,000 (F)	64,000 (A) 64,000 (E) 128,000 (F)
Maximum h-Element Number	8,000 (A) 8,000 (E) Unlimited (F)	16,000 (A) 16,000 (E) Unlimited (F)	64,000 (A) 64,000 (E) Unlimited(F)
Maximum p-Element Number	2,000 (A) N/A (E) N/A (F)	4,000 (A) N/A (E) N/A(F)	16,000 (A) N/A (E) N/A (F)

a. see [F3]

Notes:

1. A University license cannot be used for consulting or any other commercial activity.
2. The license term is the academic year from September 1 to August 31.
3. The license fee includes Ansys/Mechanical (A), Emag (E) and FLOTRAN (F).
4. Options 1 and 2 do not include User Element capability. Option 3 does if applicable.
5. Customer support is not included.
6. p-Element technology is only applicable to linear structural analysis.

Summary

Although ANSYS was not specifically designed for the use with MEMS its reasonable price together with its broad range of features makes it the ideal tool to start up a simulation project. The fact that the university package consist of the full version of ANSYS/Multi-physics with just a limitation of the maximum number of usable nodal points is perfect to explore all the different areas of simulation that are possible

Also the fact that Ansys, Inc., signed two cooperation agreements with three major companies in the MEMS area suggests that future versions of ANSYS will be even better for the simulation of MEMS devices.

F.3.2.2 ABAQUS¹

ABAQUS is like ANSYS one of the worlds leading finite element packages. It is also the second most mentioned program in articles on MEMS simulation. However, its when contacted the developers of ABAQUS recommended to use MEMCAD or IntelliSuite rather than ABAQUS for the simulation of MEMS.

Summary

ABAQUS is a very powerful FEA package that can very well be used for the simulation of part of microsystems. Especially its non-linear analysis features are very advanced. The lack of a wide variety of coupled domain analyses, however, makes ABAQUS not the perfect candidate for the simulation of MEMS. On the other hand, if an ABAQUS installation already exists in a department it would still be a good tool to start a simulation project with.

1. See [F4]

F.3.3 Comparison

Although the presented packages are quite different in contents they all include some of the features that are important for simulating MEMS devices. The following table list some of the key features that are important for MEMS simulation.

Table F-2: Comparison of Some Important Features of the Different Programs

	MEMCAD	IntelliSuite	MEMS Pro	ANSYS/Multiphysics	ABAQUS
Layout Editor	yes	yes	L-Edit	no	no
Layout Import/Export (CIF, GDSII, etc.)	yes	yes	yes	no	no
Process Simulation	yes	yes	yes	no	no
Analysis Pre-Processor	yes	yes	Export to Ansys	yes	yes
Structural Analysis	yes	yes	no	yes	yes
Fluid Analysis	yes	yes	no	yes	yes
Electromagnetic/Electrostatic Analysis	yes	yes	no	yes	yes
Electro-Structural Analysis	yes	yes	no	no	no
Fluid-Electro Analysis	yes	no	no	no	no
Fluid-Structural Analysis	no	no	no	yes	pore flow only
Piezoelectric Analysis	yes	no	no	yes	yes
Analysis Post-Processor	yes	yes	no	yes	yes
Result Export (TIFF, PS, etc.)	yes	yes	no	yes	yes

As can be seen from Table F-2: MEMCAD and Intellisense cover most of the important features including some coupled analyses whereas MEMS Pro is basically a pure layout and design package. ANSYS does not feature any MEMS specific tools but a large amount

of coupled analyses whereas ABAQUS is a pure finite element package not allowing for coupled analysis (except pore fluid flow-mechanical).

F.4 Conclusion

The previous two chapters introduced the problems that might be encountered during performance analysis of MEMS and gave an overview of different approaches as well as different software for the simulation. In this section the status quo at the DalTech MEMS group is presented and some recommendations are given.

F.4.1 Status Quo

At the moment the DalTech MEMS group owns the following MEMS related software:

- L-Edit - Mask layout editor
- ANSYS/ED - Student version of ANSYS (limit: 100 elements)
- On-line Etch Simulator - Self-developed

L-Edit is a quite comfortable tool for the design of mask layouts but it clearly lacks a 3D visualization tool. The cross-section tool works fine for extremely simple devices but is of no use for more complex designs.

ANSYS/ED is very good to get comfortable with the user interface but is far to limited for the tasks at hand.

The On-line Etch Simulator is a fine tool that is completely sufficient for our requirements. Also the future area of work will shift from bulk to surface micromachining.

F.4.2 Recommendations

Due to budget limitations it will probably not be possible to buy a license for MEMCAD or IntelliSuite. Also these programs, especially MEMCAD, provide a lot of features that would not be used which seems like a waste of money. Although especially the process simulation and the 3D model of the layout would be very nice to have.

ANSYS is definitely the choice over ABAQUS as it features more coupled field analyses and the ANSYS/ED version is already available in the lab. The very good prices for the university packages also favour ANSYS. The one year license also leaves the possibility to change to another program if ANSYS should not be sufficient any more in a year.

In FEA there are two basic approaches to meshing: shell elements and solid elements. Shell elements are 2D elements with an assigned thickness. Unfortunately the theory only works well for element dimensions that are large compared to the element thickness. As MEMS sometimes involve parts with dimensions that come close to their thickness (e. g. the fingers of a combdrive) solid elements would have to be used. The downside of the solid elements is the necessity for more than one layer of elements to adequately simulate bending. This usually results in a large number of elements.

Considering this the recommendation for ANSYS would be to buy the *University High* package. The *Research Student* package would be even better but probably too expensive.

Using the existing C-program for the conversion of a L-Edit CIF-file into a postscript file it should not be too difficult to write a program that creates an ANSYS session file to set up the geometry in ANSYS. Using a small sample file this could even be done with ANSYS/ED before the acquisition of ANSYS/Multiphysics in the fall in case there is no possibility to get the university package in the summer instead of the fall.

Another recommendation would be to take a closer look at MEMS Pro. If the new version actually keeps what the developer promise in their promotion it would be a really nice tool to accompany L-Edit.

F.5 References

- [F1] Ansys, Inc. (1999). *ANSYS Website*. Available: <http://www.ansys.com> [1999].
- [F2] Folkmer, B., H.-L. Offereins, H. Sandmaier, W. Lang, P. Groth, and R. Pressmar. 1992. A Simulation Tool for Mechanical Sensor Design. *Sensors and Actuators*. A32: 521-524.
- [F3] Ginder, J. (1998, February 19). Ansys Licensing Options. Fax Transmission to James Wylde.
- [F4] Hibbitt, Karlsson & Sorensen, Inc. (1999). *ABAQUS Website*. Available: <http://www.abaqus.com> [1999].
- [F5] IntelliSense Corporation. (1999). *IntelliSuite Website*. Available: <http://www.intellisense.com> [1999].
- [F6] Lee K. W., and K. D. Wise. 1982. SENSIM: A Simulation Program for Solid-State Pressure Sensors. *IEEE Trans. Electron Devices*. 29: 42-47.
- [F7] MEMS Clearinghouse. (1999). *Industry News (Website)*. Available: <http://mems.isi.edu/marketplace> [1999].
- [F8] Microcosm Technologies, Inc. (1999). *MEMCAD Website*. Available: <http://www.memcad.com> [1999].
- [F9] Pedersen, M., W. Olthuis, and P. Bergveld. 1995. On the Simulation of Subminiature Condenser Microphones Using Finite Differences. In *Simulation and Design of Microsystems and Microstructures*. Billerica, MA: Computational Mechanics. 185-192
- [F10] Puers, B., E. Petersen, and W. Sansen. 1989. CAD Tools in Mechanical Sensor Design (CAPSIM). *Sensors and Actuators*. A17: 423-429.
- [F11] Sandmaier, H., H. L. Offereins, and B. Folkmer. 1993. CAD Tools for Micromechanics. *Journal for Micromechanics and Microengineering*. (3) 3: 103-106.
- [F12] Schwarzenbach, H. U. 1993. NM/SESES Program System for Semiconductor Sensor Simulation. *Preprint*. NM Numerical Modelling GmbH.
- [F13] Tanner EDA. (1999). *MEMS Pro Website*. Available: <http://www.tanner.com/EDA> [1999].
- [F14] Zengerle, R., M. Richter, F. Brosinger, A. Richter, and H. Sandmaier. 1993. Performance Simulation of Microminiaturized Membrane Pumps. In *Proceedings of Transducers '93, Yokohama, Japan, 1993*. 106-111.
- [F15] Zhang, Y., S. B. Crary and K. D. Wise. 1990. Pressure Sensor Design and Simulation Using the CAEMENS-D Module. In *Digest IEEE Solid-State Sensor and Actuator Workshop, Hilton Head, SC, 1990*. New York: IEEE. 32-35.